Sensitivity to technology and adjustability of substrate integrated waveguides Butler matrices, in PCB substrates at 28 GHz and in benzocyclobutene above-IC interposers at millimetre waves

Giuseppe Acri

Université Grenoble Alpes

THÈSE

Pour obtenir le grade de

DOCTEUR DE L'UNIVERSITE GRENOBLE ALPES

Spécialité : **Optique et Radiofréquence**

Arrêté ministériel : 25 mai 2016

Présentée par

Giuseppe ACRI

Thèse dirigée par **Florence PODEVIN, Maître de conférences, Université Grenoble-Alpes-Grenoble INP**, et
codirigée par **Emmanuel PISTONO, Maître de conférences, Université Grenoble-Alpes**

préparée au sein du **Laboratoire RFIC-Lab**
dans **l'École Doctorale E.E.A.T.S.**

Sensibilité à la technologie et accordabilité des matrices de Butler en guide intégré dans le substrat, déclinées sur substrat PCB à 28 GHz et sur interposer above-IC benzocyclobutène aux fréquences millimétriques

Thèse soutenue publiquement le **20/07/2020,**
devant le jury composé de :

M. Sylvain Bourdel
Professeur à Université Grenoble Alpes - Grenoble INP, Président
M. Ronan Sauleau
Professeur à Université de Rennes 1, Rapporteur
M. Thierry Parra
Professeur à Université Toulouse 3, Rapporteur
Mme. Anne-Laure Franc
Maître de conférences à Toulouse INP, Examinatrice
M. Ke Wu
Professeur à Ecole Polytechnique de Montréal, Examinateur
M. José-Luis Gonzalez Jimenez
Ingénieur à CEA-Léti, Examinateur
Mme. Florence Podevin
Maître de conférences à Université Grenoble Alpes-Grenoble INP, Directrice de thèse
M. Emmanuel Pistono
Maître de conférences à Université Grenoble-Alpes, co-directeur de thèse

Membres Invités :

Mme. Anne-Sophie Grimault-Jacquin,
Maître de conférences à Université Paris-Sud, invitée
M. Philippe Ferrari
Professeur à Université Grenoble-Alpes, co-directeur de thèse
M. Luigi Boccia
Professeur assistant à Universita' della Calabria, co-directeur de thèse

To my beloved parents Antonio and Angela

"I look for a moment that is worth a man's life."

— Giacomo Casanova

ACKNOWLEGEMENTS

It is my pleasure and privilege to thank the many persons who made this thesis possible. First of all, I would like to express my sincere gratitude to my supervisors, Mrs. Florence Podevin and Mr. Emmanuel Pistono, for continuous support and for providing me an opportunity to work for a Ph.D in RFIC-Lab, Université Grenoble Alpes . I would like to also acknowledge Prof. Philippe Ferrari and Mr. Luigi Boccia, without them I would not be in France. It was a true pleasure to work under your all supervision, you have made me feel comfortable and always motivated. I express my sincere thanks to you for your advice, consistent encouragement, and understanding throughout my thesis.

I would like to thank my Ph.D. thesis reviewers, Prof. Ronan Sauleau from Université de Rennes 1 and Prof. Thierry Parra from Université Toulouse 3, for having accepted to examine this work. Thanks to Dr. Anne-Laure Franc, Mr. José-Luis Gonzalez Jimenez and Prof. Ke Wu for accepting my invitation to become part of my jury as well. I express my thanks to Prof. Sylvain Bourdel for being the president of my thesis jury.

I would also acknowledge the ANR TERAPACIPODE project, for the grant ANR-16-CE24-0031-01 of the French Agence Nationale de la Recherche. In the same framework, I would like to thank Mr. Frédéric Aniel, Mr. Nicolas Zerounian and Mrs. Anne-Sophie Grimault- Jacquin from the Center for Nanoscience and Nanotechnology for the samples preparation that was performed.

My sincerest thanks go to Microwave Lab in University of Calabria for giving me the possibility to work on antenna design during my Ph.D and to form me throughout my master of Sc. formation journey. Especially, I thank Dr. Luigi Boccia, Pr. Giandomenico Amendola, Dr. Emilio Arnieri and all my colleagues, such as Domenico, Ciccio Greco, Carmine, Giuseppe and Vincenzo for supporting me from the work point of view and mentally, as well.

I also thank Estelle Lauga-Larroze, Jean-Daniel Arnould and all RF team. I thank Serge for the help with solving the problems with the simulation server in IMEP-LaHC. I take this opportunity to also thank the RFIC-Lab and IMEP-LaHC administration for administrative help.

Moreover, I would like to thank the technical team, Mr. Nicolas Corrao and Mr. Loïc Vincent, for useful help and productive interactions that are also the unmissable contribution for my thesis success.

My sincere thank also goes to my office mates and friends in IMEP-LAHC and RFIC-Lab, Licinius, Dimitris, Luca, Gianluca, Miltos ,Walid, Aziz, Vipin, Matthieu, Isaac, Marc, Julio, Mah Di, Mohamad, Anh Tu, and and so on. I am especially grateful to work alongside you.

Thank you to all my friends for the joy and encouragement that you shared with me in so many occasions and across these years. Especially, I would like to thank Frollo, Salvatore, Cerro, Dor, Masto Arturo, Giuseppe Cuccaro, Anastasia, Angela, Jessica, Franco, Giovanni for always supporting in the pursuit of my aspiration.

Last, but definitely not least, my deepest gratitude and appreciation are for my parents Antonio Acri and Angela Chiarelli, my sister Alessandra, my Volpe and my angel grandmother Nonna Anita. Thank you for your unlimited love, listening, understanding and supporting me for better and for worse. Finally, I would like to say that without your caring contribution this thesis would not have been possible at all.

SENSITIVITY TO TECHNOLOGY AND ADJUSTABILITY OF SUBSTRATE INTEGRATED WAVEGUIDES BUTLER MATRICES, IN PCB SUBSTRATES AT 28 GHZ AND IN BENZOCYCLOBUTENE ABOVE-IC INTERPOSERS AT MILLIMETRE WAVES.

Abstract

Networking technologies have become increasingly omnipresent over the past two decades. In particular, 5G (fifth generation) is expected to support significantly faster mobile broadband speeds, lower latencies and hundreds of times more capacity than current 4G (fourth generation) while also enabling the full potential of the Internet of Things. Specifically, the underemployed spectrum in the millimeter-wave (mm-wave) frequency bands (30-300 GHz) might be seen as a potentially profitable solution for achieving the aforementioned goals. In such a context, the switched-beam antenna (SBA) systems have become of great interest because they can achieve high spectral efficiency and increase the capacity of wireless communication systems. More specifically, Butler matrix (BM) is one of the most important multiple beam forming networks, which has been intensively explored and extensively employed in communication systems due to its unique properties as perfect matching, isolation, and equal power division, that can be obtained at the same time.

The work achieved in this PhD thesis was focused on the conception of a Butler matrix, for mm-wave applications in SIW topology. Two frequency bands were mainly addressed for that purpose. The first one is the band around 28 GHz, that is suited for 5G, where an extended beam agility concept was introduced for 4x4 Butler matrix, in PCB-SIW technology, to achieve a better spatial resolution, as compared to a 4x4 conventional system. The second one is the WR10 band (75 GHz-110 GHz), as well as some extra-bands beyond, for which the use of intermediate packaging platforms, so-called interposers, allow the frequency rising as compared to the conventional PCB technologies. In both, the proposed structures were detailed, theoretical analyses were developed, and simulation and measurement works were carried out, with retro-simulations when needed, which permitted to validate the proposed concepts. One of the main goals of this manuscript is to enhance the spatial antenna coverage and the performance of the beam forming system as compared to its conventional counterpart while keeping almost unchanged the surface (reduced costs and design complexity). Another goal is to study the sensitivity of the system, so that the weak points of the BM are revealed.

In the first chapter of this thesis, BM solutions for RF and mm-Wave circuits were presented, and beam-steering enhanced ability BMs was detailed. In the second chapter, attention focuses on a detailed sensitivity BM study based on a Monte Carlo approach and a proposed solution for extended beam Butler matrices well suited to SIW technology. In the third chapter, the pros and cons of continuous and digital phase shifting are discussed and a 28-GHz ,1-bit, SIW, phase shifter using PIN diodes, is designed and tested as a solution to be used in the extended beam matrix. In the fourth chapter, the design blocks for 28 GHz SIW Butler matrix were introduced and measured, along with the entire BM measurements. In the fifth chapter, benzocyclobutene (BCB) SIW useful for Butler matrix blocks were designed and measured in WR10 and WR5

bands, which show the very interesting performance of such an interposer. Even coupler and crossover were fabricated and measured in WR10 band. As a prospect, the extended beam agility BM concept could be implemented in BCB interposer or other kind of interposers as metallic nanowire membranes (MnM) for sub-THz applications, to test the feasibility.

Résumé

Les technologies réseau sont devenues de plus en plus omniprésentes au cours des deux dernières décennies. En particulier, la 5G (cinquième génération) devrait supporter des vitesses haut débit nettement plus rapides, des capacités de transfert cent fois plus élevées et des retards plus faibles que la générations 4G précédente tout ceci permettant d'utiliser le plein potentiel de l'Internet des Objets. Plus précisément, le spectre sous-employé des bandes de fréquences millimétriques (mm-wave) (30-300 GHz) pourrait être considéré comme une solution potentiellement rentable pour atteindre les objectifs susmentionnés. Dans un tel contexte, les systèmes d'antennes à faisceau commuté sont devenus d'un grand intérêt parce qu'ils peuvent atteindre une plus grande efficacité spectrale et améliorer le bilan de puissance des systèmes de communication sans fil. Plus spécifiquement, la matrice de Butler (BM) est l'un des réseaux de formation de faisceaux multiples les plus intéressants, intensivement exploré et largement employé dans les systèmes de communication en raison de ses propriétés conjointes d'adaptation, d'isolation, et d'équipartition de puissance.

Le travail réalisé dans le cadre de cette thèse de doctorat se concentre sur la conception de matrices de Butler en topologie SIW pour les applications millimétriques. Plusieurs bandes de fréquence ont été abordées à cette fin. La bande autour de 28 GHz intéresse particulièrement la 5G. Ainsi, le concept de matrice étendue en technologie PCB-SIW est introduit pour la BM 4x4, permettant d'atteindre une meilleure résolution spatiale que le simple système 4x4. La bande WR10 (75 GHz-110 GHz) ainsi que quelques bandes millimétriques au-delà ont également été étudiées. Pour ces dernières, le recours à des substrats intermédiaires dédiés au millimétrique, appelées interposeurs, s'est révélé indispensable. Dans les deux cas, les structures proposées ont été détaillées, des analyses théoriques élaborées et les résultats de simulation confortés par la mesure, accompagnés de rétro-simulations si besoin, dans le but de proposer des preuves de concept. L'un des principaux objectifs de ce manuscrit est d'améliorer la couverture spatiale de l'antenne et la performance du système de formation du faisceau par rapport à son homologue conventionnel tout en gardant presque inchangé la surface du réseau (coûts réduits et complexité de conception). Un autre objectif est d'étudier la sensibilité du système afin de révéler les points faibles de la matrice de Butler.

Le premier chapitre de cette thèse présente un état de l'art des dites matrices, RF et mm-wave , et détaille les solutions permettant d'étendre l'orientation du faisceau. Dans le deuxième chapitre, l'attention se concentre sur une étude Monte Carlo de sensibilité de la BM quasiment exhaustive. Dans le troisième chapitre, les avantages et inconvénients du changement continu et/ou digital de phase sont discutés et un déphaseur SIW 1-bit, 28-GHz, utilisant des diodes PIN, est conçu et testé. Ce déphaseur est un des blocs phare de la matrice de Butler étendue. Le quatrième chapitre présente la conception et la mesure des blocs de la BM à 28 GHz ainsi que

l’ensemble des mesures du système complet étendu. Dans le cinquième chapitre, des guides, coupleurs et crossovers SIW sur interposeur BCB (benzocyclobutene), tous blocs de la matrice, ont été conçus et mesurés en bande WR10 et WR5. Ils confirment les performance très intéressante du BCB. En perspective, le concept de matrice de Butler étendue pourrait être mis en œuvre sur interposeur BCB mais aussi dans d’autres technologies telles que les membranes à nanofils métalliques (MnM) pour des applications sous-THz.

Table of contents

Glossary

Beam-Forming Network: BFN
BenzoCycloButene: BCB
Butler Matrix: BM
Fifth Generation: 5G
Fourth Generation: 4G
Internet of Things: IoT
Line-of-Sight: LoS
millimeter-Wave: mm-Wave
MultiBeam Antenna: MBA
multiple beam forming network: MBFN
Non-Line-of-Sight: NLoS
Phase Shifter: PS
Printed Circuit Board: PCB
Radio frequency: RF
Side lobe level:SLL
Signal-to-Interference-plus-Noise Ratio: SINR
Slow-wave SIW:SSIW
Substrate Integrated Waveguide: SIW
Switched-Beam Antenna: SBA

Introduction

Networking technologies have become increasingly omnipresent over the past two decades. Recent years have seen the attachment of a big range of devices to the network. The latter ones have included vehicles, household appliances, medical devices, electric energy meters and controls, street lights, traffic controls, smart TVs and digital assistant devices. One of the most dynamic and exciting developments in information and communications technology is the advent of the Internet of Things (IoT).

In parallel to the growth in the number of interconnected devices, there has been a strong demand for higher data rates, of hundreds of times more capacity compared to current 4G (fourth generation) cellular networks. Indeed, 5G (fifth generation), and future mobile data generations for communication, are expected to support significantly faster mobile broadband speeds and lower latencies than previous generations while also enabling the full potential of the IoT. In this context, lower latency of around one millisecond, reduced energy consumption, improved reliability and security and higher scalability are required. Following this trend, hundreds of Giga-bit-per-second (100 Gbps) and even Terabit-per-second (Tbps) links are expected to become a reality, in the next years.

Thus, new spectral bands as well as advanced physical layer solutions are required to support these demands for future wireless communications. Specifically, the underemployed spectrum in the millimeter-wave (mm-wave) frequency bands (30-300 GHz) might be seen as a potentially profitable solution for achieving the aforementioned goals.

Historically, mm-wave bands were excluded for cellular usage mainly due to concerns regarding short-range and non-line-of-sight (NLoS) coverage issues. Today, mm-wave communication systems have been officially adopted in 5G cellular systems, which have, more probably, a frequency band range going from 28 GHz up to 86 GHz, with carriers or bandwidths as 28 GHz, 38 GHz, 71–76 GHz and 81–86 GHz.

In such a context, the switched-beam antenna (SBA) systems have become of great interest because they can achieve higher spectral efficiency and increase the capacity of wireless communication systems. The standard SBA array is generally made up of three parts: switches, a beam-forming network (BFN), and an antenna array. The BFN is the core part of the SBA array as the main beam will point at different directions based on the signals created by it.

Butler matrix (BM) is one of the most important multiple beam forming networks (MBFN), which has been intensively explored and extensively employed in communication systems due to its unique properties as perfect matching, isolation, and equal power division, that can be obtained at the same time. Compared with other MBFNs, such as Blass matrix, Nolen matrix, and Rotman lens, BM has some attractive features such as the realizable bandwidth, structural simplicity and very low current consumption.

A typical $2^N \times 2^N$ BM connecting a 2^N-element linear antenna array can generate 2^N independent beams with spatially orthogonal directions from the same aperture. Because of the pretty large number of couplers and crossovers used in the network, the circuit complexity increases dramatically as the desired number of beams increases. One of the most common BM

is the 4x4, which provides ±48.6° and ±14.5° of main beam direction, if its radiating elements are spaced by $\lambda_0/2$ between each other, λ_0 being the free-space wavelength.

Nowadays, the spatial coverage becomes very significant when dealing with the current wireless technologies, which aim for as much spatial resolution as possible. In that case, two ways are possible to enhance it: the first one, is to increase N, e.g. N=3, 4 and so on, but with a consequent increase in the circuit complexity; second one is to provide the antenna arrays with more progressive output phase shifts than in a conventional 4x4 BM, while keeping the 4x4 BM structure and size. The second way expands the beam controllability, which is possible if using particular phase shifters in the network and represents one of the best solutions, in terms of circuit complexity, size and costs.

In this work, the main targeted frequency is 28 GHz that is suited for both 5G mobile communications and IoT applications, and require low-loss PCB. A second strand concerns frequency rising, up to the sub-THz, for 6G technology, wireless sensor networks and automotive radars; intermediate platforms, so-called interposer, are used for that purpose. Among them the BenzoCycloButene (BCB) above-IC platform appears to be a very promising technology. In both cases, the choice for a substrate integrated waveguide (SIW) topology enables to preserve electromagnetic immunity. In this context, the focus of this PhD thesis is to study the "sensitivity to technology and adjustability of substrate integrated waveguides Butler matrices, in PCB substrates at 28 GHz and in benzocyclobutene above-IC interposers at millimetre-wave". PCB –based demonstrators were fabricated in Cirly factory (Lyon, France) while BCB-based demonstrators were developed by the laboratory C2N. Design blocks and complete systems were designed under the supervision of RFIC-Lab (Grenoble, France) and Microwave Lab (Arcavacata di Rende, CS, Italy). Measurements were performed on the open platform CIME-Nanotech (Grenoble, France).

Based on these previous considerations, the BM research topic led to the following outline.

In the first chapter, the multibeam antenna (MBA) system role and its applications in radio frequency (RF) circuits is made. An introduction of the theory for a conventional BM and other BFNs is given. Then the most classical SIW (substrate integrated waveguide) BM structures are compared to each other based on whether they are realized on a single-layered or multi-layered technology. Furthermore, the chapter provides a distinction between microstrip and SIW BM topologies and most used techniques to improve the performance. Finally, extended beam agility BMs are then detailed and they are compared to each other. It allows demonstrating ever-increasing researcher's interests concerning this system in recent years.

In the second chapter, attention focuses, thus, on a concept of tunable BM based on reconfigurable phase shifters to enhance the spatial resolution and beam controllability. First, a detailed sensitivity study of a conventional BM system is proposed, by considering a Monte Carlo approach based on the impact of the crossover isolation on the overall BM performance. In particular, this sensitivity study allows highlighting the impact of each sub-circuit of the BM (couplers, crossovers, phase shifters) on the radiation pattern. Analytical electromagnetic equations are then derived to prove the concept. Second, the theory of the novel extended beam

BM concept is introduced. This concept becomes much more interesting if associated with reconfigurable radiating elements, which are capable of improving the lateral beam-steering generation of the antenna array. Then, in order to show the interest of the proposed concept, a state-of-the-art of reconfigurable beam antenna is proposed.

The third chapter is dedicated to the presentation of tunable phase shifters for RF extended beam capability BM, based on SIW technology. First, a brief state-of-the-art about phase shifters (PSs) is made herein, showing the difference between continuous and digital ones and their main advantages based on SIW technology and also their limitations. The chapter highlights the design methodology for a novel SIW PSs at 5.8 GHz and 28 GHz, showing the difficulty to rise the frequency. A detailed study on how to optimize the phase shifter will be introduced, along with the presentation of the DC bias circuit, at 28 GHz.

In the fourth chapter, the design blocks for 28 GHz SIW Butler matrix are introduced. Firstly, 3-dB coupler and crossover are realized in short-slot topology. Secondly, all the phase shifters included in the system are designed and fabricated. For a proof-of-concept, for each 1-bit phase shifter, two not reconfigurable phase shifters are realized, representing either a RF path or the other. Afterwards, they are arranged in the system with the couplers and crossovers. The latter results in two realized Butler matrices, each one providing four different progressive output phases. In the last part of the chapter, the measurements of all the aforementioned devices give rise to a detailed analysis of the results and of their impact on the radiation pattern of the array antenna system.

The fifth chapter introduces a new type of 3D platform called interposer, which is able to provide 3D integration while overcoming the frequency rising issue with respect to PCB technology. Firstly, a brief review about the current interposers is introduced. Then, the BCB interposer technology is presented and the design of SIW lines in three different mm-wave frequency bands is introduced. Measurements in the first band (WR1 75-110 GHz) are shown along with the analysis of the results. Moreover, SIW coupler and crossover are designed and measured in WR1 band. The aim of this chapter is to show that different types of SIW components can be embedded into the interposer, thus leading to a functionalized interposer for mm-waves and beyond, with passive devices performance increasing with frequency.

Finally, a general conclusion summarizes the main results obtained in the framework of this PhD thesis and some prospects are suggested.

Chapter 1:

Classical and extended beam Butler Matrix: state-of-the-art

In the present days, wireless communication system has become a fundamental part of various types of communication devices. Many applications use wireless communication, such as mobile and cordless telephones, ZigBee, GPS, Wi-Fi, satellite television, and computers, among others. To enhance the link budget and relax the constraint as much as possible on the amplifiers gain, all those usages require high gain and, when mobility is mandatory, multi-directions arrays of antennas. The latter are rather known as multibeam antenna (MBA), enabled through efficient beam forming network (BFN). Butler matrix (BM) is one of the most important multiple beam forming network, which has been intensively studied and extensively applied in communication systems. In order to achieve a better balance between complexity and capability, many efforts for simplifying or diversifying BMs have been reported in the literature. For example, many authors have worked on reducing the effective size of the system, improve the bandwidth (BW) or reduce the side lobe level (SLL) of the beam pattern. However, one of the most interesting features would be to extend the beam-steering capability with minimum added complexity.

In this chapter, after a brief description of MBA applications in the context of 5G, IoT and satellite communications, we present the BM solution for RF and mm-wave circuits, with a state-of-the-art of the most classical BM structures. They are realized either with microstrip lines or substrate integrated waveguides (SIW). We also present the pro & cons between single-layered or multi-layered technology. Finally, beam-steering enhanced ability BMs are detailed in this chapter. The techniques to improve the spatial coverage allow demonstrating ever-increasing researcher's interests concerning this system in recent years. The latter one opens the way to the introduction of the main goal of the thesis, which is to enhance the spatial antenna coverage while keeping almost unchanged the surface (reduced costs and design complexity) and the performance of the extended beam-forming system as compared to its conventional counterpart.

1.1 Today's role of multibeam antenna

It is clear that MBA is inevitable in the framework of the mm-waves 5G and 5G for IoT (Internet of Things) applications, many automotive radars around 77 GHz, future 6G or automotive radars at 120 GHz. In the next section, we focus on the 5G and 5G for IoT applications, since the MBA system developed in this thesis is concerning this application in terms of operating frequency.

1.1.1 5G and 5G for IoT applications

Because of the extraordinarily rapid growth of consumer wireless devices and the new concept of the IoT [1]–[3], the number of mobile connections is expected to exceed 100 billion now in 2020. From this year, 5G technology will provide access to information and the sharing of data anywhere and anytime, and for anyone and anything [4]. It is suspected that 5G could dramatically change our lives around the world via unprecedented use cases that require high data-rate instantaneous communications, low latency, and massive connectivity for new applications for mobile, e-Health, autonomous vehicles, smart cities, smart homes, and the IoT (see Figure 1-1).

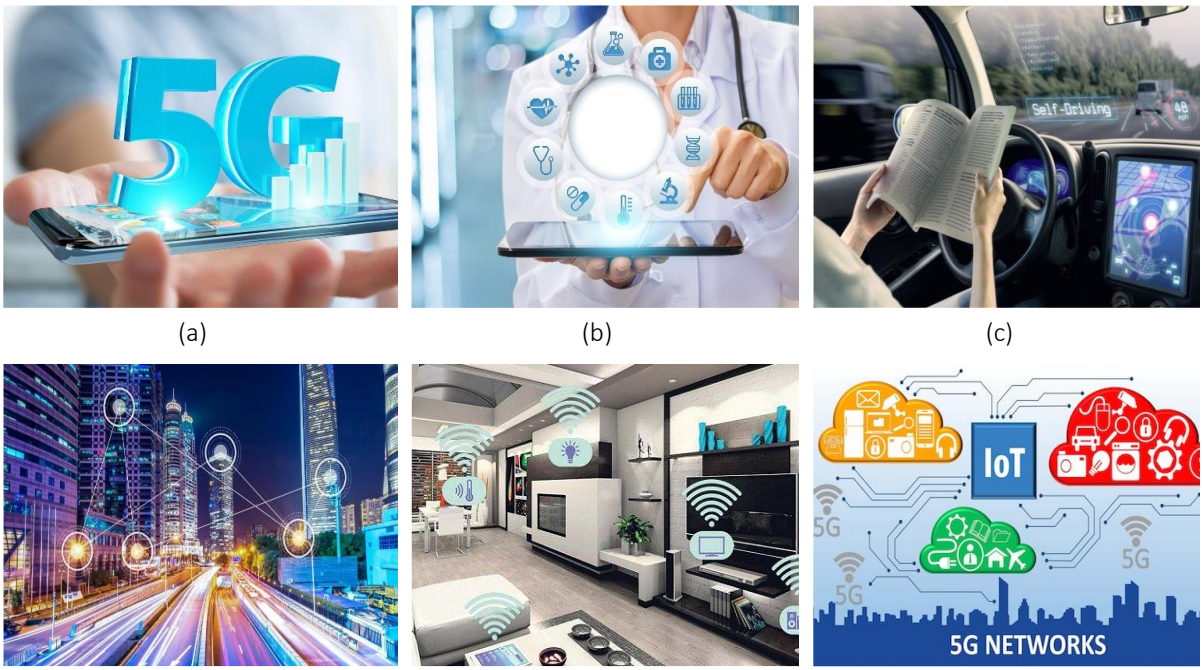

(a) (b) (c)

(d) (e) (f)

Figure 1-1: (a) 5G mobile phones [5] , (b) e-Health [6] , (c) autonomous vehicles [7], (d) smart cities [8],(e) smart home [9] and (f) IoT [10].

Concerning mobile phones (Figure 1-1(a)), better streaming is expected without the buffering, and faster video downloads, with the minimum download speeds of 10-50 gbps (gigabits per second), as much as 10 times faster than 4G. The healthcare segment (Figure 1-1(b)) is also a fast expanding market with an increase in the number of applications that will begin with sensor devices in health care centers running on existing technologies such as Wi-Fi, Bluetooth and low power related technologies. Concerning the autonomous vehicle (Figure 1-1(c)) 5G technology is expected to be a game changer for the automotive industry. The possibility for vehicles to be connected to other vehicles, pedestrians, roadside infrastructure, or application servers enables the development of multiple revolutionary services such as vehicle platooning, advanced driving and remote/cloud computing driving. Another application field is the smart cities (Figure 1-1(d)) that may be seen as a connected ecosystem of ecosystems or the smart home (Figure 1-1(e)) where 5G can bypass Wi-Fi for more reliable performance. More generally, the global ecosystem can be seen in Figure 1-1(f) as the general growth of unparalleled networks, all being closely related.

Apart from the aforementioned applications, we can finally point out wearable devices (bracelets, personal trainers, etc…), smart grids, industrial internet, smart farming and smart retail. Basically, smart grid promises to extract information on the behaviours of consumers and electricity suppliers in an automated fashion to improve the efficiency, economics, and reliability of electricity distribution. Even retailers have started adopting IoT solutions to improve store operations, increasing purchases, reducing theft, enabling inventory management, and enhancing the consumer's shopping experience.

Finally, it is worth mentioning that the intention of this general presentation is not to emit any judgement concerning consumer use cases. The previous applications might be developed in a first approach for life simplicity and quality of life enhancement, ecological purposes or energy saving, even if it is obvious that the consumer usage may also be reoriented towards a mass consumption market.

1.1.2 Multibeam antenna as a solution for mm-wave communications

In this 5G and 5G for IoT context, where increased channel capacity, improved transmission quality with minimum interference and multipath phenomena have become design constraints, MBA [11] is a key element, whatever the short, medium or long range transmission scheme, as long as mm-waves are involved. In fact, to overcome 5G constraints, new network technologies are required such as novel multiple-access strategies, ultra-dense networking, all-spectrum access, massive multiple-input multiple-output (MIMO) and full/flexible duplex [12]–[14]. Concerning the available band, due to this unprecedented growth of mobile data demand, the very limited band resources available in the sub-6-GHz spectrum are not enough to satisfy the system needs. A wider spectrum is available in the mm-wave frequency bands. In that context, the vast amount of underutilized spectrum in the 6–300 GHz range will be useful for the next-generations of commercialized communication bands.

In particular, mm-wave communication systems have been officially adopted in 5G cellular systems, which have, more probably, frequency bands ranging from 28 GHz up to 86 GHz. The 28 GHz, 38 GHz, 71–76 GHz and 81–86 GHz bands are excellent candidates for deploying 5G local area networks [15], [16]. Unfortunately, at mm-waves, the electromagnetic wave suffers from more severe free-space loss and blockage, which substantially degrades the signal-to-interference-plus-noise ratio (SINR). To remedy with this shortcoming issues, high-gain antennas with a directional beam can be used (possibly at transmitter and receiver ends) since they have already shown their interest in long-range mm-wave point-to-point communications with a line-of-sight (LoS) link [17]. But, a narrow beam provides only limited spatial coverage and, in addition, for non-line-of-sights (NLoS) communications, the single-directional beam needs to be steered either electronically or mechanically, in order to find a reliable alternative link. The solution is the use of MBAs [18], which are capable of generating a number of concurrent but independent directive beams with a high gain value to cover a predefined angular range. In MBA systems, the orthogonal beams possess a high angular selectivity, thus allowing for significant frequency reuse and yielding a much higher system capacity. Due to these joint technological benefits, the MBAs hold a great promise for both base stations and user terminals.

1.1.3 Multibeam antenna as a solution for healthcare and security imaging

The demand on advanced screening systems leads to healthcare [19] and security imaging [20] innovative applications. Multibeam antennas can have a very important role on that. An example of screening healthcare and security imaging application is shown in Figure 1-2.

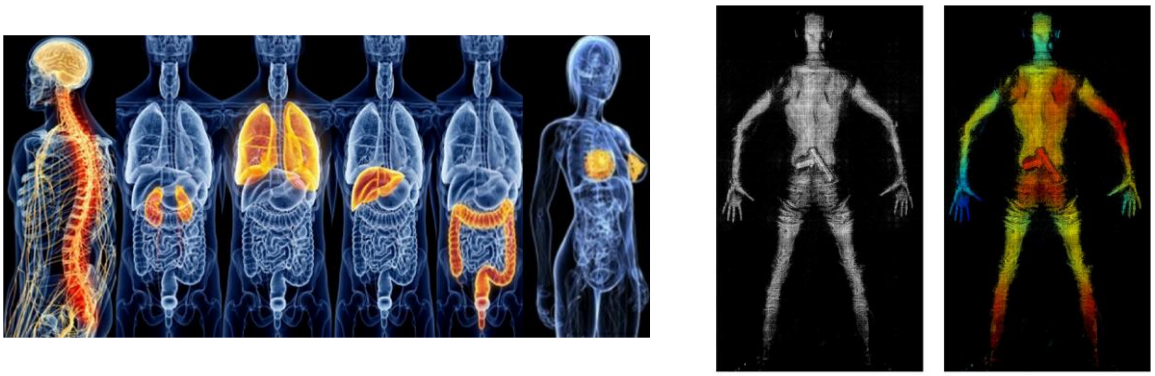

(a) (b)

Figure 1-2: (a) screening body healthcare [21] and (b) security imaging [20] applications

1.1.4 Multibeam antenna as a solution for medical sensors and THz sensing

MBAs provide an important contribution for medicine, such as medical sensors [22], [23] and Terahertz sensing technology [24], [25] for tissue identification and disease detection. Figure 1-3 shows two examples of wearable medical and radar vital sign sensors applications.

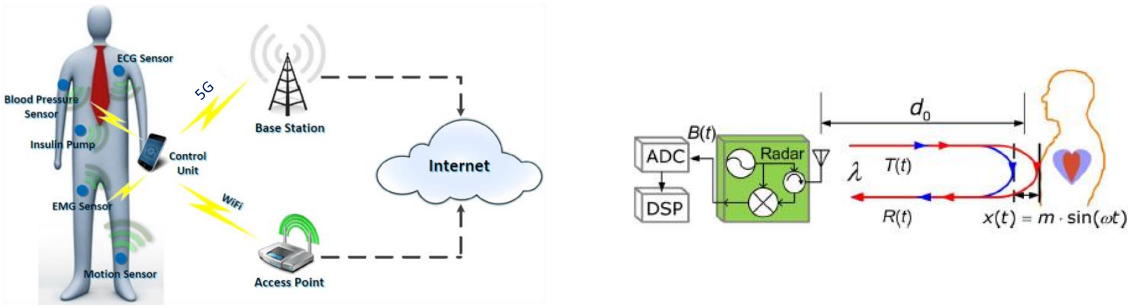

(a) (b)

Figure 1-3: (a) wearable medical sensors[26] and (b) radar vital sign sensors [23] applications

In Figure 1-3 (a) wearable medical sensors communicate with the mobile phone that, in turn, sends the signals either towards base station or to router access point, so as to reach out internet network. In Figure 1-3 (b), a Doppler radar sensor scheme is depicted for vital sign detection.

1.1.5 Multibeam antenna as a solution for radars

An important application field for MBAs is also concerning the military and automotive radar domain [27]–[29]. The picture in Figure 1-4 is depicting an example of the applications.

(a) (b)

Figure 1-4: (a) radar for military applications [30] and (b) automotive radar [31]

The military need for radar has probably been its most important application and the source of most of its major developments, along with aircraft radars. More recently, radars are used for automotive applications, as well.

1.1.6 Multibeam antenna as a solution for satellite communications

Satellite communications (SATCOM) (Figure 1-5) is another application field for MBAs. They have become more and more utilised in recent years [32]. They are used for television, telephone, radio, internet, positioning and military applications. There are about 2,000 communication satellites in Earth's orbit, used by both private and government organizations.

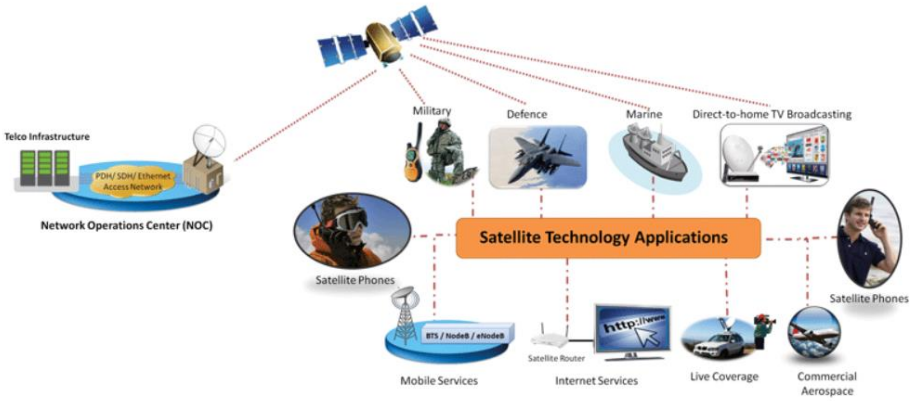

Figure 1-5: SATCOM applications [32]

In the next section, we deal with one of the most important part of a MBA, that is the beam forming network, feeding the multiple antennas, whose an overview is going to be presented in 1.2.

1.2 Phased array antennas and beam forming network overview

There exists two ways to realize a multibeam antenna. We will make a distinction between:

- The phased array where an antenna array of N antennas is fed through a power divider from $1:N$ with a controlled phase shifter on each paths.
- The switched-beam antenna (SBA) where an antenna array of N antennas is fed through a beam forming network (BFN) where the phase difference between the N output ports

depend on the chosen input port for the incident wave available through a bank of switches.

In both cases, the magnitude and phase of the signal on each antenna have to be properly controlled. Historically, for the phased array case, in order to obtain beam steering, phase shifters and attenuators were associated to each one of the radiating elements that form the antenna array [33]. This solution is effective yet but costly and a redundant way to operate, as complexity of systems grows with the number of elements that are required to ensure the appropriate angular resolution of the system. Many alternatives were used to avoid such a complexity:

- introduce a phase-shift to a group of radiating elements [34] instead of one per element, with consequent reduced scanning to certain directions in space.
- combine mechanical with electronic components to redirect a beam to the desired position [35], moving physically the antenna array.
- use optic components [36].

As an architecture alternative, the use of BFNs in a switched beam antenna array is, for sure, one of the best solution to reduce system complexity and achieve the appropriate angular resolution.

1.2.1 BFN network solutions

The BFN is the core part of the SBA as the main beam points at different directions based on the signals created by it. The goal is to provide the specific magnitude and phase responses to realize different angles of scanning beams. There are a lot of well-known solutions, as shown in Figure 1-6, offering multibeams by alternatively selecting the input excitation such as the Blass [37], the Nolen [38], the Butler Matrices [39] and the Rotman Lens [40].

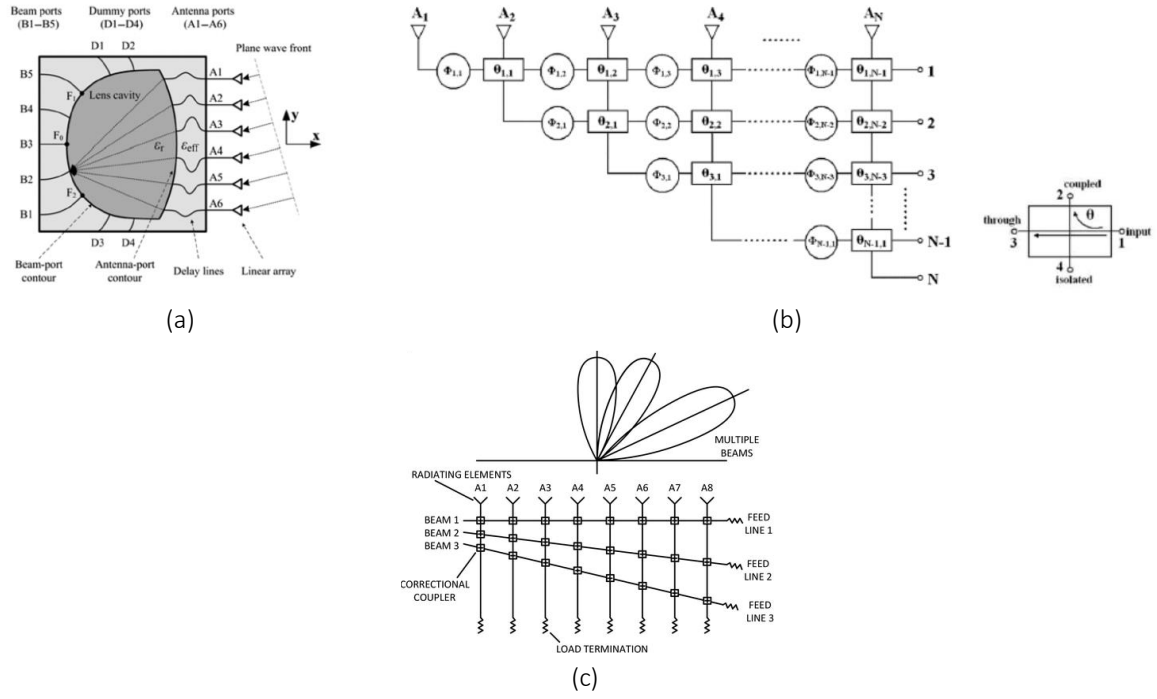

(a) (b) (c)

Figure 1-6: (a) Rotman lens [41], (b) Nolen matrix [42] and (c) Blass matrix [43].

An example of Rotman lens (Figure 1-6 (a)) is reported in [42], consisting of a lens cavity, 14 antenna ports, 11 beam ports, and 4 dummy ports. The lens cavity is used to focus the incident waves on the beam ports. The ports (A1–A14) are connected to antennas, whereas the beam ports (B1–B11) are for receiving the signals from the lens cavity. The dummy ports (D1–D4) are terminated with loads for absorbing inter-cavity reflections. The delay lines are designed to compensate for the phases of the incoming waves from different angles. These lens are used for mm-wave imaging applications [43], but they are typically limited to far-field imaging, because their parallel multibeam formation is based on the condition that the scattered waves arriving at the array are plane waves. As a consequence, the non-plane waves scattered from a near-field target spreads across several beam ports of the Rotman lens. As a result, out-of-focus blurs appear in the near-field images. Moreover, they usually suffer from low efficiency due to high coupling between adjacent ports, which make them less suitable for high power applications.

The Nolen matrix (Figure 1-6 (b)) and the Blass matrix (Figure 1-6 (c)) utilize the series feed method, which are theoretically able to form any arbitrary amplitude distribution. The schematic diagram of an NxN Nolen matrix shows the use of numerous four-port directional couplers (θ-devices) and phase shifters (ϕ-devices), (N-1)! to feed N antennas. The value of θ determines the coupler amplitude coupling coefficient. The Blass matrix consists of directional couplers connected to transmission lines with different fixed delays to supply signals to the phased array antenna with an arbitrary number of radiating elements, N. Whatever Nolen or Blass matrices, their lack of symmetry between input and output ports makes these matrices tricky to design as the paths to the N outputs, depending on the feeding input, do not present the same number of devices or lengths leading to potentially strong unbalance in terms of propagation loss. On the contrary, the BM (see 1.2.2) is a corporate multiple beam feed. Although, series feed BFNs also own critical assets. While corporate networks are mainly used in phased arrays systems, series networks can also be distinctively used in frequency scanning arrays, where the beam steering is dictated by the transmitter frequency.

In conclusion, magnitude and phase shift mismatches at the antenna ports of the series feeding BFN explain why corporate networks, as the BM, were intensively explored. The BM was chosen for the project of this thesis due to its unique properties as perfect matching, isolation, and equal power division, that can be obtained at the same time. Moreover, compared with the other BFNs, BM has some attractive features such as the realizable bandwidth, its structural simplicity and very low current consumption. Its working principle is detailed in the next section.

1.2.2 Conventional BM: working principle

BM is one of the most important multiple BFN [44], which has been intensively studied and extensively applied in communication systems due to their unique properties. A typical $2^N \times 2^N$ BM connecting a 2^N-radiating elements linear array can generate 2^N independent beams from the same aperture. One of the most common BM is the 4x4, which provides ±48.6° and ±14.5° of main beam direction, if its radiating elements are spaced by $\lambda_0/2$ between each other, λ_0 being the free-space wavelength (see Figure 1-7). If port 1 is fed, the progressive output phase between adjacent radiating elements $\Delta\varphi$ is equal to -45°, which focuses the main beam

to $\theta = +14{,}5°$, e.g. in the xOz plane, being x the axis in which the radiating elements are placed. If port 3 is fed, the progressive output phase between adjacent antenna $\Delta\varphi$ is equal to -135°, and the main beam is focused to $\theta = +48{,}6°$ in the xOz plane. The same happens for port 2 and port 4, but with the sign inverted (+ or -), because a symmetry around z-axis occurs.

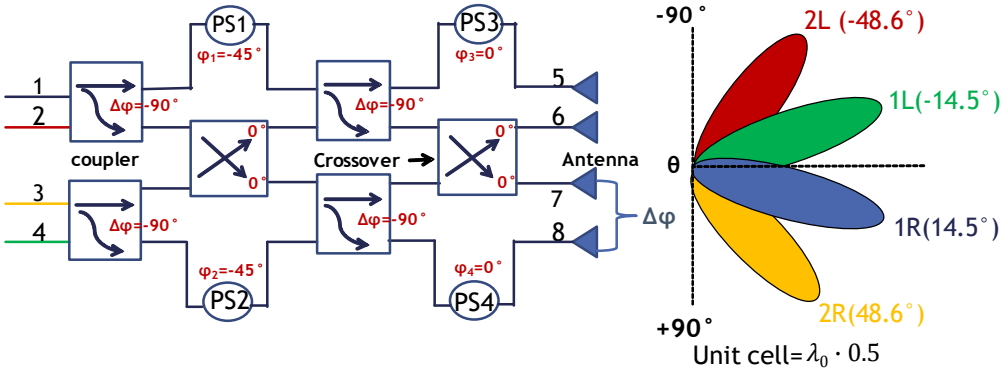

Figure 1-7:Conventional 4x4 BM

The complexity, cost and area consumption increase as N increases. As described in [45], for a traditional $2^N \times 2^N$ BM, the required number of couplers and crossovers, namely C and X, respectively, can be obtained by:

$$C(N) = N \cdot 2^{N-1} \tag{1-1}$$

$$X(N) = \begin{cases} 0 & (N = 1) \\ 2 \cdot X_{N-1} + 2^{N-1} \cdot (2^{N-1} - 1) & (N \geq 2) \end{cases} \tag{1-2}$$

Moreover, a function B can be defined, which is the average number of beams formed by one coupler.

$$B(N) = 2^N / C_N \tag{1-3}$$

Therefore, B represents the efficiency of each coupler to produce beams. Expression (1-3) clearly reveals that the coupler in a higher order BM will have less efficiency in producing beams. This is why techniques to improve the performance will be presented in the following sections as well as the state-of the art of both conventional and extended beam BM.

1.3 BM design techniques for performance improvement

In order to achieve a compromise between complexity and capability, some fruitful efforts for simplifying, or diversifying BMs have been reported. For example, multi-layered transmission line technologies [46]–[51] can be applied to avoid using crossovers, which when realized as a tandem connection, due to its limited isolation, increase the amplitude and phase imbalance of BM. The latter point was particularly observed in [47] and [52].

The avoidance of crossovers was exploited also to broaden the bandwidth in [47] and [48], where multi-section coupled-line couplers based on multi-layered microstrip lines were introduced and exploited in 4×4 and 8×8 BMs. For similar intention, multi-layered CPW technology [51] was utilized in a 4×4 BM. Advanced designs with wideband operation [53]

were reported, mostly at the expense of extra power loss and higher design complexity. Low-temperature co-fired ceramic [54], and CMOS technologies [55], [56] were used, as well. Rearrangement of the feeding network was discussed in [48] as an alternative solution.

Being a passive structure, consisting of quarter-wavelength couplers and crossovers, the physical size of the conventional BM is relatively large. Thus, many authors have worked on reducing the effective size of the structure, [50], [57], [58]. Higher order Butler matrices, e.g. 8 × 8, are impractically large in size, due to a large number of couplers and crossovers; thus, they are rarely reported. Nevertheless, a multi-layered implementation of 8 × 8 BM is presented in [54]. Also, in [56], the 8×8 structure is realized in CMOS technology. Both cases have a noticeable cost compared to a single-layered microstrip realization. Moreover, by applying the couplers with quasi-arbitrary phase differences [59], phase shifters can be removed in terms of appearance [60].

The reduction of the SLL of the beam pattern was also dealt with in [61], [62].

An 8 × 8 BM with broadside beam, termed as the modified BM [63], was realized in stripline technology in [64]. Furthermore, some non-2^N beams BMs, such as 3×3 [65] and quasi-6×6 [66] BMs, might also be helpful to enrich the options of beams number, and thus, improve the configuration flexibility.

The idea to enrich the beam steering ability is discussed in a detailed form in 1.6, as it is the main goal of this manuscript and it deserves more attention. But before focusing on this specific point assuming tunability opportunities, an overview of different process topologies is going to be detailed. Indeed, in the last decades, many work was performed to facilitate the design and fabrication of the BM:

- in microstrip (MS): [45]–[50], [52]–[58], [60], [63], [64], [66]–[79] ([55] and [56] being integrated in a CMOS technology),
- in CPW: [51] and [80],
- in Substrate Integrated Waveguide (SIW): [81]–[106]

As a matter of fact, 1.4 will provide a short description of the design techniques used in MS topologies while 1.5 will focus on SIW topologies, which we are more interested in, in the framework of this work.

1.4 Butler matrix design overview in microstrip

A description of the most interesting conventional BMs, in microstrip, is going to be given through this section with two approaches: the single-layered and the multi-layered substrate.

1.4.1 Single-layered microstrip based Butler matrices

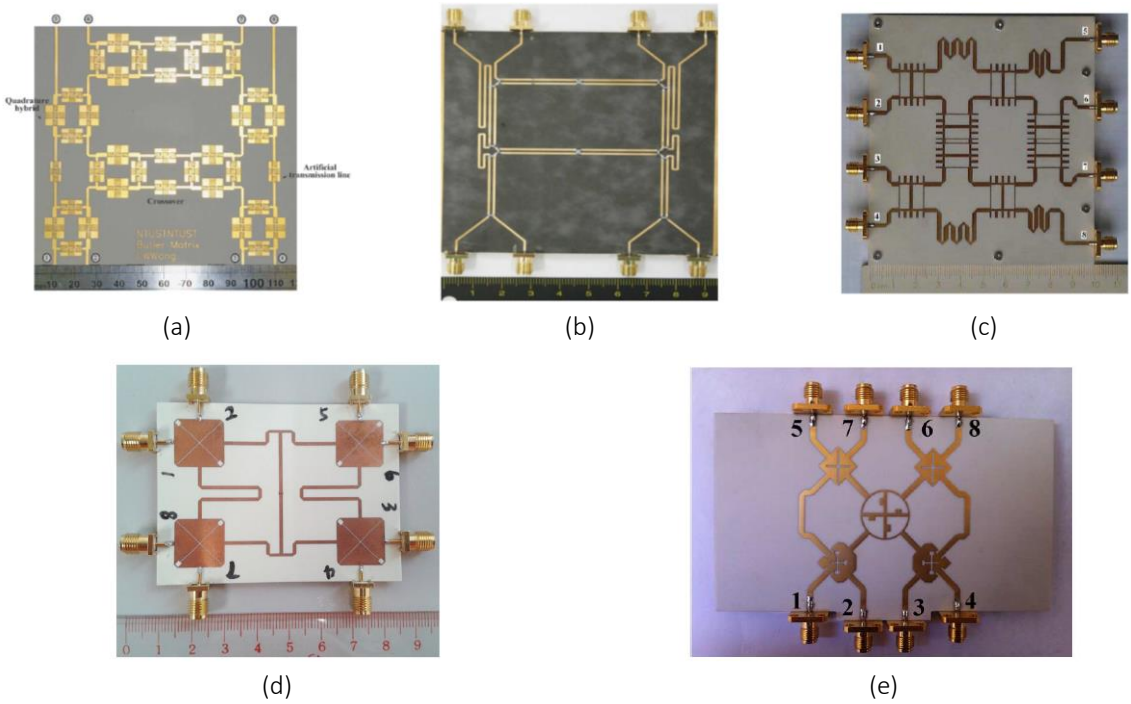

Figure 1-8: Single-layered microstrip based Butler matrices: (a) [57], (b) [58], (c) [72], (d) [73] and (e) [60]

In Figure 1-8, five 4x4 MS single-layered BMs are depicted. In Figure 1-8 (a) a BM based on a planar artificial transmission line is presented for application in ultra-high-frequency (UHF) radio-frequency identification (RFID) systems. Figure 1-8 (b) shows a size reduction technique for designing a BM using a particular type of coupler, which has swapped port characteristic wherein the locations of the isolation and coupled ports are switched.

Figure 1-8 (c) describes the use of eight 3-branch-lines couplers with lumped-distributed elements that are adopted to reduce the size, and multi-U-shaped coupled-line Schiffman phase shifters are designed to achieve good transmission and phase performance. In Figure 1-8 (d) and Figure 1-8 (e), a miniaturised BM using 3-dB cross-slotted patch hybrids and a BM using only MS couplers and a crossover are proposed, respectively.

1.4.2 Multi-layered microstrip based Butler matrices

As an alternative to single-layered BMs, multi-layered MS technology was used for designing three 4x4 BMs and one 8x8 BM, as illustrated in Figure 1-9. An approach for the realization of broadband 4x4 BMs, in which broadband symmetrical multi-sections of 3-dB/90° directional couplers are used as basic elements, is presented in Figure 1-9 (a). Also a new technique for the realization of a center crossover together with 45° phase shifters is proposed where phase correction networks, consisting of a number of coupled-line sections, are applied.

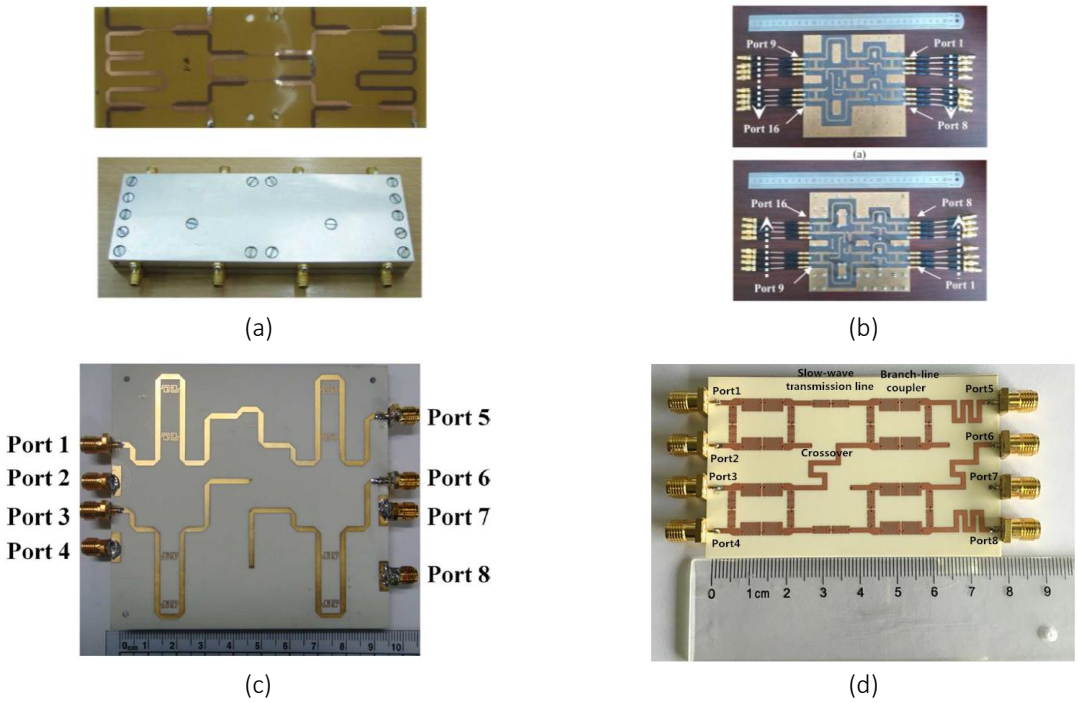

Figure 1-9: Multi-layered microstrip based Butler matrices: (a) [47],(b) [46], (c) [74] and (d) [76]

In Figure 1-9 (b), the double-layer structure is adopted to place components on the top and bottom layers without using crossover. Two-section stepped coupling microstrip Schiffman phase shifters with $\lambda g/8$ length were used to realize wideband phase shift. In Figure 1-9 (c), a broadband BM by combining a broadband forward-wave directional coupler(FWDC) and a broadband middle network was proposed, while in Figure 1-9 (d) a slow-wave structure with high slow-wave factor is proposed. The structure is composed of meandered lines, low-impedance transmission lines and interdigital structures and, for these reasons, is capable of reducing the circuit size significantly due to its good slow-wave property.

1.5 Butler matrices based on substrate integrated waveguides

As a general way, the interest in SIW technology is booming since the two last decades, as shown by the significantly increasing number of scientific publications, special sessions, and workshops at international conferences. An extremely condensed review ([107]–[113]) briefly shows a large panel of studied devices as filters, mixers, couplers, antennas… Thanks to its high *Q*-factor, high power capability, low-loss and high electromagnetic compatibility, SIW technology appears to be a good candidate for the implementation of BM, as well as the smart antenna systems, when compared to MS or CPW technologies.

As a matter of fact, in Figure 1-10 (a) and (b) two single-layered SIW BMs are introduced. A BM based on a systematic approach was designed at 60-GHz. The systematic approach involves design equations, simulations, and measurements. In the second one, wideband operation is achieved thanks to improved cross-couplers. These components are also characterized by higher power handling when compared to E-plane couplers (where the coupling occurs in the vertical plane). On the contrary, in Figure 1-10 (c) and (d), two 4x4 multi-layered SIW BMs are presented. A space saving design is proposed in Figure 1-10 (c) making optimum the use of the two-layer technology and the SIW topology leading to a

significant size reduction. Instead, in Figure 1-10 (d), the proposed design prevents the loss of amplitude and phase shifts and decreases amplitude imbalance in BM. This is achieved by reducing the size of BM and avoiding the use of an interconnexion line length which causes a parasitic phase shift.

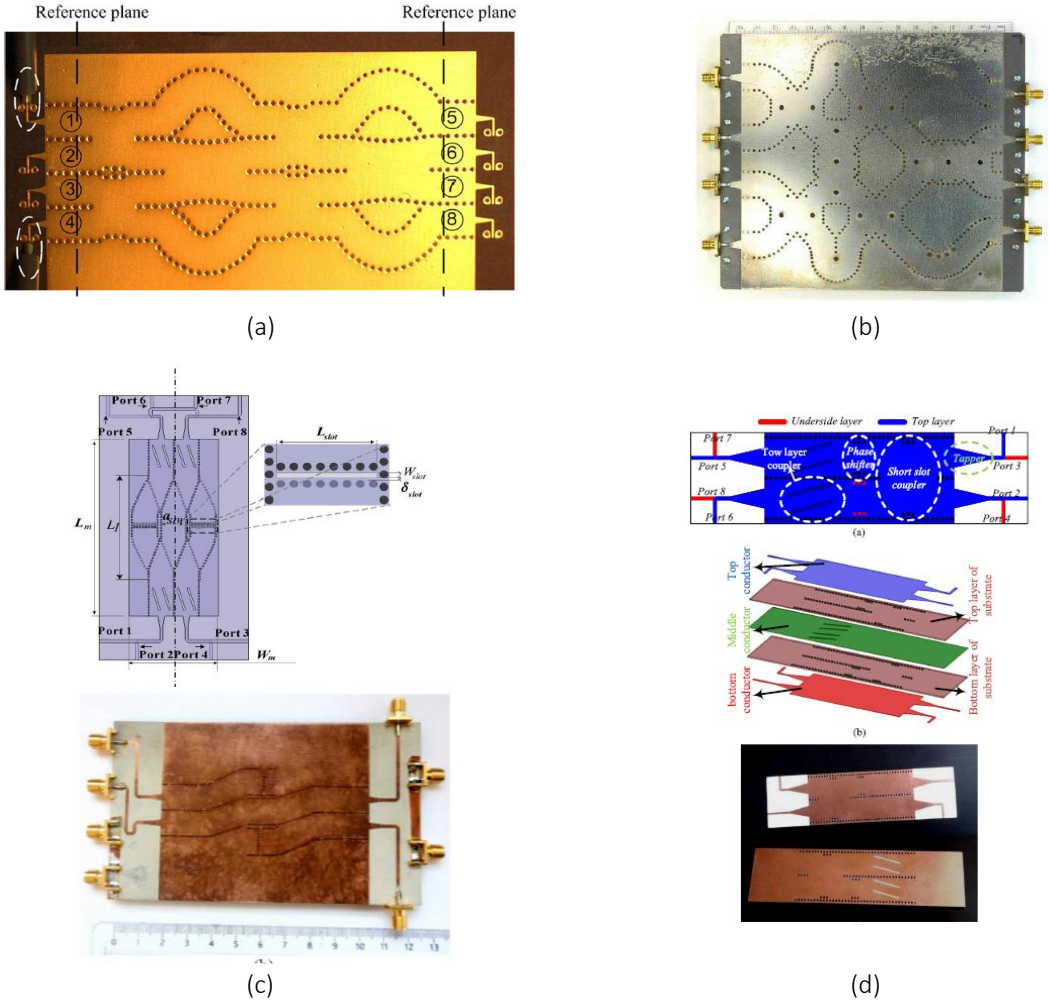

Figure 1-10: Butler matrices based on SIW: (a)[85], (b)[87], (c)[88] and (d)[93]

Based on the system requirements, a BM can be thus integrated in either a single-layered or multi-layered substrate. In this context, one of the main advantages of multi-layered substrate over the single-layered one is obviously size reduction thanks to the easiness in making crossovers. Moreover, the crossovers generate a stronger amplitude and phase output system imbalance when used as a tandem connection of two couplers in single-layered configuration, as discussed in [47] and [52].

The number of the required crossovers can be calculated as given by equation (1-2), where it can be noticed that when the number of crossovers involved in the implementation of conventional BMs is high, a larger size is requested for single-layered planar structures. For this reason, a configuration without planar crossovers need to be considered to achieve miniaturization. That's the reason for the occurrence of multi-layered Butler matrices. Nevertheless, another important factor when dealing with SIW is the simplicity in the design. In fact, single- layered appears to be simpler to design, and this is the reason why many authors preferred dealing with single-layered structures.

1.5.1 Single-layered substrate integrated waveguides Butler matrices

The first single-layered SIW BM design, using a post-wall waveguide approach, was proposed in [81], at 26 GHz. In this work, the amplitude imbalance between the output ports of the BM is less than 1 dB near the design frequency. The phase imbalance is almost ±5° while the average transmission coefficient is around -8.8 dB, that means the extra loss due to the feeding network is therefore around 3 dB. On the overall, if we look at the measured Butler matrices, the [85] and [86] present acceptable performance: the average transmission coefficient and maximum amplitude imbalance are at least 1.5 dB and ±1 dB, respectively, while keeping a relative bandwidth at least equal to 24% around 12.5 GHz. On the contrary, the maximum phase imbalance is higher than ±15° which can impact the radiation pattern shape as compared to the ideal one, as will be shown in the next chapter.

Ref.	Year	Substrate	f (GHz)	Size (mm·mm) ($\lambda_0 \cdot \lambda_0$)	BW (%) (GHz)	Avg Transmission coeff. (dB)	Max Ampl. imb. (dB)	Max Phase imb. (°)
[85]	2010	Rogers RT5880 (ε_r=2.2)	60	27.1·17.8 (5.42·3.56)	31.7 (48-67)	-8.2	±1.5	±17
[86]	2010	Rogers 5870 (ε_r=2.33)	12.5	144·146 (6·6.08)	24 (11-14)	-7.5	±1	±15
[90]*	2012	RT Duroid 6002 (ε_r=2.94)	77	31.5·28.5 (8.09·7.31)	12.3 (72-81.5)	-6.7	±0.3	±4
[92]*	2015	Rogers 5880 (ε_r=2.2)	60	14.98·17.75 (3·3.55)	11.67 (57-64)	-7	±1.5	±14
[94]*	2016	Rogers 5880 (ε_r=2.2)	30	61.9·27.4 (6.19·2.74)	13.3 (28-32)	-6.8	±1	±10
[95]*	2016	Rogers Duroid 5880 (ε_r=2.2)	30	110.3·42.5** (11.03·4.25)	13.3 (28-32)	-6.75	±0.7	±7

Table 1-1: Summary of the State-of-the-art for Single-Layered SIW BM

(*) the results of the BM are simulated but the entire antenna system was fabricated and measured.
(**) area including access lines and antennas.

Table 1-1 shows a performance summary of the state-of-the-art for 4x4 single-layered SIW BM, for different operating frequencies. The reference, year, substrate, central frequency, size, BW, average transmission coefficient, maximum amplitude imbalance and phase imbalance, at the central frequency, are listed. The BW is considered for an input impedance matching equal or better than 10 dB. In 1.5.2 the state-of-the-art of multi-layered SIW BM is going to be addressed.

1.5.2 Multi-layered SIW Butler matrices

With the aim to achieve a compact structure by avoiding the planar crossovers required in the construction of the single-layered BM, the multi-layered SIW has been studied by many researchers. The first publication about this structure was proposed in 2008 [82]. In this work, a two-layered SIW broadband broad-wall waveguide coupler and a novel low insertion-loss

two-layered SIW transition were analyzed and optimized to build up a BM at an operating frequency of 12.5 GHz. A broadband performance was achieved over the extended frequency band from 11.5 GHz to 13.5 GHz. The amplitude imbalance between the output ports was around 1.1 dB while the maximum phase dispersion was ±2° with respect to theoretical parameters. The average transmission coefficient was about -6.2 dB. After this first publication, more and more scientists have been continuing working on this domain with different structures on multi-layered SIW BM. Table 1-2 presents a performance summary of the state-of-the-art of multi-layered SIW BM during the last 10 years.

Ref.	Year/ Type	Substrate	f (GHz)	Size (mm·mm) ($\lambda_0 \cdot \lambda_0$)	BW (%) (GHz)	AvgTransmission coeff. (dB)	Max Ampl. imb. (dB)	Max Phase imb. (°)
[89]*	2011 4x4	RT Duroid 6002(ε_r=2.94)	24	51·28 (4.08·2.24)	N/A	-6.35	±0.11	±5
[88]	2011 4x4	RT Duroid 6002(ε_r=2.94)	12.5	36.25·83.18 (1.51·3.46)	24 (11-14)	-6.7	±0.6	±7
[91]*	2014 4x4	Rogers RT/Duroid 6010(ε_r=10.5)	26.5	N/A	10.71 (25-28)	-7.3	±0.75	±12
[93]	2015 4x4	Rogers 4003(ε_r=3.55)	9.5	55·34 (1.74·1.07)	42.1 (7.5-11.5)	-6.2	±0.6	±5
[97]*	2017 4x8	Rogers 5880(ε_r=2.2)	38	N/A	10.5 (36-40)	-10.8	±0.8	±5
[99]*	2017 8x8	Rogers 5880(ε_r=2.2)	29.5	101.7·40.68 (10·4)	10.17 (28-31)	-11	N/A	±15
[96]*	2017 4x4	Rogers 4003C(ε_r=2.2)	60	N/A	33.3 (50-70)	-8.2	±1	±5
[103]*	2017 4x4	LTCC(ε_r=5.9)	94	N/A·	2.13 (93-95)	-7.2	±0.3	±5
[105]*	2017 4x4	Rogers 5880(ε_r=2.2)	60	150·150 (30·30)	23.33 (54-68)	-7.5	±1.4	±9
[106]*	2018 4x4	Rogers 5880(ε_r=2.2)	30	165·45 (16.5·4.5)	14.29 (28-32)	-7	±2	±18

Table 1-2: Summary of the State-of-the-art for Multi-Layered SIW BM

(*) the results of the BM are simulated but the entire antenna system was fabricated and measured.

The measured Butler matrices [88] and [93] in Table 1-2, present a low average transmission coefficient and maximum amplitude imbalance equal to at the most 0.7 dB and ±0.6 dB, respectively. The relative bandwidth is at least equal to 24% around 12.5 GHz. This time, the maximum phase imbalance is lower than ±7°. On the overall, good performance is provided for not impacting a lot the radiation pattern, as compared to the ideal radiation pattern shape.

In order to end this general overview concerning Butler matrices, now that compactness, design capabilities and performance enhancement have been discussed, a final point is addressed concerning the extended beam ability of the BMs that is going to be detailed in 1.6.

1.6 Extended beam BM

During the last decades, many authors have worked on reducing the effective size of the system, or improve the bandwidth or reduce the SLL of the beam pattern. But in many today's applications, another parameter may be required that concerns the high beam resolution. The matter is that, although increasing the order of the BM can improve the beam resolution, the circuit size also becomes impractically large. Thus, one of the most interesting features would be to extend the beam-steering ability without increasing too much complexity and size. A possible approach is to use tunable phase shifters for each output branch to generate a continuous beam orientation. However, this requires a significant amount of phase tuning for the same spatial coverage, thus implying a great design challenge. More efficient techniques along with the BM performance are introduced in this section. The corresponding devices are shown in Figure 1-11 while Table 1-3 provides a general summary of the most relevant publications concerning extended beam Butler matrices.

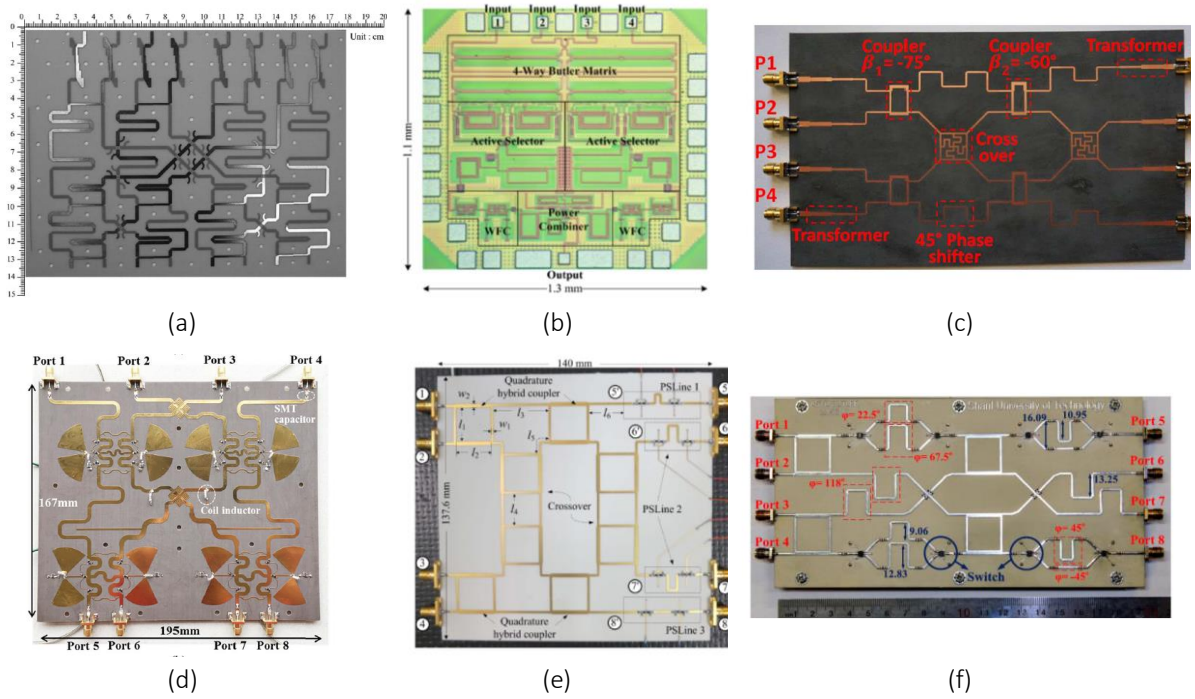

Figure 1-11: Extended beam Butler matrices: (a) [68],(b) [114] ,(c) [115],(d) [45],(e) [77]and (f) [78]

In [68], an extended 8x8 switching/steering BM is proposed for the first time (Figure 1-11 (a)). The radiation beam is initially switched to a certain direction through the BM, and then slightly adjusted by tunable phase shifters, which are only responsible for a small steering range between two adjacent beams. By using this approach, the beam resolution is dramatically improved, while the BM still remains low order and only a small amount of phase tuning is needed, that alleviates the design difficulty of the beamforming circuitry. In addition to its extended functionality, this switching/steering BM is also intended to achieve wideband performance and ultra-compact circuit size.

A compact low-power CMOS phased array receiver with continuous beam steering is presented in [114], based on the subsector beam steering technique (Figure 1-11 (b)). The entire beam steering spatial range is divided into five subsectors from four characteristic beams of the

BM. In each subsector the received beam is steered by a tricky weighted combination of the received signals from the array of antennas.

[115] introduces a novel BM topology (Figure 1-11 (c)), which can realize relatively flexible phase differences at the output ports. The flexible phase differences are achieved by employing couplers with arbitrary phase differences to replace the quadrature couplers of the conventional BM. By controlling the phase differences of the applied couplers, the progressive phase differences among output ports of the proposed BM can be relatively flexible.

The same concept as in [115] was used in [45], where a switchable 12-beam forming network based on 4×4 BM (Figure 1-11 (d)) with wideband properties is proposed. By changing the coupling coefficient of hybrids or the phase difference between two output ports, BM may have a kind of capability multiplication.

In [77], a new beam-switching array system, capable of providing four sets of switchable beams, is proposed and demonstrated (Figure 1-11 (e)). The core building block is a phase reconfigurable synthesized transmission line (PRSTL), whose electrical length is switched between two states as a 1-bit phase shifter. By cascading the PRSTLs to the outputs of a standard 4x4 BM, the progressive phase shifts between adjacent antenna elements can be controlled in a variety of fashions. The new design aims to provide a low-complexity solution to expand the beam controllability as well as spatial coverage of a conventional beam-switching system with 16 switchable beams. Finally, in [78] the authors propose a general structure for the BM (Figure 1-11 (f)). Until now, new structures for the BM with flexible output phase differences have been demonstrated. For example, flexible couplers instead of the conventional branch line coupler (BLC) or a subsector beam steering technique were reported. Furthermore, RTPSs (Reflection-Type Phase Shifter) and PRSTLs are used at the end of the BM, for the same purpose. In [78], the authors propose conventional BLCs and more constant phase shift sections to generate, in theory, any progressive phase difference (PPD) from −180° to 180°. An asymmetrical 4x4 BM providing 8 beams is fabricated to prove the concept. The performance of all these designs is detailed in Table 1-3.

Ref.	Year / Type	Substrate	f(GHz)	Size (mm·mm) ($\lambda_0 \cdot \lambda_0$)	BW (%)(GHz-GHz)	AvgTransmission coeff. (dB)	Max Ampl. imb.(dB)	Max Phase imb.(°)
[68]	2010 8x8	Three 25N PCBs (εr=3.38)	2.2	160·100 (1.1730.733·)	54.55 (1.6-2.8)	-10.1	±2.2	±20.7
[114]	2010	0.13µm CMOS	25	0.28mm^2 ($1.9 \cdot 10^3\ \lambda_0{}^2$)	40 (20-30)	-7.4	±0.5	±5
[115]	2016	RT/Duroid 5880(εr=2.2)	6	182.8·75.2 (3.65·1.5)	17.24 (5.6-6.6)	-7.56	±0.75	±6
[77]	2018	Rogers 4003C (εr=3.55)	2.4	137.6·140 (1.1·1.12)	16.67 (2.2-2.6)	-7.7	±1.2	±9.3

[45]	2019	Rogers Duroid 5880 (εr=2.2)	2.4	195·167 (1.56·1.336)	37.5 (1.9-2.8)	-7.8	±1.7	±12
[78]	2019	Rogers 4003 (εr=3.55)	2.45	342.86·171.43 (2.8·1.4)	20.41 (2.06-2.56)	-7.8	±3.77	±9.4

Table 1-3: Summary of the State-of-the-art of extended spatial coverage angle BM

(*) the results of the BM are simulated but the entire antenna system was fabricated and measured.

1.7 Conclusion

A short historical background of MBA systems along with its application fields was given at the beginning of this chapter. The role of phased array systems was explained especially for mm-wave power consumption and line-of-sight issues. In addition, an overview of four possible BFNs was reported. Among them, BM has a fundamental role because of its characteristics that made it the first choice to realize this work. A short overview concerning the techniques utilized to improve the performance of BM, such as better BW, lower SLL and reduced size and costs was given. The BM topologies and their design were discussed and among them it was explained that the telecommunication systems can become more efficient by using SIW technology since it permits to integrate all planar components in a PCB or in a monolithic microwave integrated circuit with higher quality factors than classical transmission lines like microstrips and CPWs. After that the focus was to show how to improve the spatial coverage of BMs. The main works about beam-steering enhanced ability (extended beam) BMs were detailed in the last part of this chapter. These techniques to improve the spatial coverage allowed demonstrating ever-increasing researcher's interests concerning this system in recent years.

This last part opens the way to the introduction of the main goal of the work presented in this manuscript, which is to demonstrate a prototype of an enhanced beam-steering ability 4x4 SIW BM that provides for 9 beams in its 2D (two dimensional) radiation pattern. The latter one is for 5G and IoT modern applications.

REFERENCE

[1] M. Ben-Daya, E. Hassini, and Z. Bahroun, 'Internet of things and supply chain management: a literature review', *International Journal of Production Research*, vol. 57, no. 15–16, pp. 4719–4742, Aug. 2019, doi: 10.1080/00207543.2017.1402140.

[2] S. Balandin, S. Andreev, and Y. Koucheryavy, Eds., *Internet of things, smart spaces, and next generation networking: 13th international conference, NEW2AN 2013, and 6th Conference, ruSMART 2013, St. Petersburg, Russia, August 28-30, 2013 ; proceedings*. Berlin: Springer, 2013.

[3] Miao Wu, Ting-Jie Lu, Fei-Yang Ling, Jing Sun, and Hui-Ying Du, 'Research on the architecture of Internet of Things', in *2010 3rd International Conference on Advanced Computer Theory and Engineering(ICACTE)*, Aug. 2010, vol. 5, pp. V5-484-V5-487, doi: 10.1109/ICACTE.2010.5579493.

[4] M. Beccaria, L. H. Manh, A. Massaccesi, N. H. Trung, N. Khac Kiem, and P. Pirinoli, '5G Communication System Antenna Design', in *2019 IEEE International Conference on Environment and Electrical Engineering and 2019 IEEE Industrial and Commercial Power Systems Europe (EEEIC / I CPS Europe)*, Jun. 2019, pp. 1–4, doi: 10.1109/EEEIC.2019.8783900.

[5] https://www.journaldunet.com/web-tech/dictionnaire-de-l-iot

[6] 'Top Digital Health Trends Transforming the Global Healthcare Industry in 2019', *Technavio*, Aug. 13, 2019. https://blog.technavio.com/blog/top-digital-health-trends-transforming-healthcare-industry (accessed Dec. 02, 2019).

[7] 'https://www.bbc.com/news/business-45048264

[8] https://www.computerworld.com/article/3427978/5g-and-smart-cities-trends-for-2019.html

[9] http://www.intempusbuilders.com/services/home-automation-security-and-networking/

[10] https://www.positanonews.it/2019/05/5g-internet-of-things-un-po-chiarezza/3308444/

[11] W. Hong *et al.*, 'Multibeam Antenna Technologies for 5G Wireless Communications', *IEEE Transactions on Antennas and Propagation*, vol. 65, no. 12, pp. 6231–6249, Dec. 2017, doi: 10.1109/TAP.2017.2712819.

[12] F. Boccardi, R. W. Heath, A. Lozano, T. L. Marzetta, and P. Popovski, 'Five disruptive technology directions for 5G', *IEEE Communications Magazine*, vol. 52, no. 2, pp. 74–80, Feb. 2014, doi: 10.1109/MCOM.2014.6736746.

[13] A. Gupta and R. K. Jha, 'A Survey of 5G Network: Architecture and Emerging Technologies', *IEEE Access*, vol. 3, pp. 1206–1232, 2015, doi: 10.1109/ACCESS.2015.2461602.

[14] E. Dahlman *et al.*, '5G wireless access: requirements and realization', *IEEE Communications Magazine*, vol. 52, no. 12, pp. 42–47, Dec. 2014, doi: 10.1109/MCOM.2014.6979985.

[15] A. Ghosh *et al.*, 'Millimeter-Wave Enhanced Local Area Systems: A High-Data-Rate Approach for Future Wireless Networks', *IEEE Journal on Selected Areas in Communications*, vol. 32, no. 6, pp. 1152–1163, Jun. 2014, doi: 10.1109/JSAC.2014.2328111.

[16] J. Qiao, X. Shen, J. Mark, Q. Shen, Y. He, and L. Lei, 'Enabling device-to-device communications in millimeter-wave 5G cellular networks', *IEEE Communications Magazine*, vol. 53, no. 1, pp. 209–215, Jan. 2015, doi: 10.1109/MCOM.2015.7010536.

[17] M. Ando, J. Hirokawa, T. Yamamoto, A. Akiyama, Y. Kimura, and N. Goto, 'Novel single-layer waveguides for high-efficiency millimeter-wave arrays', *IEEE Transactions on Microwave Theory and Techniques*, vol. 46, no. 6, pp. 792–799, Jun. 1998, doi: 10.1109/22.681202.

[18] T. E. Bogale and L. B. Le, ‘Massive MIMO and mmWave for 5G Wireless HetNet: Potential Benefits and Challenges’, *IEEE Vehicular Technology Magazine*, vol. 11, no. 1, pp. 64–75, Mar. 2016, doi: 10.1109/MVT.2015.2496240.
[19] J. S. Iwanczyk, *Radiation Detectors for Medical Imaging*. CRC Press, 2015.
[20] S. S. Ahmed, A. Genghammer, A. Schiessl, and L.-P. Schmidt, ‘Fully Electronic E-Band Personnel Imager of 2 m ^{2} Aperture Based on a Multistatic Architecture’, *IEEE Transactions on Microwave Theory and Techniques*, vol. 61, no. 1, pp. 651–657, Jan. 2013, doi: 10.1109/TMTT.2012.2228221.
[21] http://www.presidentialhealthcarecenter.com/executive-physicals/
[22] X. Chen, W. Rhee, and Z. Wang, ‘Low power sensor design for IoT and mobile healthcare applications’, *China Communications*, vol. 12, no. 5, pp. 42–54, May 2015, doi: 10.1109/CC.2015.7112043.
[23] C. Li, V. M. Lubecke, O. Boric-Lubecke, and J. Lin, ‘A Review on Recent Advances in Doppler Radar Sensors for Noncontact Healthcare Monitoring’, *IEEE Transactions on Microwave Theory and Techniques*, vol. 61, no. 5, pp. 2046–2060, May 2013, doi: 10.1109/TMTT.2013.2256924.
[24] P. H. Siegel, ‘Terahertz technology in biology and medicine’, *IEEE Transactions on Microwave Theory and Techniques*, vol. 52, no. 10, pp. 2438–2447, Oct. 2004, doi: 10.1109/TMTT.2004.835916.
[25] P. H. Siegel, ‘Terahertz technology’, *IEEE Transactions on Microwave Theory and Techniques*, vol. 50, no. 3, pp. 910–928, Mar. 2002, doi: 10.1109/22.989974.
[26] L. Smith, ‘Body Area Network: Connecting The Human Body Through Next-Gen Telecommunication Technologies’, *TMR Blog*, Jun. 26, 2019. https://tmrblog.com/body-area-network-connecting-the-human-body-through-next-gen-telecommunication-technologies/ (accessed May 02, 2020).
[27] C. Pfeffer, R. Feger, C. Wagner, and A. Stelzer, ‘FMCW MIMO Radar System for Frequency-Division Multiple TX-Beamforming’, *IEEE Transactions on Microwave Theory and Techniques*, vol. 61, no. 12, pp. 4262–4274, Dec. 2013, doi: 10.1109/TMTT.2013.2287675.
[28] W. Menzel and A. Moebius, ‘Antenna Concepts for Millimeter-Wave Automotive Radar Sensors’, *Proceedings of the IEEE*, vol. 100, no. 7, pp. 2372–2379, Jul. 2012, doi: 10.1109/JPROC.2012.2184729.
[29] Y. L. Sit, C. Sturm, and T. Zwick, ‘Interference cancellation for dynamic range Improvement in an OFDM joint radar and communication system’, in *2011 8th European Radar Conference*, Oct. 2011, pp. 333–336.
[30] https://sites.google.com/site/dppassg1/home/chapter-3/applicatinos-of-radars/military-applications.
[31] https://ctcadvanced.com/fr/modernization-of-automotive-radar-systems-test-lab/
[32] https://www.gl.com/telecom-test-solutions/testing-satellite-communications.html .
[33] R. J. Mailloux, *Phased Array Antenna Handbook, Third Edition*. Artech House, 2017.
[34] R. Garg, P. Bhartia, I. J. Bahl, and A. Ittipiboon, *Microstrip Antenna Design Handbook*. Artech House, 2001.
[35] Z. Golubicic, S. Dragas, and Z. Cvetkov, ‘A K- and Ka-band vehicular phased-array antenna’, *Microwave Journal*, vol. 47, Jan. 2004.
[36] A. K. Bhattacharya, *Phased Array Antennas: Floquet Analysis, Synthesis, BFNs and Active Array Systems*. Newark, NJ: Wiley, 2006.
[37] J. Blass, ‘Multidirectional antenna - A new approach to stacked beams’, in *IRE International Convention Record*, New York, NY, USA, 1960, vol. 8, pp. 48–50, doi: 10.1109/IRECON.1960.1150892.

[38] N. J. G. Fonseca, 'Printed S-Band 4x4 Nolen Matrix for Multiple Beam Antenna Applications', *IEEE Transactions on Antennas and Propagation*, vol. 57, no. 6, pp. 1673–1678, Jun. 2009, doi: 10.1109/TAP.2009.2019919.
[39] J. Butler and R. Lowe, 'Beam forming matrix simplifies design of electronically scanned antennas', *Electron. Des.*, vol. 9, pp. 170 – 173, 1961.
[40] W. Rotman and R. Turner, 'Wide-angle microwave lens for line source applications', *IEEE Transactions on Antennas and Propagation*, vol. 11, no. 6, pp. 623–632, Nov. 1963, doi: 10.1109/TAP.1963.1138114.
[41] M. E. Belkin, D. A. Fofanov, T. N. Bakhvalova, and A. S. Sigov, 'Design of Reconfigurable Multiple-Beam Array Feed Network Based on Millimeter-Wave Photonics Beamformers', *Array Pattern Optimization*, Sep. 2019, doi: 10.5772/intechopen.89076.
[42] Y. Min, D. Zhao, Y. Jin, and B.-Z. Wang, 'Near-Field Image Restoration for Rotman Lens by Localized Angle-Time Spread Function-Based Filtering Method', *Antennas and Propagation, IEEE Transactions on*, vol. 63, pp. 2353–2358, May 2015, doi: 10.1109/TAP.2015.2408362.
[43] S. Clark, C. Martin, V. Kolinko, J. Lovberg, and P. J. Costianes, 'A real-time wide field of view passive millimeter-wave imaging camera', in *32nd Applied Imagery Pattern Recognition Workshop, 2003. Proceedings.*, Oct. 2003, pp. 250–254, doi: 10.1109/AIPR.2003.1284280.
[44] J. Shelton and K. Kelleher, 'Multiple beams from linear arrays', *IRE Transactions on Antennas and Propagation*, vol. 9, no. 2, pp. 154–161, Mar. 1961, doi: 10.1109/TAP.1961.1144964.
[45] K. Ding and A. A. Kishk, 'Extension of Butler Matrix Number of Beams Based on Reconfigurable Couplers', *IEEE Transactions on Antennas and Propagation*, vol. 67, no. 6, pp. 3789–3796, Jun. 2019, doi: 10.1109/TAP.2019.2902668.
[46] K. Ding, F. He, X. Ying, and J. Guan, 'A compact 8x8 Butler matrix based on double-layer structure', in *2013 5th IEEE International Symposium on Microwave, Antenna, Propagation and EMC Technologies for Wireless Communications*, Chengdu, China, Oct. 2013, pp. 650–653, doi: 10.1109/MAPE.2013.6689925.
[47] S. Gruszczynski and K. Wincza, 'Broadband 4x4 Butler Matrices as a Connection of Symmetrical Multisection Coupled-Line 3-dB Directional Couplers and Phase Correction Networks', *IEEE Transactions on Microwave Theory and Techniques*, vol. 57, no. 1, pp. 1–9, Jan. 2009, doi: 10.1109/TMTT.2008.2009081.
[48] K. Wincza, S. Gruszczynski, and K. Sachse, 'Broadband Planar Fully Integrated 8x8 Butler Matrix Using Coupled-Line Directional Couplers', *IEEE Transactions on Microwave Theory and Techniques*, vol. 59, no. 10, pp. 2441–2446, Oct. 2011, doi: 10.1109/TMTT.2011.2164092.
[49] Y. Zhai, X. Fang, K. Ding, and F. He, 'Miniaturization Design for 8 × 8 Butler Matrix Based on Back-to-Back Bilayer Microstrip', *International Journal of Antennas and Propagation*, vol. 2014, pp. 1–7, 2014, doi: 10.1155/2014/583903.
[50] K. Wincza, K. Staszek, and S. Gruszczynski, 'Broadband Multibeam Antenna Arrays Fed by Frequency-Dependent Butler Matrices', *IEEE Transactions on Antennas and Propagation*, vol. 65, no. 9, pp. 4539–4547, Sep. 2017, doi: 10.1109/TAP.2017.2722823.
[51] M. Nedil, T. A. Denidni, and L. Talbi, 'Novel butler matrix using CPW multilayer technology', *IEEE Transactions on Microwave Theory and Techniques*, vol. 54, no. 1, pp. 499–507, Jan. 2006, doi: 10.1109/TMTT.2005.860490.
[52] K. Wincza and S. Gruszczynski, 'A Broadband 4x4 Butler Matrix for Modern-Day Antennas', p. 4, 2005.

[53] C.-H. Chen, X.-P. Zhang, and J. Xu, 'Implementation of a low-loss wide-band flat-topped beam-forming network based on butler martix', in *2015 Asia-Pacific Microwave Conference (APMC)*, Dec. 2015, vol. 3, pp. 1–3, doi: 10.1109/APMC.2015.7413400.
[54] G. Tudosie, R. Vahldieck, and A. Lu, 'A novel modularized folded highly compact LTCC Butler matrix', in *2008 IEEE MTT-S International Microwave Symposium Digest*, Atlanta, GA, USA, Jun. 2008, pp. 691–694, doi: 10.1109/MWSYM.2008.4632926.
[55] T.-Y. Chin, J.-C. Wu, S.-F. Chang, and C.-C. Chang, 'A V-Band 8x8 CMOS Butler Matrix MMIC', *IEEE Transactions on Microwave Theory and Techniques*, Dec. 2010, doi: 10.1109/TMTT.2010.2086372.
[56] B. Cetinoneri, Y. A. Atesal, and G. M. Rebeiz, 'An 8x8 Butler Matrix in 0.13-um CMOS for 5–6-GHz Multibeam Applications', *IEEE Transactions on Microwave Theory and Techniques*, vol. 59, no. 2, pp. 295–301, Feb. 2011, doi: 10.1109/TMTT.2010.2097751.
[57] C.-W. Wang, T.-G. Ma, and C.-F. Yang, 'A New Planar Artificial Transmission Line and Its Applications to a Miniaturized Butler Matrix', *IEEE Transactions on Microwave Theory and Techniques*, vol. 55, no. 12, pp. 2792–2801, Dec. 2007, doi: 10.1109/TMTT.2007.909474.
[58] Yae Suk Jeong and Tae Wook Kim, 'Design and Analysis of Swapped Port Coupler and Its Application in a Miniaturized Butler Matrix', *IEEE Transactions on Microwave Theory and Techniques*, vol. 58, no. 4, pp. 764–770, Apr. 2010, doi: 10.1109/TMTT.2010.2041571.
[59] Y. S. Wong, S. Y. Zheng, and W. S. Chan, 'Quasi-Arbitrary Phase-Difference Hybrid Coupler', *IEEE Transactions on Microwave Theory and Techniques*, vol. 60, no. 6, pp. 1530–1539, Jun. 2012, doi: 10.1109/TMTT.2012.2187918.
[60] G. Tian, J.-P. Yang, and W. Wu, 'A Novel Compact Butler Matrix Without Phase Shifter', *IEEE Microwave and Wireless Components Letters*, vol. 24, no. 5, pp. 306–308, May 2014, doi: 10.1109/LMWC.2014.2306898.
[61] K. Tekkouk, J. Hirokawa, R. Sauleau, M. Ettorre, M. Sano, and M. Ando, 'Dual-Layer Ridged Waveguide Slot Array Fed by a Butler Matrix With Sidelobe Control in the 60-GHz Band', *IEEE Transactions on Antennas and Propagation*, vol. 63, no. 9, pp. 3857–3867, Sep. 2015, doi: 10.1109/TAP.2015.2442612.
[62] J. Shelton, 'Reduced sidelobes for Butler-matrix-fed linear arrays', *IEEE Transactions on Antennas and Propagation*, vol. 17, no. 5, pp. 645–647, Sep. 1969, doi: 10.1109/TAP.1969.1139525.
[63] M. Koubeissi, C. Decroze, T. Monediere, and B. Jecko, 'A new method to design a Butler matrix with broadside beam: Application to a multibeam antenna', *Microwave and Optical Technology Letters*, vol. 48, no. 1, pp. 35–40, 2006, doi: 10.1002/mop.21253.
[64] K. Wincza and S. Gruszczynski, 'Broadband Integrated 8x8 Butler Matrix Utilizing Quadrature Couplers and Schiffman Phase Shifters for Multibeam Antennas With Broadside Beam', *IEEE Transactions on Microwave Theory and Techniques*, vol. 64, no. 8, pp. 2596–2604, Aug. 2016, doi: 10.1109/TMTT.2016.2582877.
[65] K. Ding, X. Fang, Y. Wang, and A. Chen, 'Printed Dual-Layer Three-Way Directional Coupler Utilized as 3$\,\times\,$ 3 Beamforming Network for Orthogonal Three-Beam Antenna Array', *IEEE Antennas and Wireless Propagation Letters*, vol. 13, pp. 911–914, 2014, doi: 10.1109/LAWP.2014.2321971.
[66] K. Ding, J. Bai, and A. Kishk, 'A quasi butler matrix with 6×6 beam-forming capacity using 3×3 hybrid couplers', in *2017 XXXIInd General Assembly and Scientific Symposium of the International Union of Radio Science (URSI GASS)*, Aug. 2017, pp. 1–4, doi: 10.23919/URSIGASS.2017.8120341.
[67] W. F. Moulder, W. Khalil, and J. L. Volakis, '60-GHz Two-Dimensionally Scanning Array Employing Wideband Planar Switched Beam Network', *IEEE Antennas and*

Wireless Propagation Letters, vol. 9, pp. 818–821, 2010, doi: 10.1109/LAWP.2010.2070056.

[68] Chia-Chan Chang, Ruey-Hsuan Lee, and Ting-Yen Shih, 'Design of a Beam Switching/Steering Butler Matrix for Phased Array System', *IEEE Transactions on Antennas and Propagation*, vol. 58, no. 2, pp. 367–374, Feb. 2010, doi: 10.1109/TAP.2009.2037693.

[69] C. Dall'Omo, T. Monediere, B. Jecko, F. Lamour, I. Wolk, and M. Elkael, 'Design and realization of a 4 × 4 microstrip Butler matrix without any crossing in millimeter waves', *Microwave and Optical Technology Letters*, vol. 38, no. 6, pp. 462–465, Sep. 2003, doi: 10.1002/mop.11090.

[70] Chao-Hsiung Tseng, Chih-Jung Chen, and Tah-Hsiung Chu, 'A Low-Cost 60-GHz Switched-Beam Patch Antenna Array With Butler Matrix Network', *IEEE Antennas and Wireless Propagation Letters*, vol. 7, pp. 432–435, 2008, doi: 10.1109/LAWP.2008.2001849.

[71] Chia-Chan Chang, Ting-Yueh Chin, Jen-Chieh Wu, and Sheng-Fuh Chang, 'Novel Design of a 2.5-GHz Fully Integrated CMOS Butler Matrix for Smart-Antenna Systems', *IEEE Transactions on Microwave Theory and Techniques*, vol. 56, no. 8, pp. 1757–1763, Aug. 2008, doi: 10.1109/TMTT.2008.926528.

[72] C. Chen, H. Wu, and W. Wu, 'Design and Implementation of a Compact Planar 4 × 4 Microstrip Butler Matrix for Wideband Application', *Progress In Electromagnetics Research C*, vol. 24, p. 13, 2011.

[73] Y.-L. Li, Q. S. Liu, S. Sun, and S. S. Gao, 'A miniaturised Butler matrix based on patch hybrid couplers with cross slots', in *2013 IEEE Antennas and Propagation Society International Symposium (APSURSI)*, Orlando, FL, USA, Jul. 2013, pp. 2145–2146, doi: 10.1109/APS.2013.6711731.

[74] T.-H. Lin, S.-K. Hsu, and T.-L. Wu, 'Bandwidth Enhancement of 4x4 Butler Matrix Using Broadband Forward-Wave Directional Coupler and Phase Difference Compensation', *IEEE Transactions on Microwave Theory and Techniques*, vol. 61, no. 12, pp. 4099–4109, Dec. 2013, doi: 10.1109/TMTT.2013.2288597.

[75] W. Nie, Y. Fan, S. Luo, and Y. Guo, 'A switched-beam microstrip antenna array with miniaturized butler matrix network', *Microwave and Optical Technology Letters*, vol. 57, no. 4, pp. 841–845, Apr. 2015, doi: 10.1002/mop.28972.

[76] F. Wu and L. Sun, 'Miniaturization of 4x4 Butler Matrix Using High Slow-Wave Factor Structure', p. 4, 2017.

[77] H. N. Chu and T.-G. Ma, 'An Extended 4x4 Butler Matrix With Enhanced Beam Controllability and Widened Spatial Coverage', *IEEE Transactions on Microwave Theory and Techniques*, vol. 66, no. 3, pp. 1301–1311, Mar. 2018, doi: 10.1109/TMTT.2017.2772815.

[78] A. Tajik, A. Shafiei Alavijeh, and M. Fakharzadeh, 'Asymmetrical 4x4 Butler Matrix and its Application for Single Layer 8x8 Butler Matrix', *IEEE Transactions on Antennas and Propagation*, vol. 67, no. 8, pp. 5372–5379, Aug. 2019, doi: 10.1109/TAP.2019.2916695.

[79] Q. Shao, F.-C. Chen, Y. Wang, Q.-X. Chu, and M. J. Lancaster, 'Design of Modified 4x6 Filtering Butler Matrix Based on All-Resonator Structures', *IEEE Transactions on Microwave Theory and Techniques*, vol. 67, no. 9, pp. 3617–3627, Sep. 2019, doi: 10.1109/TMTT.2019.2925113.

[80] W.-Y. Chen, Y.-R. Hsieh, C.-C. Tsai, Y.-M. Chen, C.-C. Chang, and S.-F. Chang, 'A compact two-dimensional phased array using grounded coplanar-waveguides butler matrices', in *2012 42nd European Microwave Conference*, Amsterdam, Oct. 2012, pp. 747–750, doi: 10.23919/EuMC.2012.6459244.

[81] S. Yamamoto, J. Hirokawa, and M. Ando, 'A beam switching slot array with a 4-way Butler matrix installed in a single layer post-wall waveguide', in *IEEE Antennas and Propagation Society International Symposium (IEEE Cat. No.02CH37313)*, San Antonio, TX, USA, 2002, vol. 1, pp. 138–141, doi: 10.1109/APS.2002.1016269.
[82] A. Ali, N. Fonseca, F. Coccetti, and H. Aubert, 'Novel Two-Layer Broadband 4 x 4 Butler Matrix in SIW Technology For Ku-Band Applications', p. 4, 2008.
[83] Yu Jian Cheng, Wei Hong, and Ke Wu, 'A two-dimensional multibeam array antenna based on substrate integrated waveguide technology', in *2008 Asia-Pacific Microwave Conference*, Macau, Dec. 2008, pp. 1–4, doi: 10.1109/APMC.2008.4958075.
[84] P. Chen *et al.*, 'A Multibeam Antenna Based on Substrate Integrated Waveguide Technology for MIMO Wireless Communications', *IEEE Transactions on Antennas and Propagation*, vol. 57, no. 6, pp. 1813–1821, Jun. 2009, doi: 10.1109/TAP.2009.2019868.
[85] C. Chen and T. Chu, 'Design of a 60-GHz Substrate Integrated Waveguide Butler Matrix—A Systematic Approach', *IEEE Transactions on Microwave Theory and Techniques*, vol. 58, no. 7, pp. 1724–1733, Jul. 2010, doi: 10.1109/TMTT.2010.2050097.
[86] T. Djerafi, N. J. G. Fonseca, and K. Wu, 'Design and Implementation of a Planar 4 × 4 Butler Matrix in Siw Technology for Wide Band High Power Applications', *Progress In Electromagnetics Research B*, vol. 35, p. 23, 2011.
[87] T. Djerafi, N. J. G. Fonseca, and K. Wu, 'Design and Implementation of a Planar 4×4 Butler Matrix in SIW Technology for Wideband Applications', p. 4, 2011.
[88] A. A. M. Ali, N. J. G. Fonseca, F. Coccetti, and H. Aubert, 'Design and Implementation of Two-Layer Compact Wideband Butler Matrices in SIW Technology for Ku-Band Applications', *IEEE Transactions on Antennas and Propagation*, vol. 59, no. 2, pp. 503–512, Feb. 2011, doi: 10.1109/TAP.2010.2093499.
[89] T. Djerafi and K. Wu, 'Multilayered substrate integrated waveguide 4 × 4 butler matrix', *International Journal of RF and Microwave Computer-Aided Engineering*, vol. 22, no. 3, pp. 336–344, May 2012, doi: 10.1002/mmce.20602.
[90] T. Djerafi and K. Wu, 'A Low-Cost Wideband 77-GHz Planar Butler Matrix in SIW Technology', *IEEE Transactions on Antennas and Propagation*, vol. 60, no. 10, pp. 4949–4954, Oct. 2012, doi: 10.1109/TAP.2012.2207309.
[91] A. B. Guntupalli, T. Djerafi, and K. Wu, 'Two-Dimensional Scanning Antenna Array Driven by Integrated Waveguide Phase Shifter', *IEEE Transactions on Antennas and Propagation*, vol. 62, no. 3, pp. 1117–1124, Mar. 2014, doi: 10.1109/TAP.2013.2292935.
[92] N. Tiwari and T. R. Rao, 'A switched beam antenna array with butler matrix network using substrate integrated waveguide technology for 60 GHz communications', in *2015 International Conference on Advances in Computing, Communications and Informatics (ICACCI)*, Kochi, India, Aug. 2015, pp. 2152–2157, doi: 10.1109/ICACCI.2015.7275935.
[93] S. Karamzadeh, V. Rafii, M. Kartal, and B. S. Virdee, 'Compact and Broadband 4x4 SIW Butler Matrix With Phase and Magnitude Error Reduction', *IEEE Microwave and Wireless Components Letters*, vol. 25, no. 12, pp. 772–774, Dec. 2015, doi: 10.1109/LMWC.2015.2496785.
[94] Q.-L. Yang, Y.-L. Ban, K. Kang, C.-Y.-D. Sim, and G. Wu, 'SIW Multibeam Array for 5G Mobile Devices', *IEEE Access*, vol. 4, pp. 2788–2796, 2016, doi: 10.1109/ACCESS.2016.2578458.
[95] Q.-L. Yang, Y.-L. Ban, J.-W. Lian, Z.-F. Yu, and B. Wu, 'SIW Butler Matrix with Modified Hybrid Coupler for Slot Antenna Array', *IEEE Access*, vol. 4, pp. 9561–9569, 2016, doi: 10.1109/ACCESS.2016.2645938.
[96] Y. Li and K.-M. Luk, '60-GHz Dual-Polarized Two-Dimensional Switch-Beam Wideband Antenna Array of Aperture-Coupled Magneto-Electric Dipoles', *IEEE*

Transactions on Antennas and Propagation, vol. 64, no. 2, pp. 554–563, Feb. 2016, doi: 10.1109/TAP.2015.2507170.

[97] Y. Cao, K.-S. Chin, W. Che, W. Yang, and E. S. Li, 'A Compact 38 GHz Multibeam Antenna Array With Multifolded Butler Matrix for 5G Applications', *IEEE Antennas and Wireless Propagation Letters*, vol. 16, pp. 2996–2999, 2017, doi: 10.1109/LAWP.2017.2757045.

[98] Y. J. Cheng and Z. J. Xuan, 'Two-dimensional beam scanning antenna array with 90-degree SIW twist', in *2017 International Workshop on Antenna Technology: Small Antennas, Innovative Structures, and Applications (iWAT)*, Athens, Greece, 2017, pp. 264–266, doi: 10.1109/IWAT.2017.7915375.

[99] L.-H. Zhong, Y.-L. Ban, J.-W. Lian, Q.-L. Yang, J. Guo, and Z.-F. Yu, 'Miniaturized SIW Multibeam Antenna Array Fed by Dual-Layer 8 × 8 Butler Matrix', *IEEE Antennas and Wireless Propagation Letters*, vol. 16, pp. 3018–3021, 2017, doi: 10.1109/LAWP.2017.2758373.

[100] F. Ren, W. Hong, and K. Wu, 'W-band series-connected patches antenna for multibeam application based on SIW Butler matrix', in *2017 11th European Conference on Antennas and Propagation (EUCAP)*, Paris, France, Mar. 2017, pp. 198–201, doi: 10.23919/EuCAP.2017.7928649.

[101] Z. Chen, X. Wu, and F. Yang, 'A compact SIW butler matrix with straight delay lines at 60 GHz', in *2017 IEEE International Symposium on Antennas and Propagation & USNC/URSI National Radio Science Meeting*, San Diego, CA, USA, Jul. 2017, pp. 2141–2142, doi: 10.1109/APUSNCURSINRSM.2017.8073113.

[102] X. Li, M. Cai, H. Shen, and G. Yang, 'A compact two-dimensional multibeam antenna fed by two-layer SIW butler matrix', in *2017 IEEE International Symposium on Antennas and Propagation & USNC/URSI National Radio Science Meeting*, San Diego, CA, USA, Jul. 2017, pp. 305–306, doi: 10.1109/APUSNCURSINRSM.2017.8072195.

[103] W. Yang, Y. Yang, W. Che, C. Fan, and Q. Xue, '94-GHz Compact 2-D Multibeam LTCC Antenna Based on Multifolded SIW Beam-Forming Network', *IEEE Transactions on Antennas and Propagation*, vol. 65, no. 8, pp. 4328–4333, Aug. 2017, doi: 10.1109/TAP.2017.2710229.

[104] M. K. Khattak *et al.*, 'A flat, broadband and high gain beam-steering antenna for 5G communication', in *2017 International Symposium on Antennas and Propagation (ISAP)*, Phuket, Oct. 2017, pp. 1–2, doi: 10.1109/ISANP.2017.8228856.

[105] Y. Li, J. Wang, and K.-M. Luk, 'Millimeter-Wave MultiBeam Aperture-Coupled Magnetoelectric Dipole Array With Planar Substrate Integrated Beamforming Network for 5G Applications', *IEEE Transactions on Antennas and Propagation*, vol. 65, no. 12, pp. 6422–6431, Dec. 2017, doi: 10.1109/TAP.2017.2681429.

[106] J.-W. Lian, Y.-L. Ban, Q.-L. Yang, B. Fu, Z.-F. Yu, and L.-K. Sun, 'Planar Millimeter-Wave 2-D Beam-Scanning Multibeam Array Antenna Fed by Compact SIW Beam-Forming Network', *IEEE Transactions on Antennas and Propagation*, vol. 66, no. 3, pp. 1299–1310, Mar. 2018, doi: 10.1109/TAP.2018.2797873.

[107] M. Bozzi, 'Substrate integrated waveguide (SIW) technology: New research trends for low-cost and eco-friendly wireless systems', in *2012 IEEE MTT-S International Microwave Workshop Series on Millimeter Wave Wireless Technology and Applications*, Sep. 2012, pp. 1–1, doi: 10.1109/IMWS2.2012.6338240.

[108] S. Sirci *et al.*, 'Design and Multiphysics Analysis of Direct and Cross-Coupled SIW Combline Filters Using Electric and Magnetic Couplings', *IEEE Transactions on Microwave Theory and Techniques*, vol. 63, no. 12, pp. 4341–4354, Dec. 2015, doi: 10.1109/TMTT.2015.2495287.

[109] Y. Shen, H. Wang, W. Kang, and W. Wu, 'Dual-Band SIW Differential Bandpass Filter With Improved Common-Mode Suppression', *IEEE Microwave and Wireless Components Letters*, vol. 25, no. 2, pp. 100–102, Feb. 2015, doi: 10.1109/LMWC.2014.2382683.
[110] D.-F. Guan, Z.-P. Qian, Y.-S. Zhang, and Y. Cai, 'A Hybrid SIW and GCPW Guided-Wave Structure Coupler', *IEEE Microwave and Wireless Components Letters*, vol. 24, no. 8, pp. 518–520, Aug. 2014, doi: 10.1109/LMWC.2014.2321497.
[111] Ji-Xin Chen, Wei Hong, Zhang-Cheng Hao, Hao Li, and Ke Wu, 'Development of a low cost microwave mixer using a broad-band substrate integrated waveguide (SIW) coupler', *IEEE Microwave and Wireless Components Letters*, vol. 16, no. 2, pp. 84–86, Feb. 2006, doi: 10.1109/LMWC.2005.863199.
[112] D. Chaturvedi, A. Kumar, and S. Raghavan, 'An Integrated SIW Cavity-Backed Slot Antenna-Triplexer', *IEEE Antennas and Wireless Propagation Letters*, vol. 17, no. 8, pp. 1557–1560, Aug. 2018, doi: 10.1109/LAWP.2018.2855051.
[113] Z. Zhang, X. Cao, J. Gao, S. Li, and J. Han, 'Broadband SIW Cavity-Backed Slot Antenna for Endfire Applications', *IEEE Antennas and Wireless Propagation Letters*, vol. 17, no. 7, pp. 1271–1275, Jul. 2018, doi: 10.1109/LAWP.2018.2842046.
[114] T.-Y. Chin, S.-F. Chang, J.-C. Wu, and C.-C. Chang, 'A 25-GHz Compact Low-Power Phased-Array Receiver With Continuous Beam Steering in CMOS Technology', *IEEE Journal of Solid-State Circuits*, Nov. 2010, doi: 10.1109/JSSC.2010.2064010.
[115] H. Ren, B. Arigong, M. Zhou, J. Ding, and H. Zhang, 'A Novel Design of 4x4 Butler Matrix With Relatively Flexible Phase Differences', *IEEE Antennas and Wireless Propagation Letters*, vol. 15, pp. 1277–1280, 2016, doi: 10.1109/LAWP.2015.2504719.

Chapter 2:

Butler Matrix: sensitivity and concept of tunability

Nowadays, spatial coverage becomes very relevant when dealing with the current wireless technologies, which aim for as much spatial resolution as possible in order to optimize the energy per transferred bit. Increasing the spatial resolution typically triggers the complexity of the antenna architecture and, in turn, its costs. In the case of BM, in fact, higher steering resolution can be achieved by increasing the BM order adopting, for instance, an 8x8 BM in place of a 4x4 BM. However, this option implies not only an increase of the area consumed by the BM and by the single radiators but also of its overall complexity. As an alternative approach, it is possible to expand the beam controllability of a BM without increasing its order. Such a result can be achieved by combining a BM with a reduced number of elements with a set of phase shifters (PSs) employed to control critical paths in the BM. Thanks to this approach a BM can have two means of radiation pattern control: one depending on the BM structure and one determined by the PS reconfigurability.

The objective of this chapter is twofold. Firstly, a sensitivity analysis performed using the Monte Carlo (MC) approach is used to highlight the impact of each sub-circuit of the BM (couplers, crossovers, phase shifters) on the radiation pattern. Analytical electromagnetic equations are then derived to prove the concept on a particular parameter that is the transmission path isolation of the crossover, which has a high impact on the global sensitivity. Secondly, the theory of the novel extended beam BM concept is introduced. It will be also shown how this concept becomes much more interesting if associated with reconfigurable radiating elements, capable of improving the lateral beam-steering of the antenna array. Eventually, in order to show the interest of the proposed concept, a state-of-the-art of reconfigurable beam antenna is proposed, the design constraints of those antennas is given and their impact on the performance of the system is highlighted.

2.1 Introduction to sensitivity study of the conventional Butler matrix

As explained in Section 1.5, a SIW-based BM integrated in a single-layered substrate is simpler to design with respect to multi-layered structures [1]–[6]. On the contrary, BM integration in a multi-layer stack-up allows to shrink the size thanks to the capability to stack the different BM building blocks, including the crossover whose performance have been proved to strongly affect the BM amplitude-and-phase-output imbalance [7], [8]. Hence, the crossover is a very critical block in the BM design. As a consequence, it is essential to assess the BM sensitivity with respect to the crossover performance which, for the proposed single-layered approach, can be detrimental.

In sub-section 2.1.1, the MC study aims at figuring out the radiation pattern sensitivity of a 4-element linear array, when the different amplitudes and phases are delivered by the BM defined in Figure 2-1, to which sensitivity ranges are applied in accordance to the technological

tolerances. In sub-sections 2.1.3 and 2.1.4, a detailed sensitivity analysis is performed in analytical form and through full-wave simulations of the individual blocks, respectively.

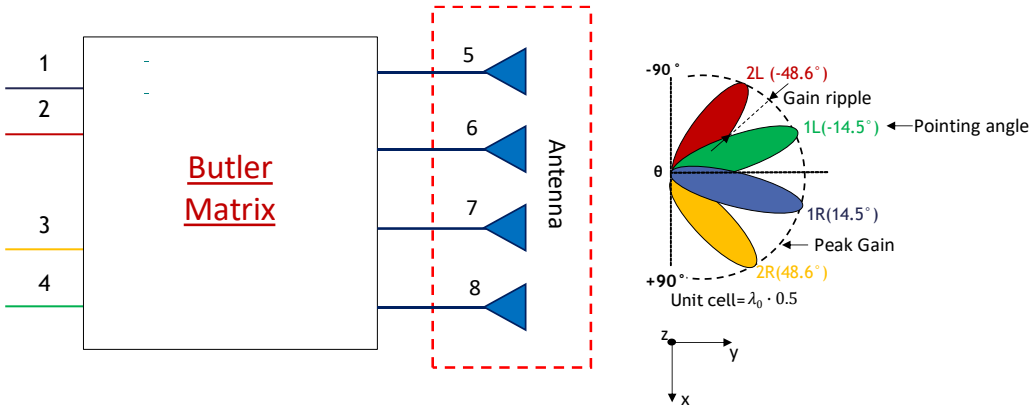

Figure 2-1: General beam-steering antenna array based on BM and elementary antenna sources

Figure 2-1 depicts three important aspects related to the evaluation of the performance of a 4-elements array fed with a BM:

- The peak gain is the maximum gain value of the array;
- The beam pointing angle is the direction of the array main beam;
- The gain ripple is the ripple between the maximum and minimum achievable gain when the beam is scanned over the spatial coverage;

2.1.1 Monte Carlo analysis on the sensitivity of the antenna-array radiation pattern to the input signals

Due to fabrication issues, the RF signal at the BM output ports (namely at ports 5, 6, 7, 8) might be different from the expected ones. In this paragraph, we want to figure out what might happen to the antenna-array radiation pattern if an unexpected amplitude/phase imbalance is generated by the BM and used to fed an N-element array. For that purpose, four isotropic elementary antenna sources are taken into account evaluating their radiation pattern when the input amplitude and phase is varied within a certain range, according to a uniform MC distribution. The relationship between the antenna-array radiation pattern (AP), the array factor (AF) and the elementary antenna radiation pattern (EP) is given by equation (2-1).

$$AP = AF \cdot EP \tag{2-1}$$

In other words, the antenna-array radiation pattern is plotted according to the total radiated far-field formula [9] of equation (2-2) and represents the variation of the total radiated far-field, $\left\|\overrightarrow{E_{tot}}\right\|$. Assuming an alignment along the x-axis of N isotropic antennas, that is to say radiating the same $\overrightarrow{E_0}$ in any directions of space, and conventional spherical coordinates (r, θ, φ), in the $(Oxyz)$ basis of Figure 2-1, it yields:

$$\overrightarrow{E_{tot}} = \left(\sum_{k=0}^{N-1} A_k \cdot e^{j \cdot \gamma_k}\right) \cdot \overrightarrow{E_0} \tag{2-2}$$

with:

$$\gamma_k = \delta_k + \beta_0 \cdot k \cdot d \cdot \sin(\theta) \,.\, \cos(\varphi) \qquad (2\text{-}3)$$

where A_k, δ_k, β_0 and d are the amplitude and phase of the k^{th} current source feeding the k^{th} antenna, the free space propagation constant and the center-to-center distance between antennas, respectively. Using a simple Matlab code, the total radiated field is calculated using a MC analysis of a distribution of $N \cdot A_k$, that guarantees a fixed power balance, whatever the amplitude imbalance ranging between 0 and the maximum allowed deviation. The phase imbalance is evaluated at each branch by adding to δ_k a positive or negative phase, ranging between 0 and the maximum considered deviation. For $N = 4$ and by choosing $d = 0.5 \cdot \lambda_0$, where λ_0 is the free-space wavelength, the radiation pattern can be plotted in the xz plane, defined by $\varphi = 0°$. 2000 iterations were chosen for the MC study. Conditions on the radiation pattern were chosen as an example only. They may seem drastic for short range wireless mm-waves communication but they are insufficient, in terms of pointing, for backhauling systems whose requirements might be difficult to achieve with a BM only without any fine tuning system (varactor based for example).

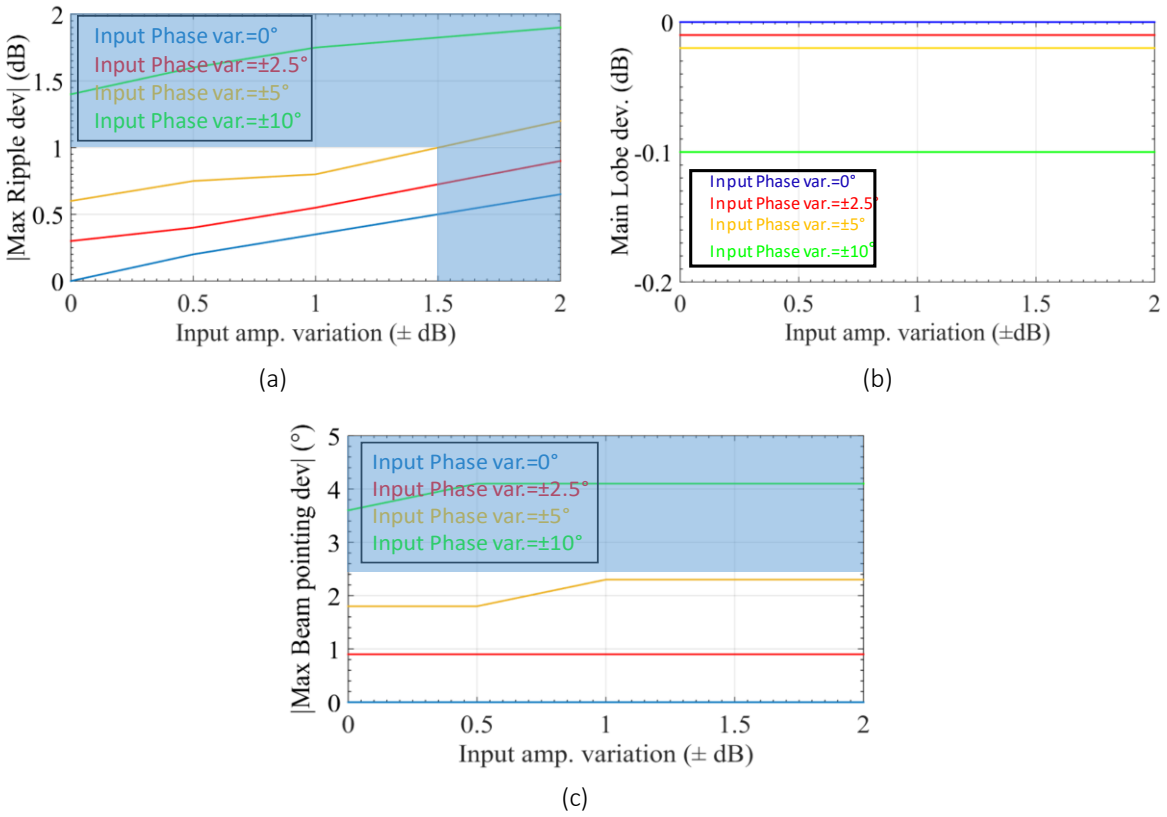

Figure 2-2: (a) Maximum ripple, (b) main lobe variation to 6 dB and (c) beam pointing deviation, based on MC study

The absolute values of the maximum ripple deviation (dev), main lobe (peak gain) deviation and beam pointing (angle) deviation are depicted in Figure 2-2 versus the input amplitude variation (varying from 0 to ±2 dB), and for different input phase variations (0, ±2.5°, ±5° ±10°). Those values of input amplitude and phase variations were chosen based on typical BM values [3], [10].

As it can be noticed, the maximum ripple deviation varies between 0 and 0.65 dB (for a 0° input phase variation) and between 1.4 and 1.9 dB (for a ±10° input phase variation), respectively. This may be important as the ripple is already reaching 3.7 dB, theoretically. The main lobe deviation is equal to -0.1 dB in the worst case of a ±10° input phase variation. In other words, negligible impact may be observed in the considered range of variation. Finally, the maximum beam pointing deviation ranges between 0° and 4.1° when the input phase variation is equal to 0° and ±10°, respectively. On the other hand, it remains almost unchanged when input amplitude is varied. The latter deviations show a relative robustness to the BM output imbalances, as long as beams are wide with apertures of 10° (backhaul applications would be naturally ruled out). The worst-case radiation pattern is represented in Figure 2-3, where input amplitude and phase variation are ±2 dB and ±10°, respectively. Radiation patterns correspond to the 1R (blue), 2R (yellow), 1L (green) and 2L (red) of Figure 2-1. The ideal case is depicted in black. The main lobe may be slightly deviated but it keeps its theoretical value of 6 dB as pointed out in Figure 2-2 (b) and (c). The maximum lateral lobes deviation may be as high as 4.3 dB for pattern 1L but the lateral lobes always stay smaller than 7 dB as compared to the main lobe whatever the considered pattern.

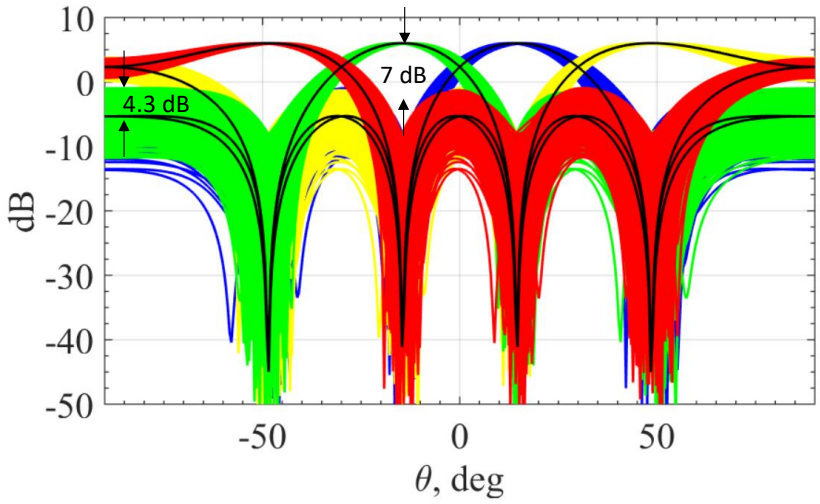

Figure 2-3: Worst case input variation radiation pattern, when input amplitude and phase variation are ±2 dB and ±10°.

Finally, in order to get (i) a maximum ripple deviation lower than 1 dB as compared to the typical case (3.7 dB), (ii) a maximum main lobe (peak gain) deviation lower than 0.1 dB as compared to 6 dB and (iii) a maximum beam pointing (angle) deviation lower than 2.5°, it is necessary to narrow the input amplitude and phase variation to ±1.5 dB and ±5° around the -6 dB of amplitude and the theoretical phase for each antenna branch. It is important to point out that the ±5° is a decisive point in terms of ripple. The target (i, ii, and iii) corresponds to an imbalance of ±3 dB between two output ports (adjacent or not) and ±10° between adjacent output ports if a BM system is considered. It is particularly important to notice that considering a maximum deviation of ±3 dB between output ports and ±10° between adjacent output ports without showing what happens at each branch might not be acceptable. Indeed, an additional deterioration could be observed eventually if deviation exceeds ±1.5 dB and ±5° at one branch.

2.1.2 Monte Carlo analysis on the sensitivity of the Butler matrix to the electrical parameters of its constituting blocks

In this paragraph, the MC method is applied separately to each building block forming the 4×4 BM in order to figure out which component is causing the biggest output amplitude imbalance between two ports (adjacent or not) and the biggest phase imbalance between two adjacent ports. Couplers, crossovers and phase shifters of Figure 2-4 are going to be analyzed in the next paragraphs. Simulations were carried out using ADS by Keysight.

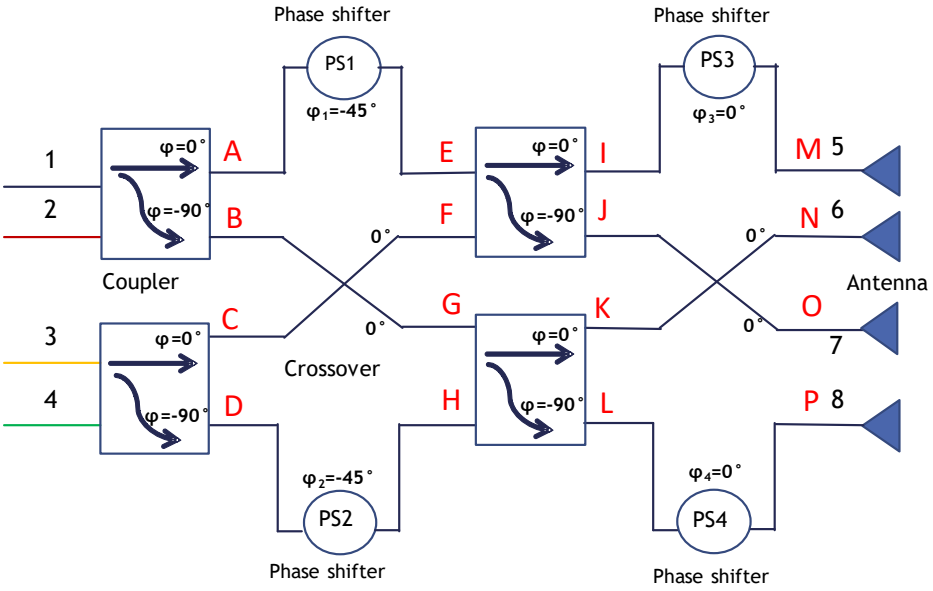

Figure 2-4: The conventional BM under study with 4 couplers, 2 crossovers and 2 phase-shifters (PS1 and PS2). PS3 and PS4 do have a null phase shift in the conventional BM and are not considered herein. The phases in black at the outputs of each blocks correspond to the absolute phase-shifts induced by each block, in an ideal BM, without any offset due to technical implementation.

2.1.2.1 Couplers impact

The first block to be taken into account is the coupler, for which both output amplitude and phase imbalance is considered. For this analysis, the crossovers and phase shifters are being considered as ideal, as well as the coupler matching and isolation.

Phase and amplitude deviations are taken identical for all the four couplers as they mainly depend on technological process variation. There are several ways to consider a deviation from the ideal case. For the case at hand, the simulation was carried out so that the phase imbalance for a coupler represents the difference between the opposite phase variations around the two references 0° at node A and -90° at node B, in Figure 2-4.

Concerning the amplitude imbalance, it is automatically calculated using ADS where it was created a dedicated coupler block so that power budget, perfect input matching and isolation are idealized while observing the targeted amplitude imbalance between nodes A and B.

In order to define the coupler and crossover ports, a simple picture is shown in Figure 2-5.

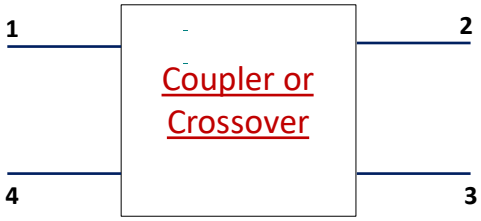

Figure 2-5: Coupler and crossover ports definition

In Figure 2-6, the resulting output amplitude and phase imbalance of the BM is reported.

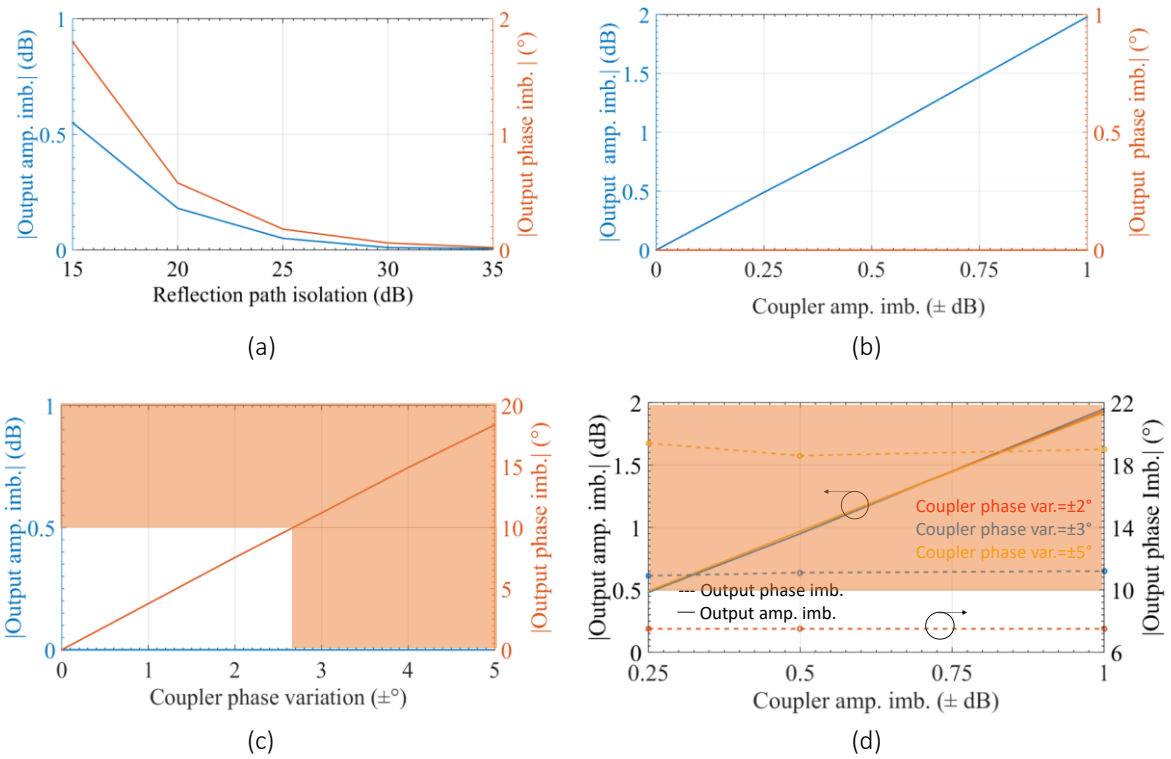

Figure 2-6: BM output amplitude and phase imbalance, for couplers (a) reflection path isolation $(-S_{41_{dB}})$ only, (b) amplitude imbalance only, (c) phase variation only, and (d) both amplitude and phase imbalance

Figure 2-6 (a) shows quite a weak impact of reflection path isolation, i.e. $(-S_{41_{dB}})$, in a clock wise counting, that is less than 0.2 dB and 0.6° for $(-S_{41}) = 20$ dB. Reflection path isolation is not the major parameter. Similarly, return loss $(-S_{11_{dB}})$ should be of the same order, 20 dB. Figure 2-6 (b) is achieved when only the output amplitude imbalance of all the couplers is varied between 0 and ±1 dB. No BM output phase imbalance is reported in this first case. On the contrary, only BM output phase imbalance changes when a phase imbalance is generated in the couplers, as shown in Figure 2-6 (c). The BM output phase imbalance ranges between 0° and 18.4°. As it is easy to imagine, when the coupler amplitude and phase imbalance are taken into account at the same time, both the previously mentioned effects affect the BM output as highlighted in Figure 2-6 (d). In the worst case, those variations might spoil the radiation pattern, as discussed earlier. In this example, the coupler affects the radiation pattern more significantly when phase imbalance takes place. Typically, a coupler imbalance of ±1 dB can be tolerated while the phase variation might not exceed ±2.7°.

2.1.2.2 **Phase shifters impact**

In this study the phase range of each phase shifter (PS) was varied from 0 to ±5° at nodes E, H, M and P simultaneously, the crossovers and couplers being considered as ideal. For a phase variation of ±5°, an output BM phase imbalance as large as 29.4° was obtained. This big phase imbalance can provide radiation patterns deviating more than 5°, as shown in Figure 2-2 (c). As for the couplers, for a ±10° output phase imbalance, i.e. a beam pointing deviation lower than 2.5°, phase variation may not exceed ±3°.

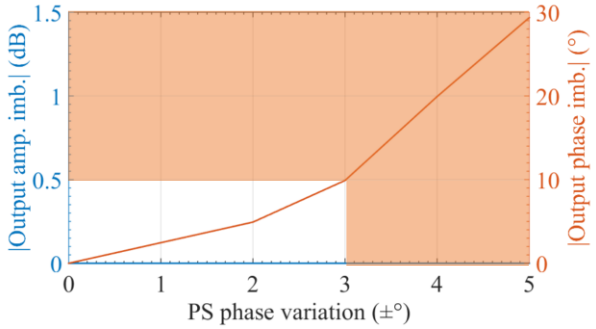

Figure 2-7: BM output amplitude and phase imbalance, for PSs phase variation

2.1.2.3 **Crossovers impact**

Finally, a similar study was carried out for the crossovers of the BM. In this case the couplers and PSs were considered as ideal components. Figure 2-8 (a) shows a weak impact of the crossover reflection path isolation, i.e. $\left(-S_{41_{dB}}\right)$, in a clock wise counting. The resulting amplitude variations do not exceed 0.15 dB and no impact on the phase is observed, provided S_{41}< -20 dB.

In Figure 2-8 (b), the output amplitude imbalance goes from 0.33 dB to 3.6 dB, and the output phase imbalance goes from 1.5° to 18.2°, when the crossover transmission path isolation, i.e. $\left(-S_{21_{dB}}\right)$ in a clock wise counting, varies from 35 dB down to 15 dB. In Figure 2-8 (c), the variation in phase of the coupled path only impacts the output phase imbalance going from 0 up to 10°. Finally, variations on both the transmission path isolation and the phase of the coupled path are shown in Figure 2-8 (d). The BM output amplitude imbalance varies from 0.35 to 3.7 dB, when the transmission path isolation varies from 35 dB down to 15 dB. No variation occurs when the crossover output phase changes.

On the contrary, when the transmission path isolation and the phase of the coupled path vary from 35 dB down to 15 dB and between ±2° to ±5°, respectively, the BM output phase imbalance varies from 6.2° to 20° and, from 14.5° to 25.1°. Hence, the transmission path isolation S_{21} magnitude level is critical for both output amplitude and phase imbalance. S_{21} = -17.5 dB causes an output amplitude imbalance of ±3 dB. Even S_{21} = -25 dB impacts the output phase imbalance that becomes greater than ±10° whilst the crossover phase variation is still small (±3°).

As a result, a strong impact is observed on radiation pattern. Crossover can be an issue for designers and it is worth to study it in depth by providing analytical formulas that can better describe the problem of the crossover transmission path isolation sensitivity.

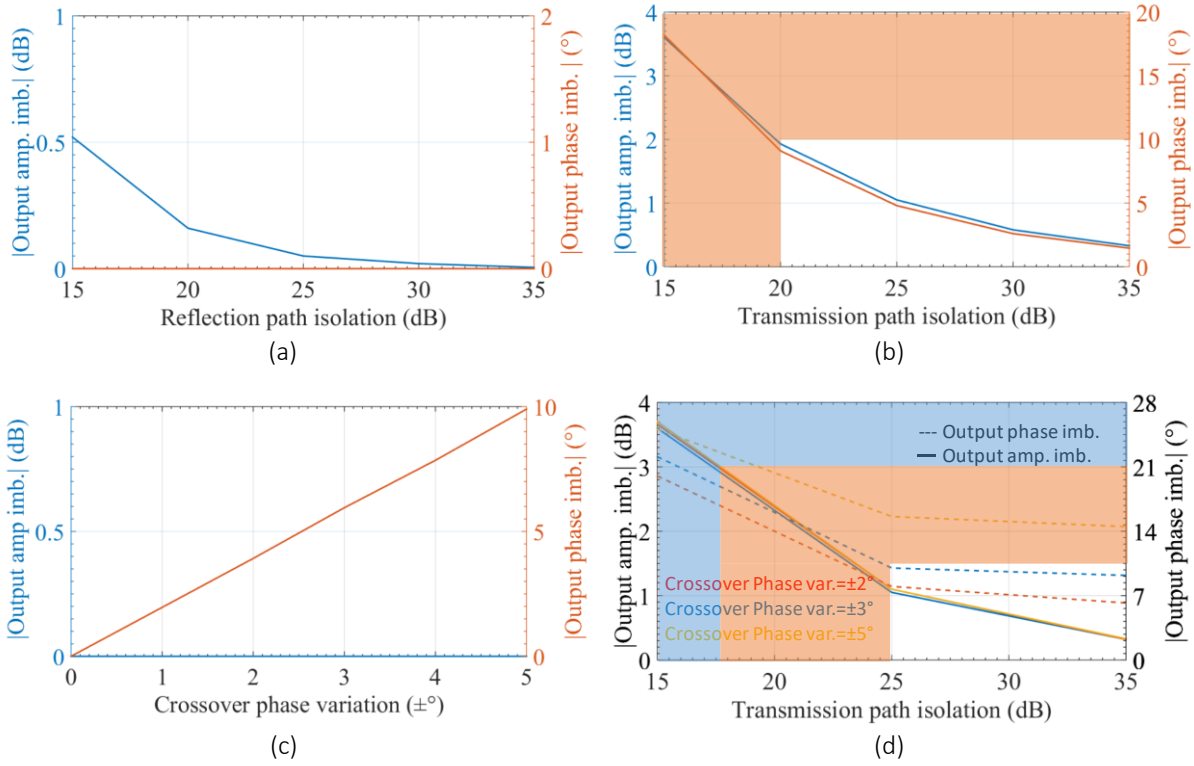

Figure 2-8: BM output amplitude and phase imbalance, for crossovers (a) reflection path isolation $(-S_{41_{dB}})$ only, (b) transmission path isolation $(-S_{21_{dB}})$ only, (c) coupled path phase variation only, and (d) both transmission path isolation and coupled path phase variations.

2.1.3 Theoretical analysis on the sensitivity of the Butler matrix to the crossover's transmission path isolation $(-S_{21_{dB}})$

Ideally, the crossover of a BM has perfect matching, perfect transmission path isolation $(-S_{21_{dB}})$, perfect reflection path isolation $(-S_{41_{dB}})$, that can be obtained simultaneously. Sometimes, the requirements for the stand-alone devices forming the system might not be perfectly respected, due to fabrication uncertainty for example, thus inducing amplitude and output phase imbalance between the output ports of the BM. It has been seen that crossovers transmission path isolation (Figure 2-8) is the main parameter to be considered in terms of modulus, having an impact on both output magnitude and phase imbalance. In parallel, phases variations at each block mostly impact the output phase imbalance that will mostly impact the beam de-pointing, in return. Hence couplers and crossover phase variations are also important parameters but prototypes may be improved in terms of final lengths, by the end, whereas a transmission path isolation of 25 dB may be simply unreachable in the chosen technology. In this paragraph an analytical study is going to be proposed to illustrate the dependence of the BM performance on the crossover behaviour. Lossless circuits are considered as ideal stand-alone circuits except for the crossover whose S_{21} (ideally linearly nul) will be varied. Hence, the following parameters are considered:

- 3dB Couplers:
  - Perfect matching $(S_{11} = S_{22} = S_{33} = S_{44} = 0)$

- Perfect isolation ($S_{41} = 0$),
- No phase or amplitude output imbalance:

  $S_{21} = T \cdot e^{j0} = T = \frac{1}{\sqrt{2}}$ and $S_{31} = \sqrt{1-T^2} \cdot e^{-\frac{j\pi}{2}} = -j\sqrt{1-T^2} = -j\frac{1}{\sqrt{2}}$

- Phase shifters:
  - Perfect matching ($S_{11} = S_{22} = 0$)
  - No phase error ($S_{21} = e^{j\varphi_i}$)

- Crossovers:
  - Perfect matching ($S_{11} = S_{22} = S_{33} = S_{44} = 0$)
  - Perfect reflection path isolation between port 1 and 4 ($S_{41} = 0$),
  - Coupling parameter ($S_{31} \neq 1$) leading to a non-ideal transmission path isolation parameter ($S_{21} \neq 0$):

    $S_{31} = \sqrt{1-\varepsilon^2} \cdot e^{j0} = \sqrt{1-\varepsilon^2}$ and $S_{21} = \varepsilon \cdot e^{\frac{j\pi}{2}} = j\varepsilon$

The BM output S-parameters will be given in function of the transmission path isolation S_{21} (parameter ε should be as small as possible). The study is done at a fixed frequency.

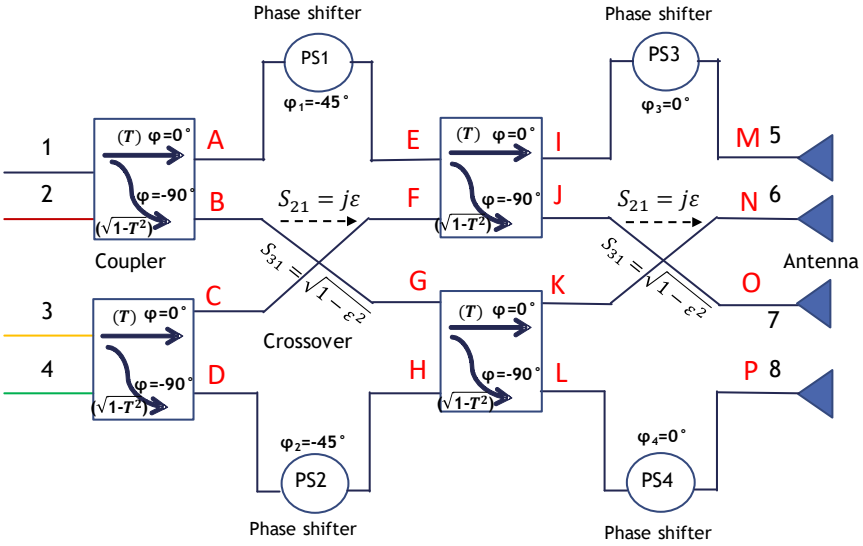

Figure 2-9: The conventional BM of Figure 2-4 with the crossovers non-ideal electrical parameters under study.

Only two cases are considered, when either port 1 or port 2 are feeding the BM, other ports being matched. Indeed, due to the symmetry of the system, feeding port 4 or 1 is equivalent (idem for port 3 and 2). The BM scheme is depicted in Figure 2-9, that is the same as Figure 2-4, with the specific highlighted electrical parameters.

Port 1 feeding: let us consider reduced power waves.

$$\begin{cases} b_5 = T\,(e^{j\varphi_1})T(e^{j\varphi_3}) + \left(\sqrt{1-T^2}\,e^{-\frac{j\pi}{2}}\right)\left(\varepsilon e^{\frac{j\pi}{2}}\right)\left(\sqrt{1-T^2}\cdot e^{-\frac{j\pi}{2}}\right)(e^{j\varphi_3}) \\ b_6 = T\,e^{j\varphi_1}\left(\sqrt{1-T^2}\,e^{-\frac{j\pi}{2}}\right)\left(\varepsilon e^{\frac{j\pi}{2}}\right) + \left(\sqrt{1-T^2}\,e^{-\frac{j\pi}{2}}\right)\left(\left(\varepsilon e^{\frac{j\pi}{2}}\right)T\left(\varepsilon e^{\frac{j\pi}{2}}\right) + \left(\sqrt{1-\varepsilon^2}\right)T\left(\sqrt{1-\varepsilon^2}\right)\right) \\ b_7 = T(e^{j\varphi_1})\left(\sqrt{1-T^2}\,e^{-\frac{j\pi}{2}}\right)\left(\sqrt{1-\varepsilon^2}\right) + \left(\sqrt{1-T^2}\,e^{-\frac{j\pi}{2}}\right)\left(\left(\varepsilon e^{\frac{j\pi}{2}}\right)T\left(\sqrt{1-\varepsilon^2}\right) + \left(\sqrt{1-\varepsilon^2}\right)T\left(\varepsilon e^{\frac{j\pi}{2}}\right)\right) \\ b_8 = \left(\sqrt{1-T^2}\,e^{-\frac{j\pi}{2}}\right)\left(\sqrt{1-\varepsilon^2}\right)\left(\sqrt{1-T^2}\,e^{-\frac{j\pi}{2}}\right)(e^{j\varphi_4}) \end{cases} \quad (2\text{-}4)$$

Equation (2-4) is simplified to (2-5), recalling that $\varphi_3 = \varphi_4 = 0$ in conventional matrices and that $T = \sqrt{1-T^2} = \frac{1}{\sqrt{2}}$.

$$\Leftrightarrow \begin{cases} b_5 = T^2(e^{j\varphi_1} + e^{-\frac{j\pi}{2}}\varepsilon) \\ b_6 = T^2\left(e^{-\frac{j\pi}{2}} + \varepsilon\left(e^{j\varphi_1} + 2\varepsilon e^{\frac{j\pi}{2}}\right)\right) \\ b_7 = T^2\left(e^{j\left(\varphi_1 - \frac{\pi}{2}\right)} + 2\varepsilon\right)\left(\sqrt{1-\varepsilon^2}\right) \\ b_8 = -T^2\left(\sqrt{1-\varepsilon^2}\right) \end{cases} \quad (2\text{-}5)$$

Remark: if $\varepsilon = 0$ and for $\varphi_1 = -45°$

$$\begin{cases} b_5 = T^2(e^{j\varphi_1}) \rightarrow phase\ shift\ of - 45° \\ b_6 = T^2 e^{-j\frac{\pi}{2}} \rightarrow phase\ shift\ of - 90° \\ b_7 = T^2(e^{j(\varphi_1 - \pi/2)} \rightarrow phase\ shift\ of - 135° \\ b_8 = -T^2 \rightarrow phase\ shift\ of - 180° \end{cases}$$

<u>Port 2 feeding</u>:

$$\begin{cases} b_5 = \sqrt{1-T^2}\,e^{-\frac{j\pi}{2}}(e^{j\varphi_1})T(e^{j\varphi_3}) + T\left(\varepsilon e^{\frac{j\pi}{2}}\right)\left(\sqrt{1-T^2}\cdot e^{-\frac{j\pi}{2}}\right)(e^{j\varphi_3}) \\ b_6 = \left(\sqrt{1-T^2}\,e^{-\frac{j\pi}{2}}\right)(e^{j\varphi_1})\left(\sqrt{1-T^2}\,e^{-\frac{j\pi}{2}}\right)\left(\varepsilon e^{\frac{j\pi}{2}}\right) + T^2\left(\left(\varepsilon^2 e^{\frac{j2\pi}{2}}\right) + \left(\sqrt{1-\varepsilon^2}\right)^2\right) \\ b_7 = \left(\sqrt{1-T^2}\,e^{-\frac{j\pi}{2}}\right)(e^{j\varphi_1})\left(\sqrt{1-T^2}\,e^{-\frac{j\pi}{2}}\right)\left(\sqrt{1-\varepsilon^2}\right) + 2\left(T^2\left(\varepsilon e^{\frac{j\pi}{2}}\right)\left(\sqrt{1-\varepsilon^2}\right)\right) \\ b_8 = T\left(\sqrt{1-\varepsilon^2}\right)\left(\sqrt{1-T^2}\,e^{-\frac{j\pi}{2}}\right)(e^{j\varphi_4}) \end{cases} \quad (2\text{-}6)$$

Equation (2-6) is simplified to (2-7).

$$\Leftrightarrow \begin{cases} b_5 = T^2(e^{j\left(\varphi_1 - \frac{\pi}{2}\right)} + \varepsilon) \\ b_6 = T^2\left(1 + \varepsilon\left(e^{j\left(\varphi_1 - \frac{\pi}{2}\right)} - 2\varepsilon\right)\right) \\ b_7 = T^2\left(e^{j(\varphi_1 - \pi)} + 2\varepsilon e^{\frac{j\pi}{2}}\right)\left(\sqrt{1-\varepsilon^2}\right) \\ b_8 = \left(T^2 e^{-\frac{j\pi}{2}}\right)\left(\sqrt{1-\varepsilon^2}\right) \end{cases} \quad (2\text{-}7)$$

It might be noticed that if $\varepsilon = 0$ and $\varphi_1 = -45°$ then

$$\begin{cases} b_5 = T^2\left(e^{j(\varphi_1 - \frac{\pi}{2})}\right) \rightarrow phase\ shift\ of -135° \\ b_6 = T^2 \rightarrow phase\ shift\ of\ 0° \\ b_7 = T^2\left(e^{j(\varphi_1 - \pi)}\right) \rightarrow phase\ shift\ of -225° = +135° \\ b_8 = T^2 e^{-\frac{j\pi}{2}} \rightarrow phase\ shift\ of -90° = +270° \end{cases}$$

In Figure 2-10, the S-parameters amplitude and phase of the resulting system are plotted. The transmission path isolation ($S_{21} = j\varepsilon$, ideally = 0) is varied between 10 dB and 60 dB. Before describing the study, let us remember that, as proposed in sub-section 2.1.1, maximum output amplitude and phase imbalance of ±3 dB between two output ports (adjacent or not) and ±10° between adjacent output ports must be met to achieve:

- a maximum ripple deviation lower than 1 dB,
- a maximum main lobe gain reduction of less than 0.1 dB, and
- a maximum beam pointing deviation lower than 2.5°.

As it can be noticed, for a transmission path isolation of 17.5 dB, the output amplitude imbalance is 2.5 dB (2.6 dB, respectively), and the output phase imbalance is 13.1° (12.2°, respectively), when port 1 (port 2, respectively) is fed, which does not allow the exampled criteria of the BM to be guaranteed. On the contrary, for a transmission path isolation of 30 dB, the output amplitude imbalance and the output phase imbalance are 0.6 (0.6 dB, respectively) and 2.7° (2.6°, respectively) when port 1 (port 2, respectively) is fed, which, on the basis of paragraph 0, would lead to a maximum ripple of 0.35 dB, no main lobe variation and a maximum de-aiming lower than 1°, if couplers and PSs are perfect components.

It is important to note that 30 dB may be difficult to obtain, at illustrated by the the state-of-art. It's worth noticing that S_{81} (S_{82}) remains almost unchanged from 10 to 60 dB of transmission path isolation.

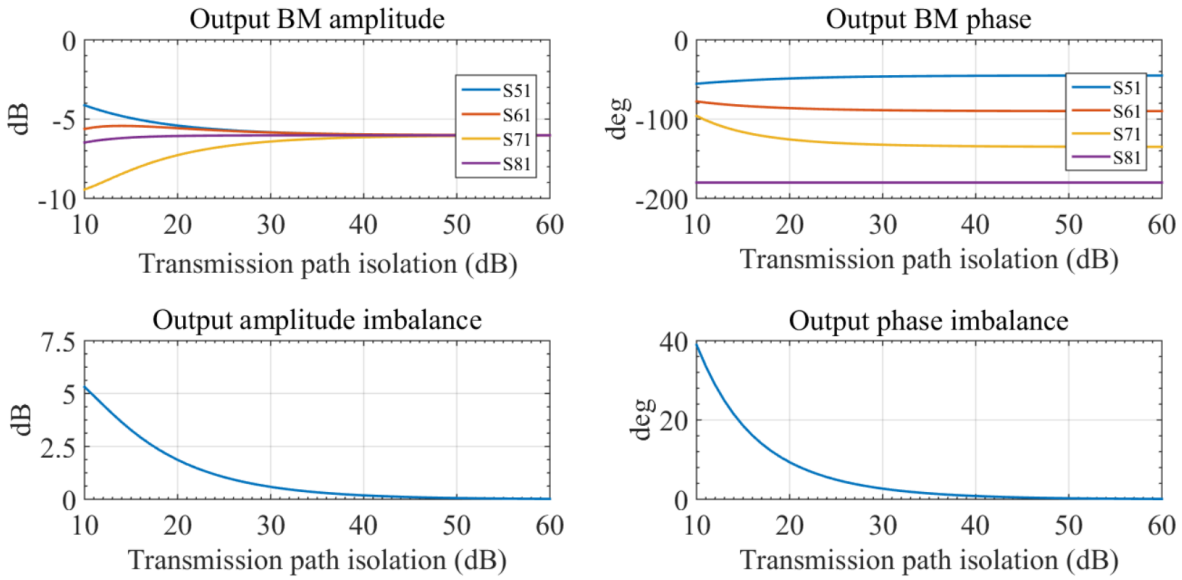

(a)

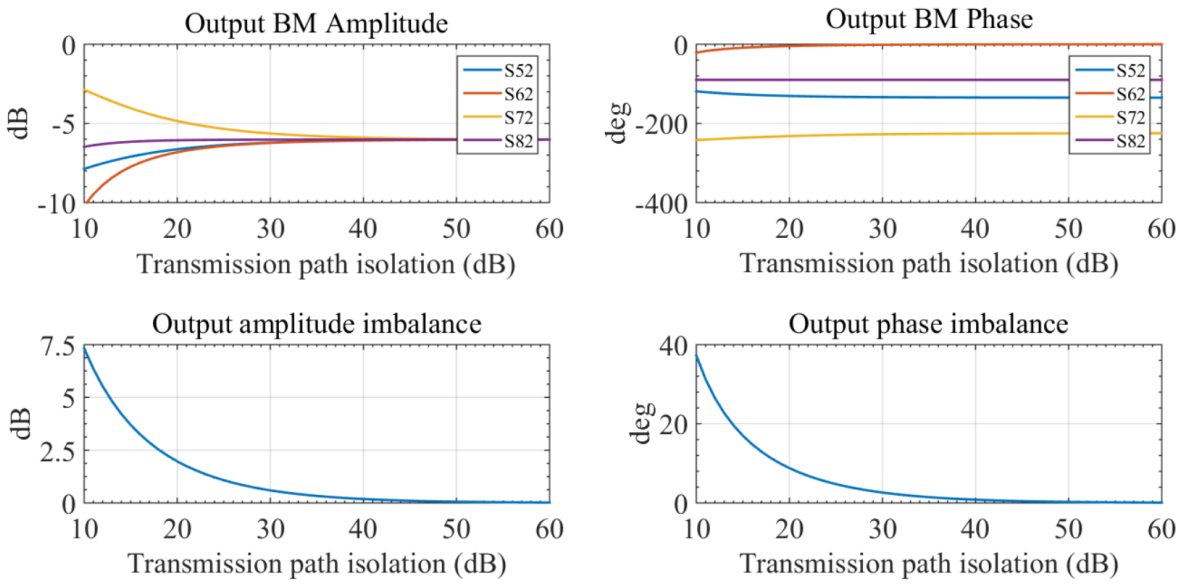

(b)

Figure 2-10: S-parameters of the overall system when: (a) port 1 is fed and (b) port 2 is fed

In conclusion, the BM designers should pay attention to the implementation of the crossover before designing BM because its transmission path isolation might dramatically spoil the performance of the overall system, if its value is not high enough.

In the next paragraph, the impact of the PCB technology on the transmission path isolation of a SIW slot-based crossover is addressed to consolidate the aforementioned analysis and conclusion.

2.1.4 Electromagnetic simulations analysis on the sensitivity of the Butler matrix due to the PCB SIW technological variations

2.1.4.1 Crossover transmission path isolation performance variation

A crossover based on a 0-dB short-slot coupler [11] is depicted in Figure 2-11. Its working principle is detailed in Chapter IV. We will use this crossover to show how realistic technological variations degrade the isolation performance of the crossover, and thus the overall performance of the BM.

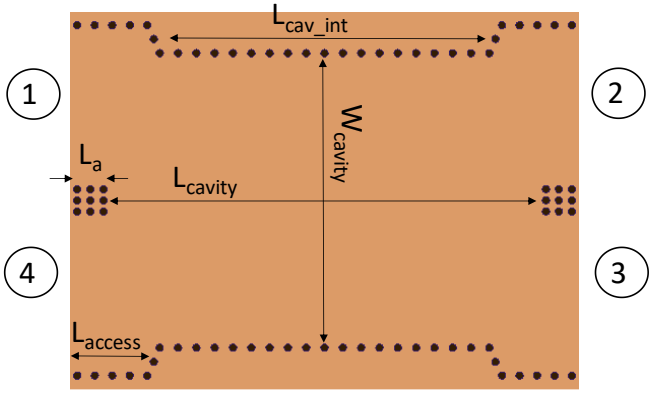

Figure 2-11: PCB crossover based on 0-dB short-slot coupler [11]

In this section, we consider that, due to defects or inaccuracy in the fabrication process, W_{cavity} might vary around its average designed value. This variation makes the transmission path isolation S_{21} and output phases (ϕ_{21} and ϕ_{31}) vary as well. A coupling width W_{cavity} is considered varying from 7.6 mm to 7.9 mm (in bold in Table 2-1) leading to a variation inaccuracy of ±150 µm around 7.75 mm, due to the fabrication process. In Table 2-1, seven simulated variations of the designed crossover are taken into account and the S-parameters are reported, at 28 GHz. The return loss ($-S_{11_{dB}}$) and reflection path isolation ($-S_{41_{dB}}$) are for all the variations better than 20 dB between 27 and 29 GHz, and better than 33 dB at the considered central frequency (28 GHz).

Config.	W_{cavity} (mm)	S_{31} (dB)	ϕ_{31} (deg)	S_{21} (dB)	$\Delta\phi = \phi_{21} - \phi_{31}$ (deg)
1	**7.6**	-0.3	-56.7	-26.8	-87.6
2	**7.65**	-0.29	-58.5	-33	-87.4
3	**7.7**	-0.28	-61.6	-45.2	NA
4	**7.75**	**-0.28**	**-63.5**	**-37.1**	**85.6**
5	**7.8**	-0.28	-66	-29.5	87.8
6	**7.85**	-0.29	-68.2	-25.7	89.6
7	**7.9**	-0.30	-70.2	-23.2	89.2

Table 2-1: Crossover transmission path isolation ($-S_{21_{dB}}$) and output phase variation, with finite conductivity ($58 \cdot 10^6$ S/m) walls considered in the EM simulations at 28 GHz.

As it can be noticed, a variation of ±150 µm (~2%) around the designed value of 7.75 µm can cause an output phase variation of ±7°, and with more impact a transmission path isolation ($-S_{21_{dB}}$) varying from 23.2 dB to 45.2 dB. $\Delta\phi$ of configuration 3 was not inserted because of value uncertainty, due to very low level of transmission path isolation (45 dB).

In the next step, each crossover variation (s4p file) is inserted in the system represented in Figure 2-12 and simulated with ADS in order to show the impact of S_{21} (and hence the impact of the process variations) on the output of the BM system.

2.1.4.2 Impact on the Butler matrix system performance

In this section the impact of the non-null transmission path isolation ($-S_{21_{dB}}$) on BM is discussed in relation to a PCB process. The study is based on the system represented in Figure 2-12. EM simulations are first performed with HFSS for stand-alone 'real' crossovers, while considering ideal PSs, then the system-level simulations are done with ADS between 26 GHz and 30 GHz.

Concerning the couplers, they were optimized in order to obtain: a low loss (0.2 dB), a low output amplitude imbalance (0.5 dB, from 26 up to 30 GHz), a good return loss, an isolation ($-S_{41_{dB}}$) better than 20 dB between 27 GHz and 30 GHz, and an almost constant output phase difference of 90° all along the simulated frequency band.

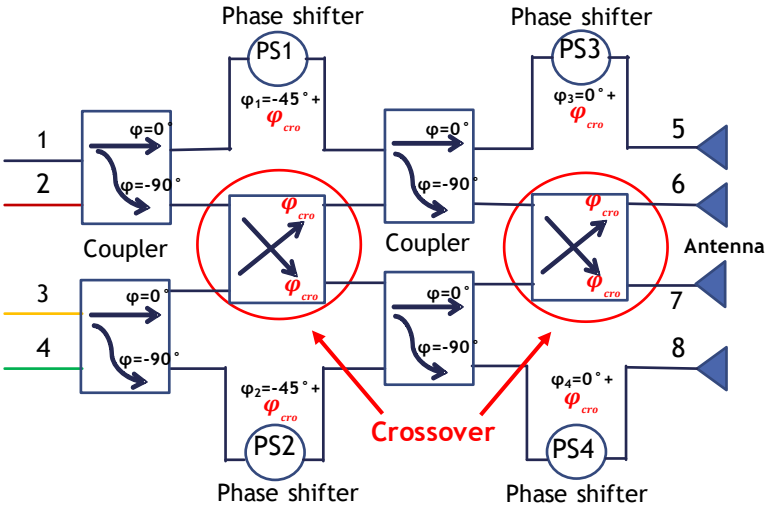

Figure 2-12: BM system used for sensitivity study on PCB. The phases in black at the outputs of each coupler or PS correspond to the absolute phase-shifts induced by those blocks, in an ideal BM, without any offset due to practical implementation. The phases in red are due to the crossover practical implementation including process variation. In order to keep the good progressive phases difference at the BM output, the PSs phases are corrected.

The PSs were considered as ideal for analyses simplicity. Accordingly, these components are evaluated with no loss, perfect matching, and output phase lagged either of -45° (PS1 and PS2) or 0° (PS3 and PS4), with respect to the output phase of the crossovers, all along the simulated frequency band. To better figure out the link between the PSs and crossovers output phase, it is important to consider a typical example. Being in compliance with that link allows having, theoretically, no phase imbalance in the system. For instance, let insert in the system the 'crossover 4' of Table 2-1, exhibiting a transmission path isolation equal to 37.1 dB. Since at 28 GHz the output phase ϕ_{31} equals -70° , the absolute output phase of PS1 and PS2 must be equal to -115° (that is, -115° = -70°-45°), and the absolute output phase of PS3 and PS4 must be equal to -70° (that is, -70° = -70°-0°), instead of -45° and 0° as shown in Figure 2-12.

The study steps of the system-level simulations are as follows:

- The s4p file corresponding to a first crossover variation (e.g. crossover 1, in Table 2-1) is inserted in the dedicated 'SnP' block ('Data Items' of ADS). Couplers and PSs are considered as explained earlier. Both the BM crossovers are modified at the same time.
- The ADS simulation, with 50-Ω port terminations, is carried out in order to obtain the output S-Parameters of the overall system.
- The maximum output amplitude and phase imbalance of the system are extracted.
- Then, another crossover variation (e.g. crossover 2 in Table 2-1) is considered and we go back to the first step.

The results are reported in Table 2-2 and in Figure 2-13, i.e. the maximum output amplitude and phase imbalance, at 28 GHz, along with the 10-dB relative bandwidth (RBW) of the overall system.

Crossover			BM performance		
Config.	W_{cavity} (mm)	S_{21} (dB)	Max ampl. imb. (dB)	Max phase imb. (deg)	RBW (%)/(GHz)
1	7.6	-27	1.3	5.4	5.4/26.5-30
2	7.65	-33	0.78	3.1	5.4/26.5-30
3	7.7	-45	0.59	1.6	5.4/26.5-30
4	7.75	-37	0.59	1.4	5.4/26.5-30
5	7.8	-30	0.93	2.9	5.4/26.5-30
6	7.85	-26	1.3	4.6	5.7/26.4-30
7	7.9	-23	1.7	6.3	5.7/26.4-30

Table 2-2: Sensitivity study on output BM system performance, at 28 GHz.

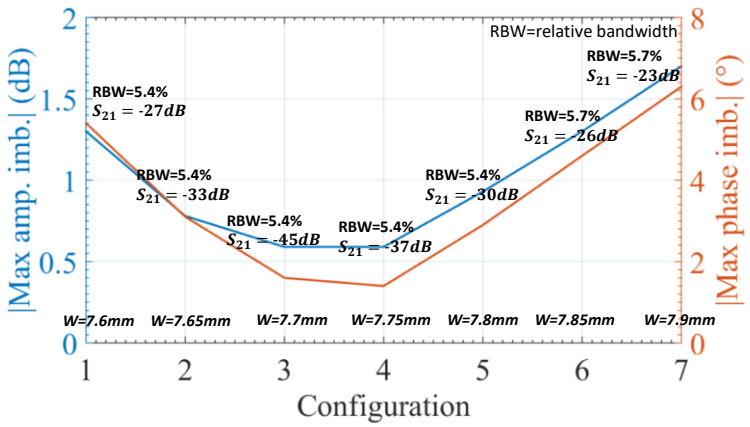

Figure 2-13: Sensitivity study on output BM system performance, at 28 GHz.

The strong impact of the crossover transmission path isolation ($-S_{21_{dB}}$) on the system performance makes the maximum amplitude and phase imbalance vary from 0.59 dB to 1.7 dB, and from 1.4° up to 6.3° respectively, when the crossover cavity width deviates with ±150 µm. The relative bandwidth RBW, calculated on the basis of 10 dB input return loss ranges between 5.4% to 5.7%. It was difficult to make a comparison among configuration 3 and 4 (Table 2-2) because of its weak value of S_{21} (-45 dB).

2.1.5 Partial conclusion on sensitivity study

The previous sensitivity study outlines some specific weaknesses of a BM, especially due to crossovers. This aspect, as introduced in Chapter I, was already introduced in [7], [8], but in the present work this effect has been quantified and related to the manufacturing technology. Another drawback specific to Butler matrices is the discrete approach that induces a lack of resolution for 4×4 matrices. A solution was introduced in Chapter I with the extended beam concept.

2.2 Extended beam BM concept

In many current applications, high beam resolution becomes very important. A way to increase the spatial resolution is to increase the order of the BM, but the circuit size becomes impractically large. Thus, one of the most interesting features can be to extend the beam-

steering ability. Several techniques were reported in Chapter I [12]–[17]. In this work, in order to increase the number of steered beams of the antenna array, tunable phase shifters are considered. This concept is similar to the one recently published in [15]. In our case, a higher frequency is considered. This design is not intended as a full replacement of the conventional 8×8 BM, but it provides the 4×4 BM with extra beam control agility, together with a wide equivalent spatial coverage having high peak gain and low gain ripple, which is not feasible by its conventional counterpart. The solution proposed in this document is to integrate the tunable PSs directly in the BM network, that is by replacing the two 0° and 45° fixed PSs by four tunable 1-bit PSs, depicted in Figure 2-14 as two circles (path 1 and 2) surrounded by dotted square. The proposed design does not add a lot of extra power losses, as compared to conventional BM design. The proposed design losses are discussed in Chapter IV.

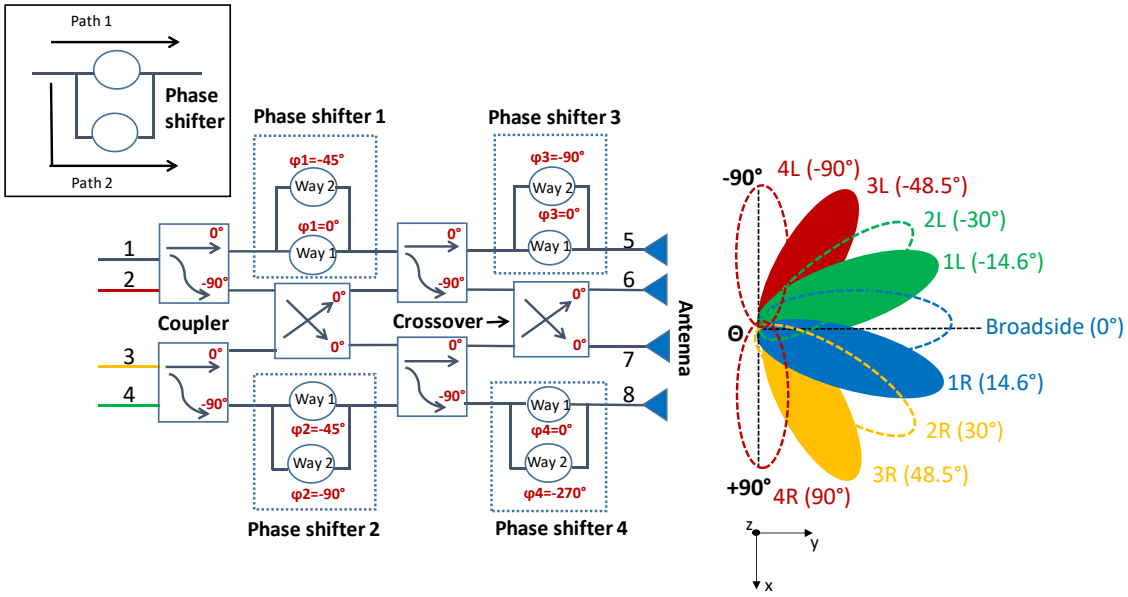

Figure 2-14: Extended beam BM network concept based on reconfigurable phase shifters. The phases in red at the outputs of each block correspond to the absolute phase-shifts induced by those blocks, in an ideal extended beam BM, without any offset due to technical implementation.

The extra lobes, allowing improving the spatial coverage with respect to a conventional 4×4 BM, are plotted with dotted lines in the radiation pattern in Figure 2-14. The colors of the beams are related to the input feeding ports. In parenthesis, the maximum beam radiation intensity direction (beam pointing angle), θ_{max}, is calculated considering isotropic sources distanced by $0.5 \cdot \lambda_0$. This network can provide up to 9 beams with 8 different progressive output phases yet using a compact structure. The 180° progressive output phase shift provides both '4L' and '4R' as referred to in Figure 2-14. Hence, the main advantage of this solution is to reduce the ripple from 3.7 dB down to 0.8 dB, as compared to conventional 4x4 BM, as shown in Figure 2.15.

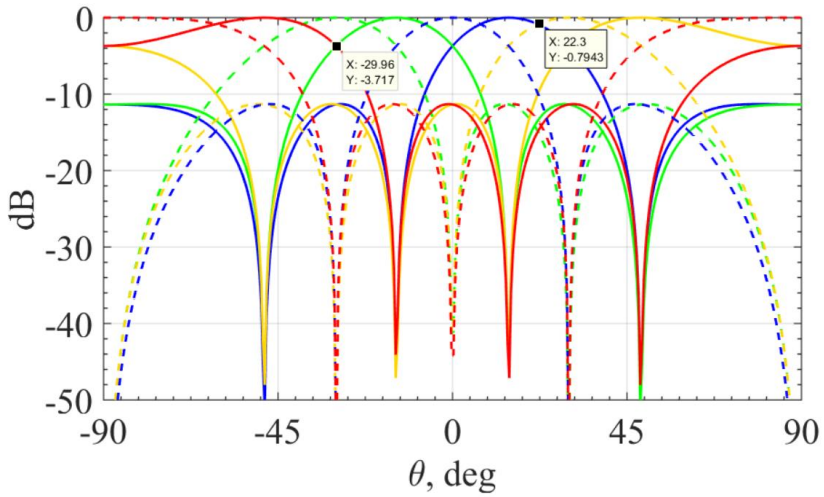

Figure 2-15: Normalized array factor of the extended beam concept, for d=$\lambda_0 \cdot 0.5$

To better figure out the principle, an example is reported down here. If the port number 1 is fed and PS1 is on the path 1 (0° phase shifting), PS3 on the path 2 (-90° phase shifting) and PS4 on the path 2 (-270° phase shifting), then the progressive output phases between adjacent antennas is equal to 0° and, in turns, a boresight beam is obtained ($\theta_{max} = 0°$). Let us notice that in this first example, PS2 is not considered because it is not in the signal path. The same principle is valid for the other combinations to obtain the 9 beams. Phase shifters state, progressive output phases (PoP) and maximum beam radiation intensity direction are summarized in Table 2-3.

Port	**PS 1**		**PS 2**		**PS 3**		**PS 4**		**PoP (°)**	**θ (°)**
Path 1: ON/OFF Path 2: ON/OFF	**Path 1**	**Path 2**	**Path 1**	**Path 2**	**Path 1**	**Path 2**	**Path 1**	**Path 2**	/	/
1	ON	OFF	n/p	n/p	OFF	ON	OFF	ON	0	**0**
	OFF	ON	n/p	n/p	ON	OFF	ON	OFF	-45	**14.6**
2	ON	OFF	n/p	n/p	OFF	ON	OFF	ON	±180	**±90**
	OFF	ON	n/p	n/p	ON	OFF	ON	OFF	135	**-48.5**
3	n/p	n/p	OFF	ON	OFF	ON	OFF	ON	-90	**30**
	n/p	n/p	ON	OFF	ON	OFF	ON	OFF	-135	**48.5**
4	n/p	n/p	OFF	ON	OFF	ON	OFF	ON	90	**-30**
	n/p	n/p	ON	OFF	ON	OFF	ON	OFF	45	**-14.6**

n/p stands for not in the signal path.

Table 2-3: Extended beam BM PSs combinations for enhanced spatial agility

In Chapter IV, the realization of these PSs is described in SIW with a particular technique based on the use of floating and short-circuited vias combined with metal strips acting as PIN diodes. The other blocks of the BM are studied again in Chapter IV, along with the complete BM implementation in PCB technology.

In the next paragraph, reconfigurable radiation pattern antennas are studied and designed to fully exploit the expanded spatial coverage array factor (AF) solution.

2.3 Reconfigurable antennas for extended beam BM agility

2.3.1 Impact of the elementary antenna pattern and cell size on the array pattern

On the basis of equation (2-1), the array pattern (AP) is the product of the array factor (AF) with the elementary antenna pattern (EP), that is anisotropic. In fact, some pointing directions of Figure 2-15 might be useless if the EP is not wide enough. Microstrip patch antennas are the ideal candidate for this purpose. It is well-known that their gain is rather small, but this is the price to pay to get the widest EP as possible. As an example, to match our proper case, we will assume that our extended BM is feeding some classical patch antennas simulated in the RO4003 PCB technology, $\varepsilon_r = 3.55$. The gain of those typical patch antennas is plotted in Figure 2-16 showing a wide broadside lobe. Two ground plane widths are considered, one is equal to $0.5 \cdot \lambda_0$ and the other one is equal to $0.65 \cdot \lambda_0$. See Figure 2-19 (i) or Figure 2-20 for ground plane width illustration.

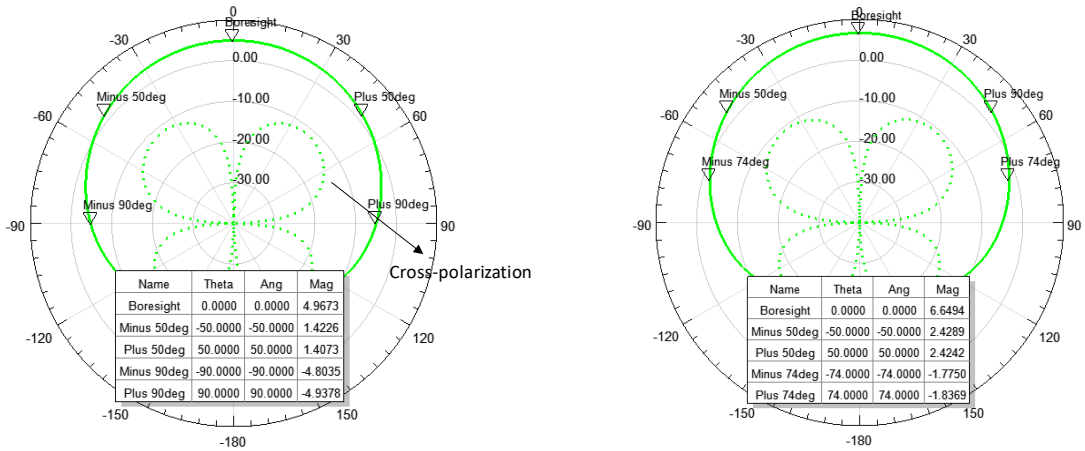

(a) (b)

Figure 2-16: Typical patch antenna gain, for (a) ground width= $0.5 \cdot \lambda_0$ and (b) ground size= $0.65 \cdot \lambda_0$

With a wider ground plane, it can be observed more gain (+1.7 dB) which is more preferable even if at the expense of less compactness. For the width of $0.5 \cdot \lambda_0$, 3.5 dB are lost as compared to the maximal gain for $\theta = \pm 50°$. For the width of $0.65 \cdot \lambda_0$, this loss is amplified up to 4.4 dB, still for $\theta = \pm 50°$. In fact, even the ±48.5°, pointing directions of Figure 2-15 might be strongly impacted. Hence, if the $0.65 \cdot \lambda_0$ is preferred for its higher gain, an approach to enhance the spatial coverage of the system implies that the space covered by the elementary antenna might be enlarged by having its beam direction adjustable for example.

In the further illustrations showing the impact of the EP on the AP, the polar coordinates are φ=0° whist θ varies, that is to say the xz plane of Figure 2-1 or Figure 2-14. Figure 2-17 and Figure 2-18 are representing the array factors, as well as the elementary pattern for two different centre-to-centre distances d between elementary radiative elements, i.e. $d = 0.5 \cdot \lambda_0$ and $d = 0.65 \cdot \lambda_0$, respectively. In both cases, the normalized array patterns of the extended beam network (considering the reconfigurable phase shifters) are also plotted.

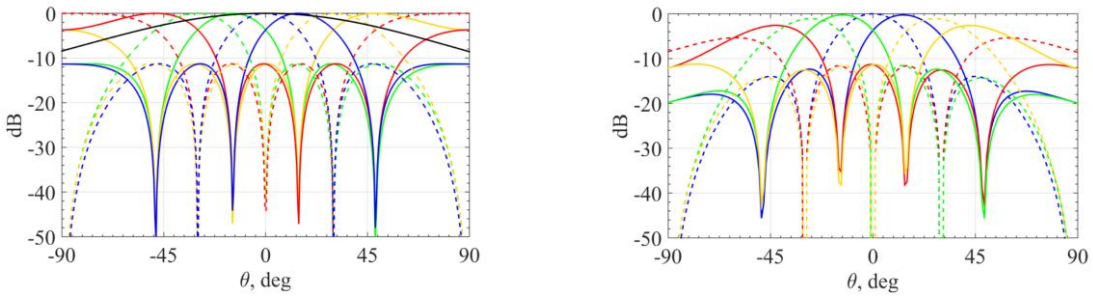

(a) (b)

Figure 2-17: (a) AF of the extended beam network (coloured lines) for $d = 0.5 \cdot \lambda_0$, and EP of the patch element (bold black line), and (b) AP of the extended beam network (coloured lines) for $\mathrm{d} = 0.5 \cdot \lambda_0$.
Max gain for $AP = 6\ \mathrm{dB} + 4.97\ \mathrm{dB} = 11\ \mathrm{dB}$.

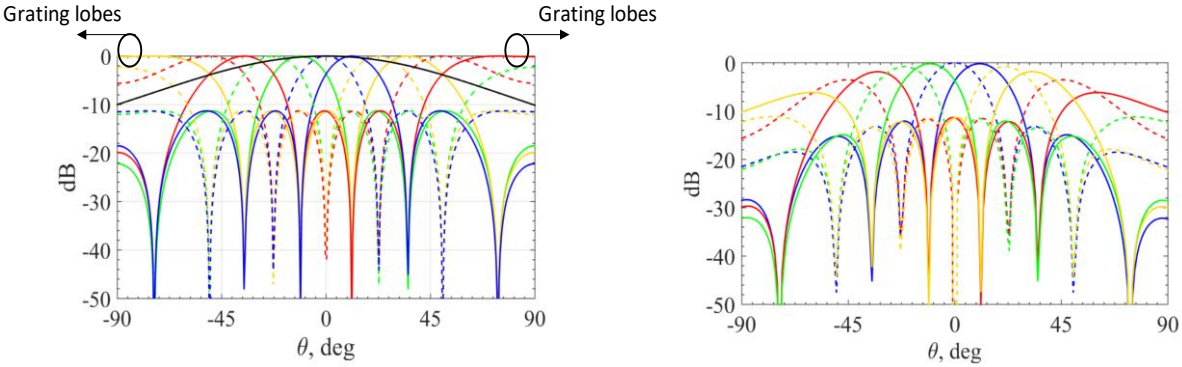

(a) (b)

Figure 2-18: (a) AF of the extended beam network (coloured lines) for $d = 0.65 \cdot \lambda_0$, and EP of the patch element (bold black line), and (b) AP of the extended beam network (coloured lines) for $d = 0.65 \cdot \lambda_0$.
Max gain for $AP = 6\ dB + 6.65\ dB = 12.65\ dB$.

As expected, by considering the distance $d = 0.65 \cdot \lambda_0$ (i.e. greater than $0.5 \cdot \lambda_0$), the AP spatial coverage, θ_{HPBW} defined in equation (2-8) as in [14], is reduced from ±49° to ±31°.

$$\theta_{HPBW} = |\theta_L - \theta_R| \tag{2-8}$$

where θ_L and θ_R are the two outermost angles at which the gain of beam k is exactly 3 dB below the maximum boresight gain. Equation ((2-8) is subject to the constraint that:

$$SLL_k \leq (G_{kmax} - 6\ dB) \tag{2-9}$$

Here, SLL_k and $G_{k\,max}$ are, respectively, the sidelobe level and peak gain of beam k. In other words, some beam might be removed due to the violation of ((2-9), since a large progressive phase shift and a big distance d degrade the radiation performance due to higher sidelobe levels [18]. For the patch antenna, a higher gain between $-31° < \theta < 31°$ (see Figure 2-16) can be obtained. It can be thus interesting to vary the cell size and to compare the AF to the $0.5 \cdot \lambda_0$ reference case. The impact of the cell size on AF and AP is summarized in

Table 2-4 for d varying from $0.5 \cdot \lambda_0$ to $0.65 \cdot \lambda_0$.

Cell dim.	*EP* Gain	*AP* Grating lobes	*AP* Ripple	*AP* Spatial Coverage
$d = 0.5 \cdot \lambda_0$	5 dB	-11.2 dB / ±78°	2.75 dB	±49
$d = 0.55 \cdot \lambda_0$	5.7 dB	-8.85 dB / ±72°	2.5 dB	±46°
$d = 0.65 \cdot \lambda_0$	6.65 dB	-6.15 dB/ ±60°	1.26 dB	±31

Table 2-4: Antenna cell dimensions impact on AP (for patch antenna EP)

As it can be noticed, it appears that a good compromise of cell size could be $0.55 \cdot \lambda_0$. Nevertheless, this value can only be used for small footprint of the elementary radiating element. In parallel, in order to fully exploit the extended beam concept, reconfigurable radiation pattern antennas become essential to steer the single element beam towards the most lateral AF pointing lobes. Practically, when the AF is steered for θ inside the ~ ±30° spatial range, a single element pattern pointing to $\theta = \theta_{max}$ =0° is enough, but when the AF points between 30° and the maximum angle or -30° and the minimum angle, then the single element pattern must be driven to point towards these directions in order to maintain a sufficient directivity without impairing the total AP. A brief state-of-the-art on reconfigurable radiation pattern antennas is going to be introduced in the next sub-section in order to illustrate possible solutions for AP improvement and it will be seen that reconfigurable radiation pattern patch antennas need larger footprint than $0.55 \cdot \lambda_0$, typically $0.65 \cdot \lambda_0$. Finally, it is obvious that the higher grating lobes disadvantage the case $d = 0.65 \cdot \lambda_0$. But such drawback could be fixed as well by using a reconfigurable antenna. By switching its pointing direction towards the AF, the impact of grating lobes will be meanwhile reduced.

2.3.2 Reconfigurable radiation pattern antennas state-of-the-art techniques

In this section, an overview of the techniques used for reconfigurable pattern antenna are given (in the text) along with their performance (Table 2-5). Pattern reconfigurable antennas have been applied in modern wireless communication systems and different topologies were studied and developed, depicted in Figure 2-19.

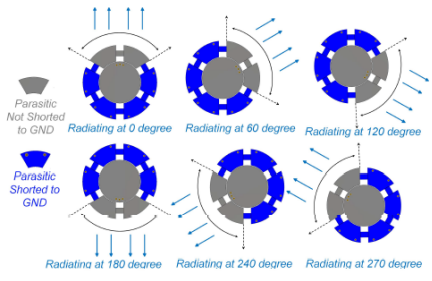

(a) [19]

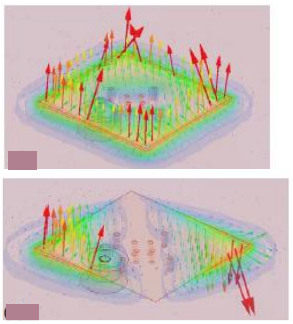

(b) [20]

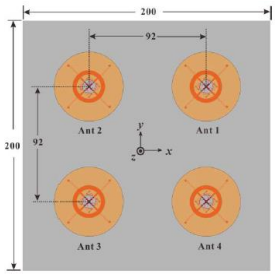

(c) [21]

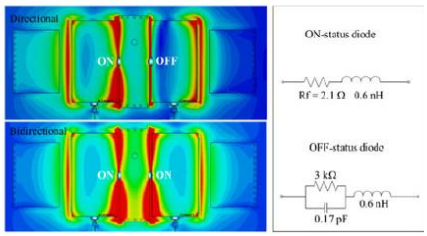

(d) [22]

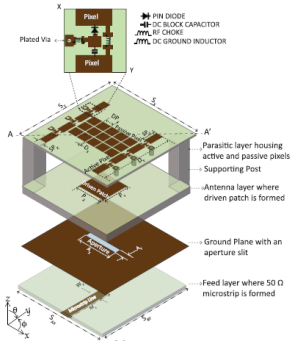

(e) [23]

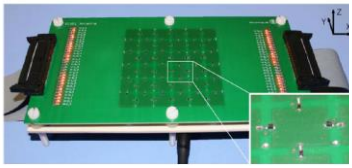

(f) [24]

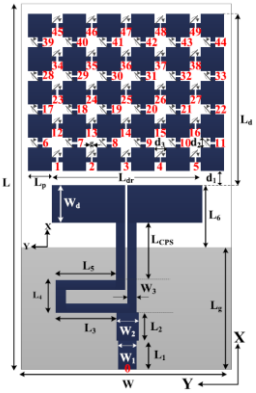

(g) [25]

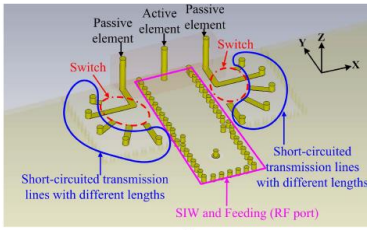

(h) [26]

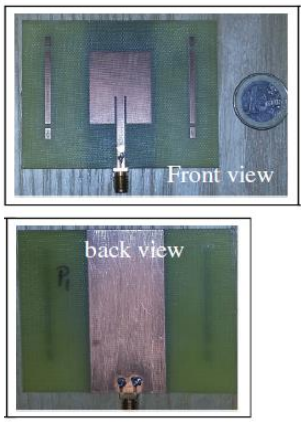

(i) [27]

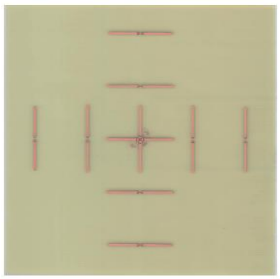

(j) [28]

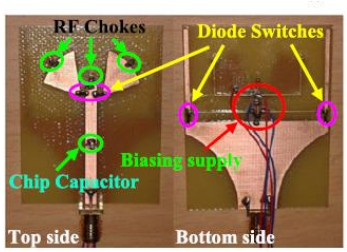

(k) [29]

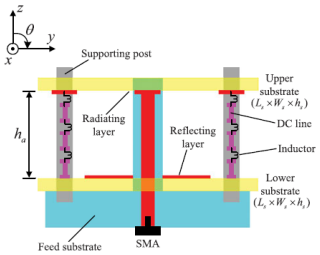

(l) [30]

Figure 2-19: Different reconfigurable antennas topologies

The different approaches can be grouped in three main groups. One of the technique is to use shorting posts with RF switches ([19] to [22]). Typically, in [19] , the shorting post can be simply connected to the ground by turning the switch ON or disconnected from the ground by turning the switch OFF (see Figure 2-19 (a)). Another option consists in driving the antenna element with a pixelated parasitic layer ([23] to [25]). The latter technique should lead to large footprints and as a corollary to large cell sizes. A last proposition appears to be quite well applicable to patch antennas, based on the Yagi –Uda principle with director and reflector wires ([26] to [29]). The simplest one, with the smallest footprint that could be suitable for a cell size of $0.65 \cdot \lambda_0$, has been published in [27], see Figure 2-19 (i); this technique will be applied to our own case, in sub-section 2.3.3. For information, there also exist mixed solutions as in [30].

The state-of-the-art performance of the reconfigurable radiation pattern antennas is summarized in Table 2-5. In [27], it can be seen that gain variations between the various positions is disadvantageous (1.9 dB). This may be due to technology limitations as the results

for a different implementation [28] looks promising. The higher gain of [28] is due to the double directors (/reflectors) implying large footprint, and it cannot be applied to the BM design which requires smaller radiating elements.

Technique	Ref.	f (GHz)	Number of states	Gain variation (dBi)	$Gain_{max}$ (dBi)	θ_{max} pointing (°)
Shorting post with RF switches	[19]	5.7	6	0	10	0, 60, 120, 180, 240, 300
	[20]*	3.67	3	2.5	6.2	0, ±45in two planes
	[21]	2.4	4	5.7	12.5 (array 2x2)	0, ±30 and omni-dir. in three planes
	[22]	5.8	3	N/A	N/A	±45, 180 in two planes
Driven antenna element with a pixelated parasitic layer	[23]	4.9-5.1	12 (most advantageous)	N/A	8 (average)	0, ±30, ±40 in four planes
	[24]	2.7	5 (most advantageous)	0.6	6.7	0, ±30 in two planes
	[25]	2.5	11 (> steering angles can be obtained)	4	9.5	0,±30, ±60, ±90, ±120, ±150
Yagi-Uda antenna principle	[26]	28	5	5	7 to 9.3 in 26-28 GHz	180 to 360 continuous
	[27]	2.45	4	1.9	5.8	0,±63, ±85
	[28]	2.3	4	0.39	10.74	0, 90, 180, 270 in two planes
	[29]	2.4	4	≥ 0.9	3.7	0, 45, 135, 180
Mixed approach	[30]	2.45	5	1.3	6.5 (realized gain)	0,±45, ±90

*simulations

Table 2-5: Reconfigurable radiation pattern antenna state-of-the-art

2.3.3 Design topology of reconfigurable antenna and impact on array factor

As in [27], two parasitic elements on either side of the driven microstrip patch antenna are designed to act as the director or the reflector depending on the ON/OFF states of the PIN diodes. The proposed reconfigurable antenna layout is depicted in Figure 2-20, together with a possible way to make the bias circuit.

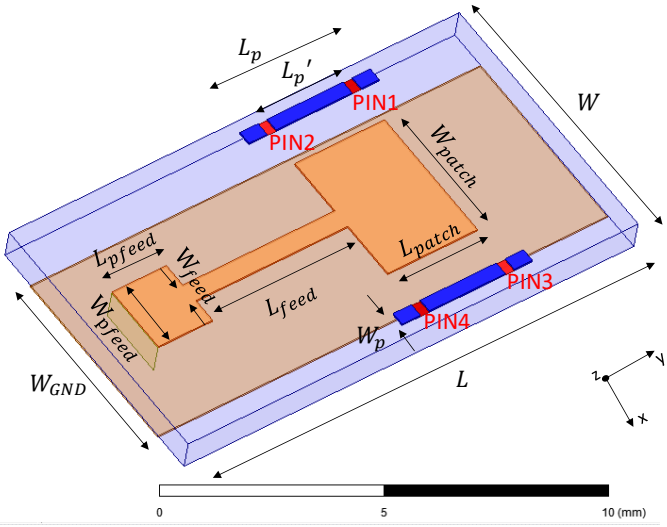

Figure 2-20: Reconfigurable pattern microstrip patch antenna with lateral parasitic elements.

Firstly, the stand-alone driven patch element along with its feeding line was designed and optimized through HFSS simulations for achieving the best performance. W_{patch}, L_{patch}, W_{feed}, L_{feed}, W_{pfeed}, L_{pfeed}, W and W_{GND} are 3.6 mm, 2.48 mm, 0.51 mm, 4.2 mm, 1.79 mm, 1.5 mm, 6.93 mm and 4.93 mm, respectively. Then, the lateral parasitic elements were designed to be approximately $\lambda_g/2$ long, λ_g being the guided wavelength. W_p, L_p and L_p' are 0.35 mm, 3.6 mm and 2.1 mm, respectively. Beam switching is carried out using the four switches PIN1, PIN2, PIN3 and PIN4. When PIN1 and PIN 2 are ON we obtain a right end-fire beam for φ=0° plane, because the left-hand side parasitic strip acts as a reflector and the right-hand side as a director. A spatial symmetrical opposed beam occurs when PIN3 and PIN4 are ON. For the boresight direction, the combination all PIN diodes ON was preferred over all OFF because of higher gain. In Figure 2-21, the input matching of the radiating element and the gain of its EP are shown.

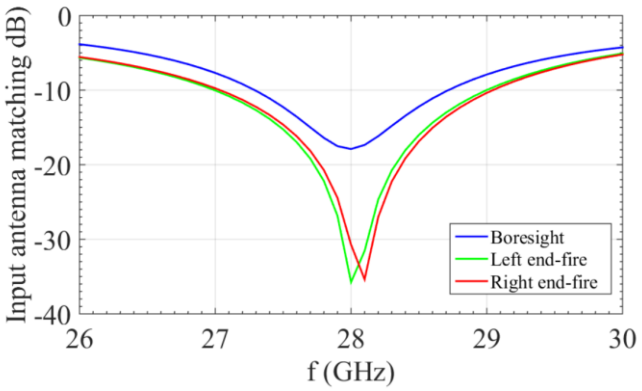

(a)

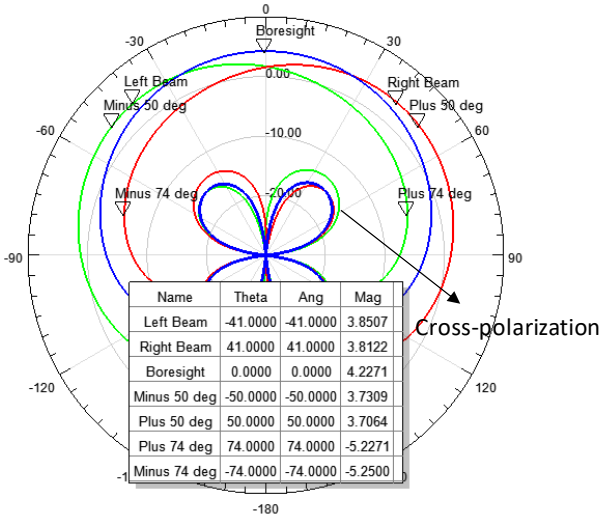

(b)

Figure 2-21: (a) Input matching of the radiating element of Figure 2-20, and (b) its EP: boresight (blue), left end-fire (green) and right end-fire (red)

It can be observed that input matching is better than 17 dB for the boresight beam and better than 30 dB for the two remaining ones, at 28 GHz. The cross-polar gain pattern is lower than 14 dB with respect to the co-polar one which, at the boresight has a gain equal to 4.23 dB, a slightly lower value compared to a conventional patch antenna with the same cell size (in the latter case the gain would be 6.65 dB). This is mainly due to the smaller ground plane (~ -1 dBi) which causes high back-lobes and to the parasitic elements utilised in the design (~ -1.5 dBi of gain loss). The left and right end-fire beams θ are -41° and +41°, respectively. Their gain is 3.85 dB, which is only 0.4 dB smaller than boresight gain. Moreover, the left and right end-fire beams gain at -50° and +50° is 3.7 dB, ±50° being the most lateral θ_{max} of the AF. Their gain is 6.5 dB lower in the opposite symmetrical direction (-50° or +50°); this is important to break down the occurring image opposite lobe. It may be thus interesting to compare the AP of Figure 2-18 with the one that could be obtained with this adjustable element, presented in Figure 2-22.

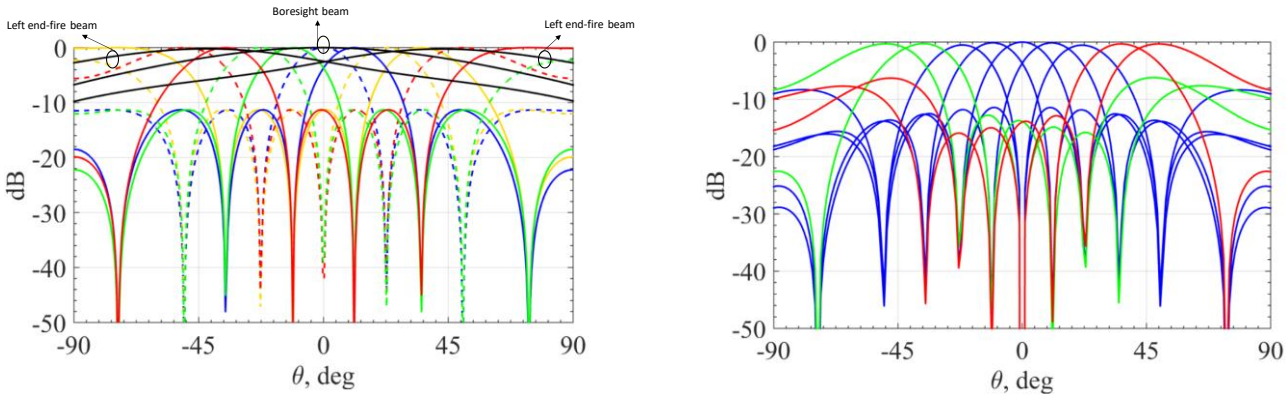

(a) (b)

Figure 2-22: (a) AF of the extended beam network (coloured lines) for $d = 0.65 \cdot \lambda_0$, and EP of the reconfigurable radiation pattern patch element (bold black line), and (b) AP of the extended beam network (coloured lines) for $d = 0.65 \cdot \lambda_0$. Max gain for $AP = 6\ dB + 4.2\ dB = 10.2\ dB$.

The proposed solution is compared with conventional patch antenna performance for $d = 0.5 \cdot \lambda_0$, $0.55 \cdot \lambda_0$ and $0.65 \cdot \lambda_0$, as shown earlier. The comparison is highlighted in Table 2-6.

Technique	Cell dim.	*EP* Gain	*AP* Grating lobes	*AP* Ripple	*AP* Spatial Coverage
Conventional patch	$\boldsymbol{d = 0.5 \cdot \lambda_0}$	5 dB	-11.2 dB / ±78°	2.75 dB	±49°
Conventional patch	$\boldsymbol{d = 0.55 \cdot \lambda_0}$	5.7 dB	-8.85 dB / ±72°	2.5 dB	±46°
Conventional patch	$\boldsymbol{d = 0.65 \cdot \lambda_0}$	6.65 dB	-6.15 dB/ ±60°	1.26 dB	±31°
Reconfigurable antenna	$\boldsymbol{d = 0.65 \cdot \lambda_0}$	4.2 dB	-7.6/±65° →grating lobes -6.5 dB/±50° →opposite image lobes	1.55 dB →max between 2R and 3R or 2L and 3L beams	±67°

Table 2-6: Reconfigurable pattern and conventional patch antenna *AP* comparison

Thus, for the EP at hand and by considering a maximum scan loss of 1.5 dB (that corresponds to the maximum difference between the boresight lobe gain and the gain observed when adjacent beams are crossing on Figure 2-22 (b)), the gain remains higher than 8.7 dBi whatever the direction between ±60°. Spatial coverage goes up to ±67° if θ_{HPBW} is considered.

In comparison, the conventional patch antenna has a gain equal to 2.42 dB in the ±50°directions, resulting in 4.2 dB of loss with respect to boresight direction (6.65 dB). As a consequence, the opposite image lobes are not lowered. Even if in the boresight direction, 12.65 dB of gain can be achieved with conventional patch, this configuration leads to big $G_{k\,max}$ variation. Concerning grating lobes, the AF grating lobes for $d = 0.65 \cdot \lambda_0$ appear at ±74° and, for this value of θ the reconfigurable pattern antenna gain is 9.5 dBi lower than the boresight gain, against 8.4 dBi of a conventional patch antenna. Even in the latter case, the reconfigurable antenna results in better reducing the grating lobes.

2.4 Conclusion

A detailed sensitivity study based on a Monte Carlo approach was presented in the first part of this second chapter. Firstly, the MC variations in terms of phase and amplitude were applied at the input of four antennas to evaluate their influence on the radiation pattern, according to a uniform distribution. Secondly, the MC was carried out for stand-alone BM building blocks such as couplers, crossovers and phase shifters, in order to evaluate their impact on the previous radiation pattern study.

The crossover transmission path isolation $(-|S_{21}|_{dB})$ level was proved to be critical for the BM design, because it causes amplitude and phase imbalance on the output of the overall system, when it is higher than -20 dB. Typically, PCB uncertainties may easily affect this transmission path isolation. Analytical electromagnetic equations were provided to validate the thesis.

In the central part of the chapter, the extended beam concept was discussed by proving and, 8 different progressive output phases were generated for a 4x4 BM system, providing 9 different spatial beams through the use of tunable phase shifters.

In the final part, reconfigurable radiation pattern for extended beam BM agility were introduced along with a short state-of-the-art. BM radiating elements with a weak beam pattern reconfigurability can significantly improve the overall BM antenna system performance. To this end, a reconfigurable antenna element was designed and optimized at 28 GHz in PCB technology. The results show the advantages of using such a kind of antenna when compared to conventional single beam antennas. However, if the uniformity of the array pattern is ensured, in the boresight direction a 2-3-dB gain reduction is observed with respect to a conventional patch antenna. The next step might be to simulate the proposed antenna in a 1×4 array, and to experimentally validate this concept.

In the next chapter, phase shifters used for enhanced BM beam steering will be introduced in detail, before realizing the extended beam BM in Chapter IV.

REFERENCE

[1] D. Deslandes and K. Wu, 'Design Consideration and Performance Analysis of Substrate Integrated Waveguide Components', in *32nd European Microwave Conference, 2002*, Milan, Italy, Oct. 2002, pp. 1–4, doi: 10.1109/EUMA.2002.339426.

[2] P. Chen *et al.*, 'A Multibeam Antenna Based on Substrate Integrated Waveguide Technology for MIMO Wireless Communications', *IEEE Transactions on Antennas and Propagation*, vol. 57, no. 6, pp. 1813–1821, Jun. 2009, doi: 10.1109/TAP.2009.2019868.

[3] C. Chen and T. Chu, 'Design of a 60-GHz Substrate Integrated Waveguide Butler Matrix—A Systematic Approach', *IEEE Transactions on Microwave Theory and Techniques*, vol. 58, no. 7, pp. 1724–1733, Jul. 2010, doi: 10.1109/TMTT.2010.2050097.

[4] T. Djerafi, N. J. G. Fonseca, and K. Wu, 'Design and Implementation of a Planar 4 × 4 Butler Matrix in Siw Technology for Wide Band High Power Applications', *Progress In Electromagnetics Research B*, vol. 35, p. 23, 2011.

[5] Z. Chen, X. Wu, and F. Yang, 'A compact SIW butler matrix with straight delay lines at 60 GHz', in *2017 IEEE International Symposium on Antennas and Propagation & USNC/URSI National Radio Science Meeting*, San Diego, CA, USA, Jul. 2017, pp. 2141–2142, doi: 10.1109/APUSNCURSINRSM.2017.8073113.

[6] Y. Yang, W. Luo, and C. Zhang, 'A Novel Millimeter Wave Multiple Beam Antenna with SIW Butler Matrix', in *2019 IEEE International Conference on Computational Electromagnetics (ICCEM)*, Shanghai, China, Mar. 2019, pp. 1–3, doi: 10.1109/COMPEM.2019.8779056.

[7] S. Gruszczynski and K. Wincza, 'Broadband 4x4 Butler Matrices as a Connection of Symmetrical Multisection Coupled-Line 3-dB Directional Couplers and Phase Correction Networks', *IEEE Transactions on Microwave Theory and Techniques*, vol. 57, no. 1, pp. 1–9, Jan. 2009, doi: 10.1109/TMTT.2008.2009081.

[8] K. Wincza and S. Gruszczynski, 'A Broadband 4x4 Butler Matrix for Modern-Day Antennas', p. 4, 2005.

[9] C. A. Balanis, *Antenna theory: analysis and design*, 3rd ed. Hoboken, NJ: John Wiley, 2005.

[10] T. Djerafi, N. J. G. Fonseca, and K. Wu, 'Design and Implementation of a Planar 4×4 Butler Matrix in SIW Technology for Wideband Applications', p. 4, 2011.

[11] H. J. Riblet, 'The Short-Slot Hybrid Junction', *Proceedings of the IRE*, vol. 40, no. 2, pp. 180–184, Feb. 1952, doi: 10.1109/JRPROC.1952.274021.

[12] T.-Y. Chin, S.-F. Chang, J.-C. Wu, and C.-C. Chang, 'A 25-GHz Compact Low-Power Phased-Array Receiver With Continuous Beam Steering in CMOS Technology', *IEEE Journal of Solid-State Circuits*, Nov. 2010, doi: 10.1109/JSSC.2010.2064010.

[13] H. Ren, B. Arigong, M. Zhou, J. Ding, and H. Zhang, 'A Novel Design of 4x4 Butler Matrix With Relatively Flexible Phase Differences', *IEEE Antennas and Wireless Propagation Letters*, vol. 15, pp. 1277–1280, 2016, doi: 10.1109/LAWP.2015.2504719.

[14] H. N. Chu and T.-G. Ma, 'An Extended 4x4 Butler Matrix With Enhanced Beam Controllability and Widened Spatial Coverage', *IEEE Transactions on Microwave Theory and Techniques*, vol. 66, no. 3, pp. 1301–1311, Mar. 2018, doi: 10.1109/TMTT.2017.2772815.

[15] A. Tajik, A. Shafiei Alavijeh, and M. Fakharzadeh, 'Asymmetrical 4x4 Butler Matrix and its Application for Single Layer 8x8 Butler Matrix', *IEEE Transactions on Antennas and Propagation*, vol. 67, no. 8, pp. 5372–5379, Aug. 2019, doi: 10.1109/TAP.2019.2916695.

[16] Chia-Chan Chang, Ruey-Hsuan Lee, and Ting-Yen Shih, 'Design of a Beam Switching/Steering Butler Matrix for Phased Array System', *IEEE Transactions on*

Antennas and Propagation, vol. 58, no. 2, pp. 367–374, Feb. 2010, doi: 10.1109/TAP.2009.2037693.
[17] K. Ding and A. A. Kishk, 'Extension of Butler Matrix Number of Beams Based on Reconfigurable Couplers', *IEEE Transactions on Antennas and Propagation*, vol. 67, no. 6, pp. 3789–3796, Jun. 2019, doi: 10.1109/TAP.2019.2902668.
[18] O. KOBAYASHI, 'A novel Butler matrix based beam forming network architecture for multiple antenna beam steering', *Proc. of ISAP'96, Chiba, Japan, Sept.*, 1996, Accessed: May 19, 2020. [Online]. Available: https://ci.nii.ac.jp/naid/10022116719/.
[19] Y. Yang and X. Zhu, 'A Wideband Reconfigurable Antenna With 360° Beam Steering for 802.11ac WLAN Applications', *IEEE Transactions on Antennas and Propagation*, vol. 66, no. 2, pp. 600–608, Feb. 2018, doi: 10.1109/TAP.2017.2784438.
[20] N. Nguyen-Trong, A. T. Mobashsher, and A. M. Abbosh, 'Reconfigurable shorted patch antenna with polarization and pattern diversity', in *2018 Australian Microwave Symposium (AMS)*, Brsibane, QLD, Feb. 2018, pp. 27–28, doi: 10.1109/AUSMS.2018.8346965.
[21] J.-S. Row and Y.-J. Huang, 'Reconfigurable Antenna With Switchable Broadside and Conical Beams and Switchable Linear Polarized Patterns', *IEEE Transactions on Antennas and Propagation*, vol. 66, no. 7, pp. 3752–3756, Jul. 2018, doi: 10.1109/TAP.2018.2820325.
[22] R. Wang, B.-Z. Wang, G.-F. Gao, X. Ding, and Z.-P. Wang, 'Low-Profile Pattern-Reconfigurable Vertically Polarized Endfire Antenna With Magnetic-Current Radiators', *IEEE Antennas and Wireless Propagation Letters*, vol. 17, no. 5, pp. 829–832, May 2018, doi: 10.1109/LAWP.2018.2817682.
[23] M. A. Towfiq, I. Bahceci, S. Blanch, J. Romeu, L. Jofre, and B. A. Cetiner, 'A Reconfigurable Antenna With Beam Steering and Beamwidth Variability for Wireless Communications', *IEEE Transactions on Antennas and Propagation*, vol. 66, no. 10, pp. 5052–5063, Oct. 2018, doi: 10.1109/TAP.2018.2855668.
[24] D. Rodrigo, B. A. Cetiner, and L. Jofre, 'Frequency, Radiation Pattern and Polarization Reconfigurable Antenna Using a Parasitic Pixel Layer', *IEEE Transactions on Antennas and Propagation*, vol. 62, no. 6, pp. 3422–3427, Jun. 2014, doi: 10.1109/TAP.2014.2314464.
[25] P. Lotfi, S. Soltani, and R. D. Murch, 'Printed Endfire Beam-Steerable Pixel Antenna', *IEEE Transactions on Antennas and Propagation*, vol. 65, no. 8, pp. 3913–3923, Aug. 2017, doi: 10.1109/TAP.2017.2716399.
[26] S. Zhang, I. Syrytsin, and G. F. Pedersen, 'Compact Beam-Steerable Antenna Array With Two Passive Parasitic Elements for 5G Mobile Terminals at 28 GHz', *IEEE Transactions on Antennas and Propagation*, vol. 66, no. 10, pp. 5193–5203, Oct. 2018, doi: 10.1109/TAP.2018.2854167.
[27] A. R. Chandran, S. Morris, S. Raman, N. Timmons, and J. Morrison, 'Microstrip patch based switched beam antenna at 2.45 GHz for wireless sensor network applications', *Journal of Electromagnetic Waves and Applications*, vol. 31, no. 13, pp. 1333–1341, Sep. 2017, doi: 10.1080/09205071.2017.1348260.
[28] S.-J. Lee, W.-S. Yoon, and S.-M. Han, 'Planar Directional Beam Antenna Design for Beam Switching System Applications', *Journal of electromagnetic engineering and science*, vol. 17, no. 1, pp. 14–19, Jan. 2017, doi: 10.5515/JKIEES.2017.17.1.14.
[29] M. S. Alam and A. M. Abbosh, 'Wideband Pattern-Reconfigurable Antenna Using Pair of Radial Radiators on Truncated Ground With Switchable Director and Reflector', *IEEE Antennas and Wireless Propagation Letters*, vol. 16, pp. 24–28, 2017, doi: 10.1109/LAWP.2016.2552492.

[30] S.-L. Chen, P.-Y. Qin, W. Lin, and Y. J. Guo, ‘Pattern-Reconfigurable Antenna With Five Switchable Beams in Elevation Plane’, *IEEE Antennas and Wireless Propagation Letters*, vol. 17, no. 3, pp. 454–457, Mar. 2018, doi: 10.1109/LAWP.2018.2794990.

Chapter 3:

SIW tunable phase shifter for tunable Butler Matrix

Over the last decade, many microwaves and mm-waves SIW components have been proposed. Among these components, phase shifters are very important devices for signal modulation and demodulation, output phase adjustment for signal processing, and antenna beam steering. Comparing to other planar phase-shifter structures, the SIW based phase shifters offer the advantages of excellent shielding to electromagnetic interference, and high power handling capacity. Various configurations of phase shifters can be used to achieve broad-band phase and amplitude balance [1], [2].

If we focus on the phased array application, as already stated, Butler matrix is a very effective solution. In order to provide phased arrays with more progressive output phase shifts and to expand the beam controllability, discrete 1-bit phase shifters can be used for the 4x4 Butler matrix. It represents one of the best solutions in terms of circuit complexity, size and cost. In this manuscript, the digital solution is preferable as compared to a continuous tuning, the latest being suitable for fine tuning in a reduced spatial coverage where the scan loss can be maintained in an acceptable range.

In this chapter, a novel SIW 1-bit phase shifter principle is described. Two operating frequencies are considered, 5.8 GHz and 28 GHz, respectively. As will be shown hereafter, the 28-GHz operating frequency forces us to consider very important challenges.

A detailed study on how to optimize the phase shifter is presented, along with the description of the DC bias circuit, at 28 GHz. The state-of-the-art of these tunable devices is reported and their impact on the performance of the system is discussed through measurement results. The chapter is organized as follows: in the first section, a state-of-the-art of continuous and digital phase shifters topology is introduced; in the second section, the SIW 1-bit phase shifter principle is detailed; this principle is exploited to design a 5.8-GHz and 28-GHz phase shifter in section third and fourth, respectively. Design optimization, simulated and measured results are detailed along with the description of the DC bias circuit. The conclusions are reported in the fifth section.

3.1 Introduction to SIW phase shifters and state-of-the-art

3.1.1 Continuous versus digital tunable phase shifters topology

Passive phase shifters (PS) can be classified into three categories: digital, continuous, and mixed digital and continuous phase shifting. In this section, the use of the term “digital” is referred as a switched scheme carried out in the RF path. Three different topologies of PSs are usually used, such as loaded-lines [3]–[5], RTPS (Reflection Type Phase Shifter) [6], [7] and switched lines [8]–[10]. Usually, loaded-lines are for continuous phase shifting (but there are many with digital control), whereas switched lines are for digital phase shifting, while RTPS

may combine both approaches as it consists in better matching than for loaded or switched lines through the use of a 3-dB coupler.

The choice among digital or continuous phase shifting is application dependent. For instance, for communication purposes, between a transmitter and a receiver, with antenna aperture of more than 10°, digital phase shifting could be considered as the best choice, since it is not necessary to get a very fine tuning to get a good communication. On the contrary, when dealing with very small antenna aperture of 1° or less, in the case of big phased arrays, it is then preferable to use continuous phase shifting, since the number of bytes that would be required for digital tuning could be very high, with an increase in complexity, size, cost and power consumption. Due to the low *Q*-factor of varactors at mm-waves, the continuous phase shifting leads to high amplitude imbalance and not negligible IL in the BM, as compared to its digital counterpart where more performing devices are exploited, at the cost, however, of higher consumption. This is the reason why at mm-waves, innovative solutions with MEMS [8] (digital while presenting few IL) or liquid crystals [11] (continuous and mostly performing above 100 GHz) are explored, even if they are more complex. In this work, at the interface of RF and mm-waves, and for a sake of simplicity, we preferred to adopt an easier digital solution with PIN diodes integrated in SIW technology, which are low-loss until 40 GHz.

As shown in chapter 2, our choice to enhance the beam capability is to use four 1-bit digital switched line PSs, whose PS1 provides 0° and -45°, PS2 -45° and -90°, PS3 0° and -90° and PS4 0° and -270° absolute output phases, as compared to a 0° crossover absolute output phase (unless offset). If they are combined as explained in Table 2-3, they are able to provide 8 progressive output phases (PoP) for the BM system. The latter means that we get 45° over 360° of progressive output phase resolution.

If a continuous approach had been considered, also described in chapter 2, leading to PS1 and PS2 varying between 0° and -90° and, PS3 and PS4 varying between -90° and 90°, the 360° PoP would have been totally covered. But the rules of Table 2-3 might have been respected too and, for each phase variation of PS1 and PS2 a double phase variation of PS3 and PS4 would have been required to ensure the right progressive output phase. This means, at 28 GHz, many losses as varactors would have been used for continuous phase shift.

Consequently, the switched line approach was finally chosen because it is a good compromise between ripple (0.8 dB, see chapter 2) and few losses as compared to a continuous topology that would lead to no ripple but higher loss. The trade-off is illustrated in Figure 3-1. The picture was made by considering isotropic ideal sources and for a distance between radiating elements $d = 0.5 \cdot \lambda_0$.

By the next, a state-of-the-art for phase shifters is presented, restricted to SIW topology.

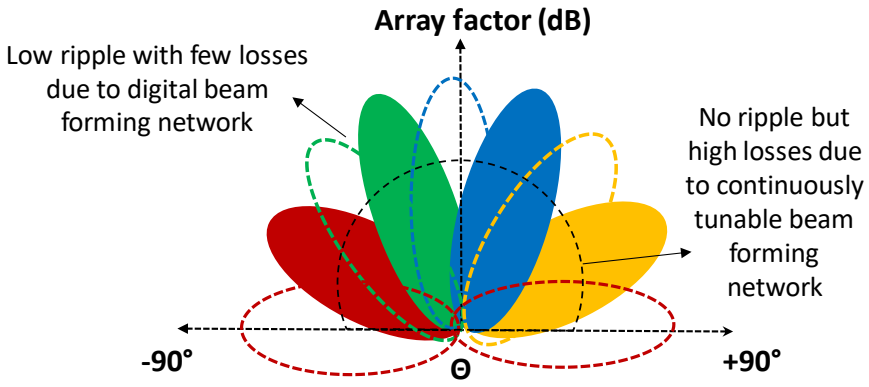

Figure 3-1: Array factor for digital (colored beams) versus continuous (dotted line) phase shifting. $d = 0.5 \cdot \lambda_0$.

3.1.2 SIW phase shifters state-of-the-art in PCB technology

SIW phase shifter in PCB technology state-of-the-art is carried out in this section. The phase shifter most important figure of merit (FoM) is equal to:

$$FoM = \frac{Max\ relative\ phase\ shift\ (°)}{Max\ insertion\ loss\ (dB)} \quad (3\text{-}1)$$

State-of-the-art phase shifter results are summarized in Table 3-1.

Ref.	PS type	Tunability	Method	f (GHz)	RBW_{10dB}^{**} (%)	Max IL^{*} (dB)	Max Phase range* (°)	FoM^{*} (°/dB)	Amp. imb. (dB) / RBW(%)	Phase imb. (°)/RBW(%)	Surface ($\lambda_0 \cdot \lambda_0$)
[12]	Continuous	Tunable	RTPS	26	13.8	7.2	360	50	6±1.2 / 1.9	±5 / 1.9	~7.7
[13]		Tunable	In-Line	26	N/A	1.26	24.8	19.7	1.09±0.17 / 30	±2.2 / 30	~0.38
[13]		Tunable	RTPS	26	15.3	4.67	180	38.5	3.8±0.87 / 15.3	±10 / 7.5	10.89
[14]		Tunable	SSIW	3	31.9	4	80.7	20.2	3.2±0.8 / 13.3	±10 / 28.3	0.26
[15]		*Fixed ##*	*SSIW*	*15*	*53*	*2*	*230.1*	*115*	*1.5±0.5 / 32.5*	*±5 / 32.5*	*0.59*
[1]	Digital	Tunable	2-layers SSIW	12	33.3	1.25	133	94.7	1±0.25 / 20.8	±4 / 33.3	~1.1
[2]		Tunable	SSIW	8	31	1.4	90	64.3	1.1±0.5 / 31	±4 / 31	0.23
[16]		*Fixed ##*	*SSIW*	*14*	*62.3*	*1*	*90*	*90*	*1±0.6 / 62.3****	*±5 / 62.3*	*0.94*
[17]#		*Fixed ##*	*Air holes SIW*	*9.5*	*31.5*	*0.8*	*24.8*	*31*	*N/A*	*±4.7 / 31.5*	*0.67*
[18]		*Fixed ##*	*Circular SSIW*	*24*	*10.4*	*1.5*	*60*	*40*	*N/A*	*±5 / 10*	*10.24*
[19]		*Fixed ##*	*SSIW PI*	*10*	*47*	*1*	*180*	*180*	*1+1.1 / 47****	*±10 / 9*	*0.62*

Simulated results.
Fixed capacitor or metal welding for proof-of-concept.
* Maximum IL, maximum phase range and FoM are considered at center frequency.
** RBW_{10dB}: relative bandwidth corresponding to a 10-dB matching.
*** Amp. imb. is considered for the most lossy state, i.e. for which the IL is maximum at center frequency.

Table 3-1: Phase shifter state-of-the-art comparison.

A continuous (*fixed*) phase shift can be realized with the aid of varactors (*capacitors*) placed above SIW slots, in [12]–[15], as shown in Figure 3-2. In [12], a 360° phase shift was obtained by cascading two 180° RTPS together, the reflection coefficient being controlled by varactors on the load (see Figure 3-2 (a)). It was found that the variation of the phase shift is quite linear and the average insertion loss is 6 dB with magnitude imbalance lower than ±1.2 dB between 25.5 GHz and 26 GHz. In [13], a similar technique was used for an in-line phase shifter and a RTPS, at 26 GHz (see Figure 3-2 (b)). The in-line phase shifter provides a phase shift of 24.8° (± 2.2°) and a transmission of 1.09 dB (± 0. 17 dB) in a 30% frequency bandwidth. On the contrary, the RTPS design provides a large 180° phase shift but at the expense of a high insertion loss of 3.8 dB (± 0.87 dB) within a bandwidth of 15.3% (from 24 GHz to 28 GHz), the return loss remaining better than 10 dB.

The slotted substrate integrated waveguide (SSIW) PS with periodic loading varactors was introduced in [14] (see Figure 3-2 (c)), leading to return loss and insertion loss mostly better than 10 dB and 5 dB, respectively, in a 32% relative bandwidth (from 2.5 GHz to 3.45 GHz). At the center frequency of 3 GHz a maximum phase shift of 80° is obtained, leading to a low FoM of 20°/dB. In [15], the phase shifter is obtained by creating transverse slots loaded with capacitive elements on the top plane of a SIW (see Figure 3-2 (d)). The concept is demonstrated by considering different fixed capacitors instead of tunable ones. A large phase shift of 230.1°, at the working frequency of 15 GHz, is achieved. A relatively small insertion loss in its passband, i.e. 1-2 dB over the operating frequency band is obtained.

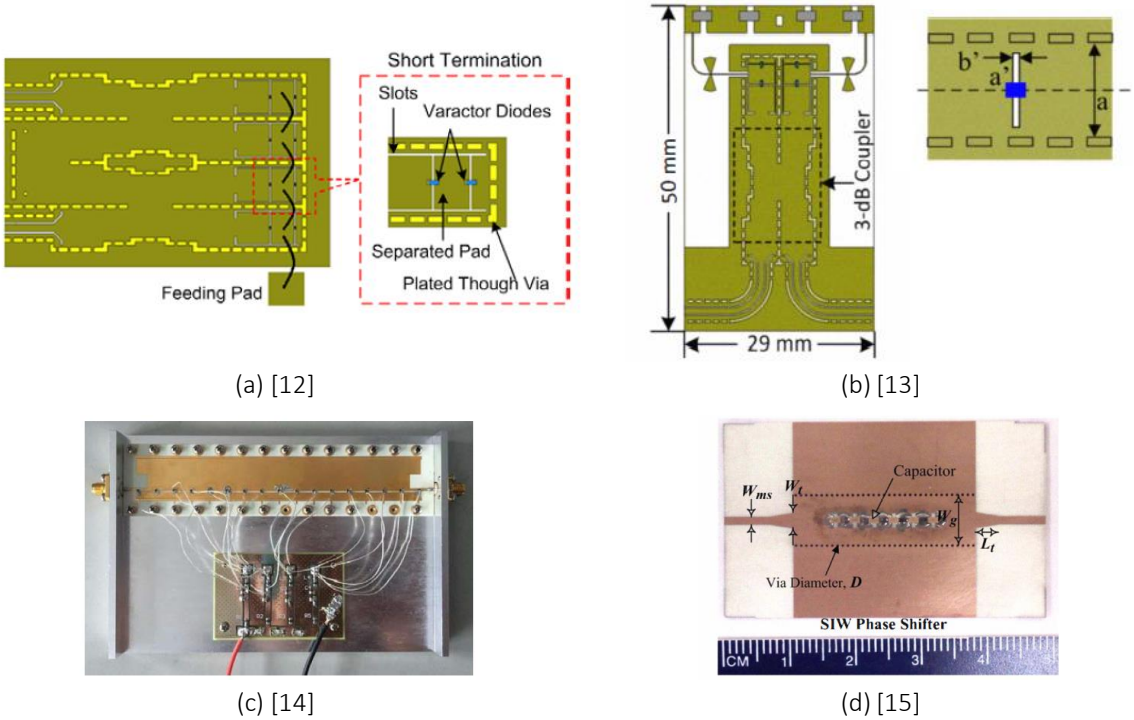

(a) [12] (b) [13]

(c) [14] (d) [15]

Figure 3-2: PCB SIW phase shifters with continuous phase shift. *(fixed as a demo for [15]).*

As proposed in [1], [2], [16]–[19], a mixed continuous and digital tuning can be realized when dealing with switched and loaded lines together. Most of the structures use SIW slots to control phase shift, as shown in Figure 3-3. In [1], an electronically controllable two-layers SIW PS is presented, where PIN diodes are used to achieve electronic control (see Figure 3-3 (a)).

Return loss is better than 15 dB from 10 to 14 GHz, providing a RBW_{10dB} of around 33%. A continuous phase shift of 180° is achieved. The measured phase imbalance is lower than ±4° over the [10-14 GHz] frequency band. The insertion loss is equal to 1±0.25 dB in a more reduced bandwidth between 10 and 12.5 GHz. Those results are particularly excellent but at the expense of more complexity in the substrate topology with a multi-layered approach.

In [2], transverse slots etched over the top metallic surface of SIW are proposed (see Figure 3-3 (b)). Here again, a PIN diode is mounted on each transverse slot. Slots are made "enabled" or "disabled" by switching the state of the PIN diode. Maximum insertion loss is 1.6 dB for a RBW_{10dB} of 31%. Around 90°±4° of phase shift is achievable, with average insertion loss 1.1±0.5 dB, from 6.75 GHz to 9.25 GHz.

In [16]–[19], concepts of potential PS are proposed but without tunable element for the realization. In [16], a fixed phase shifter with embedded air strips (slots) is presented (see Figure 3-3 (c)). The phase shift could be generated based on the variable widths of SIW, variable lengths of microstrip line and a row of embedded air strips. Measured results of different prototypes indicate that the proposed SIW phase shifters for the 45° and 90° versions have achieved the fractional BWs of 59.6% from 10.2 to 18.85 GHz with the accuracy of 2.5°, and of 62.3% from 9.5 GHz to 18.1 GHz with the accuracy of 5°. In addition, the insertion losses are both found to be better than 1.6 dB in the considered bands.

Another PS was designed in [17] (see Figure 3-3 (d)) by placing multiple rows of air holes in a single substrate, which modifies the effective dielectric constant of the material, thus leading to tunable phase shift, while maintaining insertion loss less than 0.8 dB. The phase shifter operates in X band (8-12 GHz). A phase shift of 24.8°±4.7° is obtained throughout the operating band.

In [18], the proposed PS consists of several phase channels made by SIW resonators loaded with extra metallic posts (see Figure 3-3 (e)). These metallic posts act as inductive posts controlling the resonant frequency of the SIW resonators. Experimental results demonstrate that the resulting phase shifter has more than 10% fractional bandwidth for a 15° phase shift across adjacent channels with a phase error of ±5°.The maximum phase range is 60°. The insertion loss is less than 1.5 dB in the considered bandwidth. Let us notice that this technique is similar to the one presented in [20] where phase shifting was achieved by changing the diameter and the position of inductive posts inserted in the SIW substrate. [20] results are older and were not presented herein.

In [19], similar to the principle of a microstrip phase inverters (PI) but constituted by an interdigital slot and metallic vias in the SIW topology, four types of SIW PI are proposed (see Figure 3-3 (f)). Measured results show that both prototype and compensation-type PIs (to compensate signal delay) have acceptable transmission performance with return loss better than 10 dB in the 8.3–13 GHz bandwidth and insertion losses between 1 and 2.1 dB in this band, while the insertion losses are lower than 1.6 dB in the 10–11 GHz bandwidth. The phase differences of the compensation-type are within 180° ± 10° in the 9.5–10.9 GHz frequency range.

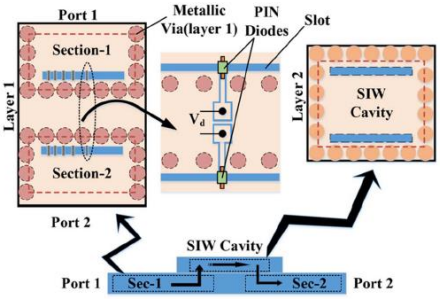

(a) [1]

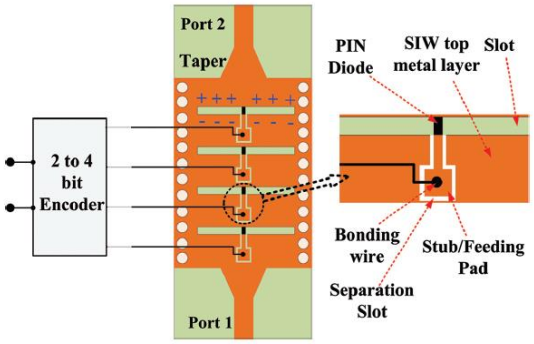

(b) [2]

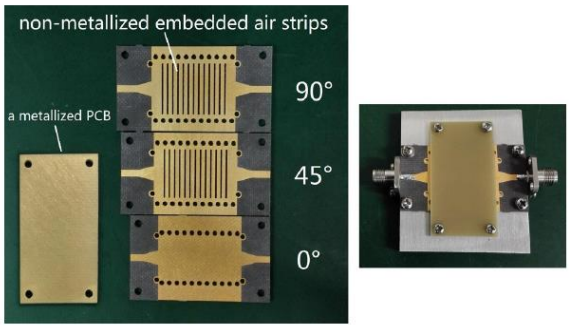

(c) [16]

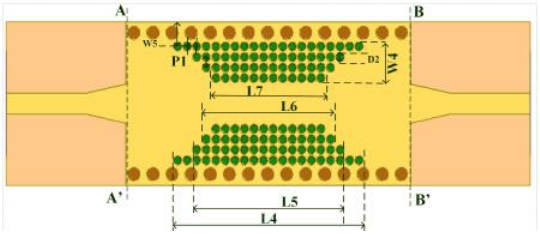

(d) [17]

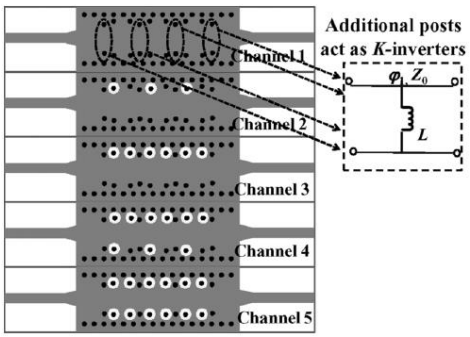

(e) [18]

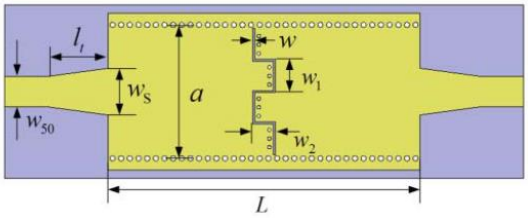

(f) [19]

Figure 3-3: PCB SIW phase shifters with mixed digital and continuous phase shift. *(fixed as a demo for [16]-[19]).*

Armed with this wealth of knowledge, we can focus now on our proposed approach in section 3.2. It is inspired from the circular slot of [18] and [20], even if our enabled/disabled floating vias do not act as inductive posts but as metallic/transparent walls, respectively.

3.2 SIW 1-bit phase shifter principle

The principle of the 1-bit SIW phase shifter is detailed here and illustrated based on PS4 (see Figure 2-14), which is the most intuitive one. The concept falls within the digital switched line topology. Besides phase shifters [18], [20], a similar technique was used for different SIW devices, e.g. antennas [21]–[23], filters [24], [25] and switches [26], [27]. The principle of the phase shifter consists in routing the EM wave towards one over two possible paths, path 1 and path 2, by enabling or disabling floating vias, as depicted in Figure 3-4. In Figure 3-4 (a), the vias "ON" on the longest path ("OFF" on the short path) force the signal to favor the short path (path 1, phase 1), the vias "ON" acting as electromagnetic walls. On the contrary, the switching

of the vias makes the longest path be favored (way 2, phase 2), as shown in Figure 3-4 (b). Thus, two absolute phases and a relative phase shift are generated.

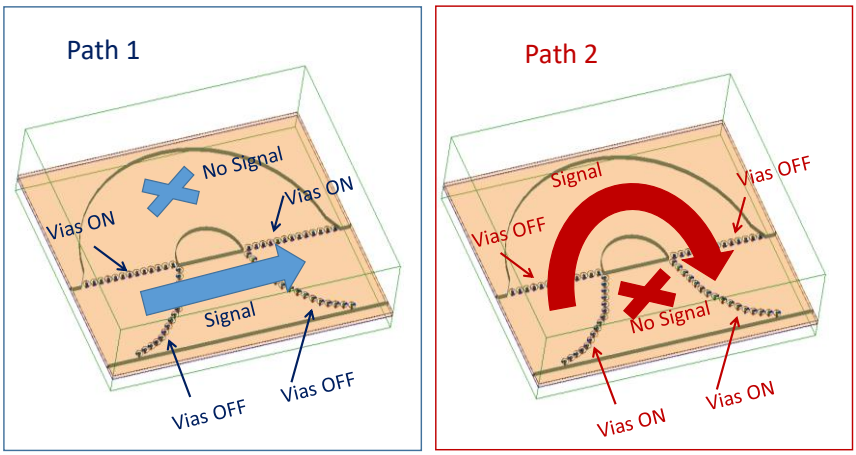

Figure 3-4: Two-state phase shifter: (a) path 1, phase 1 and (b) path 2, phase 2

The vias switching principle is explained in Figure 3-5. PIN diodes allow to connect (vias "ON") or not (vias "OFF") the lower metal layer to the upper metal layer of the SIW. A via is "ON" when the PIN diode is forward biased, ensuring a connection between the lower cover and the top of the SIW, i.e. a short circuit preventing the signal from passing. The via is "OFF" when the PIN diode is reverse biased, so it lets the signal go through the SIW.

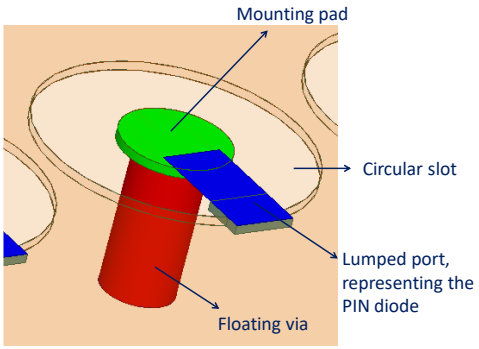

Figure 3-5: Zoom in on a floating via

Consequently, by modifying the state of the PIN diodes, it is possible to guide the RF signal towards one of the two paths. Since the two paths have not the same length, a two-state phase shifter (1-bit) is obtained.

3.3 5.8-GHz 1-bit SIW phase shifter

3.3.1 Design constraints

A first prototype of the PS principle described in section 3.2 was designed at 5.8 GHz in a single-layered PCB process (see Figure 3-6). Simulations were carried out by considering PIN diodes provided by MACOM (MA4AGP907) as switchable elements (see Figure 3-5), and thus a decoupling was required between RF and DC bias (by considering ATC multilayer ceramic capacitors 530Z104KT10T and RF choke inductors). The fabricated 5.8 GHz 1-bit SIW PS is depicted in Figure 3-7. For this first demonstrator, unfortunately, the measurements

could not be performed with the diodes and their decoupling elements, but with metallic strips instead in order to demonstrate the concept.

As the proposed PS is in SIW technology, the design is sensitive to many design rules that have to be strictly respected, as illustrated in [28] :

$$p > D \tag{3-2}$$

$$\frac{p}{\lambda_c} < 0.25 \tag{3-3}$$

$$p \leq 2 \cdot D \tag{3-4}$$

where λ_c is the cut-off wavelength of the TE_{10} mode in the waveguide, p is the center-to-center distance between two vias and D their diameter. These rules ensure negligible radiation loss, so that the SIW can be modelled by a conventional rectangular waveguide.

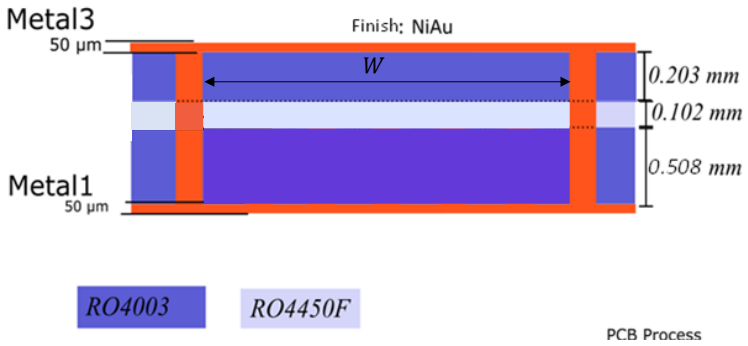

Figure 3-6: Single-layered PCB process

When following these rules, the mapping from the SIW to the rectangular waveguide is very good in the whole TE_{10} first-mode bandwidth. In addition, due to the nature of the structure, the SIW can only support the TE modes propagation while the TM modes cannot be guided, since no current can flow horizontally through the lateral walls of the SIW. In order to prevent two or more modes to exist in the SIW, other rules must be respected:

$$\lambda_c = 2 \cdot W \tag{3-5}$$

where W (SIW width) can be defined as:

$$W = \frac{c_0}{2 \cdot f_c \cdot \sqrt{\varepsilon_r}} \tag{3-6}$$

where c_0, f_c and ε_r are the speed of the light, the cut-off frequency of the TE_{10} mode and the relative dielectric constant of the medium, respectively. Moreover, the guided wavelength λ_g in the SIW is given by:

$$\lambda_g = \frac{2\pi}{\sqrt{\frac{\varepsilon_r \cdot (2\pi \cdot f)^2}{c_0^2} - \left(\frac{\pi}{W}\right)^2}} \quad (3\text{-}7)$$

The SIW phase shifter was simulated with full-wave 3D software (HFSS v.2019.2) and optimized. W was found to be equal to 20.41 mm, so that the working frequency stands in the TE_{10} mono-mode range. The diameter (D) of the via is 0.4 mm, and p is at least 0.8 mm. The PIN diode is modeled on HFSS with RLC boundary sheet, by a resistance R = 4.2 Ω when the diode is forward biased, and a capacitance C = 0.02 pF when it is reverse biased. Simulations with 'finite conductivity' for regular vias walls are always carried out, because of faster HFSS meshing operation. The PS size is 64.6 mm × 49.2 mm without feeding lines.

The reconfigurable PS could not be finalized for the moment, given the small dimensions and the number of reconfigurable vias and soldering diodes.

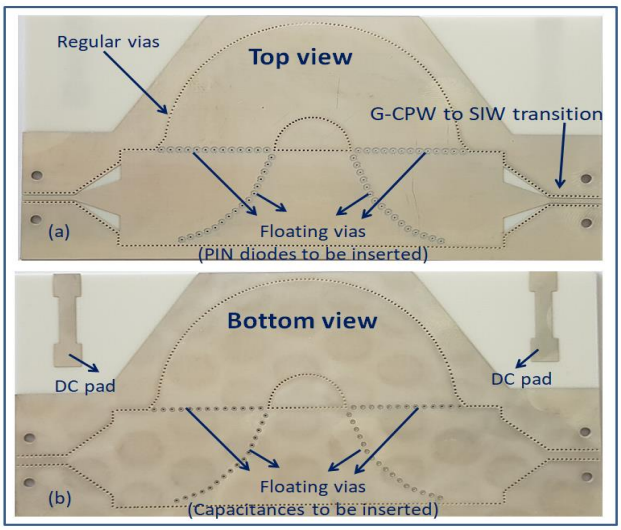

Figure 3-7: 1-bit 5.8 GHz phase shifter: (a) top view and (b) bottom view

However, in order to validate the concept, the two states could be tested independently using tin solders to simulate the two states of the phase shifter. The results are provided in section 3.3.4. Before, in the next two sections, the number of floating vias and their slots size (named as gap G) are studied.

3.3.2 Impact of the number of reconfigurable vias on the PS performance

The SIW phase shifter was optimized by varying the number of floating vias and the gap G between the floating via pad and the upper SIW metal sheet. For a fixed G = 0.35 mm, three configurations of floating vias were analyzed:

- Configuration 1: "9" vias + "16" vias
- Configuration 2: 12 + 10
- Configuration 3: 12 + 16

As referred to in Figure 3-4 (a), the first digit (“9”) in configuration 1 represents the number of reconfigurable vias "ON", while the second digit (“16”) refers to the number of reconfigurable vias "OFF".

The S-parameters of the two states for the three configurations are shown in Figure 3-8 between 4.6 and 7 GHz. The number of vias has little influence on the S-parameters unless they do not comply with the rule (3-3) and almost the same FoM equal to 270 °/dB is achieved, at 5.8 GHz. However, configurations 1 and 3 seem to represent the best compromise in terms of return loss and insertion loss for the two states at 5.8 GHz, but the configuration 3, especially, weakens the effect of resonances at 4.7, 5.5 and 6.4 GHz, because of a higher number of reconfigurable vias acting as a shield. Indeed, these resonances are due to the signal leakage in the forbidden path, which gives rise to a resonant mode: a standing wave appears, as shown in Figure 3-9.

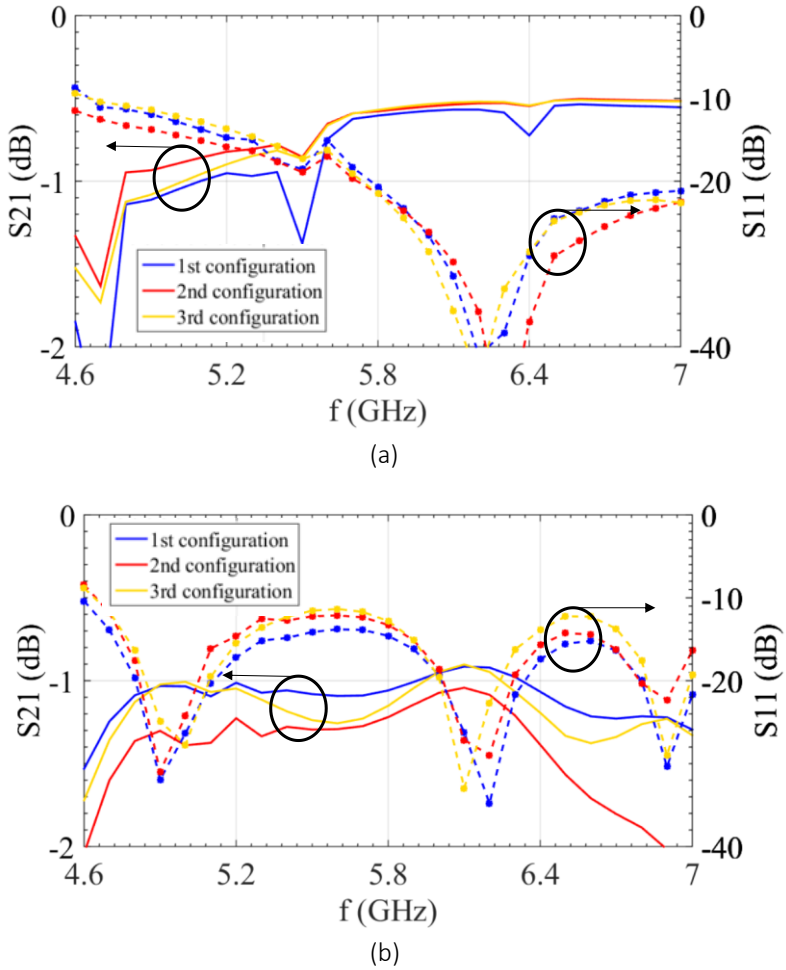

Figure 3-8: Number of reconfigurable vias study: (a) path 1 and (b) path 2

Therefore, the third configuration was considered as the most efficient one, leading to an insertion loss equal to 0.6 dB and 1.15 dB for paths 1 and 2, respectively. The relative phase shift, $\Delta\varphi$, is equal to 304° instead of 270°; it will be adjusted later on.

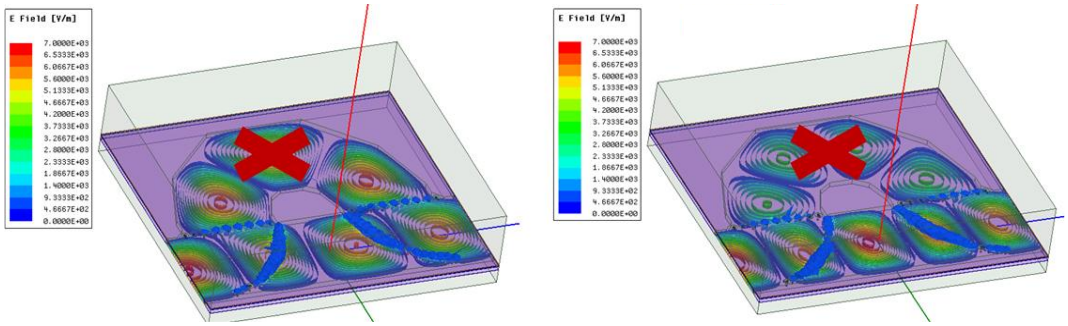

(a) (b)

Figure 3-9: Resonance due to leakage at (a) 5.5 GHz and (b) 6.4 GHz

3.3.3 Impact of the gap on the PS performance

The optimization concerning the gap (size of the circular slots all around each reconfigurable via) is carried out in this section. One reconfigurable via with a slot might be seen as in [18], where the effect of each floating via can be controlled by using circular slots around the via in the top metallic layer of the SIW. When a slot is present, the corresponding via is isolated from the ground and the corresponding inductive effect is removed. Nevertheless, the presence of the slots impacts the reactance values of the equivalent model, which works as a high-pass filter k-inverter (see Figure 3-10). Hence, if a SIW resonator is considered, the presence of the slots makes its resonance move towards the lower frequencies and a phase shift occurs at the targeted frequency as compared to the case without slot [18]. As a consequence, the choice of the value of G is very important, because it permits to tune the phase shift. Another important factor is that a small value of G can affect the return loss, because a stronger capacitance forces the current to be short-circuited in the via. On the other hand, a big G can produce radiation loss. Hence a trade-off needs to be found.

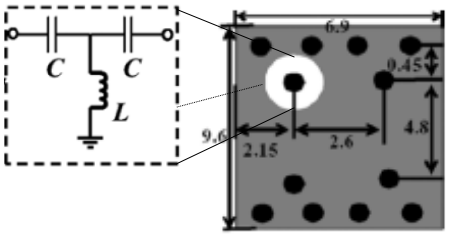

Figure 3-10: SIW resonator loaded with four additional posts and equivalent circuit for one post with slot [18].

For configuration 3, a study of the impact of the gap G was carried out, with G = 0.35 mm, 0.45 mm and 0.52 mm, respectively. The value G = 0.52 mm corresponds to the maximum allowable gap, that provides a metal track width between reconfigurable vias equal to 100 µm, which is the limit of the technology.

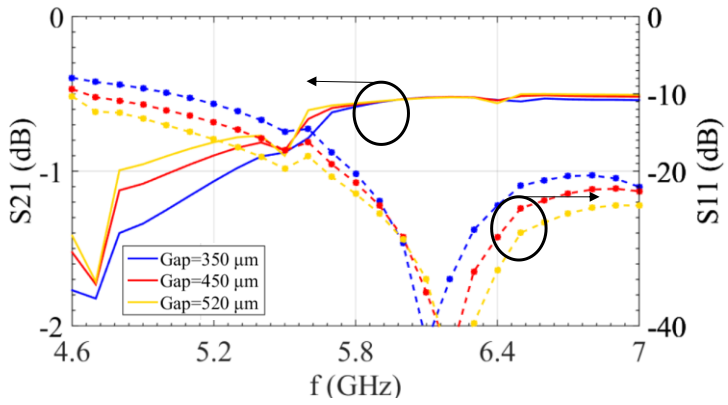

(a)

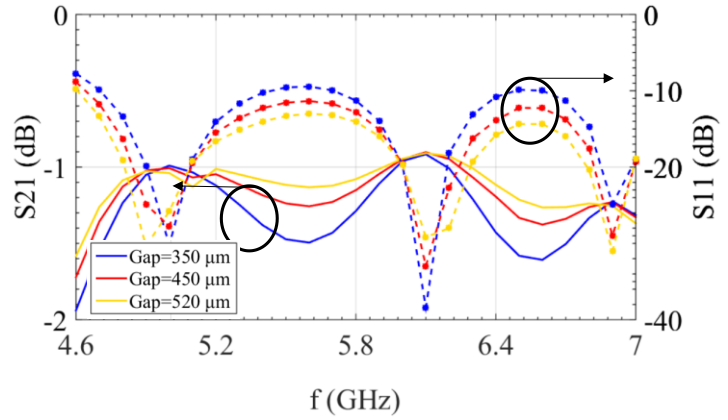

(b)

Figure 3-11: Gap study: (a) path 1 and (b) path 2

As presented in Figure 3-11, the size of the gap has little influence on path 1, whilst much more on the insertion loss of path 2. The width G = 0.45 mm was finally retained because it guarantees a capacitance linked to the value of G sufficiently low while limiting the stress on the diodes welding. In addition, it is then possible to use 240 µm tracks between each reconfigurable via, lowering the technological risk. The FoM varies from 234 °/dB up to 282 °/dB, for G = 0.35 mm and G = 0.52 mm, respectively. A FoM equal to 250 °/dB was chosen corresponding to G = 0.45 mm.

3.3.4 Simulation and measurements results

3.3.4.1 Simulated results

The final phase shifter is the one of configuration 3 with gap G = 0.45 mm but instead of having "12" vias + "16" vias, a slight improvement was made in order to even more attenuate the resonances due to standing waves, going towards "13" vias + "16" vias. Also, the PS was optimized for a 270° relative phase shift instead of the previous 304°. The simulated S-parameters in modulus and phase are given in Figure 3-12. At 5.8 GHz, paths 1 and 2 have insertion loss of 0.6 dB and 1 dB, respectively. The resonance at 5.7 GHz on path 1 is now close to 5.8 GHz but small, so not particularly awkward. Return loss is better than 15 dB over 41.4% of fractional BW. Signal in path 2 is 93° in advance, i.e. 267° lagged.

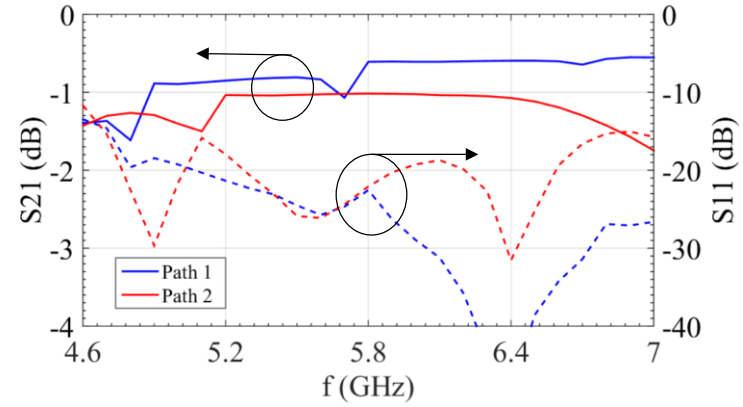

(a)

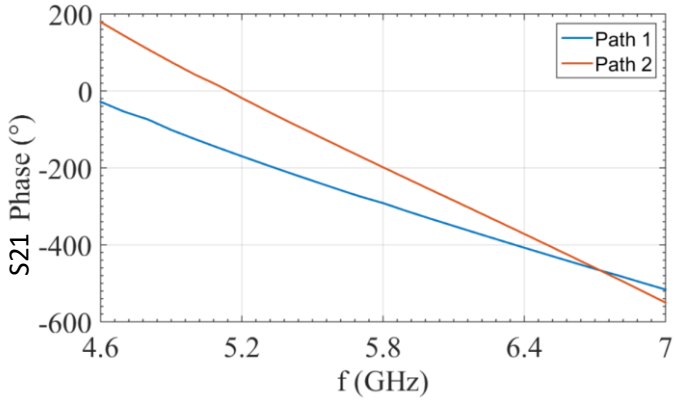

(b)

Figure 3-12: Simulated S-Parameters 1-bit SIW phase shifter: (a) amplitude and (b) phase

3.3.4.2 **Simulated impact of reconfigurable vias**

In order to estimate the impact of the reconfigurable vias on the phase shifter, a simulated reference circuit was considered, replacing the reconfigurable vias by 'finite conductivity' walls. The results show insertion loss of 0.3 dB and 0.5 dB, respectively, depending on the considered path, as shown in Figure 3-13. The impact of the diodes and floating vias is, therefore, from 0.3 (13 floating vias are made ON) to 0.5 dB (16 floating vias are made ON), for paths 1 and 2, respectively. Obviously, it can be observed that no resonance at 4.7, 5.7 and 6.7 GHz may occur anymore, contrarily to what happened with diodes and floating vias on Figure 3-12 (a), path 1.

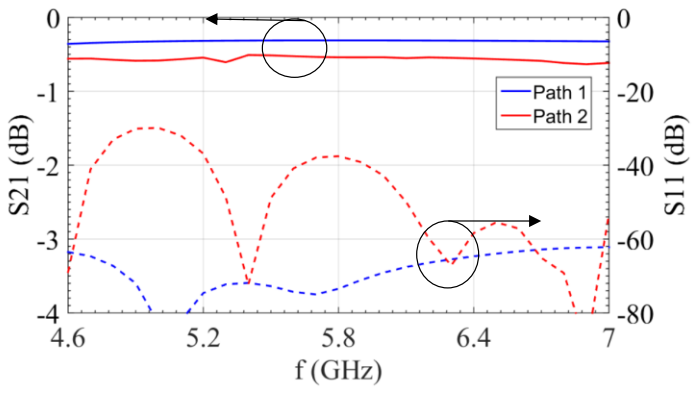

Figure 3-13: Reference SIW phase shifter circuits

The phase shift is 25.3° and 29.3° in advance as compared to the PS including diodes parasitics, for path 1 and path 2, respectively. The impact on the phase is given, mainly, by the reconfigurable vias in "OFF" state, which capacitance makes a bigger phase shift to occur along the targeted path.

3.3.4.3 **Measured results**

In order to demonstrate the validity of the proposed SIW phase shifter concept, two non-reconfigurable circuits were fabricated, on the basis of the circuit shown in Figure 3-7. A first circuit with the vias directly welded to the upper cover of the SIW favouring path 1, and a second circuit for which the welding of the vias promotes path 2. The welding was done by means of tin filling and the bottom gaps were entirely covered with it, as shown in Figure 3-14.

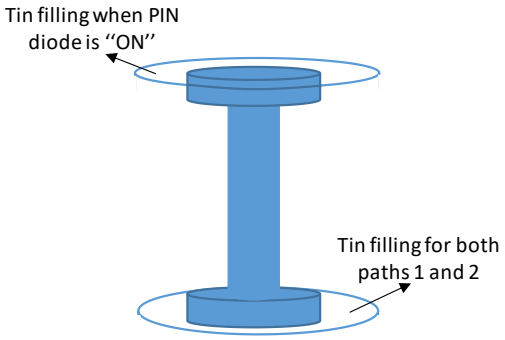

Figure 3-14: Tin filling to promote paths 1 or 2

The measurement results were compared with the simulations, taking into account the tin filling that is the more realistic simulation as possible as compared to the real case, as depicted in Figure 3-15.

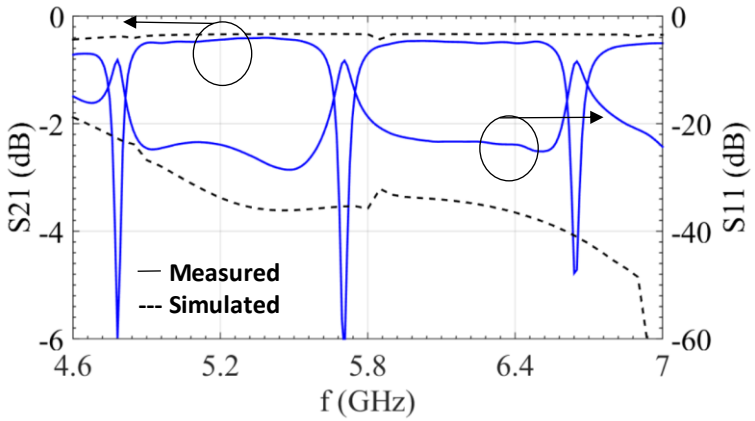

(a)

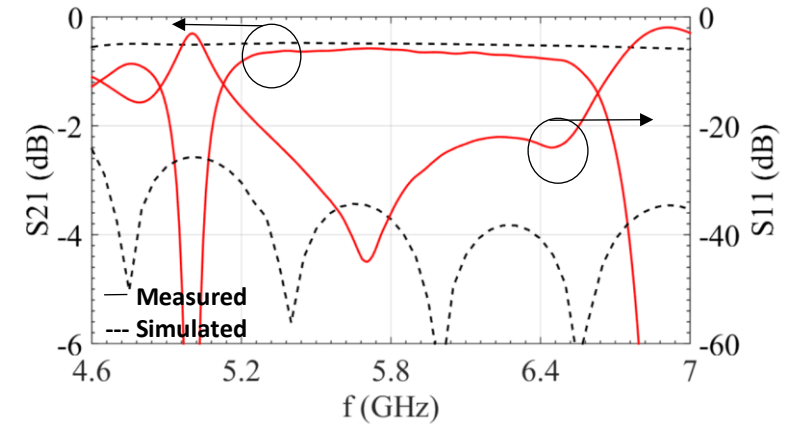

(b)

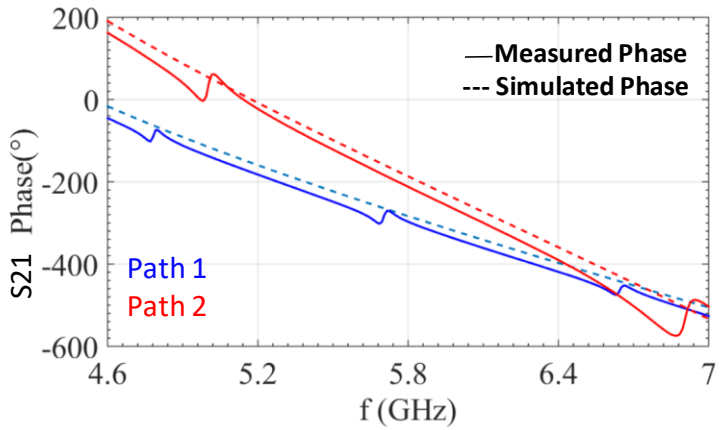

(c)

Figure 3-15: Measured and simulated 5.8 GHz SIW PS results comparison: (a) path 1 amplitude, (b) path 2 amplitude and (c) phase

Concerning path 1, the measured insertion loss is equal to 0.7 dB against 0.35 dB in simulation, at the central frequency. The return loss is better than 20 dB from 4.6 GHz to 7 GHz (i.e. 41.4% of relative BW), even if for certain frequencies (4.8 GHz, 5.7 GHz and 6.65 GHz, respectively) resonances spoil it. The latter are due to the signal leakage in the forbidden path, which gives rise to a resonant mode, as explained above. In the simulations these resonances also appear, but they are shifted by 150 MHz and are much much less sensitive. Their impact was strongly minimized by the simulations. The device will be more robust if its working frequency is centred between two resonances.

Thus, the measured device seems more suited to work around 5.4 GHz or 6.2 GHz, considering path 1. For example, at 5.4 GHz the measured insertion loss is equal to 0.45 dB against 0.35 dB in simulation, therefore very similar to each other. One possible solution to refocus the working frequency at 5.8 GHz would be to modify the width of the SIW. Concerning the absolute measured and simulated phases, they are equal to -297.4° and -283.6°, respectively, at 5.8 GHz. The phase discrepancy is due to the fact that measured phase varies around the resonance frequency and, because 'finite conductivity' walls were used for the regular vias in simulation. If a frequency of 5.4 GHz were considered, the phase discrepancy would be equal to 26°.

Concerning path 2, the device seems to work very well at 5.8 GHz. The measured insertion loss is equal to 0.6 dB against 0.5 dB in simulation, at the central frequency. The measured return loss is better than 15 dB between 5.2 GHz and 6.6 GHz (i.e. 24% of relative BW). Resonances also appear, that are the resonances observed till the beginning at the lower and upper frequencies of the observable range. They are far from the central frequency (5 GHz and 6.8 GHz, respectively). The measured and simulated absolute phase are -212.5° and -186.7°, at 5.8 GHz, respectively, showing a phase discrepancy of 26°.

Finally, the phase difference between the two measured channels is -275 °, very close to the expected -270°, with a difference of 5°.

3.4 28-GHz 1-bit phase shifter

3.4.1 Design constraints

A reconfigurable version of PS for higher frequency, i.e. 28 GHz, is introduced now, to be integrated into a phased array, for 5G. The phase shifter was fabricated in a multi-layered PCB process (see Figure 3-16), so as to ensure a middle layer to drive the DC feeding for the PIN diodes. The detailed view of this new version is given in Figure 3-17.

As it can be seen, the working principle remains the same but, now, the insert of two PIN diodes for each reconfigurable via is considered, one in the bottom and one in the top metal layer, so that the capacitive reactance of the reconfigurable via in "OFF" state is reduced, the two diodes being in a series configuration.

The return loss is improved, accordingly. But this technique also increases the insertion loss because more PIN diodes are needed and it represents one of the constraints of frequency rising. Dimensions and principle of the feeding network are explained in section 3.4.2.

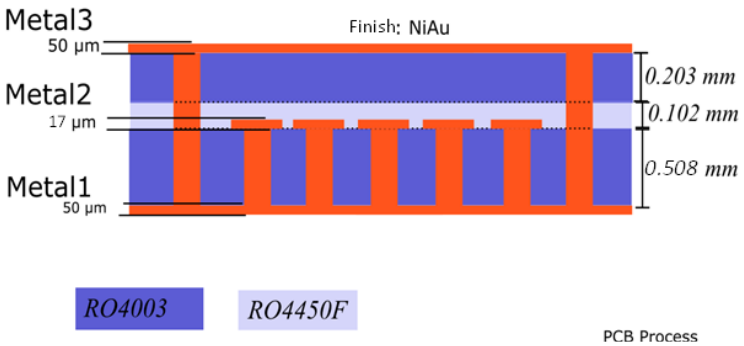

Figure 3-16: Multi-layered PCB process

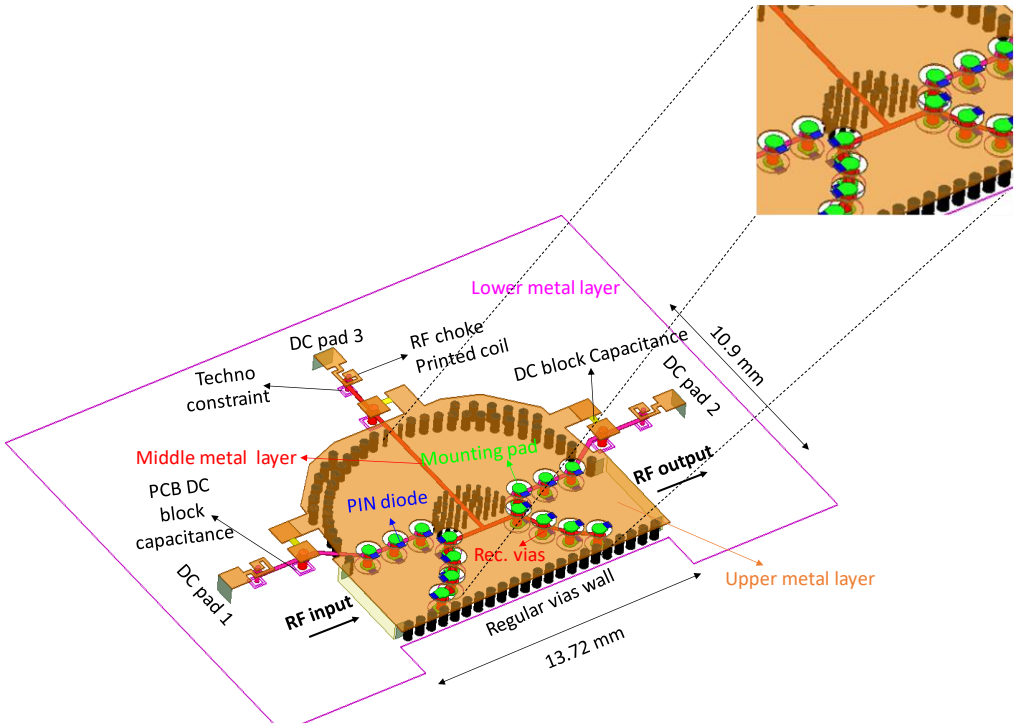

Figure 3-17: 1-bit SIW phase shifter at 28 GHz with zoom on biasing strips

Another constraint is that the value W reduces on the basis of (3-6), while we need to ensure a mounting pad and gap G big enough, by respecting the minimum metal strip width (at least 100 µm). W, G and the mounting pad diameter were chosen to be equal to 4.23 mm (mono-mode), 0.25 mm and 0.6 mm, respectively, the PIN diode package dimensions being equal to 0.67 mm × 0.35 mm. W might be slightly increased to get the right phase shift, if necessary. The mounting pad diameter is chosen to be 0.1 mm bigger than the diameter of the via, for each side. The value of G was chosen to ensure at least 0.1 mm metal strip width between two adjacent slots, acceptable return loss, while avoiding radiation loss. Hence, all the reconfigurable vias have the same G and their diameter, D, is equal to 0.4 mm, in order to ensure as much as possible shielding for the forbidden path. D equal to 0.2 mm and 0.4 mm was used for regular vias, based on circuit geometry.

The PS size is 13.72 mm × 10.9 mm without DC feeding network and access lines, where λ_g of SIW and λ_0 are 7.68 mm and 10.68 mm at 28 GHz, respectively. The longitudinal size (13.72 mm) was adjusted for further integration in a BM (same length than future crossover of chapter 4). The dimensions are listed in Table 3-2.

W (mm)	G (mm)	Diameter reconfig. vias (mm)	Diameter regular vias (mm)	Mounting pad diameter (mm)	PIN diode size (mm×mm)	PS size (mm×mm)
4.23 mm	0.25	0.4	0.2/0.4	0.6	0.67 × 0.35	13.72 × 10.9

Table 3-2: Dimensions of 1-bit 28 GHz SIW PS

Considering these constraints due to the technology and PIN diodes welding, the designed prototype might be extended up to 40 GHz, at the most.

3.4.2 Bias circuit for PIN diodes feeding

The geometry and technique to implement the RF choke and the DC block for the feeding of the PIN diodes network, is shown in Figure 3-18. For biasing purpose, all the reconfigurable vias corresponding to path 1 or path 2, respectively, were connected with each other through 0.2 mm width metal strips, whose length was set to avoid resonances in the RF path.

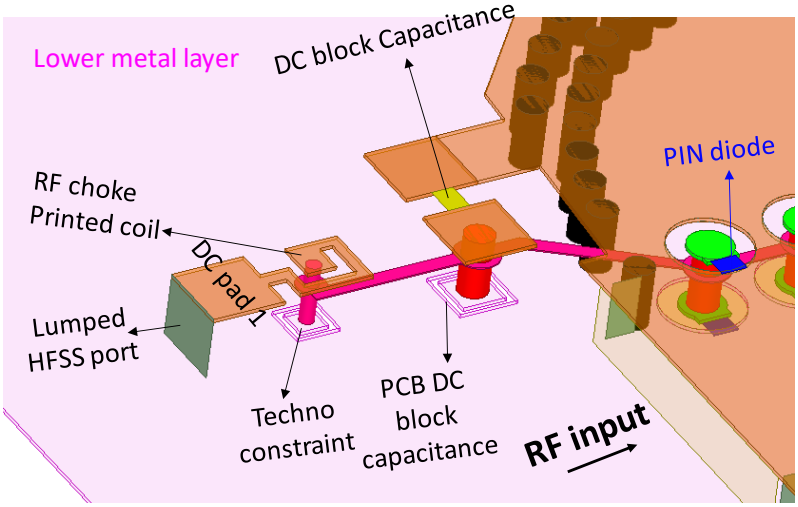

(a)

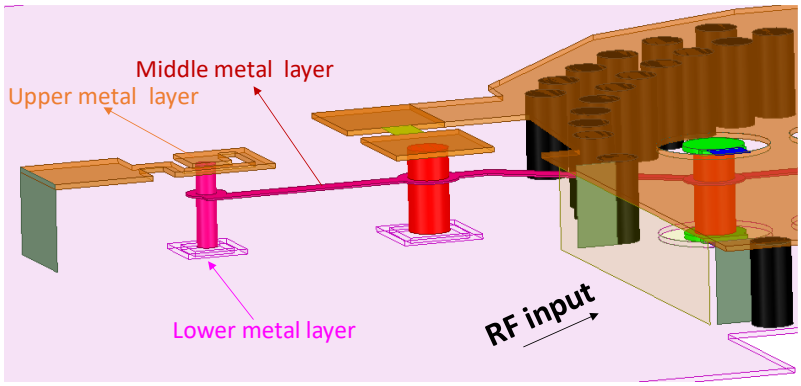

(b)

Figure 3-18: Bias circuit for PIN diodes. (a) top detailed view and (b) view showing the height of the three metal layers

Initially, the RF is choked with PCB capacitance, that is a capacitance created by etching the lower metal layer, along with a lumped parallel capacitance to be welded, to reinforce the effect. The latter one was finally not soldered, because the use of the PCB capacitance resulted in acceptable performance. Afterwards, a printed coil was designed in ADS and integrated in HFSS for full-wave simulation, to be sure to completely choke the RF.

Since two PIN diodes are used, one in the top and one in the bottom, thus, the via pads are physically separated from the DC ground by the two gaps. 'Lumped ports' were inserted on HFSS to verify the RF level that heads to DC pad. From the results (shown in Annex 1), when path 1 is enabled, the RF transmission flowing from the waveguide input port towards DC pads 1 and 2 is lower than -50 dB, while it is lower than -30 dB for DC pad 3, from 26 GHz to

30 GHz. When path 2 is enabled, the RF transmission is always lower than −40 dB, over the same frequency range. The 'lumped ports' were renormalized as either 1 Ω or 1000 Ω, to simulate the internal impedance of a DC voltage or current generator, respectively.

Indeed, in practice, a DC current generator is supposed to feed DC pads 1 and 2 when path 1 is enabled, while a DC voltage generator provides a reverse bias to DC pad 3. On the contrary, a DC current generator feeds DC pad 3 and a DC voltage generator feeds in reverse bias the DC pads 1 and 2, when path 2 is enabled.

Based on MACOM PIN diode datasheet, when a forward 10-mA DC current feeds the PIN diode at 10 GHz (not results were provided at 28 GHz), a forward voltage between 1.33 V and 1.45 V is obtained, with an equivalent resistance equal to 4.2 Ω. When the PIN diode is reversed biased and a DC voltage equal to -5 V is applied, it can be modeled by a 0.02 pF capacitance. These values of capacitance and resistance were used for HFSS simulations. No electrical model was provided for other current values.

3.4.3 Simulation and measurement results

The fabricated 1-bit PS and the measurement set-up are depicted in Figure 3-19. All the devices presented in this work were measured in RF with '2.92-mm jack (female) end launch low profile connectors' by SouthWest Microwave factory, allowing to work up to 40 GHz.

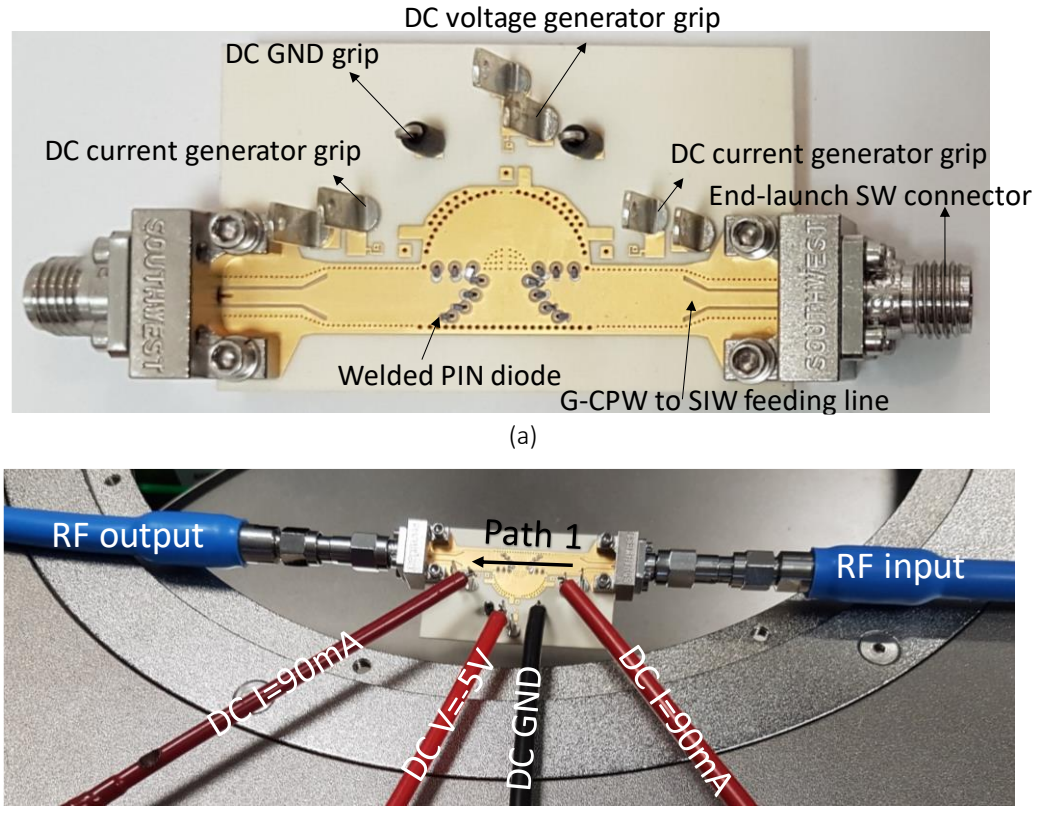

Figure 3-19: 1-bit SIW phase shifter path 1 measurement set-up: (a) PS mounting top view and (b) RF and DC testing

The feeding lines are based on G-CPWs, and G-CPW to SIW tapers were realized to turn the quasi-TEM G-CPW mode into a TE_{10} mode suited for SIW propagation. The dimensions of G-CPW feeding lines are shown in Figure 3-20, and better detailed in Annex 2.

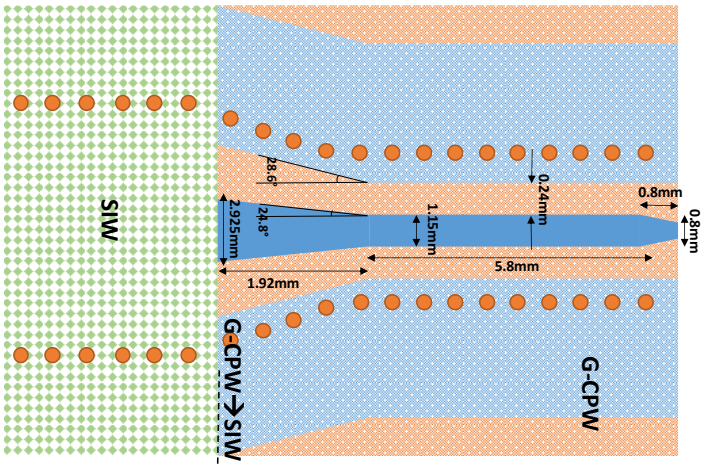

Figure 3-20: G-CPW access line dimensions

A first SOLT (short-open-load-through) calibration was done to get the error matrices including the RF cable effect and, afterwards, a TRL calibration [29] was carried out to remove the feeding lines effect, as well. The TRL standards are shown in Figure 3-21, and better detailed in Annex 3.

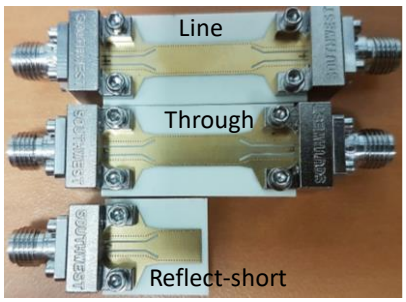

Figure 3-21: TRL standards

In Figure 3-19 (b), two grips for DC current and one for voltage generator when path 1 is enabled are shown, along with the one for DC ground, which is connected to the lower metal layer and to all the generators, to create a common ground. The other grips and a resistance to control the DC current were left unconnected because they were designed to provide a forward DC voltage feeding (to use for testing purpose, but not utilized, finally).

Concerning path 1 enabling, the DC current provided to the circuit is 180 mA for each current generator (that is 15 mA multiplied by 12 PIN diodes placed in parallel with each other). For path 2, it is 240 mA (that is 15 mA by 16 PIN diodes placed in parallel with each other). Providing 15 mA per diode, instead of 10 mA, leads to better insertion loss (0.35 dB instead of ~0.5 dB of diode loss, on datasheet, at 28 GHz) and very good return loss (> 32 dB, on datasheet, at 15 GHz, 28 GHz not being provided). Concerning the reverse biasing, -5 V is kept because it provides a good isolation (between 15 and 25 dB, on datasheet, at 15 GHz, 28 GHz not being provided). The reverse leakage current is given as 10 µA, for reverse biasing of

−50 V, on datasheet; consequently extremely few reverse current is expected at -5 V. With this measurement set-up, the DC power consumption is equal to 0.24 W (180 mA·1.33 V) and 0.32 W (240 mA·1.33 V) for paths 1 and 2, respectively. The PS simulation and measurement results are compared in Figure 3-22.

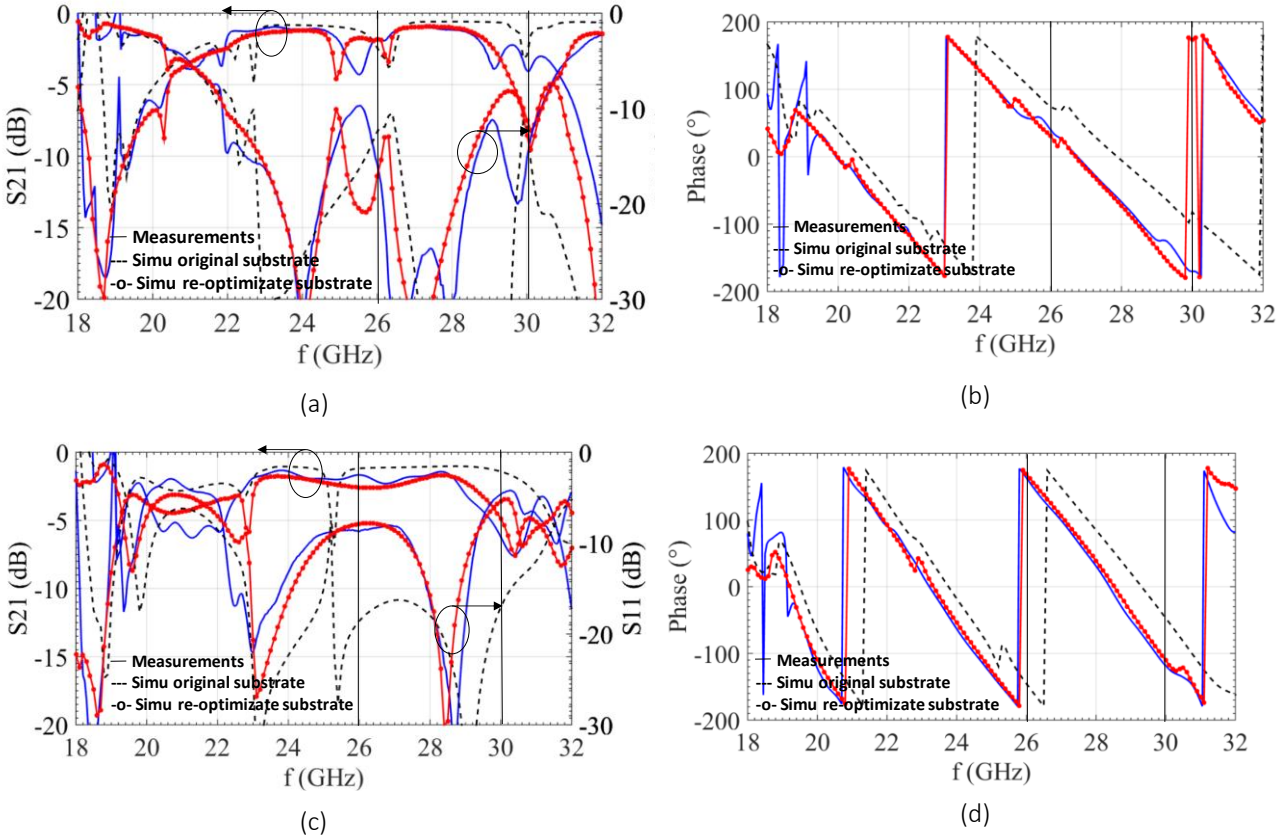

Figure 3-22: 1-bit phase shifter measurement and simulation results: (a) path 1 amplitude,(b) path 1 phase, (c) path 2 amplitude and (d) path 2 phase

The simulated results are plotted with original design substrate values (dotted black lines) and with re-optimized substrate values + new diode equivalent model ('o' marker solid red lines). Indeed, first, ε_r and $\tan\delta$ were slightly modified, so as to better match simulation with measurement results. They were re-optimized as 3.64 and 0.0055, respectively. This post-tuning was made by simulating simple SIW BM stand-alone devices (see chapter 4) with HFSS and based on Matlab simulations, and comparing with measurement results; concerning Matlab simulations SIW loss formulas were implemented, as described in [30]. Second, once implemented the substrate modification, the resistance of PIN diode and its reverse biasing capacitance were adjusted as 7.5 Ω and 0.0395 pF

A small parenthesis is mandatory concerning post-simulation process. In fact, the substrate material characteristics are given at 10 GHz in datasheet. Doubling $\tan\delta$ from 10 to 28 GHz seems completely fair, whereas increasing ε_r from 3.55 to 3.64 makes no physical sense. In parallel, having W equal to 4.35 mm, instead of 4.23 mm, while keeping ε_r = 3.55, would lead to the same phase shift. This corresponds to a deviation of 120 µm of the vias position, that is over the technology deviation corners. Another reason to explain the observed discrepancy could be the non-deembedded results in simulation. Finally, a last and very

plausible reason could be the position of the reflect in the TRL calibration set, that is tricky to fix. Simulations of the TRL features could be performed in the future for better accuracy in the measurements. On the basis of measurements results, regarding path 1, the insertion loss and absolute phase are 1.16 dB and -67°, at 28 GHz, respectively. The return loss is better than 10 dB between 25.6 and 30.4 GHz (17.1% relative BW). It is affected by resonances that occur at 25.5 GHz and 29.2 GHz. The first resonance is due to the standing wave that appears in the forbidden path and the second one is due to the length of the bias circuit, which is connected with DC pad 3. Anyway, the discrepancy, between measurement and simulation results with original substrate values, is furtherly reduced. Concerning path 2, the insertion loss and absolute phase are 1.63 dB and 30.8°, at 28 GHz, respectively. The return loss is better than 15 dB at 28 GHz, while it is better than 10 dB between 27.4 and 29.3 GHz (6.8% of RBW_{10dB}), but it remains quite poor for frequencies around the central one. Again here, the return loss is affected by a resonance due to leakage in the forbidden path, occurring at 30.3 GHz. The relative phase shift between the two paths is - 262.2° at 28 GHz, that is close to the expected -270°, and it remains ±10° apart between 27.4 and 28.5 GHz (3.9% relative BW). The latter can set the relative BW at 3.9% instead of 6.8%, but it is depending on designers' requirements. Finally, the FoM is 164°/dB. On the overall, measurement and simulation results are in good agreement.

An HFSS simulation was run at 28 GHz considering $R = 0\ \Omega$ to figure out the PIN diode impact on losses, resulting in an insertion loss equal to 0.7 dB and 1.1 dB for path 1 and path 2, respectively. Hence, the impact of the diode's forward resistance is almost 0.5 dB for both path 1 and 2, respectively.

The proposed phase shifter is compared with the state-of-the-art reconfigurable phase shifters of Table 3-3. It must be noticed that, as compared to the state-of-the-art results, the proposed PS allows obtaining not only a very high FoM (164°/dB) but also a large maximum phase tuning (262°) and moderate insertion loss (1.6 dB at center frequency). The main drawbacks of this architecture are its quite large dimensions and narrow-band behavior (6.8%).

Ref.	PS type	Tunability	Method	f (GHz)	RBW_{10dB}^{**} (%)	Max IL^{*} (dB)	Max Phase range* (°)	FoM^{*} (°/dB)	Amp. imb. (dB) / RBW(%)	Phase imb. (°)/RBW(%)	Surface ($\lambda_0 \cdot \lambda_0$)
[12]	Continuous	Tunable	RTPS	26	13.8	7.2	360	50	6±1.2 / 1.9	±5 / 1.9	~7.7
[13]		Tunable	RTPS	26	15.3	4.67	180	38.5	3.8±0.87 / 15.3	±10 / 7.5	10.89
[14]		Tunable	SSIW	3	31.9	4	80.7	20.2	3.2±0.8 / 13.3	±10 / 28.3	0.26
[1]	Digital	Tunable	2-layers SSIW	12	33.3	1.25	133	94.7	1±0.25 / 20.8	±4 / 33.3	~1.1
[2]		Tunable	SSIW	8	31	1.4	90	64.3	1.1±0.5 / 31	±4 / 31	0.23
This work		**Tunable**	**Circular SSIW**	**28**	**6.8**	**1.6**	**262.2**	**163.9**	**1.6+0.5 / 6.2*** **	**±10 / 3.9**	**1.3**

* Maximum IL, maximum phase range and FoM are considered at center frequency.
** RBW_{10dB}: relative bandwidth corresponding to a 10-dB matching.
*** Amp. imb. is considered for the most lossy state, i.e. for which the IL is maximum at center frequency.

Table 3-3: Proposed tunable phase shifters and state-of-the-art comparison.

3.5 Conclusion

The tunable phase shifter is a critical block in the extended-beam Butler matrix design, as shown in chapter 2. A specific attention was thus paid in the thesis to this tunable block in a dedicated chapter. In the first part of this chapter, the pros and cons of continuous and digital phase shifting were discussed and a detailed state-of-the-art was reported for PCB-SIW phase shifters leading to the choice of a digital switched line one.

A first prototype was presented at 5.8 GHz and its working principle was highlighted, which consists in routing the EM wave towards one or the other of the two possible paths, path 1 and path 2, by enabling or disabling floating reconfigurable vias. A detailed study based on HFSS simulation was carried out to optimize the device, according to the number of reconfigurable vias and the gap between the upper metal layer and the reconfigurable via pad. Resonances occurred at certain frequency spoiling the return loss; the cause of them was explained through HFSS simulations. The device was measured with the aid of tin instead of PIN diodes to prove the validity of the proposed concept.

In the second part of this chapter, we increased the target frequency to be suited for 5G applications. Thus, a 28-GHz 1-bit phase shifter was designed and tested, this time, with PIN diodes. A good agreement between measurement and simulation results was achieved. The bias circuit technique was introduced, which needs a three metal layer PCB technology. The measured FoM is 164°/dB at 28 GHz with a large phase shift tuning (262°) and moderate insertion loss (1.6 dB). The size of the phase shifter is 13.72 mm × 10.9 mm without feeding lines and bias circuit.

In the next chapter, all the Butler matrix blocks, couplers, crossovers and all phase shifters, will be introduced and measured and the overall Butler matrix performance will be discussed.

REFERENCE

[1] B. Muneer, Z. Qi, and X. Shanjia, 'A Broadband Tunable Multilayer Substrate Integrated Waveguide Phase Shifter', *IEEE Microwave and Wireless Components Letters*, vol. 25, no. 4, pp. 220–222, Apr. 2015, doi: 10.1109/LMWC.2015.2400923.

[2] B. Muneer, Z. Qi, and S. Xu, 'A Digital SIW Phase Shifter Implemented by Switching Transverse Slots via PIN Diodes', *Frequenz*, vol. 69, no. 9–10, Jan. 2015, doi: 10.1515/freq-2015-0007.

[3] D. Kaddour *et al.*, 'A compact and selective low-pass filter with reduced spurious responses, based on CPW tapered periodic structures', *IEEE Transactions on Microwave Theory and Techniques*, vol. 54, no. 6, pp. 2367–2375, Jun. 2006, doi: 10.1109/TMTT.2006.875290.

[4] Y. Yu *et al.*, 'A 60GHz digitally controlled phase shifter in CMOS', in *ESSCIRC 2008 - 34th European Solid-State Circuits Conference*, Edinburgh, UK, Sep. 2008, pp. 250–253, doi: 10.1109/ESSCIRC.2008.4681839.

[5] F. Ellinger, H. Jackel, and W. Bachtold, 'Varactor-loaded transmission-line phase shifter at C -band using lumped elements', *IEEE Transactions on Microwave Theory and Techniques*, vol. 51, no. 4, pp. 1135–1140, Apr. 2003, doi: 10.1109/TMTT.2003.809670.

[6] J. J. P. Venter, T. Stander, and P. Ferrari, 'X -Band Reflection-Type Phase Shifters Using Coupled-Line Couplers on Single-Layer RF PCB', *IEEE Microwave and Wireless Components Letters*, vol. 28, no. 9, pp. 807–809, Sep. 2018, doi: 10.1109/LMWC.2018.2853562.

[7] M.-D. Tsai and A. Natarajan, '60GHz passive and active RF-path phase shifters in silicon', in *2009 IEEE Radio Frequency Integrated Circuits Symposium*, Boston, MA, USA, Jun. 2009, pp. 223–226, doi: 10.1109/RFIC.2009.5135527.

[8] S. Gong, H. Shen, and N. S. Barker, 'A 60-GHz 2-bit Switched-Line Phase Shifter Using SP4T RF-MEMS Switches', *IEEE Transactions on Microwave Theory and Techniques*, vol. 59, no. 4, pp. 894–900, Apr. 2011, doi: 10.1109/TMTT.2011.2112374.

[9] Hong-Teuk Kim *et al.*, 'V-band 2-b and 4-b low-loss and low-voltage distributed MEMS digital phase shifter using metal-air-metal capacitors', *IEEE Transactions on Microwave Theory and Techniques*, vol. 50, no. 12, pp. 2918–2923, Dec. 2002, doi: 10.1109/TMTT.2002.805285.

[10] Yun-Chieh Chiang, Wei-Tsung Li, Jeng-Han Tsai, and Tian-Wei Huang, 'A 60GHz digitally controlled 4-bit phase shifter with 6-ps group delay deviation', in *2012 IEEE/MTT-S International Microwave Symposium Digest*, Montreal, QC, Canada, Jun. 2012, pp. 1–3, doi: 10.1109/MWSYM.2012.6259494.

[11] Y. Garbovskiy *et al.*, 'Liquid crystal phase shifters at millimeter wave frequencies', *Journal of Applied Physics*, vol. 111, no. 5, p. 054504, Mar. 2012, doi: 10.1063/1.3691202.

[12] Y. Ding and K. Wu, 'SIW varactor-tuned phase shifter and phase modulator', in *2012 IEEE/MTT-S International Microwave Symposium Digest*, Montreal, QC, Jun. 2012, pp. 1–3, doi: 10.1109/MWSYM.2012.6259459.

[13] Y. Ding and K. Wu, 'Varactor-tuned substrate integrated waveguide phase shifter', in *2011 IEEE MTT-S International Microwave Symposium*, Baltimore, MD, USA, Jun. 2011, pp. 1–4, doi: 10.1109/MWSYM.2011.5972725.

[14] H. Peng, X. Xia, and T. Yang, 'Slotted substrate integrated waveguide phase shifter', in *2016 IEEE Information Technology, Networking, Electronic and Automation Control Conference*, Chongqing, China, May 2016, pp. 1036–1039, doi: 10.1109/ITNEC.2016.7560521.

[15] A. Suntives, K. Payandehjoo, and R. Abhari, 'Design and Characterization of Periodically-Loaded Substrate Integrated Waveguide Phase Shifters', p. 4, 2010.

[16] H. Peng, X. Xia, S. O. Tatu, and T. Yang, 'AN IMPROVED BROADBAND SIW PHASE SHIFTER WITH EMBEDDED AIR STRIPS', *Progress In Electromagnetics Research C*, vol. 67, pp. 185–192, 2016, doi: 10.2528/PIERC16080904.
[17] P. Yadav, S. Mukherjee, and A. Biswas, 'Design of planar substrate integrated waveguide (SIW) phase shifter using air holes', in *2015 IEEE Applied Electromagnetics Conference (AEMC)*, Guwahati, India, Dec. 2015, pp. 1–2, doi: 10.1109/AEMC.2015.7509117.
[18] T. Yang, M. Ettorre, and R. Sauleau, 'Novel Phase Shifter Design Based on Substrate-Integrated-Waveguide Technology', *IEEE Microwave and Wireless Components Letters*, vol. 22, no. 10, pp. 518–520, Oct. 2012, doi: 10.1109/LMWC.2012.2217122.
[19] X. Zou, F.-Z. Geng, Y. Li, and Y. Leng, 'Phase Inverters Based on Substrate Integrated Waveguide', *IEEE Microwave and Wireless Components Letters*, vol. 27, no. 3, pp. 227–229, Mar. 2017, doi: 10.1109/LMWC.2017.2663106.
[20] K. Sellal, L. Talbi, and T. A. Denidni, 'A 28GHz phase shifter using Substrate Integrated Waveguide', in *2006 12th International Symposium on Antenna Technology and Applied Electromagnetics and Canadian Radio Sciences Conference*, Jul. 2006, pp. 1–4.
[21] L. Wu, A. J. Farrall, and P. R. Young, 'Substrate Integrated Waveguide Switched Beam Antenna', *IEEE Transactions on Antennas and Propagation*, vol. 63, no. 5, pp. 2301–2305, May 2015, doi: 10.1109/TAP.2015.2405085.
[22] B. Khalichi, S. Nikmehr, and A. Pourziad, 'RECONFIGURABLE SIW ANTENNA BASED ON RF-MEMS SWITCHES', *Progress In Electromagnetics Research*, vol. 142, pp. 189–205, 2013, doi: 10.2528/PIER13070204.
[23] J. Hu, Z.-C. Hao, and Z.-W. Miao, 'A circular polarization reconfigurable substrate integrated waveguide antenna', in *2016 IEEE International Conference on Ubiquitous Wireless Broadband (ICUWB)*, Nanjing, China, Oct. 2016, pp. 1–3, doi: 10.1109/ICUWB.2016.7790534.
[24] M. Armendariz, V. Sekar, and K. Entesari, 'Tunable SIW bandpass filters with PIN diodes', p. 4.
[25] V. Sekar, M. Armendariz, and K. Entesari, 'A 1.2–1.6-GHz Substrate-Integrated-Waveguide RF MEMS Tunable Filter', *IEEE Transactions on Microwave Theory and Techniques*, vol. 59, no. 4, pp. 866–876, Apr. 2011, doi: 10.1109/TMTT.2011.2109006.
[26] Ruo Feng Xu, B. S. Izquierdo, and P. R. Young, 'Switchable Substrate Integrated Waveguide', *IEEE Microwave and Wireless Components Letters*, vol. 21, no. 4, pp. 194–196, Apr. 2011, doi: 10.1109/LMWC.2011.2108274.
[27] A. B. Numan, J.-F. Frigon, and J.-J. Laurin, 'Single-Pole Single-Throw Switch for Substrate-Integrated Waveguide', *IEEE Microwave and Wireless Components Letters*, vol. 28, no. 3, pp. 221–223, Mar. 2018, doi: 10.1109/LMWC.2018.2804259.
[28] D. Deslandes and K. Wu, 'Design Consideration and Performance Analysis of Substrate Integrated Waveguide Components', in *32nd European Microwave Conference, 2002*, Milan, Italy, Oct. 2002, pp. 1–4, doi: 10.1109/EUMA.2002.339426.
[29] G. F. Engen and C. A. Hoer, 'Thru-Reflect-Line: An Improved Technique for Calibrating the Dual Six-Port Automatic Network Analyzer', *IEEE Transactions on Microwave Theory and Techniques*, vol. 27, no. 12, pp. 987–993, Dec. 1979, doi: 10.1109/TMTT.1979.1129778.
[30] M. Bozzi, M. Pasian, and L. Perregrini, 'Modeling of losses in substrate integrated waveguide components', in *2014 International Conference on Numerical Electromagnetic Modeling and Optimization for RF, Microwave, and Terahertz Applications (NEMO)*, Pavia, Italy, May 2014, pp. 1–4, doi: 10.1109/NEMO.2014.6995688.

Chapter 4:

Design blocks for 28 GHz Butler matrix

In this fourth chapter, the design blocks for a 28 GHz SIW extended beam Butler matrix are introduced. Firstly, 3-dB coupler and crossover (0-dB coupler) are realized in short-slot topology. Secondly, all the phase shifters included in the system are designed and fabricated. For a proof-of-concept, for each 1-bit phase shifter two not reconfigurable phase shifters are realized, representing either a RF path or the other. Afterwards, they are arranged in the system with the couplers and crossovers. The latter results in two realized Butler matrices, each one providing four different progressive output phases. In the last part of the chapter, the measurements of all the aforementioned devices give rise to a detailed analysis of the results and of their impact on the radiation pattern of the array antenna system. Moreover, the state-of-the-art of SIW coupler and crossover for PCB technology is reported all along this chapter and, as a conclusion, a discussion about new more performing technologies, that can allow the frequency rising, is dealt with.

4.1 Short-slot 3-dB SIW coupler and requirements

The short-slot coupler is a well suited topology for BM coupler and crossover realized in a PCB-SIW technology. It was first introduced by Riblet in 1950 [1] along with its theoretical description. Since 2005 several realizations of this short-slot coupler in SIW technology have been demonstrated [2]–[4].

Basically, its operation principle relies on the interference of two propagating modes, the fundamental TE_{10} and TE_{20}. In order to provide the required interference, a larger waveguide is inserted between the four waveguide accesses (see Figure 4-1). For practical reasons the accesses are operating in their mono-mode frequency band, carrying only a propagating TE_{10}. However, both TE_{10} and TE_{20} modes can propagate in the enlarged middle section and provide the power division functionality. Therefore, equal power division, and 90° of phase difference between the output ports at the central frequency is required, along with low return loss and high isolation for the largest frequency band.

4.1.1 SIW 3-dB coupler state-of-the-art

Different kinds of 3-dB couplers were treated in the literature, such as short-slot, cruciform, HMSIW (half-mode SIW) and FHMSIW (folded half-mode SIW), as reported in [2]–[8].

In [2], a 10.5 GHz single-balanced mixer is designed using a 90° SIW 3-dB coupler, while in [3] and [4] 3-dB 60-GHz and 9 GHz SIW short-slot couplers are fabricated by a standard single layer print circuit board process, which is more economical for mass-production than the advanced processes such as LTCC and thick-film process, and so on. The three couplers use the short-slot technique.

A 24 GHz cruciform coupler consisting of a simple cross-over of two SIW sections with two inductive metallic posts in a square junction, is reported in [6]. A similar one is reported in [8] where the central portion is partially etched to act as an impedance transformer and mirror.

In the microwave band, SIW couplers suffer from their big size. In [5] and [7] HMSIW and FHMSIW 3-dB couplers are proposed providing nearly a half reduction in size as compared to a conventional SIW coupler.

The performance of all the SIW couplers are listed in Table 4-4. The IL, amplitude and phase imbalance are taken at the central frequency. The relative BW is considered for frequencies where the RL is better than 10 dB.

Reference	IL (dB)	BW (%)(GHz)	Amp. imb. (dB)	Phase imb. (°)	Size $(mm^2)(\lambda_0{}^2)$	f (GHz)
[2] short-slot	1	63.8 8-14.7	1	3.4	36.8·29.3 1.32	10.5
[3] short-slot	0.3	>34.5 46.3-67	0.4	11	5.1·5.34 1.09	60
[4] short-slot	0.8 @9.5 GHz	12.2 8-9.1	2.1	3	4·26.1 0.94	9
[6] cruciform	1.45	>16.7 22-26	0.3	0.2	N.A.	24
[8] cruciform	0.65	33.33 20-28	0.9	4	N.A.	24
[5] half-mode	1	>40 10-15	0.5	2.5	31.6·13.25 0.73	12.5
[7] folded half-mode	1	>42.1 7.5-11.5	0.7	0.6	43.4·10.2 0.44	9.5
Our (4.1.2) short-slot	0.25	>26.8% 24.5-32	0.1	2.3	9.66·7.48 0.63	28

Table 4-4: Summary of SIW 3-dB coupler state-of-the-art

Our short-slot 3-dB coupler results in lowest insertion loss and amplitude imbalance as compared to the state-of-the-art, equal to 0.25 dB and 0.1 dB, respectively. The relative bandwidth, phase imbalance and size remain very competitive with the state-of-the-art.

4.1.2 Design and results

A picture of our fabricated short-slot 3-dB coupler along with its E-field is depicted in Figure 4-1.

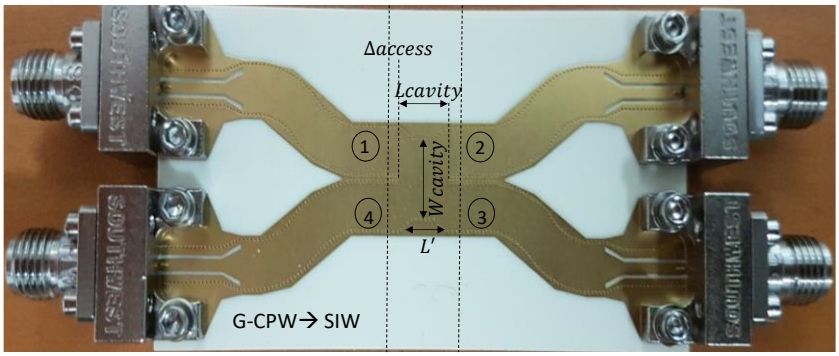

Reference planes

(a)

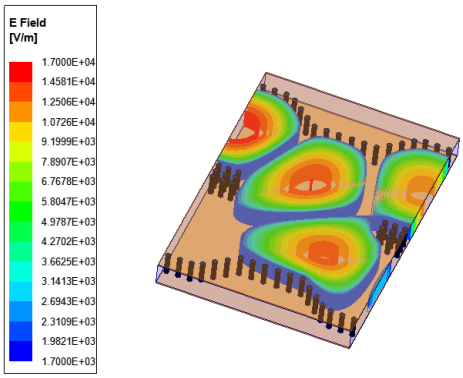

(b)

Figure 4-1: Short-slot SIW 3-dB coupler: (a) dimensions and coupler with G-CPW accesses and (b) E-field

The via diameter (D) and the center-to-center distance between vias (p) are equal to 0.2 mm and 0.45 mm. W_{cavity}, L_{cavity}, $\Delta acces$ and L' are 7.15 mm, 5.48 mm, 1.01 mm and 3.72 mm, respectively. The total length is 7.48 mm and the total width is 9.66 mm, without feeding lines. The G-CPW to SIW feeding accesses (glimpsed through Figure 4-1(a)) were de-embedded with TRL after a SOLT calibration, in the same way as discussed in Chapter III. Due to connectors size, there was a need for bending the accesses. The choice was made to have the SIW bent instead of the G-CPW, so that the field was not distorted by the windings. The resulting TRL samples are displayed in Figure 4-2. The amplitude and phase results are shown in Figure 4-3, between 16 GHz and 32 GHz.

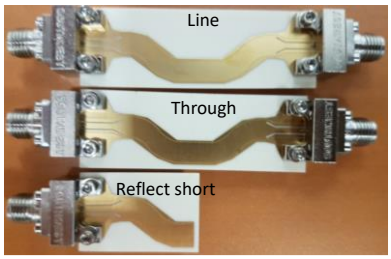

Figure 4-2:TRL de-embedding samples

The measurements (solid lines) were made with the same connectors as for the 1-bit phase shifter 4, and they are plotted and compared with original substrate (dotted lines) and re-optimized (circled lines) substrate simulations, as discussed in Chapter III. All the devices measurements, in this chapter, were carried out on an Anritsu 145 GHz ME7838D4 VNA.

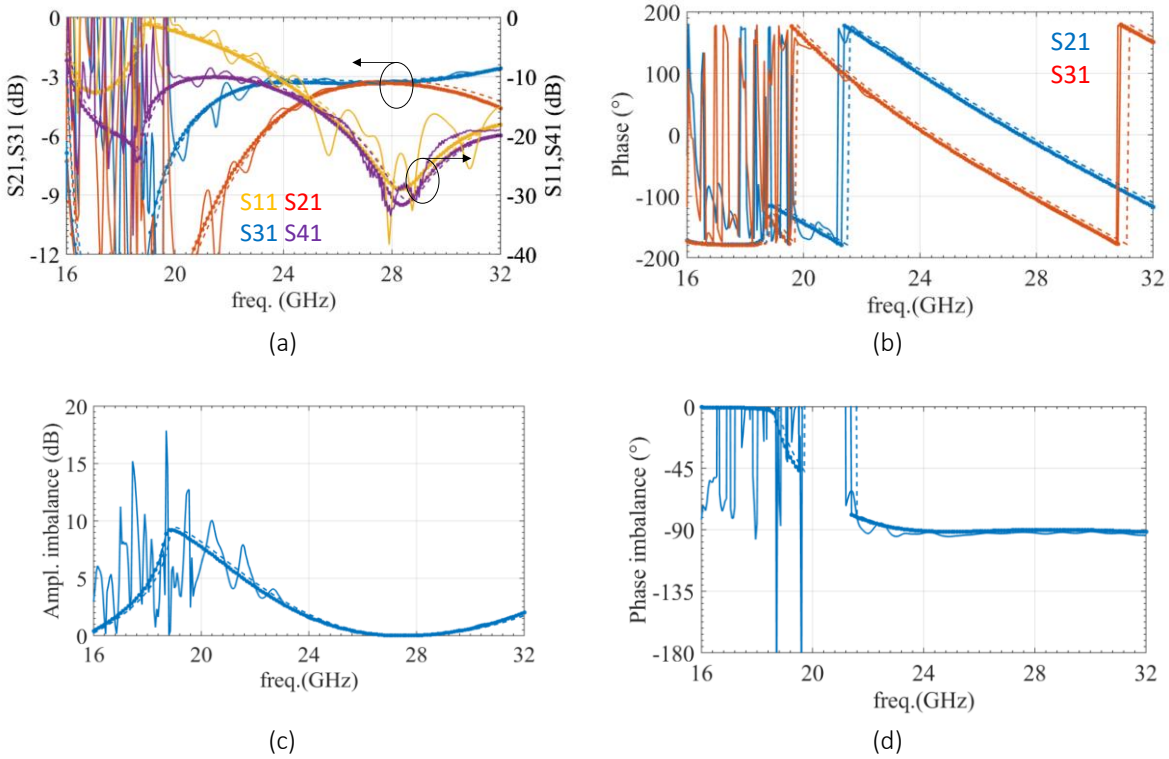

Figure 4-3:Short-slot coupler measured and simulated results: (a) amplitude , (b) phase, (c) amplitude imbalance and (d) phase imbalance. De-embedded measurements (straight line), simulations with original substrate ε_r=3.55 (dotted lines), simulations with re-optimized substrate ε_r=3.64 (circled lines).

As it can be noticed, the amplitude imbalance is 0.1 dB, being S_{21} and S_{31} equal to -3.3 dB and -3.2 dB, at 28 GHz, while remaining lower than 1 dB in the 20.7% the relative BW (24.7 GHz up to 30.5 GHz). The RL and isolation are lower than 30 dB, at 28 GHz, and they remain better than 10 dB between 24.5 GHz and 32 GHz (>26.8% of relative BW). The latter defines the bandwidth of the device. The phase of $S_{21}$and $S_{31}$are -14.7° and -107°, respectively, making the phase imbalance be equal to -2.3° at 28 GHz, while it remains within ±3° between 22.7 GHz and 32 GHz (>33.2% of relative BW). The measurements show a good agreement with simulations, are at the state-of-the-art (see Table 4-4) and respect the drastic conditions exampling the sensitivity study in Chapter II.

4.2 Short-slot 0-dB SIW coupler and requirements

The short-slot crossover, or also named 0-dB coupler, presents a similar topology as the short-slot coupler. It is used to convey all input power to the diametrically opposite output port. The width of its section should be, in the best case, equal to the one of the coupler, while the length is bigger. Thus, the short-slot crossover utilizes the same concept as short-slot coupler, but with a bigger longitudinal size. As possible, the lowest return loss and direct transmission are required for the largest frequency band. When the direct transmission is not null, a 90° phase difference between the direct and coupled output ports should occur, at the central frequency.

4.2.1 SIW 0-dB coupler state-of-the-art

Different types of 0-dB couplers were found in the literature, such as crossover junction, short-slot, cruciform and FSIW (folded SIW), as reported in [3], [9]–[13].

In [9], a 60 GHz crossover is composed of four-arms waveguide section connected by a central junction, with extremely low insertion loss but unfortunately no size information. Its topology is not suitable to our own system. In [3], [12], [13] two 60 GHz and one 30 GHz crossovers were designed with the short-slot technique, showing interestingly low insertion loss, given the considered frequencies. A compact cruciform crossover was fabricated at 12.5 GHz in [10], and a FSIW crossover was simulated at 14.9 GHz, as reported in [11], but were not considered suitable as well for our application.

The performance of all the SIW crossovers are listed in Table 4-4. The IL, the phase and direct transmission are taken at the central frequency and the relative BW is considered for frequencies where the RL is better than 10 dB.

Reference	IL $(-\lvert S_{31}\rvert)$ (dB)	Direct transmission $(-\lvert S_{21}\rvert)$(dB)	BW (%) (GHz)	Phase $\angle S_{31}$ (°)	Size (mm^2) $(\lambda_0{}^2)$	f (GHz)
[9] central junction	0.15	35	>15 55-64	N.A.	N.A.	60
[3] short slot	0.35	28	>26.7 51-67	-62	8.4·5.44 1.83	60
[12]* short slot	0.58	18	>11.7 57-64	-44.5	7.35·6.08 1.79	60
[13]* short slot	0.45	45	>13.3 28-32	N.A.	N.A.	30
[10] cruciform	0.15	>20	36 10-14.5	-121.6	56.7·25.2 2.48	12.5
[11]* folded	0.13	30.7	1 14.82-14.97	N.A.	45·10.3 1.14	14.9
Our (4.2.2) short-slot	0.5	30	35.7 20.1-30.1	-78.5	9.66·13.72 1.15	28

(*) Simulated results

Table 4-5: Summary of SIW 0-dB coupler state-of-the-art

Our short-slot 0-dB coupler results in very low size and high relative bandwidth as compared to the state-of-the-art, while the rest of the parameters comply with the state-of-the-art.

4.2.2 Design and results

A picture of the fabricated short-slot 0-dB coupler (crossover) along with its E-field is depicted in Figure 4-4.

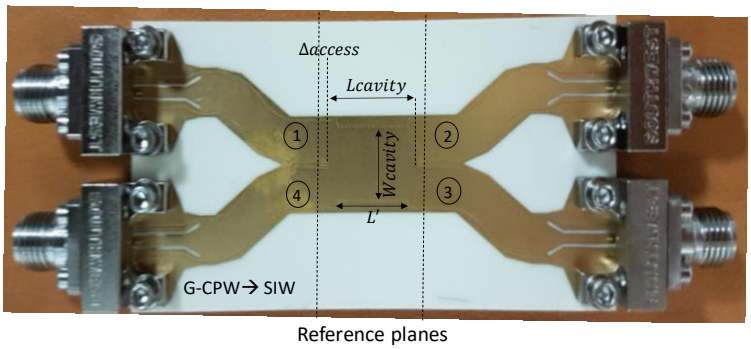

(a)

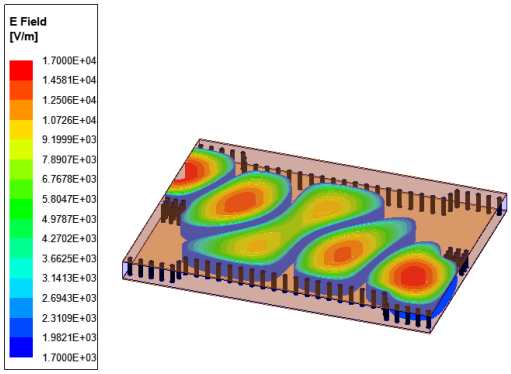

(b)

Figure 4-4: Short-slot SIW 0-dB coupler: (a) dimensions and crossover with G-CPW accesses and (b) E-field

D and p are the same as for the 3-dB coupler. W_{cavity}, L_{cavity}, $\Delta acces$ and L' are 7.75 mm, 11.72 mm, 1 mm and 9 mm, respectively. The total length is 13.72 mm and the total width is 9.66 mm, without feeding lines. The width of the cavity has been chosen equal to 7.75 mm as recommended in Chapter II for its good direct transmission. The G-CPW to SIW feeding accesses and TRL samples are the same as for the coupler. The amplitude and phase results are shown in Figure 4-5, between 16 GHz and 32 GHz. The measurements (solid lines) are plotted and compared with original substrate (dotted lines) and re-optimized (circled lines) substrate simulations.

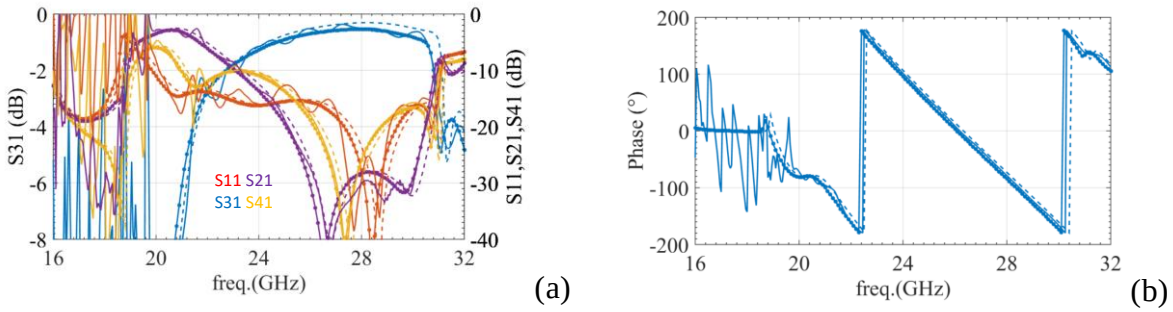

(a) (b)

Figure 4-5:Short-slot crossover measured and simulated results: (a) amplitude , (b) phase. De-embedded measurements (straight line), simulations with original substrate ε_r=3.55 (dotted lines), simulations with re-optimized substrate ε_r=3.64 (circled lines).

As it can be noticed, the measurements are in a good agreement with simulations. The measured insertion loss is 0.5 dB, at 28 GHz, while reducing by 1 dB between 23.5 GHz up to 30.7 GHz (25.7% of relative BW). The return loss and isolation are 23.5 dB and 29.8 dB at 28 GHz, respectively; the return loss remains better than 10 dB between 20.1 GHz and

30.1 GHz (35.7% of relative BW), while the isolation is better than 10 dB between 23.4 GHz and 31.2 GHz (27.9% of relative BW). The level of direct transmission is very important, as explained in Chapter II, and it is equal to 30 dB at 28 GHz, which represents a very good result, and it is better than 10 dB between 23.3 GHz and 30.9 GHz (27.1% of relative BW). In Chapter II, simulations had been carried out with full walls whereas in this case, regular vias are used which may explain an equivalent cavity width slightly wider, resulting, on the basis of Table 2.1, to a small degradation of the direct transmission. The measured phase of S_{31} is equal to -78.5° at 28 GHz, and it remains within ±10° only between 27.75 GHz and 28.25 GHz (1.8% of relative BW). That shows a quite big dispersion of the device. The aforementioned absolute phase is very important, because all the phase shifters (introduced in the next- section) were designed according to this value, so that the output BM phase imbalance is minimized, at the end.

4.3 Phase shifters for proof-of-concept: design and optimization

In this paragraph, fabricated and measured phase shifters for BM system are introduced.

Each single 1-bit SIW PS is, here, replaced by two fixed PSs that represent its ways 1 and 2, at each time. Indeed, the PIN diodes "ON" are replaced by metal strips, whereas the slots with PIN diodes "OFF" are left free. The PS4 was also conceived as not reconfigurable, so as to fabricate the whole BM as two not reconfigurable systems, to provide a proof-of-concept. This way of doing was enabling to test separately 28-GHz tunable PS4 (see Chapter III) and the concept of extended beam matrix to dissociate the causes of eventual issues.The phase shift values to be obtained for the four PSs, and their place in the beam forming network are displayed in Figure 4-6, according to the previous crossover measured phases. The coupler phases are, in this picture, adjusted as -15° and -105° (instead of -14.7° and -107°), for sake of simplicity.

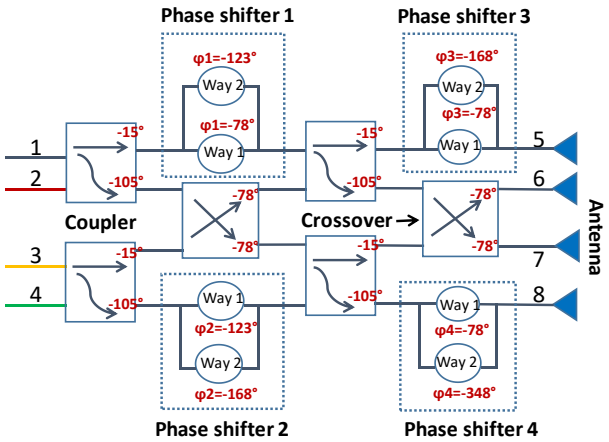

Figure 4-6: PSs place in the BM and their targeted phase shift according to crossover output phases.

A 3D layout view of the four designed SIW PSs and their E-fields, at 28GHz, is shown in Figure 4-7 for the two ways.

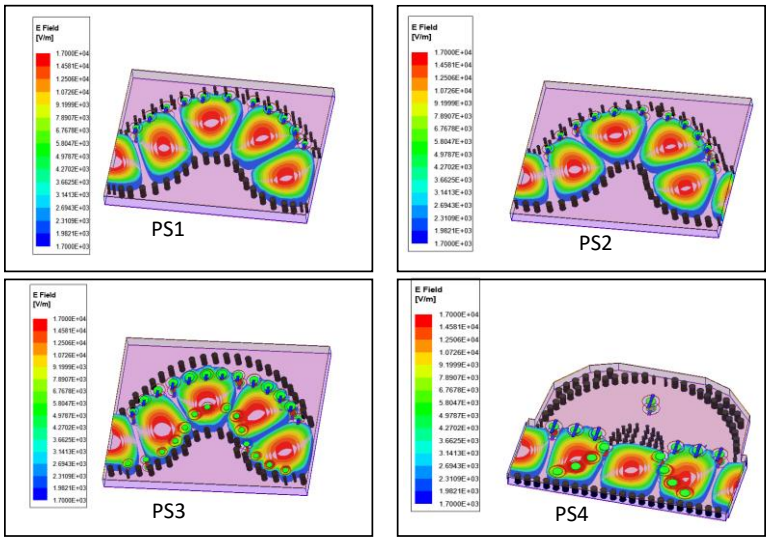

(a)

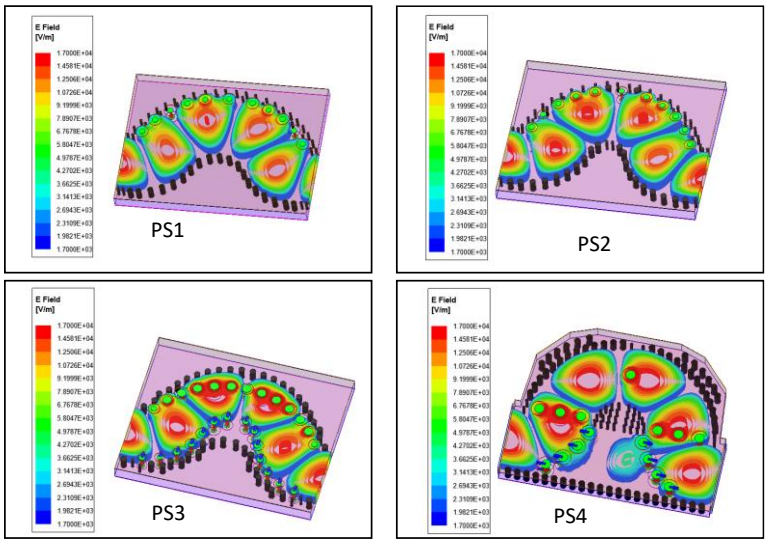

(b)

Figure 4-7: Four designed PS's (a) path 1E-field and (b) path 2 E-field

It is important, before focusing on the specific design method employed for each PS, to start with a general comment on the vias diameter and the size of the slot around the floating vias. For all the PSs, the regular and floating vias were used with diameters equal to either 200 µm or 400 µm, according to the geometry of the circuit in question. Vias were not optimized one by one but the following methodology was adopted: 400 µm by default except when the design rules led no choice except reducing the diameter of the internal vias (example of PS1, PS2 internal upper walls and PS3 internal bottom walls). Then in order to improve the sensitivity on the phase difference between path 1 and path 2 for PS1 and PS2 (that is only 45°), the external vias diameter was reduced as well, which enabled better accuracy in the phase adjustment (PS1 and PS2 external upper walls). Finally, in PS1, PS2 and PS3, the diameter of some external vias (external bottom wall) was decreased down to 200 µm for fine phase tuning and/or avoid vanishing waves. The latter was also the reason for using 200 µm as diameter for middle regular vias in PS4. The circular slots are placed both on the upper and lower metal layers of the SIW and they have to be properly sized, otherwise the signal would be partially reflected (strong capacitive effect), as explained in Chapter III. Moreover, for vias that are

placed on the external part of the signal path, the influence of the slot size on the results is smaller, because the E-field amplitude is weaker there. Obviously, there is some limit. By increasing the size of the slots in a disproportionate way (i.e. anti-pad or gap bigger than 350 µm), an increase in the phase shift is also observed due to H-field outside the structure. In that case, only magnetic energy is stored in this outside part and the structure becomes a sort of slow wave structure as the slot-type SIWs: the return loss level does not change but its shape is slightly shifted in frequency. Hence, the value of the gap depends on the position of the considered via and the decision on its size might be more or less stringent while designing.

Let's focus now on the various methodology developed to design the phase shifters.

For PS1 and PS2, concerned by a small phase difference of 45° between ways 1 and 2, and contrarily to PS4, it was not possible to design a parallel physical path, because of the technology constraints (minimum signal trace of 100 µm). That way, PS1 and PS2 have been designed by using another technique. First, on the basis of the crossover physical length, their respective length was bent to obtain -78° and -123° of absolute phase shift for PS1 and PS2, respectively. This is for path 1, when the metal strips are placed between the floating vias and the metallic layers of the SIW. On the contrary, when the metal strips are removed, the new width of the SIW along the turn increases till the upper external wall (path 2). As a consequence, the signal phase will be delayed to $-123°$ and $-168°$ for PS1 and PS2, respectively. This is due to an inherent property of the rectangular waveguides for which cut-off frequency depends on their width so that their phase constant, β, is higher for bigger widths (even if the slope of $\beta(f)$ stays the same). The latter solution is very suited for this kind of geometry, but it generates a shift to lower frequency of the excitation of the TE_{10} mode (propagation constant β starts from a lower frequency) with the consequent shift of the best matching frequency, as it will be noticed later in the results. Concerning PS1, the gap surrounding the vias was chosen to be equal to 250 µm and the floating vias have a diameter equal to 200 µm as already mentioned. Instead for PS2, the gap was chosen to be equal to 200 µm whilst the floating vias have a diameter equal to 200 µm as well.

PS3 has been designed with a different technique due to the higher phase shift to provide. In fact, two physical paths were designed showing, in the meantime, a change in the path width, which means that two degrees of freedom are, here, available. The absolute phase shift has to be equal to -78° and -168°, according to the path that we activated. The influence of the gap value becomes here more relevant because the slots are placed in the inner part of the signal paths, where the E-field is stronger. As already said, the floating vias have a diameter equal to 200 µm or 400 µm, according to the geometry of the circuit. The upper middle slots (see Figure 4-7) have a gap that was chosen to be equal to 150 µm and 200 µm elsewhere, whereas the two middle bottom slots are 200 µm and the other slots elsewhere are 250 µm and 150 µm. Indeed, this SIW PS configuration is more sensitive to the leakage through the upper floating vias so that more floating vias were needed to compensate for, which could not be reached with large slots (design rules could not be respected).

Concerning PS4, it is now a fixed one, either with metal strips, either without, contrarily to the tunable PS of Chapter III, so that its topology had to be adapted a little bit. PS4 results in the most complex device to be designed because of the -270° of required relative phase shift,

from -78° to -348°. That is why it was preferred to use an almost constant width for both the paths, so that we could have, as much as possible, a symmetry in the frequency range around 28 GHz. This resulted in only one degree of freedom to play on phase tuning. Design methodology is the same as in Chapter III. However, as explained in Chapter III, when path 1is activated, a leakage causes a standing wave to appear in the path of path 2, showing some resonance, and in turn, loss in the transmission path. In the reconfigurable version this resonance is shifted out of band thanks to the PIN diode reverse biasing capacitance. Unfortunately, when PIN diodes are replaced by metal strips, the standing wave occurs close to 28 GHz. A solution to kill it consists in placing a floating via (shorted with metal strips when path 1is aimed at, and open when path 2 is targeted) in the middle of the path inherent to path 2, with a consequent loss of signal when path 2 is targeted. Moreover, metal strips were doubled for this purpose. Otherwise, all the floating vias have a diameter equal to 400 µm, as the regular vias. Their gap was chosen to be equal to 225 µm, to increase the absolute phase.

In the next step, fabricated and measured PSs are going to be presented.

4.3.1 Phase shifter 1: layout and results

The fabricated PS1s (path 1 and 2) are depicted in Figure 4-8, along with a sketch of the propagating E-field wave to better figure out the working principle of the device.

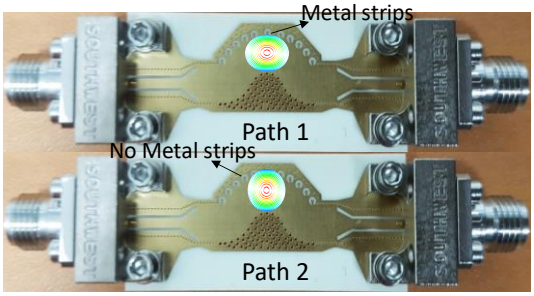

Figure 4-8:Phase shifter 1 path 1 and phase shifter 1 path 2

The VNA was calibrated directly at the input and output of the PSs, through the TRL samples shown in Figure 4-9.

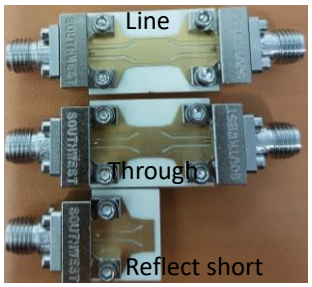

Figure 4-9:Not reconfigurable phase shifters TRL samples

The measurements (solid lines) are plotted and compared with original substrate (dotted lines) and re-optimized (circled lines) substrate simulations for path 1 and path 2, as shown in Figure 4-10. As it can be noticed, there is a shift in the return loss shape among ways 1 and 2, as predicted earlier. Concerning path 1, the return loss is better than 30 dB, while the insertion

loss is equal to 0.56 dB, at 28 GHz. The return loss remains better than 10 dB between 19.5 GHz and more than 32 GHz (44.6% of relative BW). Concerning path 2, the return loss is 20.8 dB, while the insertion loss is equal to 0.66 dB, at 28 GHz. The return loss is better than 10 dB between 19 GHz and 31.6 GHz (45% of relative BW). The absolute phases are -92.3° and -131.5°, whereas, from the theory, they should be -78° and -123° for path 1and 2, respectively. That means an error of about 14° which could impact the phase imbalance at the BM output. This will be checked at the final end. The phase difference between path 1and path 2 is -39.2°, instead of -45° as required. The latter one remains among +1° and -5°, around the value at 28 GHz, between 21 GHz and 30.4 GHz (33.5% of relative BW). The FoM is 59.4 °/dB.

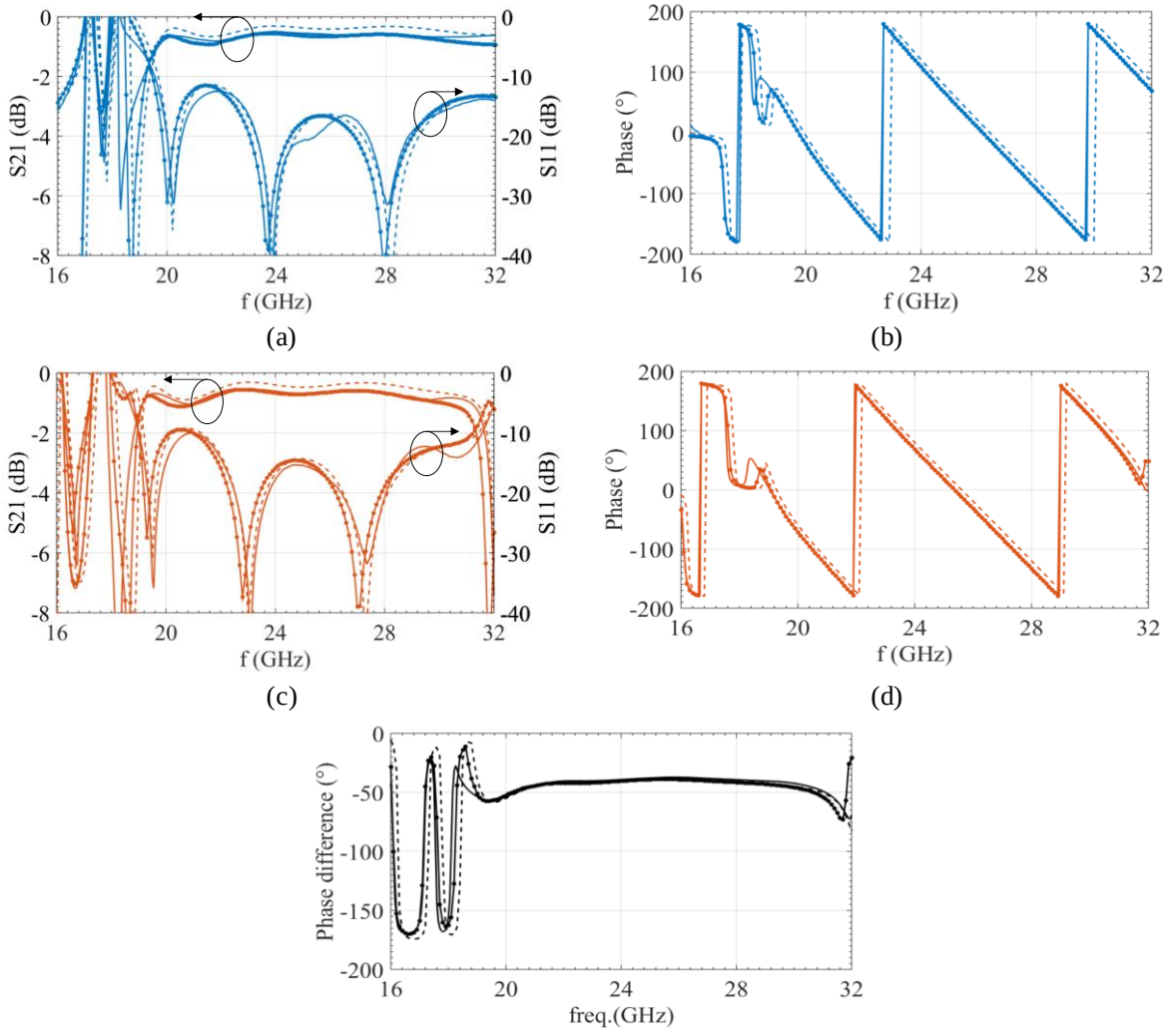

Figure 4-10: PS1s : (a) amplitude path 1, (b) phase path 1, (c) amplitude path 2, (d) phase path 2 and (e)phase difference. Measurements (straight line), simulations with original substrate ε_r=3.55 (dotted lines), simulations with re-optimized substrate ε_r=3.64 (circled lines).

4.3.2 Phase shifter 2: layout and results

The fabricated PS2s (ways 1 and 2) are depicted in Figure 4-11 and measured the same way as PS1s.

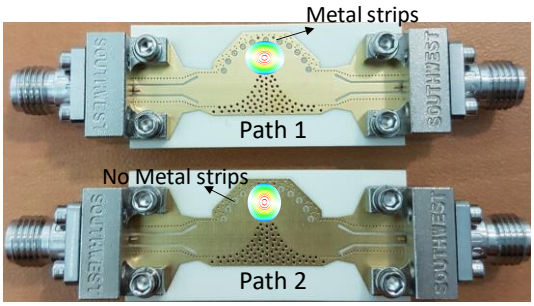

Figure 4-11:Phase shifter 2 path 1and phase shifter 2 path 2

The measurements (solid lines) are plotted and compared with original substrate (dotted lines) and re-optimized (circled lines) substrate simulations for path 1 and path 2, as shown in Figure 4-12. Even here there is a shift in the return loss shape among path 1 and 2. Concerning path 1, the return loss is 24.7 dB, while the insertion loss is equal to 0.64 dB, at 28 GHz. The return loss remains better than 10 dB between 19.4 GHz and more than 32 GHz (45% of relative BW). Concerning path 2, the return loss is 16.9 dB, while the insertion loss is equal to 0.77 dB, at 28 GHz. The return loss remains better than 10 dB between 21.6 GHz and more than 32 GHz (37.1% of relative BW). The absolute phases are -137.5° and -178.6°, whereas, from the theory, they should be -123° and -168° for path 1and 2, respectively. That is to say, the same kind of difference than in PS1. The phase difference between path 1and path 2 is -41.1°, instead of −45° as required. The latter one remains among +0.9° and -5°, around the value at 28 GHz, between 21.3 GHz and 30.3 GHz (32.2% of relative BW). The FoM is equal to 53.4°/dB.

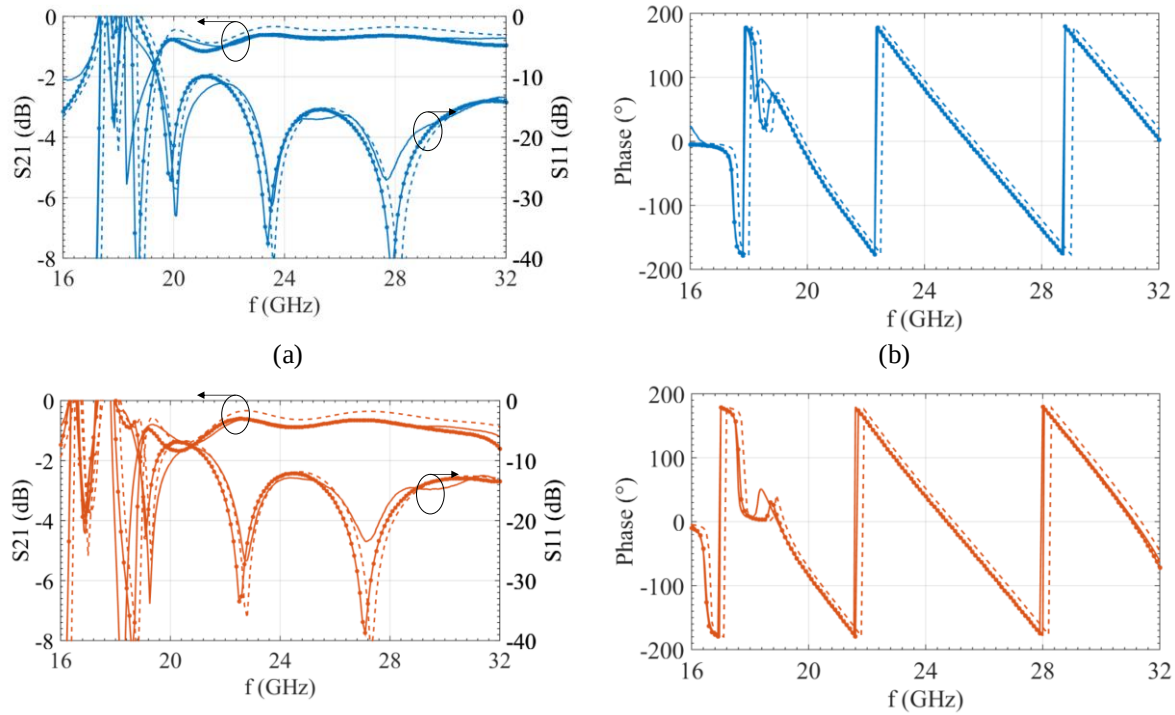

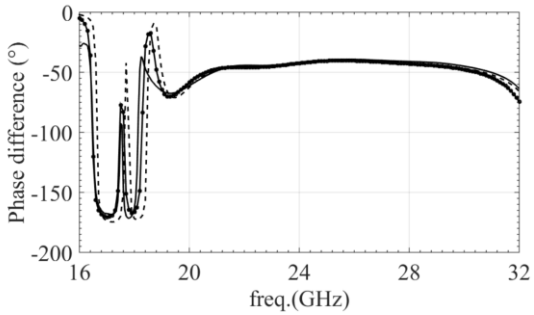

(e)

Figure 4-12: PSs 2 : (a) amplitude path 1, (b) phase path 1, (c) amplitude path 2, (d) phase path 2 and (e) phase difference. Measurements (straight line), simulations with original substrate ε_r=3.55 (dotted lines), simulations with re-optimized substrate ε_r=3.64 (circled lines).

4.3.3 Phase shifter 3: layout and results

The fabricated PS3s (ways 1 and 2) are depicted in Figure 4-13.

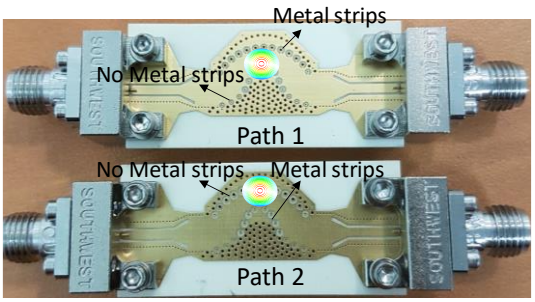

Figure 4-13:Phase shifter 3 path 1and phase shifter 3 path 2

The measurements (solid lines) are plotted and compared with original substrate (dotted lines) and re-optimized (circled lines) substrate simulations for path 1and path 2, as shown in Figure 4-14. Concerning path 1, the return loss is 28.8 dB, while the insertion loss is equal to 0.72 dB, at 28 GHz. The return loss remains better than 10 dB between 19.6 GHz and more than 32 GHz (44.3% of relative BW). Concerning path 2, the return loss is 15 dB, while the insertion loss is equal to 1 dB, at 28 GHz. The return loss remains better than 10 dB between 22.1 GHz and more than 32 GHz (35.4% of relative BW). The absolute phases are -85.6° and $-177°$, whereas, from the theory, they should be -78° and -168° for path 1and 2, respectively, that is to say about 8° of additional delay. The phase difference between path 1and path 2 is -91.4°, instead of -90° as required. The latter one remains among ±5°, around the value at 28 GHz, between 27.25 GHz and 28.85 GHz (5.71% of relative BW), which is much smaller than PS1 and PS2 relative BW, because here two signal paths were addressed; in fact, we changed both the SIW length L and width W. That makes a large BW difficult to be obtained. Indeed, we should consider a useful BW going from 27 GHz up to 29 GHz, at the most, which should not be a problem for 5G at 28 GHz. On the contrary, the FoM is bigger than for PS1 and PS2 and it is equal to 91.4°/dB.

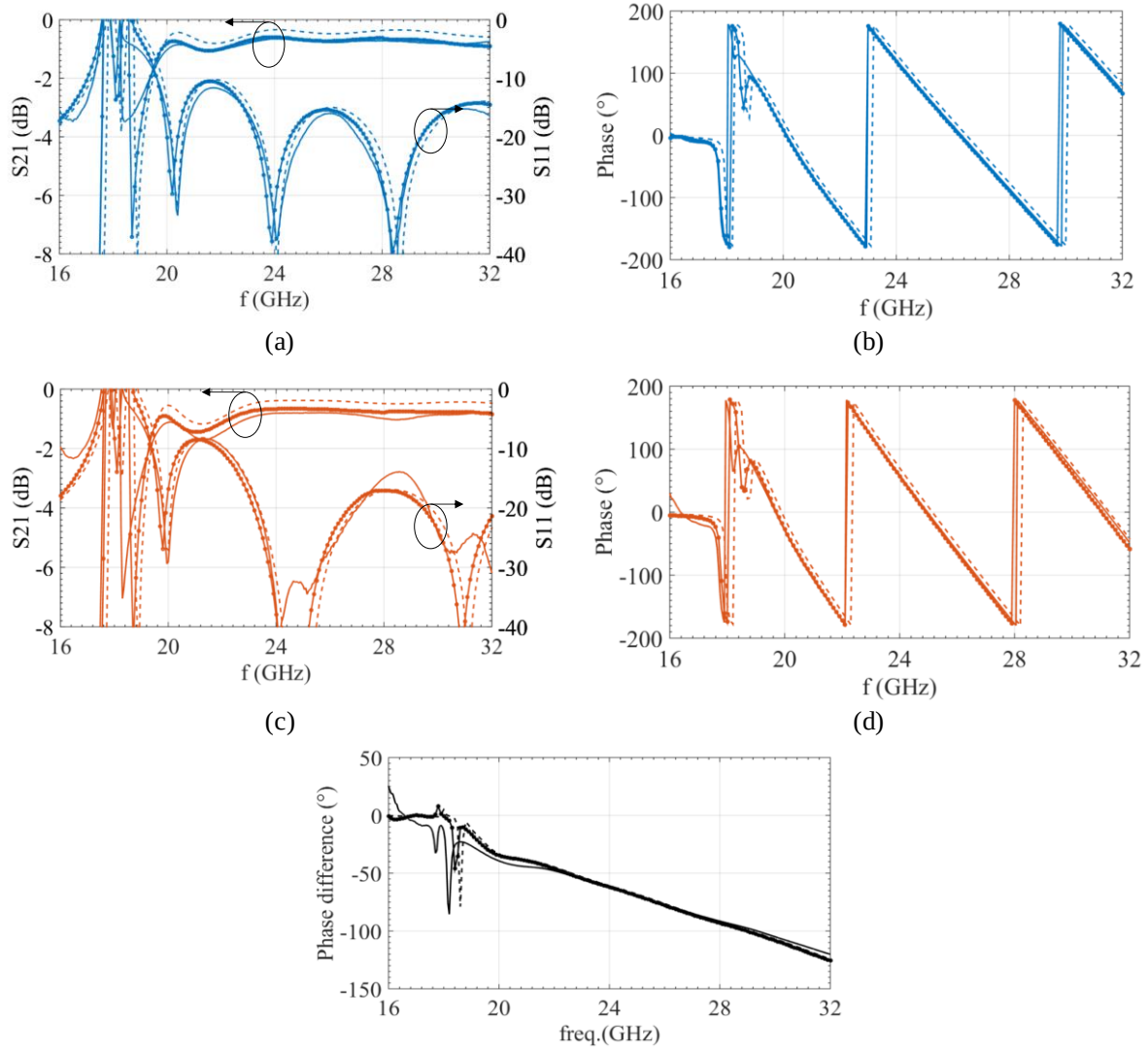

Figure 4-14: PSs 3 : (a) amplitude path 1, (b) phase path 1, (c) amplitude path 2, (d) phase path 2 and (e) phase difference. Measurements (straight line), simulations with original substrate ε_r=3.55 (dotted lines), simulations with re-optimized substrate ε_r=3.64 (circled lines).

4.3.4 Phase shifter 4: layout and results

The fabricated PS4s (ways 1 and 2) are depicted in Figure 4-15.

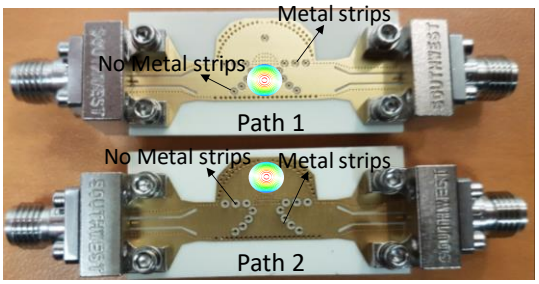

Figure 4-15:Phase shifter 4 path 1and phase shifter 4 path 2

The measurements (solid lines) are plotted and compared with original substrate (dotted lines) and re-optimized (circled lines) substrate simulations for path 1and path 2, as shown in

Figure 4-16. Concerning path 1, the measured return loss is 27.5 dB, while the insertion loss is equal to 0.69 dB, at 28 GHz. The return loss remains better than 10 dB between 20.8 GHz and more than 32 GHz (40% of relative BW). Concerning path 2, the measured return loss is 20.5 dB, while the insertion loss is equal to 0.93 dB, at 28 GHz. The return loss remains better than 10 dB between 23.8 GHz and 30.5 GHz (23.9% of relative BW). The absolute phases are +22.3° and -256°, whereas, from the theory, they should be -78° and -348° for paths 1 and 2, respectively. That is to say about 100° delay less to be compensated afterwards. The phase difference between path 1and path 2 is -278°, instead of -270°, as required. The latter one remains among ±5°, around the value at 28 GHz, between 27.75 GHz and 28.25 GHz (1.8% of relative BW), even smaller than PS3 because the difference in length L among the two SIW paths is bigger. That might dramatically reduce the overall BW of the system. Anyway, the latter point will be discussed later on, when the measurement results of the BM will be introduced. The FoM is almost equal to 300°/dB.

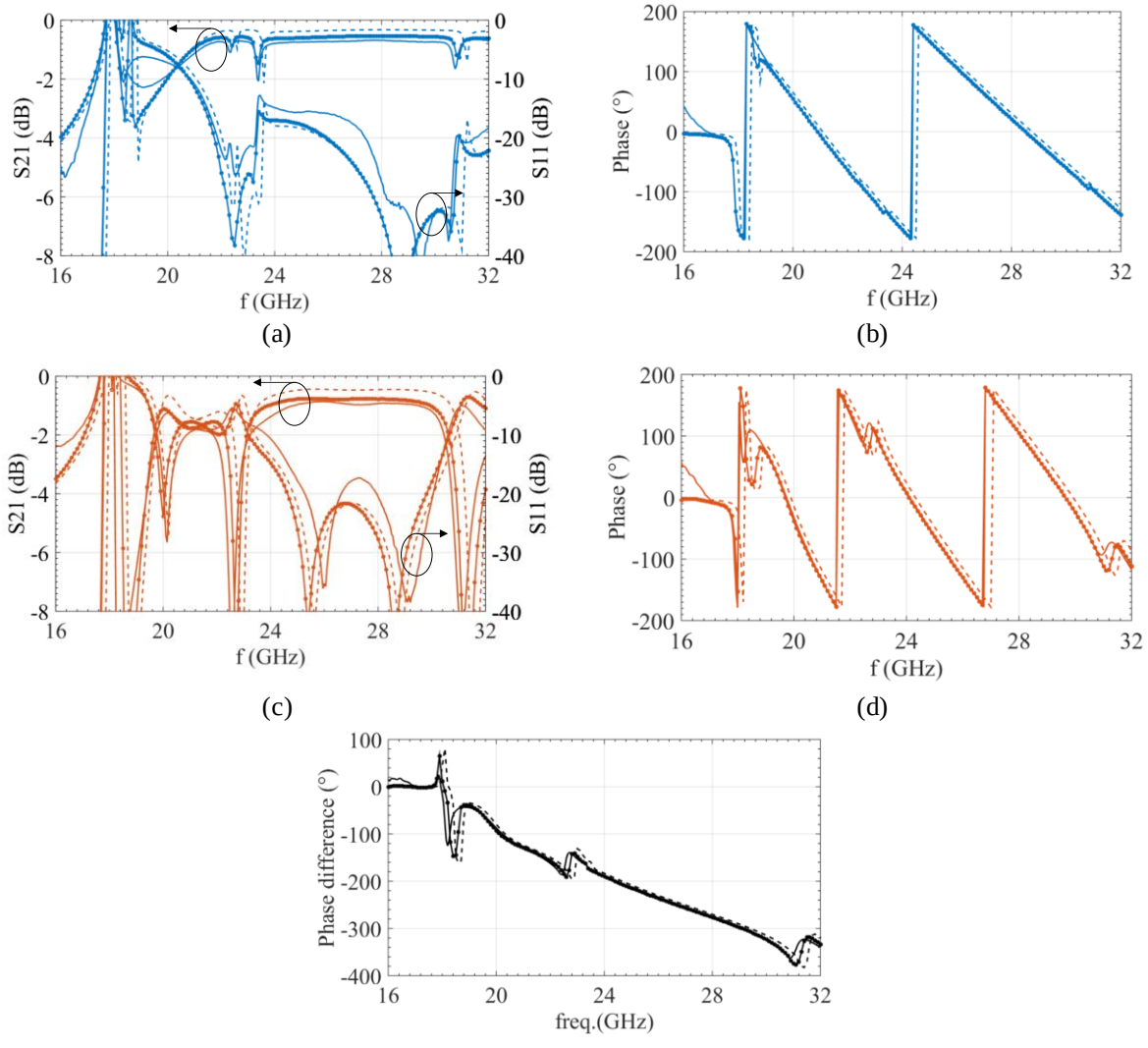

Figure 4-16: PSs 4 : (a) amplitude path 1, (b) phase path 1, (c) amplitude path 2, (d) phase path 2 and (e) phase difference. Measurements (straight line), simulations with original substrate ε_r=3.55 (dotted lines), simulations with re-optimized substrate ε_r=3.64 (circled lines).

As it can be noticed, the absolute phases do not fulfill the requirements because of the difficult design that we addressed. SIW delay lines -100° phase compensators are needed to comply with the requirements.

4.3.5 Delay lines for phase compensation

The delay lines to compensate for the PS4 absolute phase are depicted in Figure 4-17. They exploit the same technique used for PS1 and PS2. The reference was associated with BM output ports 5, 6 and 7 while the -100° lagged line was associated to port 8.

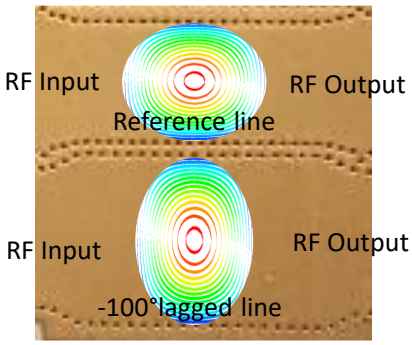

Figure 4-17: Reference line and delayed lines without access and with their E-field shape

Again, the measurements (solid lines) are plotted and compared with original substrate (dotted lines) and re-optimized (circled lines) substrate simulations, as shown in Figure 4-18. As regards the reference line, the measured return loss is 28.5 dB, while the insertion loss is equal to 0.34 dB, at 28 GHz. The return loss remains better than 10 dB between 22.3 GHz and more than 32 GHz (34.6% of relative BW). As regards the lagged line, the measured return loss is 19.1 dB, while the insertion loss is equal to 0.35 dB, at 28 GHz. The return loss remains better than 10 dB between 21 GHz and more than 32 GHz (39.3% of relative BW). The absolute phases are -65.2° and -170.5°, that allow to comply with initial requirements. The phase difference is -105.3°, instead of -100°, as required. The latter one remains among ±5° around the value at 28 GHz, between 27.3 GHz and 28.75 GHz (5.2% of relative BW), which is smaller than PS1 and PS2 relative BW, because the difference in width *W* among the two SIW paths is, now, bigger (45° against 100° phase difference).

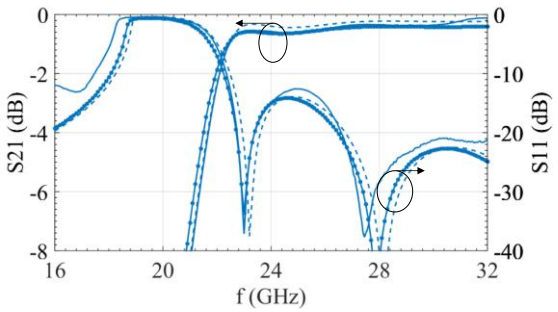

(a)

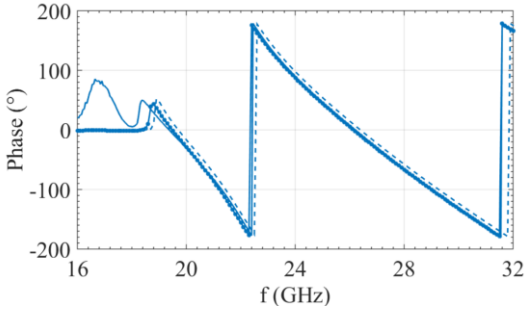

(b)

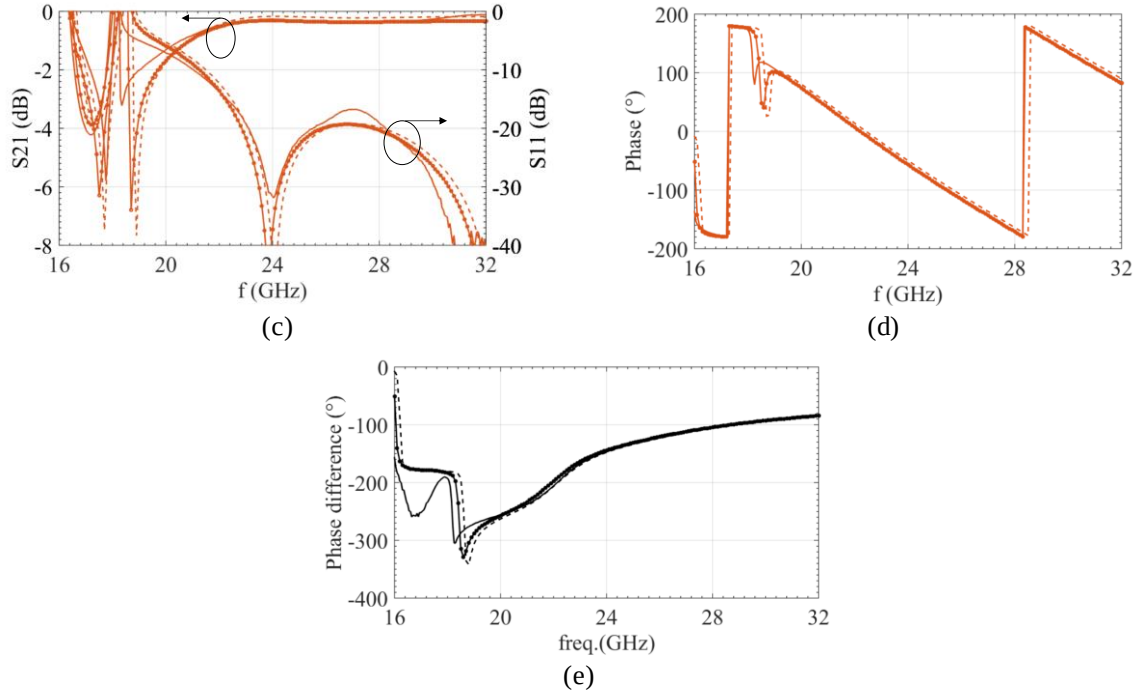

Figure 4-18: Delay lines: (a) reference line amplitude, (b)reference line phase , (c)delayed line amplitude, (d) delayed line phase and (e) phase difference. Measurements (straight line), simulations with original substrate ε_r=3.55 (dotted lines), simulations with re-optimized substrate ε_r=3.64 (circled lines).

On the overall, the measured phase shifters and associated with delay lines are in good agreement with the re-optimized simulated results. All the requirements are quite well fulfilled. The next step is to realize the full BM system, by exploiting the design blocks we dealt with, so far.

4.4 Full Butler matrix system: layout, simulation and measurements

As a proof-of-concept, two Butler matrices have been fabricated using the aforementioned design blocks, which provide 8 different progressive output phases, each matrix providing 4 of them. Two Butler matrices were needed because the phase shifters are not reconfigurable and for each BM a particular combination of those must be provided, according to Table 4-6. The working principle of that table was already explained in Chapter II. To better figure out the flow of the RF signal going through the BM 1, its HFSS E-field is depicted in Figure 4-19.

Port	Butler Matrix	PS 1		PS 2		PS 3		PS 4		PoP* (°)	θ (°)
Path 1: ON/OFF Path 2: ON/OFF	/	Path 1	Path 2	Path 1	Path 2	Path 1	Path 2	Path 1	Path 2	/	/
1	BM 1	ON	OFF	n/p	n/p	OFF	ON	OFF	ON	0	**0**
	BM 2	OFF	ON	n/p	n/p	ON	OFF	ON	OFF	-45	**14.6**
2	BM 1	ON	OFF	n/p	n/p	OFF	ON	OFF	ON	±180	**±90**
	BM 2	OFF	ON	n/p	n/p	ON	OFF	ON	OFF	135	**-48.5**
3	BM 1	n/p	n/p	OFF	ON	OFF	ON	OFF	ON	-90	**30**
	BM 2	n/p	n/p	ON	OFF	ON	OFF	ON	OFF	-135	**48.5**

4	BM 1	n/p	n/p	OFF	ON	OFF	ON	OFF	ON	90	**-30**
	BM 2	n/p	n/p	ON	OFF	ON	OFF	ON	OFF	45	**-14.6**

*PoP: progressive output phases

Table 4-6: Extended beam BM combinations for enhanced spatial agility

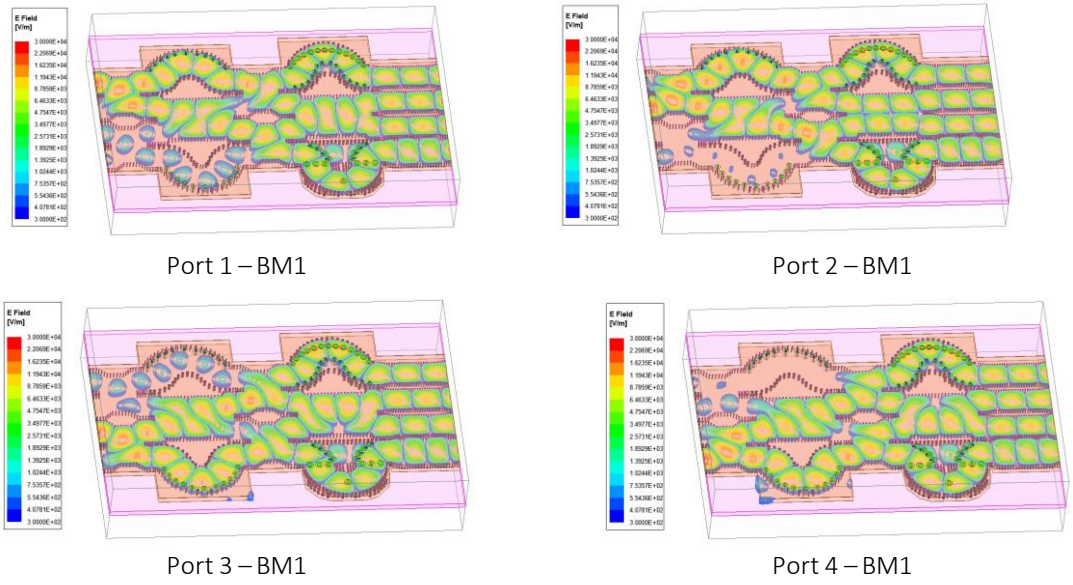

Port 1 – BM1 Port 2 – BM1

Port 3 – BM1 Port 4 – BM1

(a)

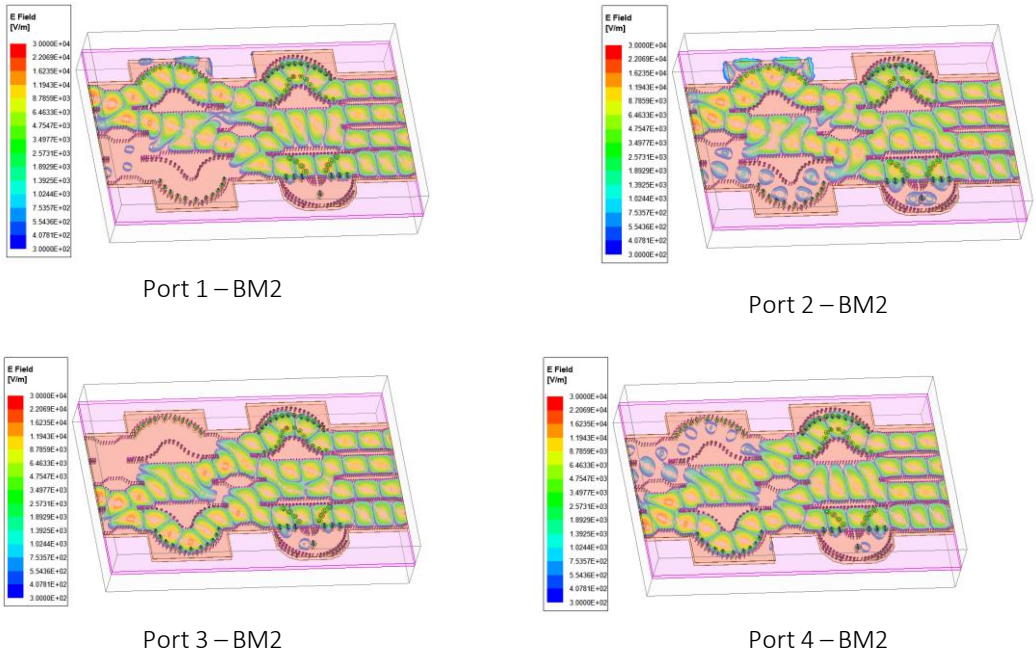

Port 1 – BM2 Port 2 – BM2

Port 3 – BM2 Port 4 – BM2

(b)

Figure 4-19: E-field for any feeding configuration (a) BM1, (b) BM2.

The BM measurement set-up is displayed in Figure 4-20. Both the Butler matrices were calibrated with SOLT calibration and, afterwards, a TRL calibration was performed, whose TRL samples are shown in Figure 4-21. As the only difference between the two Butler matrices is the presence or no of metal strips, that are not visible at system scale, matrices look similar and only BM1 was presented (see for the two possible phase shifters with and without metal strip each time in section 4.3)

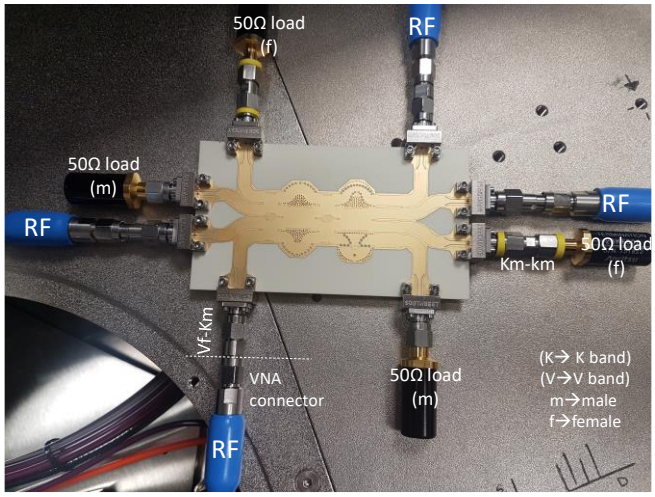

Figure 4-20: BM measurement set-up.

In Figure 4-20, 4 BM ports are connected to VNA RF ports and the remaining BM ports terminate to 50 Ω loads. Six measurements for each matrix were needed to fill the entire s8p file. K-band male-to-male and V-band female-to-male adapters were used. Both male and female loads were available.

(a) (b)

Figure 4-21: BM TRL samples: TRL for (a) internal and (b) external de-embedding of BM feeding lines.

Two types of TRL samples were used to de-embed the external and internal BM feeding lines. The two kinds of feeding lines are G-CPW to SIW-shaped to avoid the signal to be distorted by the winding accesses. For sake of simplicity, they were designed so that they had almost the same electrical characteristics. The BM size is 52.4mm x 31mm, which corresponds to $4.9\lambda_0$ x $2.9\lambda_0$. In the next section, the measurements results will be compared to simulations.

4.4.1 Butler matrix 1: measured and simulated results

Before presenting the measurements results, the simulated results of BM1 with original substrate (dotted lines) and re-optimized substrate (circled lines) are shown, between 26 GHz and 30 GHz. A detailed analysis is made at 28 GHz and between 27.5 GHz and 28.5 GHz, which might be the BW of the 28-GHz 5G mobile communication [14]. This first analysis is important to understand the impact of the lack of precise information on the dielectric permittivity. All the simulations are presented in Figure 4-22.

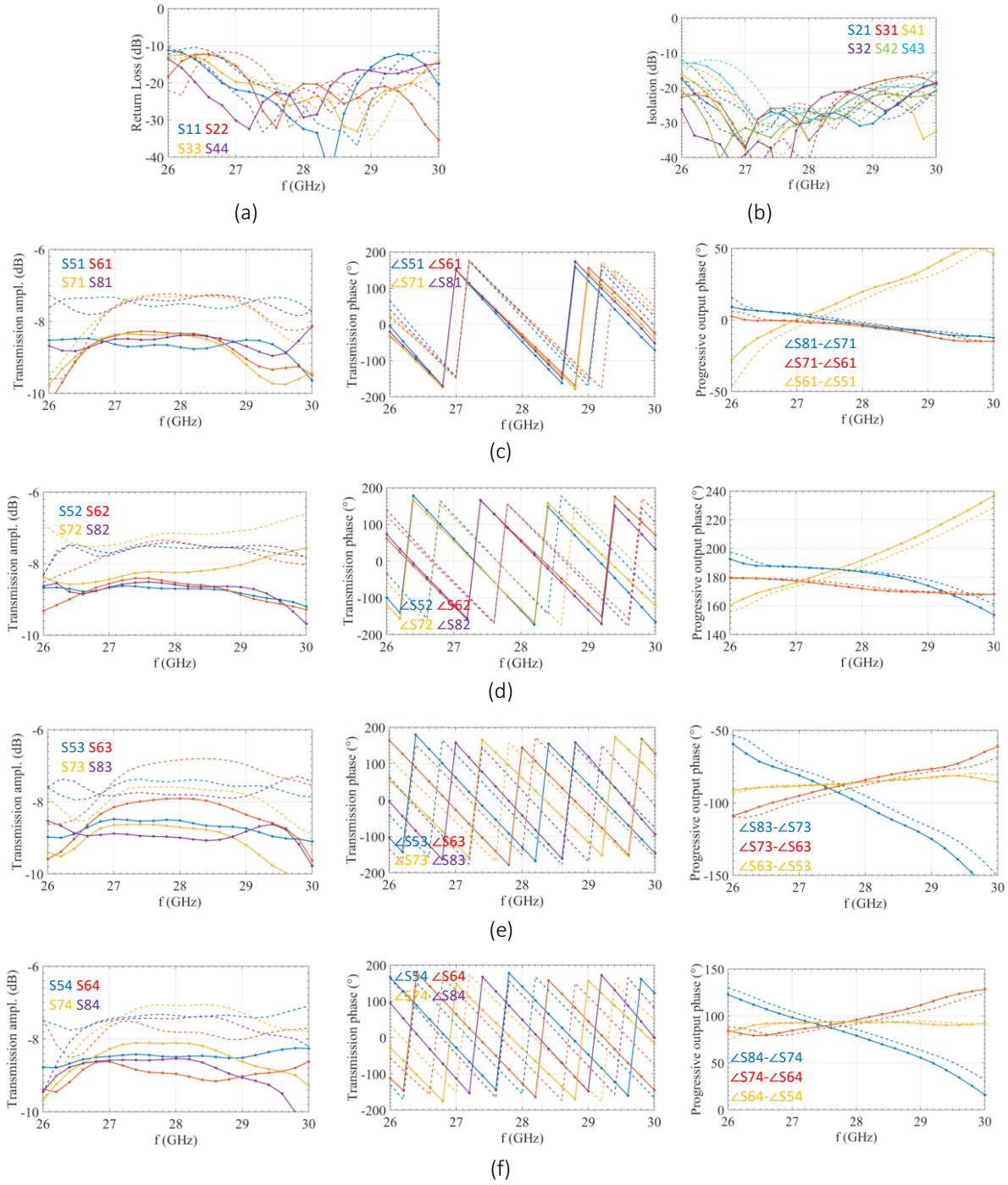

Figure 4-22: BM 1 simulated results: (a) return loss, (b) isolation, (c) port 1 feeding, (d) port 2 feeding, (e) port 3 feeding, (f) port 4 feeding. Simulations with original substrate ε_r=3.55 (dotted lines), simulations with re-optimized substrate ε_r=3.64 (circled lines).

From these results, we can notice that there is more than 1 dB of difference for the transmission amplitude which is provided by the change on $\tan\delta$ (twice the original value). Concerning the transmission phase, there is a phase delay of 60° for the re-optimized substrate structure, due to the change in $\varepsilon_r = 3.64$ instead of 3.55, while fortunately the progressive output phases are very similar. Return loss and isolation are in good agreement, except an obvious small shift towards lower frequencies. The measured results of BM1 (solid lines) and simulated ones on re-optimized substrate (circled lines) are depicted, between 26 GHz and 30 GHz, in Figure 4-23.

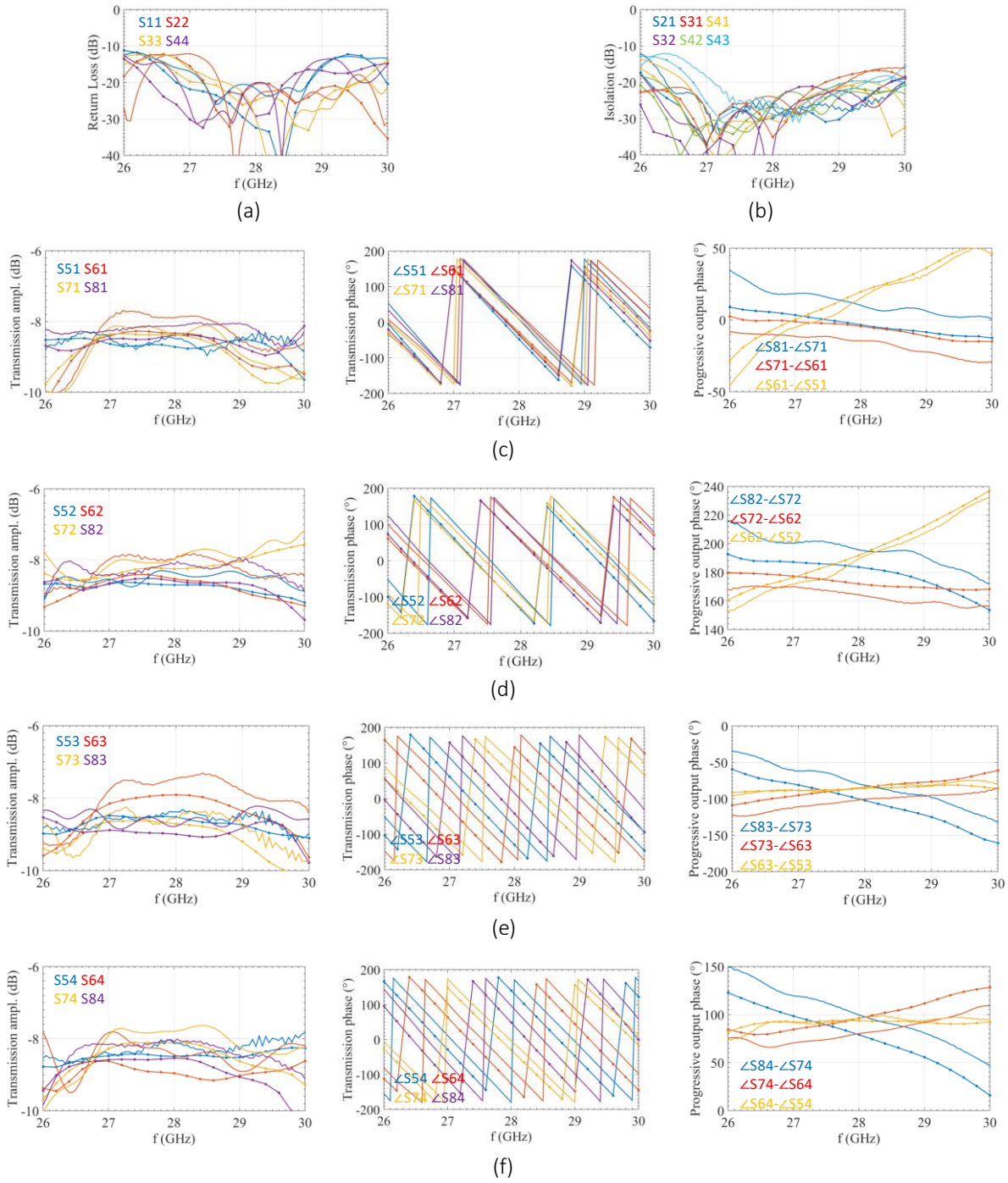

Figure 4-23: BM 1 simulated and measured results: (a) return loss, (b) isolation, (c) port 1 feeding, (d) port 2 feeding, (e) port 3 feeding, (f) port 4 feeding. Measurements (straight line), simulations with re-optimized substrate ε_r=3.64 (circled lines).

As it can be noticed from Figure 4-23 (a) and (b), the return loss and isolation are 20 dB or even better at 28 GHz, while remaining better than 10 dB in the frequency range (26 GHz up to 30 GHz), that is more than 14.3% of relative BW. When port 1 is fed, the maximum insertion loss is 2.48 dB, the maximum amplitude imbalance is 0.59 dB , whereas the absolute phases are 8.1°, 23.5°, 9° and 19.2° for S_{51}, S_{61}, S_{71} and S_{81}, respectively, at 28 GHz. As a consequence, the progressive output phases ($\angle S_{81} - \angle S_{71}$, $\angle S_{71} - \angle S_{61}$ and $\angle S_{61} - \angle S_{51}$) are

equal to 10.3°, -14.5° and 15.4°, respectively, whereas progressive output phases equal to 0° were required. If a frequency range between 27.5 GHz and 28.5 GHz (3.6% relative BW) is considered, the maximum amplitude imbalance is 1.1 dB, the maximum insertion loss is equal to 3 dB and the progressive output phases vary among 15.7° and 6.3°, -11.5° and -17.5°, and 25.7° and 1.8°, respectively. When port 2 is fed, the maximum insertion loss is 2.36 dB, the maximum amplitude imbalance is 0.4 dB , whereas the absolute phases are -92°, 97.2°, -98.3° and 97.4° for S_{52}, S_{62}, S_{72} and S_{82}, respectively, at 28 GHz. As a consequence, the progressive output phases ($\angle S_{82} - \angle S_{72}$, $\angle S_{72} - \angle S_{62}$ and $\angle S_{62} - \angle S_{52}$) are equal to 195.7 °, 164.5° and 189.2°, respectively, whereas progressive output phases equal to ±180° were required. In the 27.5 GHz-28.5 GHz frequency range, the maximum amplitude imbalance is 0.75 dB, the maximum insertion loss is equal to 2.6 dB and the progressive output phases vary among 201.1° and 194.2°, 167.6° and 160.2°, and 198° and 175.6°, respectively. When port 3 is fed, the maximum insertion loss is 2.8 dB, the maximum amplitude imbalance is 1.3 dB , whereas the absolute phases are -78.6°, -162.6°, 96.9° and 15.5° for S_{53}, S_{63}, S_{73} and S_{83}, respectively, at 28 GHz. As a consequence, the progressive output phases ($\angle S_{83} - \angle S_{73}$, $\angle S_{73} - \angle S_{63}$ and $\angle S_{63} - \angle S_{53}$) are equal to -81.4°, -100.5° and -84°, respectively, whereas progressive output phases equal to -90° were required. In the 27.5 GHz-28.5 GHz frequency range, the maximum amplitude imbalance is 1.35 dB, the maximum insertion loss is equal to 2.78 dB and the progressive output phases vary among -65.8° and -90.6°, -98.5° and -106.5°, and -79.8° and -89.2°, respectively. Finally, when port 4 is fed, the maximum insertion loss is 2.44 dB, the maximum amplitude imbalance is 0.65 dB , whereas the absolute phases are -179.5°, -83.3°, -3.1° and 96.5° for S_{54}, S_{64}, S_{74} and S_{84}, respectively, at 28 GHz. As a consequence, the progressive output phases ($\angle S_{84} - \angle S_{74}$, $\angle S_{74} - \angle S_{64}$ and $\angle S_{64} - \angle S_{54}$) are equal to 99.6°, 80.2° and 96.3°, respectively, whereas progressive output phases equal to 90° were required. In the 27.5 GHz-28.5 GHz frequency range, the maximum amplitude imbalance is 0.8 dB, the maximum insertion loss is equal to 2.5 dB and the progressive output phases vary among 112° and 90.3°, 84.7° and 73.9°, and 98.9° and 92.2°, respectively. On the overall, the requirements are quite well fulfilled and the measurements are in good agreement with simulations. All the previous measured results are summarized in

Table 4-7. The IL ranging between 2.36 dB and 2.78 dB should not impact the antenna gain more than 0.42 dB in average, at 28 GHz. The amplitude imbalance is always below 1.33 dB for each port feeding. The maximum phase imbalance is always below 16°, and the most often below 10°. Those parameters, on the basis of the sensitivity study of Chapter II should guarantee less than 4° of de-pointing (most often about 2°) and less than 1.4 dB in ripple deviation (most often about 0.75 dB) for a conventional BM but the impact should be lower with the extended beam as twice the number of main lobes are available. Anyway, a specific focus will be made on the array factor at the final end of Chapter IV, section 4.4.3, showing the exact impact.

Port 1	S_{51}	S_{61}	S_{71}	S_{81}	**28 GHz**
Max IL	2.48 dB	/	/	/	
Max amp. imb.	0.59 dB				
Trans. phase	8.1°	23.5°	9°	19.2°	
PoP	$\angle S_{81} - \angle S_{71}$	$\angle S_{71} - \angle S_{61}$	$\angle S_{61} - \angle S_{51}$		
Ideal→0°	10.3°	-14.5°	15.4°		

Port 1	S_{51}	S_{61}	S_{71}	S_{81}	**27.5-28.5 GHz**
Max IL	3 dB	/	/	/	
Max amp. imb.	1.1 dB				
PoP	$\angle S_{81} - \angle S_{71}$	$\angle S_{71} - \angle S_{61}$	$\angle S_{61} - \angle S_{51}$		
	15.7°→ 6.3°	-11.5°→ -17.5°	25.7°→ 1.8°		

Port 2	S_{52}	S_{62}	S_{72}	S_{82}	**28 GHz**
Max IL	2.36 dB	/	/	/	
Max amp. imb.	0.4 dB				
Trans. phase	-92°	97.2°	-98.3°	97.4°	
PoP	$\angle S_{82} - \angle S_{72}$	$\angle S_{72} - \angle S_{62}$	$\angle S_{62} - \angle S_{52}$		
Ideal→±180°	195.7°	164.5°	189.2°		

Port 2	S_{52}	S_{62}	S_{72}	S_{82}	**27.5-28.5 GHz**
Max IL	2.6 dB	/	/	/	
Max amp. imb.	0.75 dB				
PoP	$\angle S_{82} - \angle S_{72}$	$\angle S_{72} - \angle S_{62}$	$\angle S_{62} - \angle S_{52}$		
	201.1°→ 194.2°	167.6°→160.2°	198°→175.6°		

Port 3	S_{53}	S_{63}	S_{73}	S_{83}	**28 GHz**
Max IL	/	/	/	2.78 dB	
Max amp. imb.	1.33 dB				
Trans. phase	-78.6°	-162.6°	96.9°	15.5°	
PoP	$\angle S_{83} - \angle S_{73}$	$\angle S_{73} - \angle S_{63}$	$\angle S_{63} - \angle S_{53}$		
Ideal→-90°	-81.4°	-100.5°	-84°		

Port 3	S_{53}	S_{63}	S_{73}	S_{83}	**27.5-28.5 GHz**
Max IL	/	/	/	2.78 dB	
Max amp. imb.	1.35 dB				
PoP	$\angle S_{83} - \angle S_{73}$	$\angle S_{73} - \angle S_{63}$	$\angle S_{63} - \angle S_{53}$		
	-65.8°→-90.6°	-98.5°→ -106.5°	-79.8°→ -89.2°		

Port 4	S_{54}	S_{64}	S_{74}	S_{84}	**28 GHz**
Max IL	/	2.44 dB	/	/	
Max amp. imb.	0.65 dB				
Trans. phase	-179.5°	-83.3°	-3.1°	96.5°	
PoP	$\angle S_{84} - \angle S_{74}$	$\angle S_{74} - \angle S_{64}$	$\angle S_{64} - \angle S_{54}$		
Ideal→90°	99.6°	80.2°	96.3°		

Port 4	S_{54}	S_{64}	S_{74}	S_{84}	**27.5-28.5 GHz**
Max IL	/	2.5 dB	/	/	
Max amp. imb.	0.8 dB				
PoP	$\angle S_{84} - \angle S_{74}$	$\angle S_{74} - \angle S_{64}$	$\angle S_{64} - \angle S_{54}$		
	112°→ 90.3°	84.7°→73.9°	98.9°→92.2°		

Table 4-7: Summarized measured results for BM1

4.4.2 Butler matrix 2: measurement and simulated results

The simulated results of BM2 with original substrate (dotted lines) and re-optimized substrate (circled lines) are shown here, between 26 GHz and 30 GHz. All the results are presented in Figure 4-24. Same considerations are valid here as for BM1 simulated results.

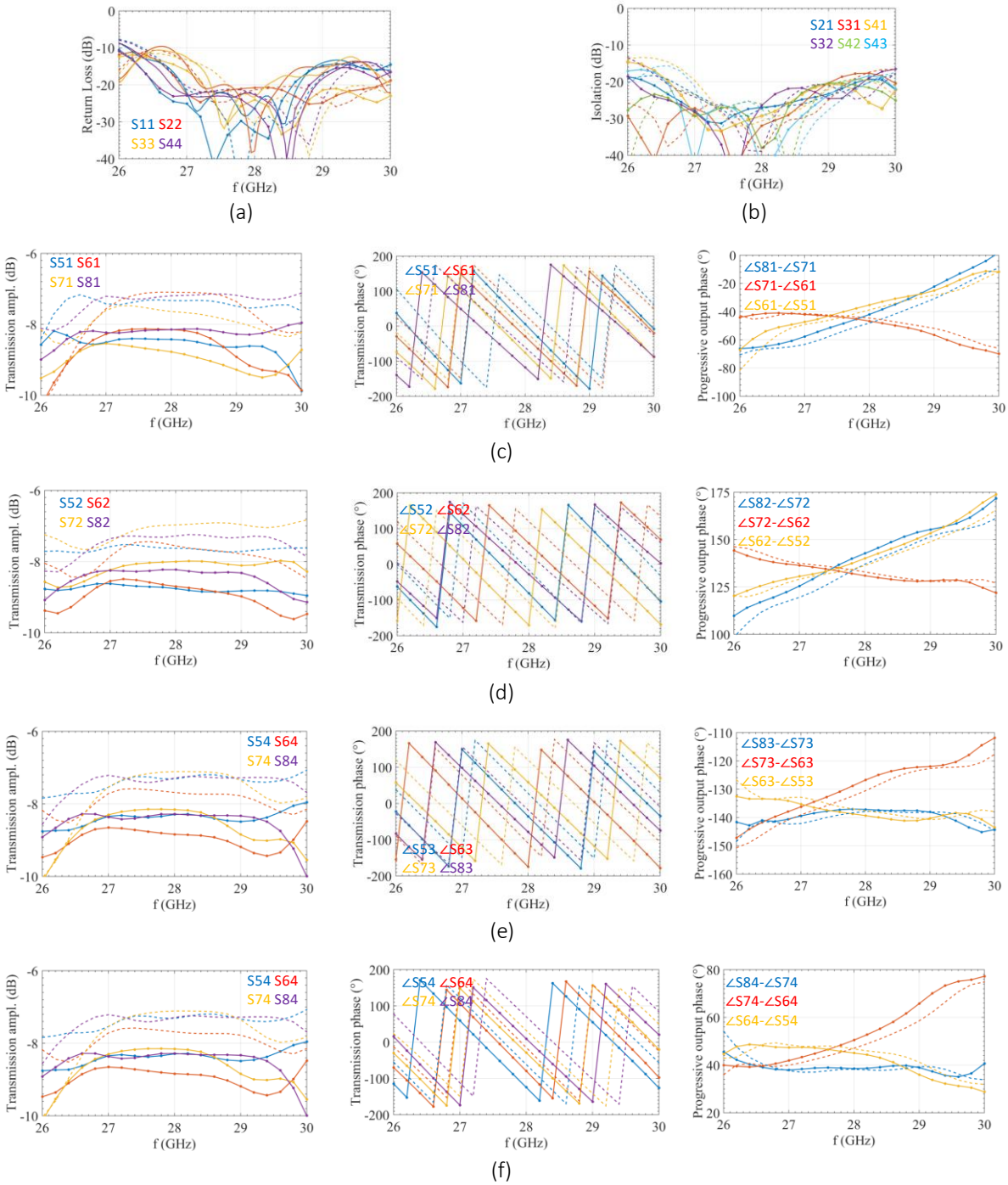

Figure 4-24: BM 2 simulated results: (a) return loss, (b) isolation, (c) port 1 feeding, (d) port 2 feeding, (e) port 3 feeding, (f) port 4 feeding. Simulations with original substrate ε_r=3.55 (dotted lines), simulations with re-optimized substrate ε_r=3.64 (circled lines).

The measured results of BM2 (solid lines) and simulated ones on re-optimized substrate (circled lines) are depicted, between 26 GHz and 30 GHz, in Figure 4-25.

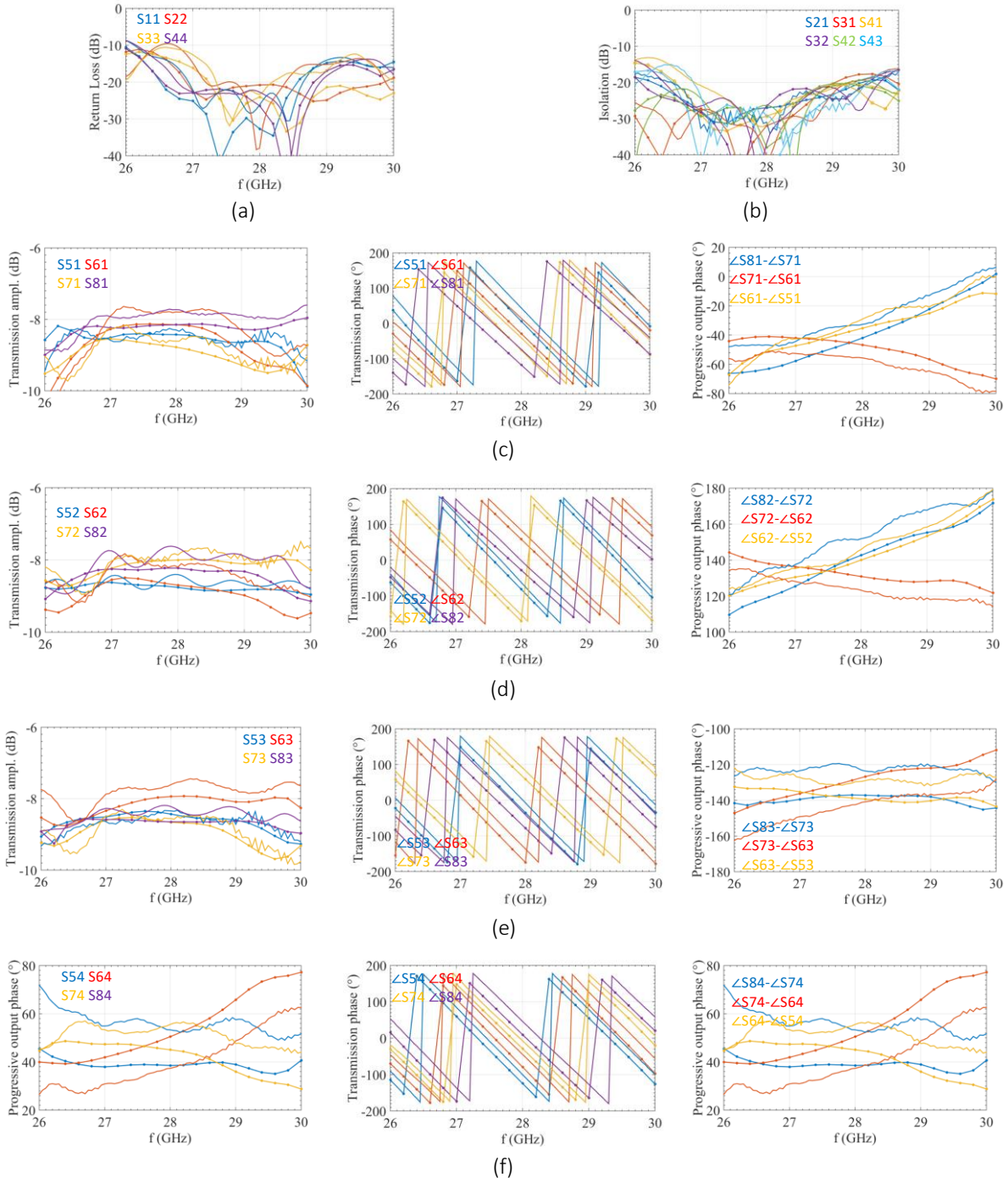

Figure 4-25: BM 2 simulated and measured results: (a) return loss, (b) isolation, (c) port 1 feeding, (d) port 2 feeding, (e) port 3 feeding, (f) port 4 feeding. Measurements (straight line), simulations with re-optimized substrate ε_r=3.64 (circled lines).

As it can be noticed from Figure 4-25 (a) and (b), the measured return loss and isolation are better than 20 dB at 28 GHz, while the return loss remains better than 10 dB between 26.7 GHz up to more than 30 GHz, that is more than 11.8% of relative BW, and the isolation is better than 10 dB in the overall considered frequency range.

When port 1 is fed, the maximum insertion loss is 2.6 dB, the maximum amplitude imbalance is 0.88 dB , whereas the absolute phases are 43.8°, 14.7°, -40.9° and -73.7° for S_{51}, S_{61}, S_{71} and S_{81}, respectively, at 28 GHz. As a consequence, the progressive output phases

($\angle S_{81} - \angle S_{71}, \angle S_{71} - \angle S_{61}$ and $\angle S_{61} - \angle S_{51}$) are equal to -32.7°, -55.6° and -29.1°, respectively, whereas progressive output phases equal to -45° were required. If a frequency range between 27.5 GHz and 28.5 GHz is considered, the maximum amplitude imbalance is 1 dB, the maximum insertion loss is equal to 2.7 dB and the progressive output phases vary among -21.5° and -34.9°, -53.9° and -62.5° and -20.9° and -39.2°, respectively.

When port 2 is fed, the maximum insertion loss is 2.4 dB, the maximum amplitude imbalance is 0.74 dB , whereas the absolute phases are -62.6°, 83.7°, -153° and -1.15° for S_{52}, S_{62}, S_{72} and S_{82}, respectively, at 28 GHz. As a consequence, the progressive output phases ($\angle S_{82} - \angle S_{72}, \angle S_{72} - \angle S_{62}$ and $\angle S_{62} - \angle S_{52}$) are equal to 151.9°, 123.3° and 145.9°, respectively, whereas progressive output phases equal to 135° were required. In the 27.5 GHz-28.5 GHz frequency range, the maximum amplitude imbalance is 1.1 dB, the maximum insertion loss is equal to 2.8 dB and the progressive output phases vary among 162.8° and 149.9°, 125.8° and 118.5° and 152.6° and 136.8°, respectively.

When port 3 is fed, the maximum insertion loss is 2.56 dB, the maximum amplitude imbalance is 0.96 dB , whereas the absolute phases are -7.6°, -136.6°, 82.6° and -41.1° for S_{53}, S_{63}, S_{73} and S_{83}, respectively, at 28 GHz. As a consequence, the progressive output phases ($\angle S_{83} - \angle S_{73}, \angle S_{73} - \angle S_{63}$ and $\angle S_{63} - \angle S_{53}$) are equal to -123.6°, -140.9° and -129°, respectively, whereas progressive output phases equal to -135° were required. In the 27.5 GHz-28.5 GHz frequency range, the maximum amplitude imbalance is 1.2 dB, the maximum insertion loss is equal to 2.7 dB and the progressive output phases vary among -119.4° and -124.3°, -137.6° and -145.7° and -127.8° and -131.6°, respectively.

Finally, when port 4 is fed, the maximum insertion loss is 2.4 dB, the maximum amplitude imbalance is 0.6 dB , whereas the absolute phases are -100.5°, -45°, -7.6° and 45.7° for S_{54}, S_{64}, S_{74} and S_{84}, respectively, at 28 GHz. As a consequence, the progressive output phases ($\angle S_{84} - \angle S_{74}, \angle S_{74} - \angle S_{64}$ and $\angle S_{64} - \angle S_{54}$) are equal to 53.3°, 37.3° and 55.6°, respectively, whereas progressive output phases equal to 45° were required. In the 27.5 GHz-28.5 GHz frequency range, the maximum amplitude imbalance is 0.6 dB, the maximum insertion loss is equal to 2.4 dB and the progressive output phases vary among 58° and 52.3°, 41° and 32.9° and 56.6° and 52.2°, respectively. On the overall, even here, the requirements are quite well fulfilled and the measurements are in good agreement with simulations.

All the previous measured results are summarized in Table 4-8. The IL ranging between 2.4 dB and 2.6 dB should not impact the antenna gain more than 0.2 dB in average, at 28 GHz. The amplitude imbalance is always below 1 dB for each port feeding. The maximum phase imbalance is always below 17°, and the most often below 10°. Those parameters, on the basis of the sensitivity study of Chapter II should guarantee less than 3.5° of de-pointing (most often about 2°) and less than 1.4 dB in ripple deviation (most often about 0.75 dB) for a conventional BM but the impact should be lower with the extended beam as twice the number of main lobes are available. Anyway, a specific focus will be made on the array factor at the final end of Chapter IV, section 4.4.3, showing the exact impact.

Port 1	S_{51}	S_{61}	S_{71}	S_{81}	**28 GHz**
Max IL	/	/	2.6 dB	/	
Max amp. imb.	0.88 dB				
Trans. phase	43.8°	14.7°	-40.9°	-73.7°	
PoP	$\angle S_{81} - \angle S_{71}$	$\angle S_{71} - \angle S_{61}$	$\angle S_{61} - \angle S_{51}$		
Ideal→-45°	-32.7°	-55.6°	-29.1°		

Port 1	S_{51}	S_{61}	S_{71}	S_{81}	**27.5-28.5 GHz**
Max IL	/	/	-2.7 dB	/	
Max amp. imb.	1 dB				
PoP	$\angle S_{81} - \angle S_{71}$	$\angle S_{71} - \angle S_{61}$	$\angle S_{61} - \angle S_{51}$		
	-21.5°→ -34.9°	-53.9°→ -62.5°	-20.9°→-39.2°		

Port 2	S_{52}	S_{62}	S_{72}	S_{82}	**28 GHz**
Max IL	2.4 dB	/	/	/	
Max amp. imb.	0.74 dB				
Trans. phase	-62.6°	83.7°	-153°	-1.15°	
PoP	$\angle S_{82} - \angle S_{72}$	$\angle S_{72} - \angle S_{62}$	$\angle S_{62} - \angle S_{52}$		
Ideal→135°	151.9°	123.3°	145.9°		

Port 2	S_{52}	S_{62}	S_{72}	S_{82}	**27.5-28.5 GHz**
Max IL	2.8 dB	/	/	/	
Max amp. imb.	1.1 dB				
PoP	$\angle S_{82} - \angle S_{72}$	$\angle S_{72} - \angle S_{62}$	$\angle S_{62} - \angle S_{52}$		
	162.8°→ 149.9°	125.8°→118.5°	152.6°→136.8°		

Port 3	S_{53}	S_{63}	S_{73}	S_{83}	**28 GHz**
Max IL	/	/	2.56 dB	/	
Max amp. imb.	0.96 dB				
Trans. phase	-7.6°	-136.6°	82.6°	-41.1°	
PoP	$\angle S_{83} - \angle S_{73}$	$\angle S_{73} - \angle S_{63}$	$\angle S_{63} - \angle S_{53}$		
Ideal→-135°	-123.6°	-140.9°	-129°		

Port 3	S_{53}	S_{63}	S_{73}	S_{83}	**27.5-28.5 GHz**
Max IL	/	/	2.7 dB	/	
Max amp. imb.	1.2 dB				
PoP	$\angle S_{83} - \angle S_{73}$	$\angle S_{73} - \angle S_{63}$	$\angle S_{63} - \angle S_{53}$		
	-119.4°→-124.3°	-137.6°→ -145.7°	-127.8°→ -131.9°		

Port 4	S_{54}	S_{64}	S_{74}	S_{84}	**28 GHz**
Max IL	/	2.4 dB	/	/	
Max amp. imb.	0.6 dB				
Trans. phase	-100.5°	-45°	-7.6°	45.7°	
PoP	$\angle S_{84} - \angle S_{74}$	$\angle S_{74} - \angle S_{64}$	$\angle S_{64} - \angle S_{54}$		
Ideal→45°	53.3°	37.3°	55.6°		

Port 4	S_{54}	S_{64}	S_{74}	S_{84}	**27.5-28.5 GHz**
Max IL	/	2.4 dB	/	/	
Max amp. imb.	0.6 dB				
PoP	$\angle S_{84} - \angle S_{74}$	$\angle S_{74} - \angle S_{64}$	$\angle S_{64} - \angle S_{54}$		
	58°→ 52.3°	41°→32.9°	56.6°→52.2°		

Table 4-8: Summarized measured results for BM 2

4.4.3 Array factor and array pattern of measured extended beam Butler matrix

The not normalized array factor is plotted in Figure 4-26, which exploits the aforementioned measured results (colored lines), and it is compared to the theoretical one (black lines), for isotropic sources distanced by $0.5 \cdot \lambda_0$. This distance has been chosen to represent the AF because it is the most common one.

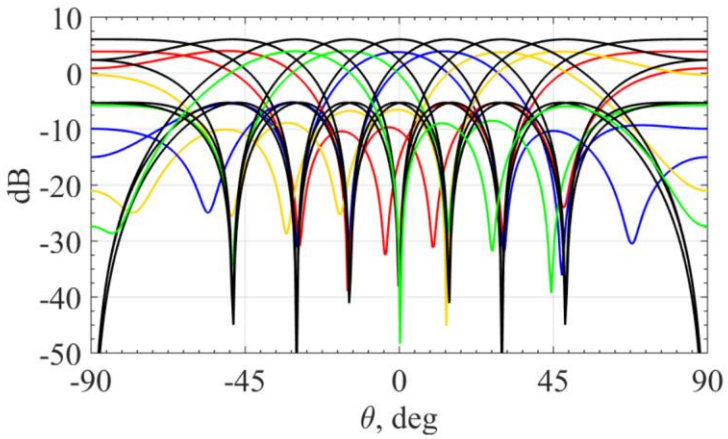

Figure 4-26: Array factor for measured and theoretical results. $d = 0.5 \cdot \lambda_0$

Concerning the beam maximum amplitude, the beams present almost the same with the biggest discrepancy between the beam 1L (most performing) and 2R (least performing) equal

to 0.23 dB, the 1L beam gain being equal to 3.97 dB and the 2R beam gain equal to 3.74 dB. On the overall, the average beam gain is around 3.8 dB which means a gain loss equal to 2.2 dB as compared to the theoretical 6 dB one. The maximum scan loss (ripple) is 1.1 dB between the beams 2R and 3R, while the minimum is 0.78 dB between 4L and 3L. The typical scan loss is 0.8 dB. The measured beams pointing are equal to -89.4°, -50.2°, -30.4°, -15.1°, -0.7°, 13.3°, 30°,47.1° and 83.1° for the beams from 4L to 4R, respectively. The deviation with respect to the ideal beams pointing are 0.6°, 1.7°,0.4°, 0.5°, 0.7°, 1.3°, 0°, 1.4°, 6.9° for the beams from 4L to 4R, respectively. Finally, the maximum side-lobe level (SLL) increase is of 2.2 dB, related to the beam 1R. On the overall, the measured array factor is very similar to the ideal one, except the maximum gain that is 2.2 dB below due to the beam forming network insertion loss.

The array pattern of the measured extended beam BM is shown in Figure 4-27, where reconfigurable antenna patterns of Chapter II were considered. In that case, the array factor has been considered for a distance between antennas of $0.65 \cdot \lambda_0$, that is the necessary distance for the footprint of the designed reconfigurable antennas.

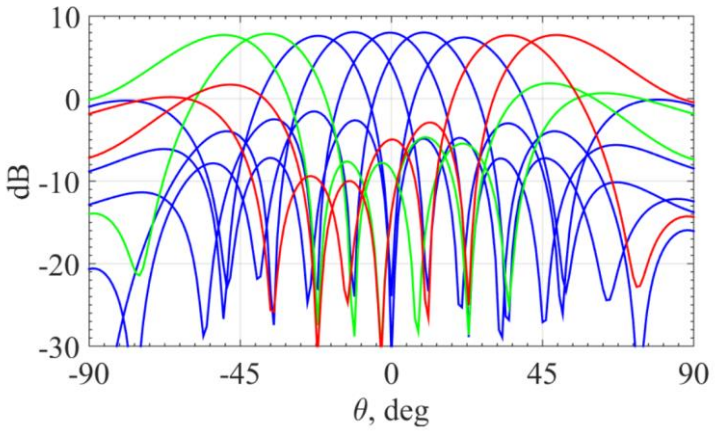

Figure 4-27: Array pattern for measured results with reconfigurable antenna pattern. Colors refers to Chapter II and concerns the reconfigurable elementary antenna pattern: boresight (blue), left end-fire (green) and right end-fire (red). $d = 0.65 \cdot \lambda_0$

As it can be noticed, the spatial coverage is ±67° according to equation (2-8) and (2-9) of Chapter II. The maximum gain occurs at 0° and it is equal to 8 dB, whilst the maximum ripple occurs between the first green or the first red main lobe and the last blue main lobe: for this θ the ripple is equal to 1.1 dB. The maximum lobe de-pointing occurs for 3R beam and it is equal to 2°.

All these results confirm the predictions based on the study of Chapter II, Table 2-6. In this real case losses due the BM are considered in the array pattern calculations. Solutions to increase the gain of the array should go through the BM loss reduction. As prospects, it should be interesting to go towards more performing waveguides, by using air filled or partially air-filled substrate integrated waveguides as an example.

4.5 Conclusion

The Butler matrix network, is a good candidate, at the moment, to achieve both high gain and wide coverage areas for possible 5G mobile terminals.

In this chapter, the designed blocks for a 28 GHz SIW Butler matrix were introduced and measured. In the first part, a 3-dB coupler and a crossover realized in short-slot topology are presented, which represent the not reconfigurable blocks in the extended beam BM theory. Moreover, the state-of-the-art of SIW coupler and crossover for PCB technology is reported. Measured results are promising and in accordance to the simulated ones. Afterwards, all the phase shifters included in the system were discussed and measured. For a proof-of-concept, for each 1-bit phase shifter two not reconfigurable phase shifters were fabricated, representing either a RF path or the other. They were arranged in the system with the couplers and crossovers, forming two different Butler matrices, each one providing four different progressive output phases, for a total of 8. Design techniques and insights were given, either.

In the second part of the chapter, the measurements of the Butler matrices give rise to a detailed analysis of the results, and their impact on the array pattern of the array antenna system was discussed, as well.

Frequencies from at least 60 GHz up to 1 THz are promising bands for the next generation of wireless communication systems, because of the wide unused and unexplored spectrum. These frequencies also offer the potential for revolutionary applications that will be made possible by new thinking, and advances in devices, circuits, software, signal processing, applications, and systems. All of that can lead to the development and implementation of the sixth generation (6G) of wireless networks, and beyond.

New more performing technologies so-called interposers, that can allow the frequency rising, will be discussed in the next final chapter, and SIWs lines and devices will be presented in one of this technology and for high frequency.

REFERENCE

[1] H. J. Riblet, 'The Short-Slot Hybrid Junction', *Proceedings of the IRE*, vol. 40, no. 2, pp. 180–184, Feb. 1952, doi: 10.1109/JRPROC.1952.274021.

[2] Ji-Xin Chen, Wei Hong, Zhang-Cheng Hao, Hao Li, and Ke Wu, 'Development of a low cost microwave mixer using a broad-band substrate integrated waveguide (SIW) coupler', *IEEE Microwave and Wireless Components Letters*, vol. 16, no. 2, pp. 84–86, Feb. 2006, doi: 10.1109/LMWC.2005.863199.

[3] C.-J. Chen and T.-H. Chu, 'Design of 60-GHz SIW short-slot couplers', in *2009 Asia Pacific Microwave Conference*, Dec. 2009, pp. 2096–2099, doi: 10.1109/APMC.2009.5385264.

[4] S. S. Sabri, B. H. Ahmad, and A. R. Othman, 'Design and fabrication of X-band Substrate Integrated Waveguide directional coupler', in *2013 IEEE Symposium on Wireless Technology Applications (ISWTA)*, Sep. 2013, pp. 264–268, doi: 10.1109/ISWTA.2013.6688784.

[5] B. Liu, W. Hong, Y.-Q. Wang, Q.-H. Lai, and K. Wu, 'Half Mode Substrate Integrated Waveguide (HMSIW) 3-dB Coupler', *IEEE Microwave and Wireless Components Letters*, vol. 17, no. 1, pp. 22–24, Jan. 2007, doi: 10.1109/LMWC.2006.887244.

[6] T. Djerafi and K. Wu, 'Super-Compact Substrate Integrated Waveguide Cruciform Directional Coupler', *IEEE Microwave and Wireless Components Letters*, vol. 17, no. 11, pp. 757–759, Nov. 2007, doi: 10.1109/LMWC.2007.908040.

[7] G. H. Zhai *et al.*, 'Folded Half Mode Substrate Integrated Waveguide 3 dB Coupler', *IEEE Microwave and Wireless Components Letters*, vol. 18, no. 8, pp. 512–514, Aug. 2008, doi: 10.1109/LMWC.2008.2001006.

[8] T. Djerafi, J. Gauthier, and K. Wu, 'Quasi-optical cruciform substrate integrated waveguide (SIW) coupler for millimeter-wave systems', in *2010 IEEE MTT-S International Microwave Symposium*, May 2010, pp. 716–719, doi: 10.1109/MWSYM.2010.5515889.

[9] T. Djerafi and K. Wu, '60 GHz substrate integrated waveguide crossover structure', in *2009 European Microwave Conference (EuMC)*, Sep. 2009, pp. 1014–1017, doi: 10.23919/EUMC.2009.5296165.

[10] T. Djerafi, N. J. G. Fonseca, and K. Wu, 'Design and Implementation of a Planar 4 × 4 Butler Matrix in Siw Technology for Wide Band High Power Applications', *Progress In Electromagnetics Research B*, vol. 35, p. 23, 2011.

[11] W. Bhowmik, S. Srivastava, and L. Prasad, 'Design Of Multiple Beam Forming Antenna System Using Substrate Integrated Folded Waveguide (Sifw) Technology', *Progress In Electromagnetics Research B*, vol. 60, pp. 15–34, 2014, doi: 10.2528/PIERB14022603.

[12] N. Tiwari and T. R. Rao, 'A switched beam antenna array with butler matrix network using substrate integrated waveguide technology for 60 GHz communications', in *2015 International Conference on Advances in Computing, Communications and Informatics (ICACCI)*, Kochi, India, Aug. 2015, pp. 2152–2157, doi: 10.1109/ICACCI.2015.7275935.

[13] Q.-L. Yang, Y.-L. Ban, K. Kang, C.-Y.-D. Sim, and G. Wu, 'SIW Multibeam Array for 5G Mobile Devices', *IEEE Access*, vol. 4, pp. 2788–2796, 2016, doi: 10.1109/ACCESS.2016.2578458.

[14] W. Hong *et al.*, 'Multibeam Antenna Technologies for 5G Wireless Communications', *IEEE Transactions on Antennas and Propagation*, vol. 65, no. 12, pp. 6231–6249, Dec. 2017, doi: 10.1109/TAP.2017.2712819.

Chapter 5:

Butler matrix blocks in high frequency substrate technologies

The millimetre-wave (mm-wave) frequency spectrum has become the focus of many research and development projects, because of its potential for addressing high-definition multimedia mobile applications and 5G. Researchers' attention is being oriented towards circuits working at frequencies above 100 GHz for applications such as 6G, wireless sensors or automotive radars. In that context, the PCB technologies do not provide sufficient manufacturing accuracy and reliability. On the other hand, the current integrated technologies are limited when a complete integration of the systems on chip is demanded. This limitation is due to the relatively poor performance of the passives in integrated technologies and to the important surface area required for these passive circuits. Thus, it seems to be very promising to consider intermediate platforms. These ones called interposers allow the realization of high quality passive devices thanks to more appropriate dimensions and more flexibility in the design. Moreover, it makes possible the 3D connection of active chips such as CMOS/BiCMOS, GaAS dies very efficiently (through chip via and solder bumps) to the PCB. As a general rule, 3D for microelectronic systems reduces the interconnect length, wiring delay, and system size, while enhancing functionality by heterogeneous integration, and passive electrical performance. In this chapter, a specific microelectronics based technology using a benzocyclobutene material as interposer above silicon dies will be detailed and considered. This technology, considered in the framework of the TeraPacipode ANR project was developed by the laboratory C2N, in cooperation with the research units IEMN, IETR, III-IV Lab and RFIC-Lab.

In the first part of the fifth chapter, a brief review of different interposer technologies is introduced, for both commercialized and still in-research technologies. The pros and cons of those technologies are reported.

In the second part of the chapter, the design (in three different mm-wave frequency bands) of the SIW and SIW based couplers is presented. The measurements in the first band are shown along with the analysis of the results. The aim of this chapter is to show that different types of SIW components can be embedded into the interposer, thus leading to a functionalized interposer for mm-waves and beyond, with high-performance passive devices.

Perspectives and conclusions are given at the end of the chapter.

5.1 Review on various interposers technologies

Nowadays, interposer technologies based on silicon, glass or organic substrates are available. To address this concept, other substrates or techniques are the topic of intensive recent researches such as MnM (Metallic nanowire Membrane) or CNT (Carbon NanoTubes

but are still not sustained by companies R&D departments. In the framework of this study, the organic BCB material (BenzoCycloButene) which could be directly deposited above ICs dies is considered as a challenger to the latter.

5.1.1 Silicon, glass and organic interposers

Each interposer substrate material has its advantages and disadvantages. Table 5-9 summarizes the overall market penetration of the most common interposer technologies, that is to say silicon, organic and glass for high-performance applications. It also shows their major strengths and weaknesses, providing fruitful information about electrical, mechanical, thermal, and physical properties that are important material characteristics to consider, as explained in [1], along with the supply chain, cost, and current penetration level in commercial market.

Interposer	Properties						
	Electrical	Mechanical	Thermal	Physical	Supply chain	Cost	Commercial applications
Silicon	satisfactory	satisfactory	good	good	satisfactory	poor	good
Organic	good	poor	poor	satisfactory	good	satisfactory	satisfactory
Glass	good	satisfactory	satisfactory	good	poor	good	poor

Table 5-9: Silicon, organic and glass interposer properties comparison [1].

5.1.1.1 Material properties

Electrical properties of both glass and organic interposers are found to be much better as compared to silicon interposers [2]–[4]. At higher frequencies, the loss in silicon is much more prominent than organic and glass due to its intrinsic low to moderate resistivity, except if a high resistivity silicon substrate is considered. In parallel, a multi-layer approach is often necessary in order to benefit from the best of the technology for any of the various passive devices to be integrated in the same time in the interposer: planar or 3D inductors, planar or 3D capacitors, transmission lines or integrated waveguides. It is not straightforward to develop multi-layered glass, or high resistivity silicon, interposers, much less feasible and certainly much costlier than organic substrates.

Apart from that, the realization of dense electrical structures, interconnects, and pitch less than 5 µm (resolution for solder balls, for example) using organic interposers is still a challenge and requires more research effort [5]. Mechanical properties such as strength, Young modulus (measure of the ability of a material to withstand changes in length when under lengthwise tension or compression), or elasticity, of neither of these technologies can be considered as very good. The organic interposers are found to have poor performance when dealing with these factors, whereas the performance of silicon and glass is satisfactory[6]–[8]. This is a major issue that affects the reliability of the interposer when used for high-performance applications.

Concerning the thermal properties, it was observed that the silicon interposers had the least possible CTE (coefficient of thermal expansion) mismatch with the ICs/die as silicon is

the material employed by the ICs/die itself [2]. The organic interposers have the most CTE mismatch and are thus considered as the worst among the three technologies [9]. The glass interposer represents an intermediate solution under this aspect [4], [9].

Both the silicon and glass interposers have better mechanical properties enabling deep UV photolithography to achieve ultrathin dimensions [10], what's more, glass is also available in large panels for processing, while the organic interposers have not yet achieved such ultrathin dimensions. Surface finish and roughness are also better for silicon and glass substrates.

5.1.1.2 **Market aspects**

Supply chain of the organic technology is the most widespread and mature. One of the main reasons for that is the usage of organic material for other commercial applications, which is much older compared to the silicon and glass technologies [11]. The supply chain for silicon is also widespread but is not as large as that of organic, while that for glass is in an early stage; it represents the biggest drawback for glass spread.

Cost is a major factor and it was observed that the cost of glass is the least among the three interposer technologies. Silicon is still costly, because specific production lines still have to be developed, not to use the usual costly supply chains devoted to IC dies, while the organic technologies are considered to be lower in cost as compared to silicon and competitive to glass [12].

Finally, as a conclusion, it can be mentioned that due to an old-established presence, widespread all over the world, both silicon and organic interposers have been employed, by far most, for the current high-performance applications [13], [14], while there is not the same ground-breaking demonstration employing glass interposers[10], [15].

5.1.2 Carbone nanotubes

Carbon nanotubes are a discovered form of carbon, which can be thought of as a rolled-up sheet of hexagonal ordered graphite formed to give a seamless cylinder [16] .They can be 0.4–100 nm in diameter with lengths up to 1 mm. Several single-walled nanotubes (SWCNTs) can be concentrically nested inside each other, forming so-called multi-walled carbon nanotubes (MWCNTs). Due to the variety of extraordinary properties exhibited by carbon nanotubes, a large number of possible applications have been proposed. Recently, CNT interconnects and passive devices have been investigated due to their low electrical resistivity [16], [17], reduced skin effect [18], high thermal conductivity [19] and current carrying capacity [16]. In general, it is easier to grow CNTs in the vertical direction. CNTs have been grown and fabricated in [20]. Specific model to use CNT for mm-waves purpose, as an alternative for metallic walls for instance, were developed in [21]. Recent simulated results for CNT-based air-filled waveguides can be found in [22].

5.1.3 Metallic nanowires membranes

The metallic nanowire membrane concept was explained in [23]. The MnM platform is based on a nanoporous alumina substrate that has numerous benefits. Alumina is a good insulator with low loss at high frequencies. The nanoporous alumina can be obtained through

electrochemical oxidation of aluminum under specific anodizing voltages, as suggested in [24]. Typically, the diameter of the nanopores can range from 20 nm to 400 nm, and the distance pore-to-pore from a few tenths to a few hundreds of nanometers. It is possible to obtain membranes with thicknesses that can reach 300 μm. The existence of nanopores is intrinsic to the membrane fabrication and advantageous for several reasons. The nanopores can be filled with metal by electrodeposition and form a bundle of nanowires that connect both surfaces of the substrate forming TSVs, [25]. Further, as shown in [26] and [27], the nanowires can also yield slow-wave effect with high quality factor, which allows the fabrication of miniaturized microstrip lines with low characteristic impedance. The fabrication of conventional transmission lines without nanowires and high characteristic impedance with low losses is also possible, as shown in [23]. Thus, the MnM interposer shows a good potential for the development of mm-wave applications.

In the next section, a BCB interposer is going to be carefully presented, being the technology used in the framework of this chapter for the design of SIW-based circuits.

5.1.4 Benzocyclobutene (BCB) interposer, an organic layer above-IC

The organic above-IC technique is well-known in RF, typically by using a cost-effective 3-D IPD technology, with SU-8 or epoxy as the upper organic sputtered layer. Some recent examples up to 28 GHz may concern the realization of 3D inductors [28], transformers or quadrature couplers (for BM purpose) [29].

5.1.4.1 **Interest**

Some polymers have interesting properties for THz such as a low value of the real part of their dielectric permittivity, which has a double advantage: significant reduction in radiation losses for circuits and improvement of antenna performance, provided that the dielectric losses are not increased, at the same time. BCB meets these two criteria. Another advantage of polymers is the ability to deposit them on top of any type of substrate through centrifugation (separation of fluids, gases, or liquids based on density), including on top of integrated circuits. Hence BCB can be deposited very easily on top of silicon wafer or any hosting integrated circuits (above-IC) and, afterwards flip-chipped on PCB.

5.1.4.2 **Fabrication process**

In the context of the ANR TeraPacipode project, the cross-sectional view of the 3D proposed packaging technology is depicted in Figure 5-1, followed with a detailed description of the fabrication process performed at the C2N research unit.

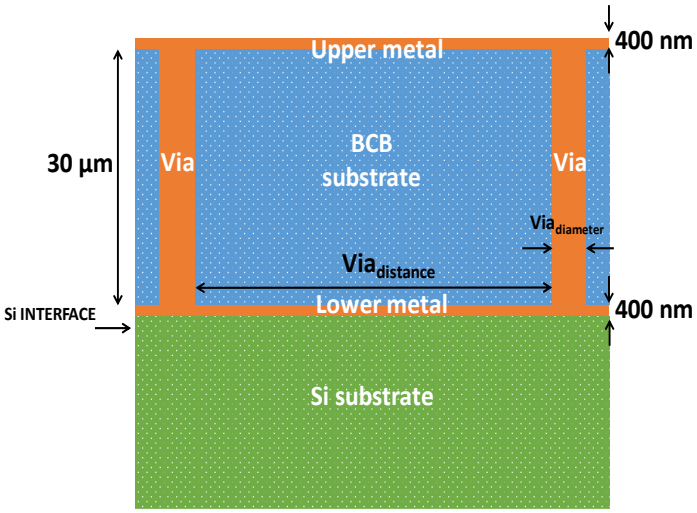

Figure 5-1: BCB 3D interposer technology

The layer stack is constituted of two 400-nm-thick gold layers that are separated by 30 µm of BCB. More precisely, the CYCLOTENE 3022-63 from DowDuPont Inc. has been chosen for its good dielectric properties at sub-mm wavelengths ($\varepsilon_r \approx 2.68$ at low frequency, decreasing to about 2.5 at 1 THz with $\tan\delta \approx 0.007$).

In order to help the adhesion of the BCB, an inductively coupled plasma etching of corrugations outside the devices area are performed on a Si wafer. Gold is then deposited by e-beam evaporation. It presents a conductivity of about $3.4 \cdot 10^7$ S/m. In order to interconnect the two layers, vias of 20 µm of diameter are electroplated in a sulphite-based gold solution through a 30-µm thick photo-resist mask. The via conductivity is around $1 \cdot 10^6$ S/m. After removal of the photo-resist, the BCB is deposited and cured in a nitrogen atmosphere. The layout of the top gold layer, also deposited by e-beam evaporation, is performed by ion beam etching using a last photolithography step. Further details on the process can be found in [30].

SIW lines and devices will be designed in the next sections, to show how high-performance passive devices can be embedded into the BCB interposer, for mm-waves and sub-THz applications.

5.2 SIW design in BCB technology, from WR10 up to WR3 band

5.2.1 SIW at mm-waves: state-of-the-art

Recently, SIW technology has been considered at mm-waves, in standard 130-nm CMOS technology, from 140 GHz to 220 GHz in [31], and from 180 GHz to 220 GHz in [32]. However, the losses are high, even at 220 GHz, due to the small dielectric thickness of advanced technologies Back-End-Of-Line (BEOL) (smaller than 10 µm), with measured attenuation constant of 2.4 dB/mm at 200 GHz in [32]. As a consequence, the electrical performance of SIWs in the BEOLs remains modest. Also the relatively large SIW width still constitutes an issue for costly advanced integrated technologies (i.e. 560 µm in [31]).

In parallel of these developments, less costly, less lossy, or still under research, packaging technologies were used to achieve high performing mm-wave SIWs, such as glass [33], [34], high resistivity-silicon (HR-Si) [35], [36] and MnM [37] interposer. Hence, in [33],

a 350-µm-thick glass substrate was used with tungsten-coated TGVs (Through Glass Via), which leads to low loss smaller than 0.16 dB/mm between 20 GHz and 45 GHz. In [35], high-performance SIWs are obtained in a 70-µm-thick HR-Si interposer, with measured attenuation constant between 0.4 dB/mm and 0.6 dB/mm in the frequency range from 110 to 170 GHz. In [36] a 280-µm-thick HR-Si substrate naturally leads to very low loss (0.12 dB/mm to 0.2 dB/mm, between 85 GHz and 105 GHz). Finally, in [37], SIWs manufactured in a 50-µm-thick MnM show an attenuation constant of about 0.5–0.8 dB/mm in the WR10-band (75–110 GHz).

The results are better summarized in Table 5-10.

Ref.	Freq. (GHz)	Technology	Thickness (µm)	α (dB/mm)
[32]	180-220	130-nm CMOS	<10	2.4
[33]	20-45	Glass	350	<0.16
[35]	110-170	HR-Si	70	0.4-0.6
[36]	85-105	HR-Si	280	0.12-0.2
[37]	75-110	MnM	50	0.5-0.8

Table 5-10: SIW waveguides in various interposer technologies

In the next step, SIWs will be addressed in BCB, in WR10 (75-110 GHz), WR5 (140-220 GHz) and WR3 (220-325 GHz) band, which will be exploited for coupler and crossover realization.

5.2.2 WR10 (75-110 GHz) band

5.2.2.1 Design

Figure 5-2 shows an example of a SIW in the BCB polymer technology wafer. The diameter D of the vias, the pitch p between the vias and the spacing W between the two rows are the physical parameters required for the design of the waveguide, as depicted in Figure 5-2 (a). It is needed to keep the pitch p quite small to reduce the leakage loss between two adjacent via holes, as already explained in chapters 3 and 4. Again several design rules, have to be strictly respected, as reported in [38].

Then, for the WR10 band (75 GHz-110 GHz), on the basis of ε_r=2.68, W is chosen equal to 1.55 mm, D equal to 20 µm and p equal to 35 µm in order to respect all of the previous rules. λ_g is equal to 2.775 mm. As shown in the example of Figure 5-2 (b), the complete waveguide structure to be measured consists of three sections: the central one is the SIW while the input-output sections ensure propagation from the GSG tips to G-CPW transitions to waveguide. The G-CPW to SIW transitions are detailed in the next sub-section.

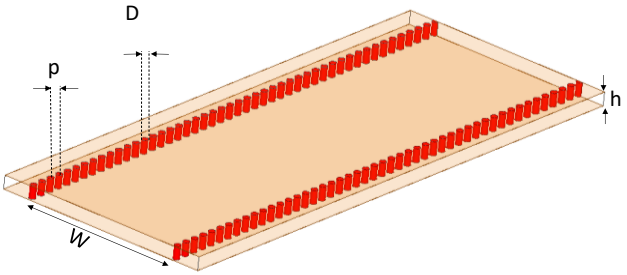

(a)

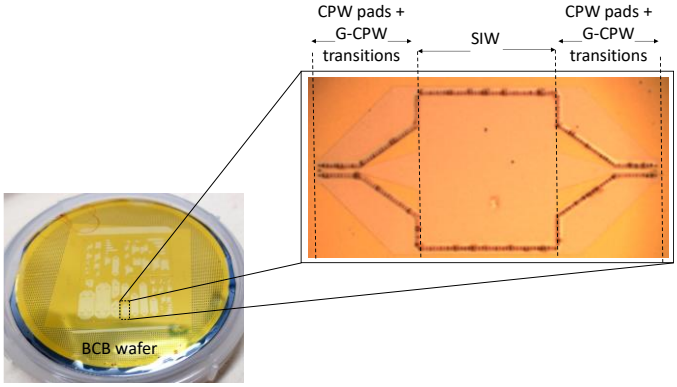

(b)

Figure 5-2: (a) SIW geometry and (b) BCB wafer with SIW in WR10 band

5.2.2.2 G-CPW to SIW feeding lines

This transition (see Figure 5-3) allows ensuring a smooth energy transfer from the pads and G-CPW feeding lines to the waveguide, from a quasi-TEM mode into a TE_{10} mode. d is hardly visible on the figure. It is the very small distance between the lateral ground edge, facing the signal trace, and the via. W_{G-CPW}, G and d are chosen to achieve a 50-Ω G-CPW. Moreover, L_{taper} was chosen to be equal to around $\lambda_{g(G-CPW)}/4$, allowing a better matching, $\lambda_{g(G-CPW)}$ being the wavelength of the G-CPW. Any values are listed in Table 5-11.

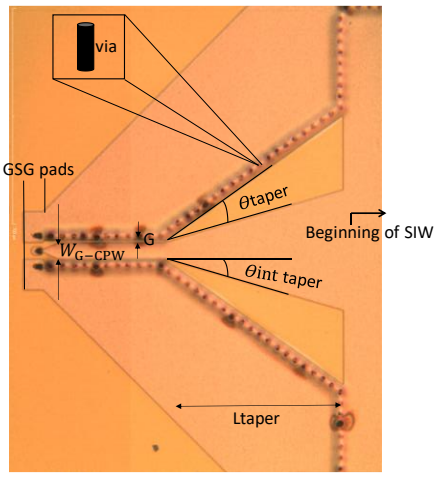

Figure 5-3: G-CPW to SIW transitions

$W_{G\text{-}CPW}$ (µm)	G (µm)	d (µm)	L_{taper} (µm)	$\theta_{int\ taper}$(°)	θ_{taper} (°)
55	5	6	573	16.3	35.2

Table 5-11: G-CPW to SIW transition dimensions for WR10 band

5.2.2.3 **Simulations and measurements**

In order to extract as much accurately as possible the SIW performance [39], and study the G-CPW access impact, four SIWs in back-to-back configuration were simulated (see Figure 5-4 (a)) with different lengths, for each band, calculated as:

$$L_i = L_0 + n \cdot \lambda_g \qquad 5\text{-}1$$

with n=0, ¼ ,1 and 2, for i=0, 1, 2 and 3, respectively. L_0 equals $\lambda_g/2$, in order to get the field well established in the waveguide. The simulations made with the electromagnetic software (HFSS v 19.2, [40]) are compared with the measurements.

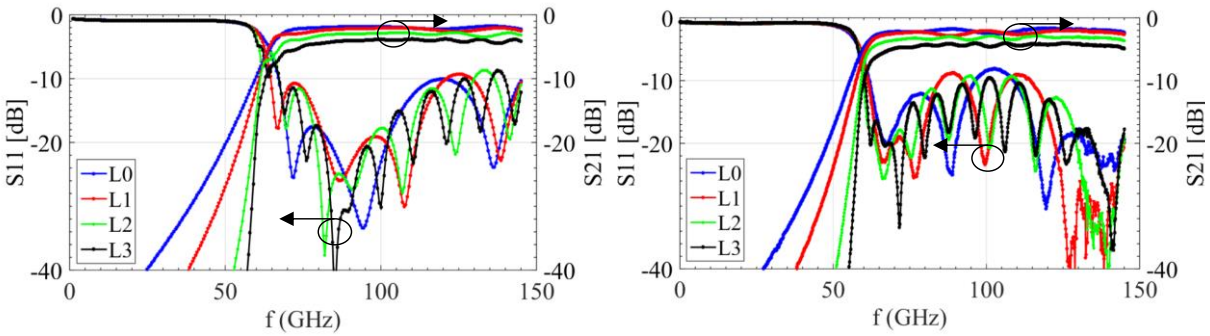

Figure 5-4: (a) Simulated and (b) measured S-Parameters back-to-back SIW results, in WR10 band

The simulated return loss is better than 15 dB between 77 GHz and 106 GHz, while the insertion loss is in between 1.8 dB and 4 dB for L_0 and L_3, respectively, at 90 GHz.

Measurements were carried out on an Anritsu ME7838D4 145 GHz VNA, using Form Factor RF microwave Infinity probes (i145) with 50 µm of pitch, from DC to 145 GHz. A LRRM calibration at pad level was implemented. The S-parameters of the four back-to-back SIWs of physical length are equal to (3.47 mm, 4.17 mm, 6.27 mm and 9.04 mm), with the G-CPW feeding lines given in Figure 5-3, without de-embedding. As expected, the slope in the cut-off region increases with the SIW length. Return loss is better than 8 dB in the 70 GHz to 145 GHz frequency band. This poor return loss is mainly due to the absence of de-embedding.

To show the performance of the realized SIWs, the propagation constant β, the attenuation constant α and the quality factor, defined by Q=$\beta/(2\cdot\alpha)$, were extracted by using the two-lines method [39]. Results are presented in Figure 5-5, with a comparison between measurement and simulation results.

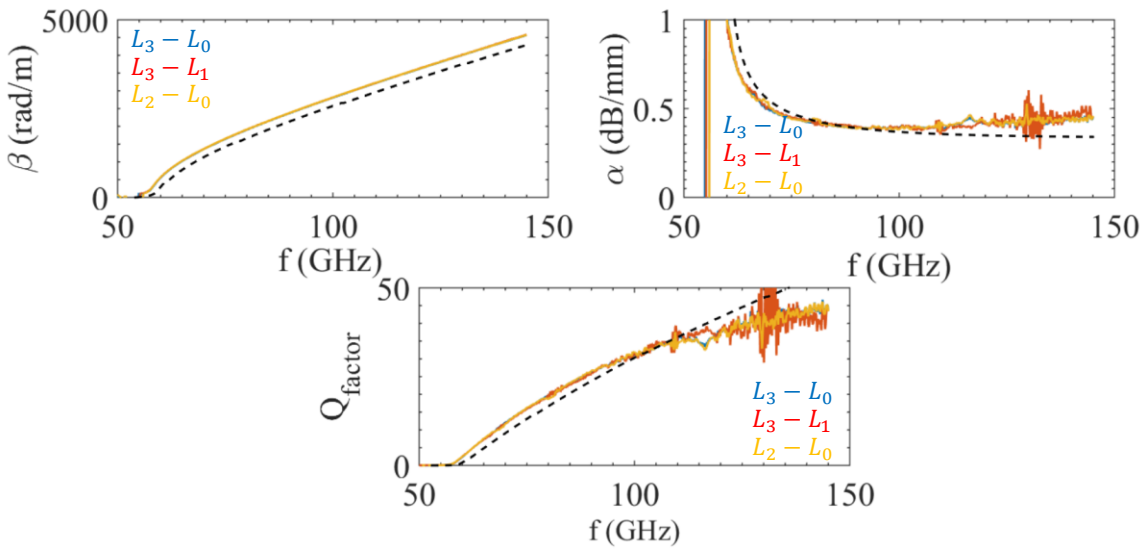

Figure 5-5: Measured (solid line) and simulated (dotted line) α, β and Q of the realized SIWs in WR10 band.

A very good agreement is obtained between simulation and measurement results in the whole frequency band from 50 GHz up to 115 GHz. Insertion loss, at 90 GHz, equals 0.39 dB/mm for both measured and simulated results. One only notice slightly higher measured insertion loss beyond 100 GHz, remaining lower than 0.5 dB up to 145 GHz. The Q factor is equal to 27, at 90 GHz and reaches more than 40 at 140 GHz. For the α an β extraction, three different pairs of measured SIWs ($L_3 - L_0$, $L_3 - L_1$ and $L_2 - L_0$) were considered, as explained earlier; the results are in very good agreement with each other. The measured cut-off frequency is found to be around 56 GHz and it is slightly shifted (2.5 GHz) towards the lower frequencies, as compared to simulations.

5.2.3 WR5 (140-220 GHz) band

Similarly, SIWs were designed in the WR5 band (140 GHz-220 GHz). The dimensions and the taper values are displayed in Table 5-12.

$W_{G\text{-}CPW}$ (µm)	G (µm)	d (µm)	L_{taper} (µm)	$\theta_{int\,taper}$(°)	θ_{taper} (°)
52	5	6	280	21.4	40.6

Table 5-12: G-CPW to SIW transition dimensions for WR5 band

Concerning waveguides, W is chosen equal to 0.797 mm, D equal to 20 µm and p equal to 35 µm. The four back-to-back SIWs have physical length equal to 2.33 mm, 2.68 mm, 3.73 mm and 5.165 mm, with G-CPW feeding lines.

First measurements of these circuits were carried out up to 145 GHz with the ANRITSU equipment to check if the simulated cut-off frequency equal to 114 GHz were respected. These first results are shown in Figure 5-6, where it is possible to notice how the cut-off frequency is slightly shifted around 109 GHz (5 GHz variation).

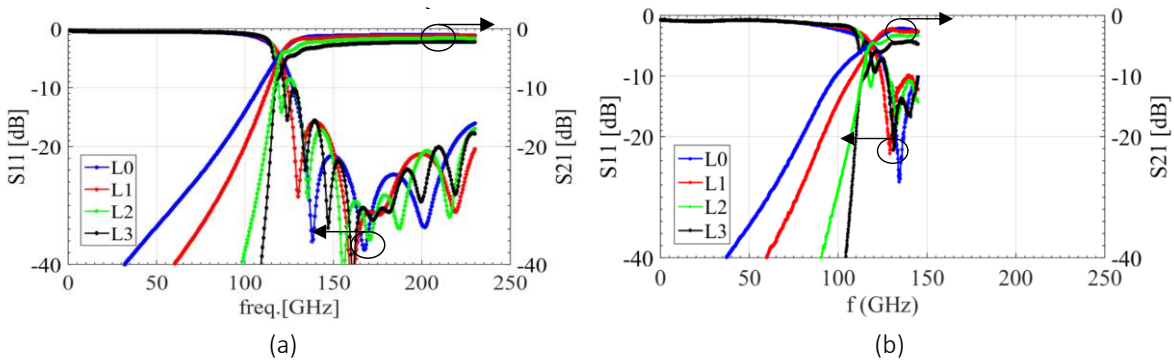

Figure 5-6: (a) Simulated and (b) measured S-Parameters back-to-back SIW results, in WR5 band

To show the performance of the simulated SIWs, the propagation constant β, the attenuation constant α and the quality factor were also extracted, from simulation only, by using the couple $L_3 - L_0$. Measurements at higher frequency are expected before conclusions. Simulated results are presented in Figure 5-7. It can be seen that small losses are expected. This is will be discussed in the next sub-section.

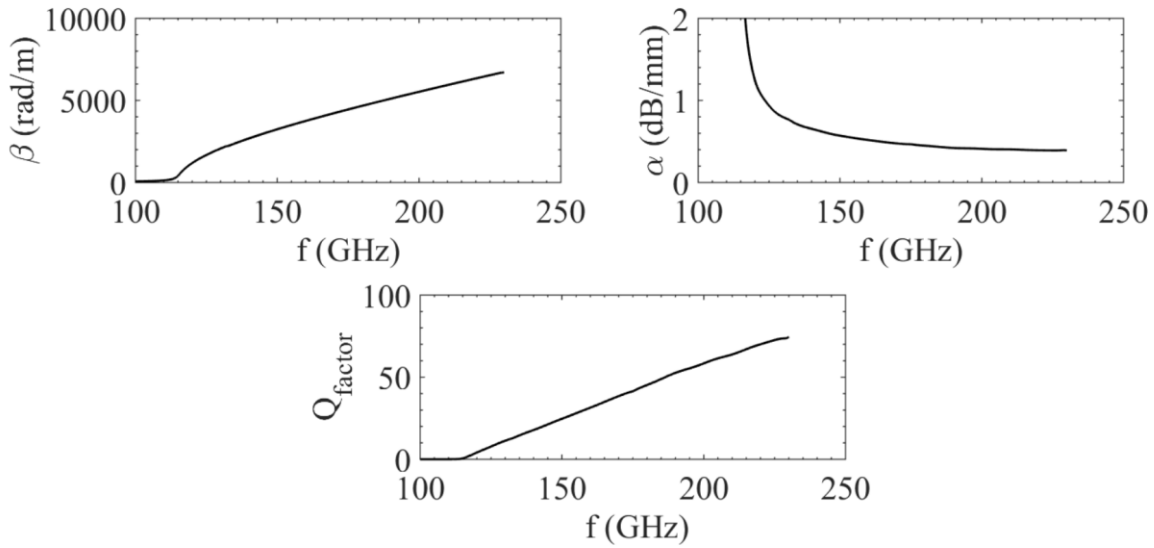

Figure 5-7: Simulated α, β and Q of the designed SIWs in WR5 band.

5.2.4 WR3 (220-325 GHz) band

SIWs corresponding to the WR3 (220-325 GHz) band were also designed in the same technology. Only simulation results are shown, since measurements have not been done yet. Simulation results of β, α and Q are shown in Figure 5-8 in order to predict the performance of such structures. The attenuation increases very slightly as compared to the WR10 band, since the loss tangent of the technology keeps low until the THz frequencies. Even more important, the form factor of the SIWs is more advantageous, with a width of 527 µm, as compared to 1.55 mm for the WR10 SIW. This leads to a ratio width/height reduced to 17.57 as compared to almost 52 and 26.6 in WR10 and WR5 band, respectively, thus leading to low overall losses equal to 0.52 dB/mm, at 270 GHz. Since β increases with frequency, the quality factor Q increases, reaching almost 100 at 350 GHz. Hence, high-performance passive circuits can be envisaged, like couplers, power dividers, and even medium band filters.

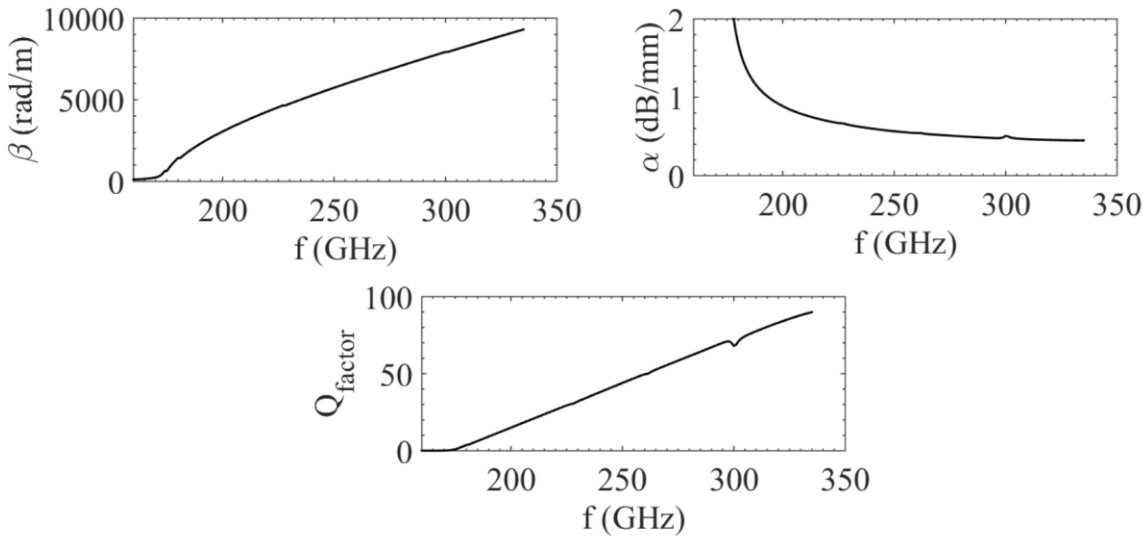

Figure 5-8: Simulated α, β and Q of the designed SIWs in WR3 band.

5.3 Short-slot 3-dB SIW coupler in BCB technology for WR10 (75-110 GHz) band

The 3-dB coupler suited for high-frequency BM is introduced in this section, showing the design, dimensions, and simulated and measured results. They were realized by using the short-slot topology [41], already presented in chapter 4.

5.3.1 Design

The BCB coupler is displayed in Figure 5-9, in WR10 frequency band.

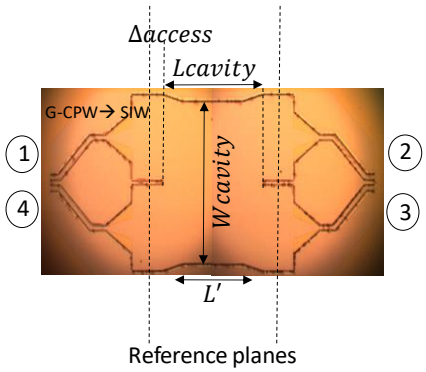

Figure 5-9: BCB SIW coupler in WR10 band

W_{cavity}, L_{cavity}, $\Delta acces$ and L' are 2.94 mm, 2.32 mm, 0.35 mm and 1.9 mm, respectively. The total length is 3.02 mm and the total width is 3.19 mm, without feeding lines. The G-CPW to SIW feeding lines were bended to favor the probes measurements and they should have been de-embedded with TRL after a LRRM calibration, but an unwanted short-circuit in the 'through' sample made it impossible to carry out. The short-circuit was generated during the fabrication process; anyway, the TRL samples are displayed Figure 5-10 and they had to be used for both coupler and crossover.

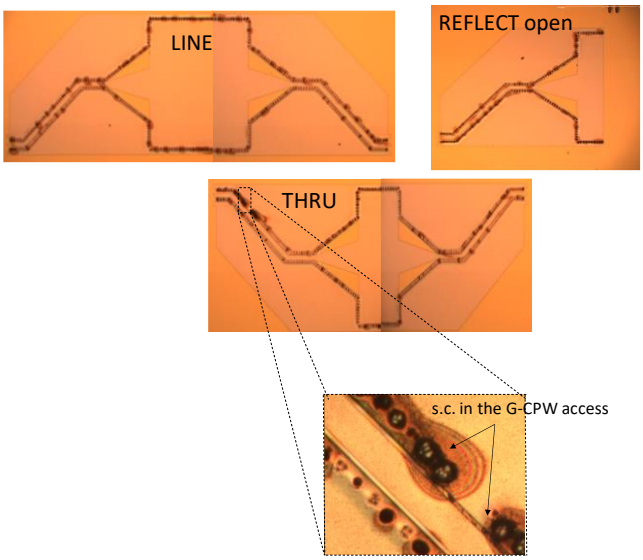

Figure 5-10: TRL samples for BCB coupler feeding lines de-embedding.

Finally, we decided to present the simulated results without feeding lines, while comparing the simulated results with feeding lines with the measurements, so that if the latter ones are in compliant with each other, we could expect a de-embedded measured device to be very similar to the simulated results without feeding lines.

5.3.2 Simulations and measurements

The HFSS simulated results without feeding lines are introduced in Figure 5-11.

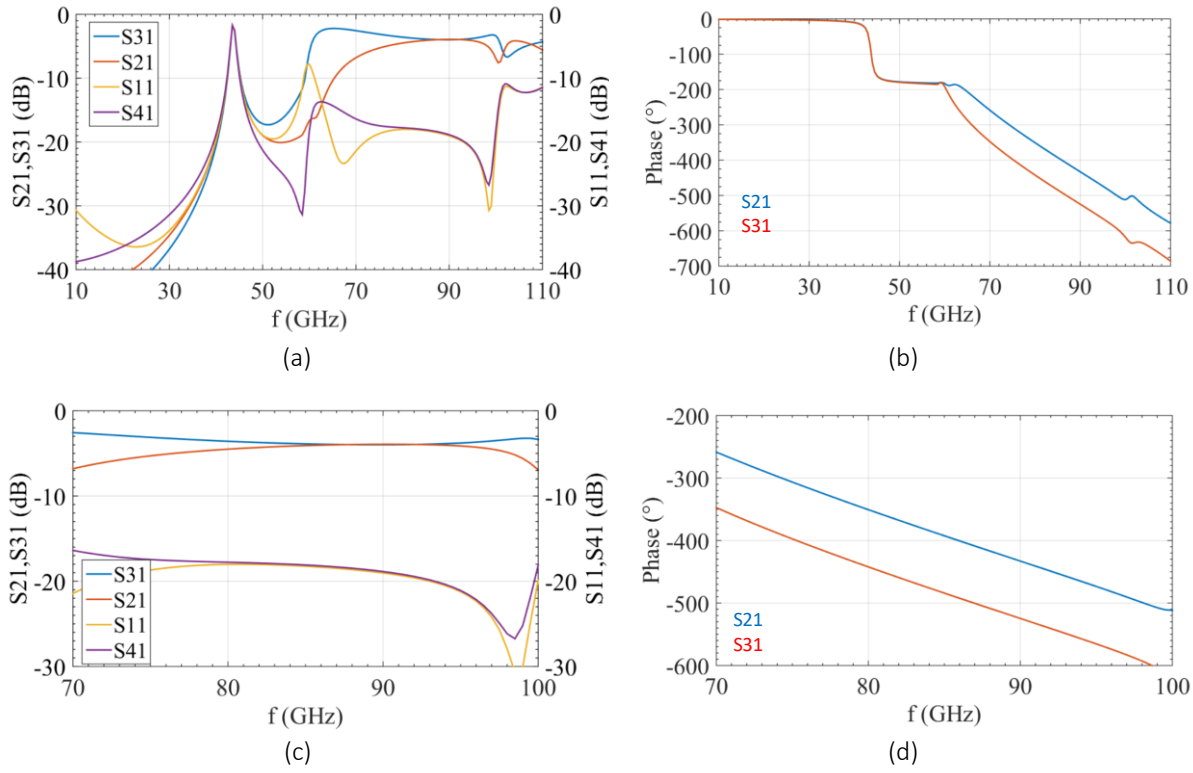

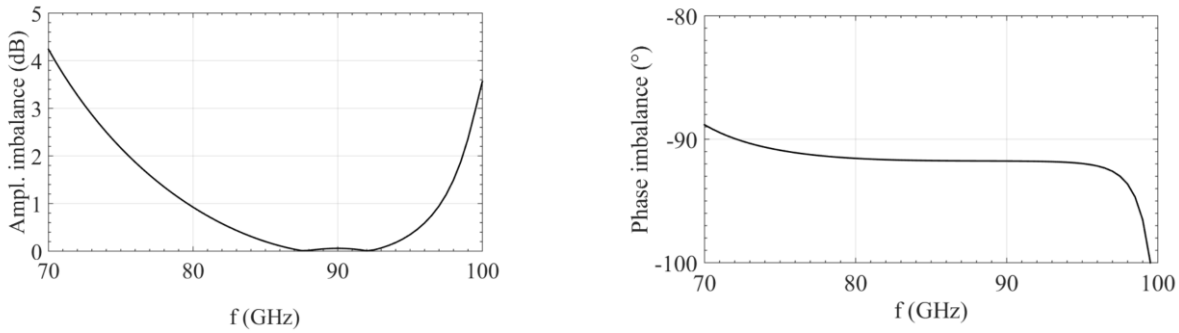

(e) (f)

Figure 5-11: Simulated BCB coupler results without feeding lines : (a) amplitude, (b) phase, (c) amplitude (zoom), (d) phase (zoom), (e) amplitude imbalance and (f) phase imbalance

The simulated amplitude imbalance is lower than 0.1 dB at 90 GHz, S_{21} and S_{31} being equal to -4 dB and -3.93 dB respectively, while remaining lower than 1 dB in a relative BW of 20% (79.5 GHz up to 97.5 GHz). The return loss and isolation are better than 18 dB, at 90 GHz, and they remain better than 10 dB in the whole WR10 band. The phase of S_{21} and S_{31} are -72.9°(-360°as an offset) and -164.7°°(-360°as an offset), respectively, making the phase imbalance equal to 1.8° at 90 GHz, while it remains within ±3° between 70 GHz and 98.5 GHz (31.7% of relative BW). The results meet typical requirements, as enlighten in chapter 2, very well.

The measured (solid lines) and simulated (dotted lines) results with feeding lines are compared in Figure 5-12.

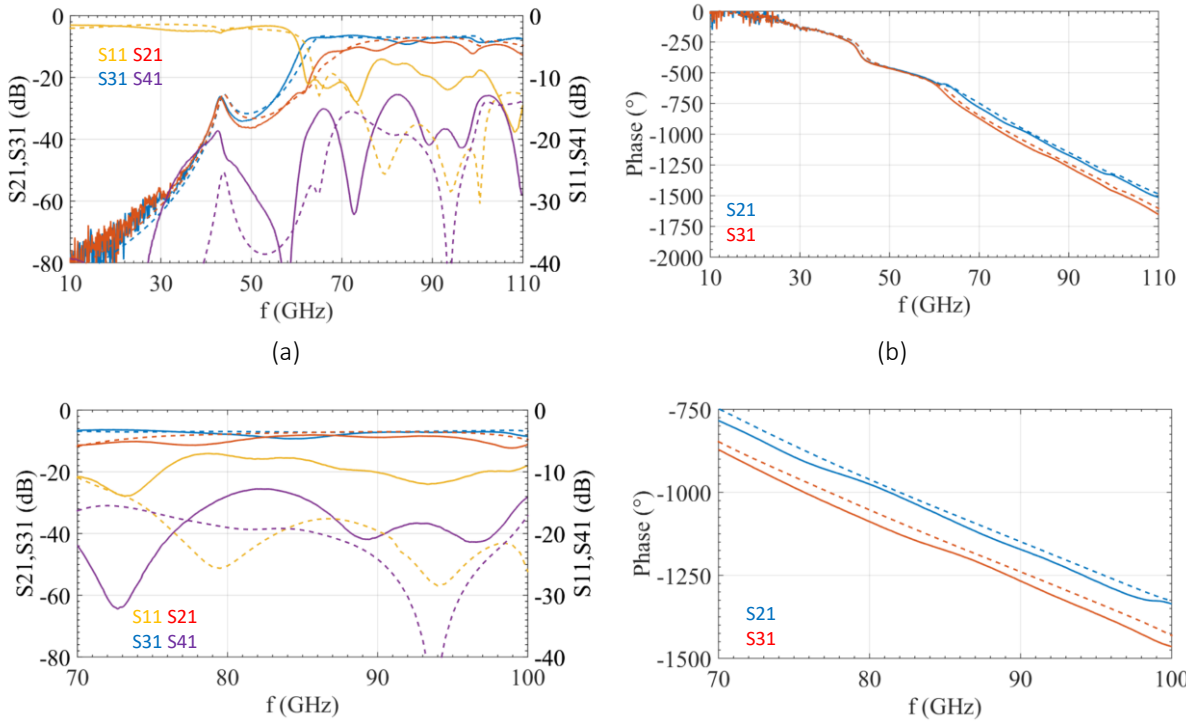

(a) (b)

(c) (d)

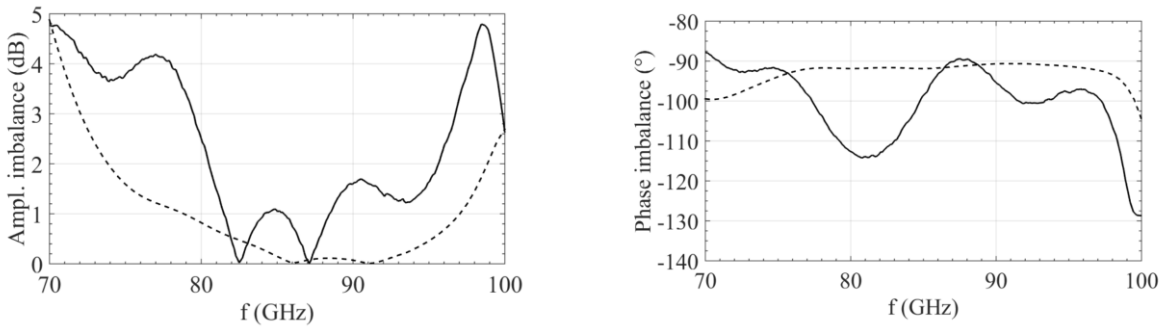

(e) (f)

Figure 5-12: Measured (solid lines) and simulated (dotted lines) BCB coupler results with feeding lines : (a) amplitude, (b) phase, (c) amplitude (zoom), (d) phase (zoom), (e) amplitude imbalance and (f) phase imbalance

Measurements were carried out on the Anritsu 145 GHz ME7838D4 VNA, using Form Factor RF microwave Infinity probes (i110) with 100 µm of pitch, from DC to 110 GHz. A LRRM calibration at pad level was implemented, as said earlier.

As it can be noticed, even if the measured return loss is worse than the simulated one, a quite good agreement is obtained between the measurements and the simulations in the whole frequency band (from 10 to 110 GHz). The measured amplitude imbalance is 1.6 dB, S_{21} and S_{31} being equal to -8.8 dB and -7.2 dB, at 90 GHz, while remaining lower than 1.6 dB in a relative BW of 15.6% (81 GHz up to 95 GHz). The return loss is equal to 10 dB, at 90 GHz, and it remains better than 10 dB between 89.6 GHz and 97 GHz (8.2% of relative BW). The latter can define the bandwidth of the device, but it is poor due to non-perfect matching between feeding lines and SIW device, whilst remaining quite good in simulation. The isolation is better than 20 dB and remains better than 10 dB in the overall WR10 band. The phase of S_{21} and S_{31} are -1173° (that is -93.2°) and -1269°(that is -189°) , respectively, making the phase deviation equal to 5.7° at 90 GHz, while the phase imbalance remains within ±3° between 89.2 GHz and 91.2 GHz (2.2% of relative BW). The return loss can be improved once the de-embedding will be done, because the effect of the feeding lines will be removed. The relative BW for phase imbalance within ±3° should also increase. Short-slot 0-dB SIW coupler in BCB technology for WR10 (75-110 GHz) band

5.3.3 Design

The BCB crossover is displayed in Figure 5-13.

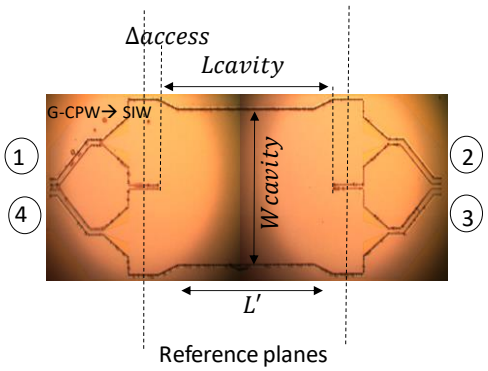

Figure 5-13: BCB SIW crossover in WR10 band

W_{cavity}, L_{cavity}, $\Delta acces$ and L' are 2.835 mm, 4.12 mm, 0.35 mm and 3.63 mm, respectively. The total length is 4.82 mm and the total width is 3.19 mm, without feeding lines. The G-CPW to SIW feeding accesses are the same as for coupler.

5.3.4 Simulations and measurements

Following the same approach as before, the simulated results without feeding lines are introduced in Figure 5-14.

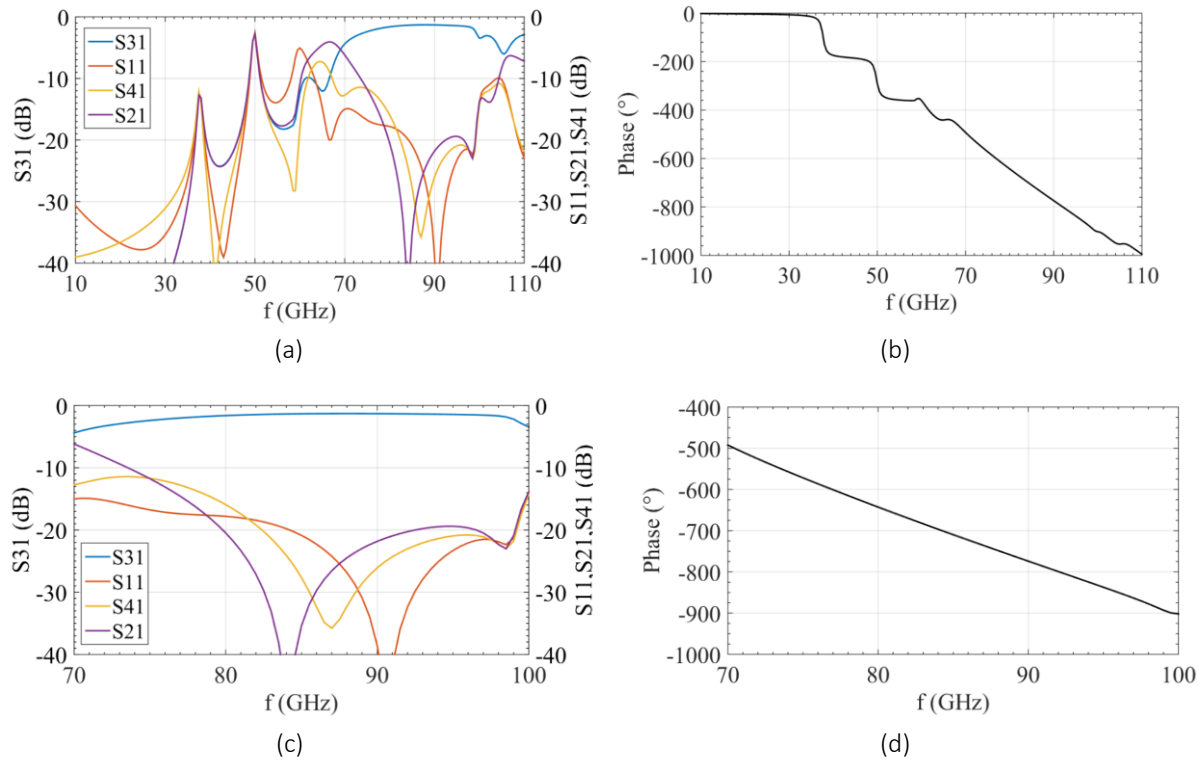

Figure 5-14: Simulated BCB crossover results without feeding lines : (a) amplitude and (b) phase,(c) amplitude (zoom), (d) phase (zoom).

The simulated insertion loss is 1.3 dB, at 90 GHz, while reducing by 1 dB in a relative BW of 26.7% (75.5 GHz up to 99.5 GHz). The return loss, transmission path isolation ($-S_{21_{dB}}$) and reflection path isolation($-S_{41_{dB}}$) are 38.6 dB, 21.8 dB and 26.1 dB at 90 GHz, respectively; the return loss and both isolations remain better than 10 dB in almost the whole WR10 band (73.5 GHz up to 104.5 GHz). The measured phase of S_{31} is equal to -773.9°(that is -53.9°) at 90 GHz, and it remains within ±10° between 89.5 GHz and 90.5 GHz (1.1% of relative BW), that shows a quite big dispersion of the device .

The same approach is used for crossover as for coupler, because of the lack of 'through' efficient sample. The measured (solid lines) and simulated (dotted lines) results with feeding lines are compared in Figure 5-15.

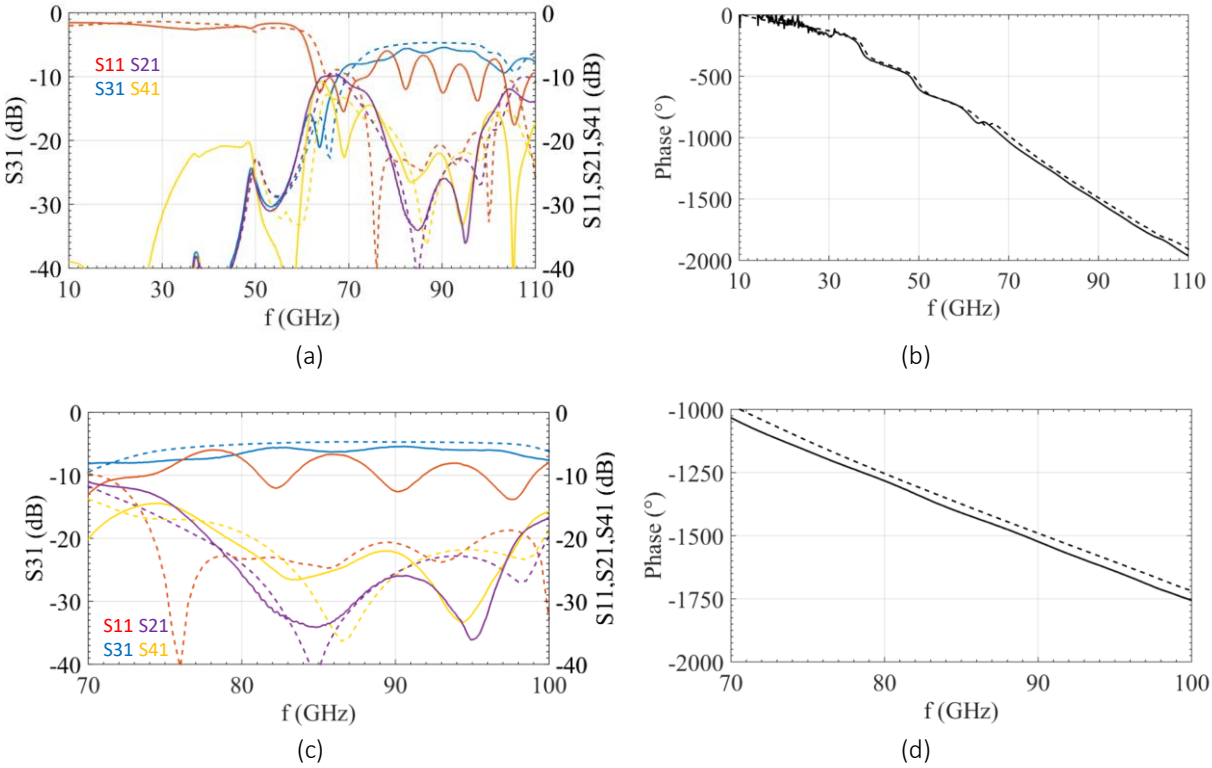

Figure 5-15: Measured (solid lines) and simulated (dotted lines) BCB crossover results with feeding lines : (a) amplitude and (b) phase,(c) amplitude (zoom), (d) phase (zoom).

Apart from the return loss, the measurements are in a quite good agreement with simulations as well as for coupler. As it can be noticed, the measured cross-coupling is 5.4 dB (4.7 dB in simulation), at 90 GHz, but no de-embedding has been performed. The transmission path isolation ($S_{21_{dB}}$ ideally equal to $-\infty$) is lower than 20 dB in a large frequency band (77.9 to 98 GHz) while the reflected path isolation remains better than 18 dB in the same frequency band. The level of the isolation on the transmission path is very important, as explained in chapter 2, and it is equal to 26 dB at 90, which represents a very good result. Anyway, it should be checked, once de-embedding is done, that in practice the part of the reflected power (bad S_{11}) should not leak towards the transmission path. The measured phase of S_{31} is equal to -1526°(that is -86°) at 90 GHz, and it remains within ±10° between 89.7 GHz and 90.5 GHz (0.9% of relative BW), that confirms the dispersion of the device. The very promising results for SIWs, coupler and crossover pave the way for high-frequency BM for 6G, wireless sensors or automotive radars, in BCB interposer technology.

5.4 Conclusion

The emergence of new applications above 100 GHz such as 6G, wireless sensors or automotive radars makes the interposers very good candidates for the frequency rising with respect to regular PCB or integrated technologies. Advantages and disadvantages of the main interposers technologies are introduced along this chapter with a general review on their respective performance. Among those technologies, the benzocyclobutene (BCB) seems to have very good properties for the design of performing high-frequency devices due to the low value of the real part of its dielectric permittivity and its low dielectric losses, at the same time.

SIWs were realized in a BCB interposer technology, available at the laboratory C2N, for WR10 (75-110 GHz), WR5 (240-220 GHz), and WR3 (220-325 GHz) bands, in order to demonstrate the performance of such packaging technology, showing interesting results in the WR10 band. Therefore, SIWs were exploited to design a 3-dB coupler and a crossover in short-slot topology for this band. Simulations and measurements were discussed, showing quite good results in terms of loss. Keeping in mind that the thickness of the organic layer is not the best suited for WR10 band, as compared to WR3, this should lead much room for state-of-art demonstrators in the WR3 band.

Finally, the results obtained in this chapter can lead to the development and implementation of a high-frequency BM network for the sixth generation (6G) of wireless networks, and beyond, built in a BCB interposer technology, as a general perspective for this work.

REFERENCE

[1] A. Usman *et al.*, 'Interposer Technologies for High-Performance Applications', *IEEE Transactions on Components, Packaging and Manufacturing Technology*, vol. 7, no. 6, pp. 819–828, Jun. 2017, doi: 10.1109/TCPMT.2017.2674686.

[2] M. Sunohara, H. Sakaguchi, A. Takano, R. Arai, K. Murayama, and M. Higashi, 'Studies on electrical performance and thermal stress of a silicon interposer with TSVs', in *2010 Proceedings 60th Electronic Components and Technology Conference (ECTC)*, Jun. 2010, pp. 1088–1093, doi: 10.1109/ECTC.2010.5490837.

[3] Soon Wee Ho, Seung Wook Yoon, Qiaoer Zhou, K. Pasad, V. Kripesh, and J. H. Lau, 'High RF performance TSV silicon carrier for high frequency application', in *2008 58th Electronic Components and Technology Conference*, May 2008, pp. 1946–1952, doi: 10.1109/ECTC.2008.4550249.

[4] V. Sukumaran, T. Bandyopadhyay, V. Sundaram, and R. Tummala, 'Low-Cost Thin Glass Interposers as a Superior Alternative to Silicon and Organic Interposers for Packaging of 3-D ICs', *IEEE Transactions on Components, Packaging and Manufacturing Technology*, vol. 2, no. 9, pp. 1426–1433, Sep. 2012, doi: 10.1109/TCPMT.2012.2204392.

[5] K. Oi *et al.*, 'Development of new 2.5D package with novel integrated organic interposer substrate with ultra-fine wiring and high density bumps', in *2014 IEEE 64th Electronic Components and Technology Conference (ECTC)*, May 2014, pp. 348–353, doi: 10.1109/ECTC.2014.6897310.

[6] N. Ranganathan, K. Prasad, N. Balasubramanian, and K. L. Pey, 'A study of thermo-mechanical stress and its impact on through-silicon vias', *Journal of Micromechanics and Microengineering*, vol. 18, no. 7, p. 075018, Jul. 2008, doi: 10.1088/0960-1317/18/7/075018.

[7] S. M. Sri-Jayantha, G. McVicker, K. Bernstein, and J. U. Knickerbocker, 'Thermomechanical modeling of 3D electronic packages', *IBM Journal of Research and Development; Armonk*, vol. 52, no. 6, pp. 623–634, Nov. 2008.

[8] V. Sukumaran *et al.*, 'Design, Fabrication, and Characterization of Ultrathin 3-D Glass Interposers With Through-Package-Vias at Same Pitch as TSVs in Silicon', *IEEE Transactions on Components, Packaging and Manufacturing Technology*, vol. 4, no. 5, pp. 786–795, May 2014, doi: 10.1109/TCPMT.2014.2303427.

[9] S. Cho, V. Sundaram, R. R. Tummala, and Y. K. Joshi, 'Impact of Copper Through-Package Vias on Thermal Performance of Glass Interposers', *IEEE Transactions on Components, Packaging and Manufacturing Technology*, vol. 5, no. 8, pp. 1075–1084, Aug. 2015, doi: 10.1109/TCPMT.2015.2450731.

[10] L. Brusberg, H. Schröder, M. Töpper, and H. Reichl, 'Photonic System-in-Package technologies using thin glass substrates', in *2009 11th Electronics Packaging Technology Conference*, Dec. 2009, pp. 930–935, doi: 10.1109/EPTC.2009.5416411.

[11] A. Yee, 'A Comparison of Low Cost Interposer Technologies', p. 16, 2013.

[12] X. Zhang *et al.*, 'Development of through silicon via (TSV) interposer technology for large die (21×21mm) fine-pitch Cu/low-k FCBGA package', in *2009 59th Electronic Components and Technology Conference*, May 2009, pp. 305–312, doi: 10.1109/ECTC.2009.5074032.

[13] 'IBM to produce Micron's hybrid memory cube in debut of first commercial, 3D chip-making capability'. https://phys.org/news/2011-12-ibm-micron-hybrid-memory-cube.html (accessed Apr. 22, 2020).

[14] 'Advanced Connectivity Solutions - Rogers Corporation'. https://www.rogerscorp.com/advanced-connectivity-solutions (accessed Apr. 22, 2020).

[15] W. Vis, B. C. Chou, V. Sundaram, and R. Tummala, 'Self-aligned chip-to-chip optical interconnections in ultra-thin 3D glass interposers', in *2015 IEEE 65th Electronic Components and Technology Conference (ECTC)*, May 2015, pp. 804–809, doi: 10.1109/ECTC.2015.7159684.
[16] F. Kreupl *et al.*, 'Carbon nanotubes in interconnect applications', *Microelectronic Engineering*, vol. 64, no. 1–4, pp. 399–408, Oct. 2002, doi: 10.1016/S0167-9317(02)00814-6.
[17] N. Srivastava, H. Li, F. Kreupl, and K. Banerjee, 'On the Applicability of Single-Walled Carbon Nanotubes as VLSI Interconnects', *IEEE Transactions on Nanotechnology*, vol. 8, no. 4, pp. 542–559, Jul. 2009, doi: 10.1109/TNANO.2009.2013945.
[18] H. Li and K. Banerjee, 'High-Frequency Analysis of Carbon Nanotube Interconnects and Implications for On-Chip Inductor Design', *IEEE Transactions on Electron Devices*, vol. 56, no. 10, pp. 2202–2214, Oct. 2009, doi: 10.1109/TED.2009.2028395.
[19] P. Kim, L. Shi, A. Majumdar, and P. L. McEuen, 'Thermal Transport Measurements of Individual Multiwalled Nanotubes', *Physical Review Letters*, vol. 87, no. 21, Oct. 2001, doi: 10.1103/PhysRevLett.87.215502.
[20] T. Xu, Z. Wang, J. Miao, X. Chen, and C. M. Tan, 'Aligned carbon nanotubes for through-wafer interconnects', *Applied Physics Letters*, vol. 91, no. 4, p. 042108, Jul. 2007, doi: 10.1063/1.2759989.
[21] P. Franck, D. Baillargeat, and B. K. Tay, 'Mesoscopic Model for the Electromagnetic Properties of Arrays of Nanotubes and Nanowires: A Bulk Equivalent Approach', *IEEE Transactions on Nanotechnology*, vol. 11, no. 5, pp. 964–974, Sep. 2012, doi: 10.1109/TNANO.2012.2209457.
[22] E. Pistono, P. Coquet, J. Wang, D. Baillargeat, J. de Saxce, and S. Bila, 'Potentialities of Air-Filled Substrate Integrated Waveguides based on Carbon Nanotubes in E-band', p. 4.
[23] M. V. Pelegrini *et al.*, 'Interposer based on metallic-nanowire-membrane (MnM) for mm-wave applications', in *2016 11th European Microwave Integrated Circuits Conference (EuMIC)*, Oct. 2016, pp. 532–535, doi: 10.1109/EuMIC.2016.7777609.
[24] H. Masuda and K. Fukuda, 'Ordered Metal Nanohole Arrays Made by a Two-Step Replication of Honeycomb Structures of Anodic Alumina', *Science*, vol. 268, no. 5216, pp. 1466–1468, Jun. 1995, doi: 10.1126/science.268.5216.1466.
[25] J. M. Pinheiro *et al.*, '110-GHz Through-Substrate-Via Transition Based on Copper Nanowires in Alumina Membrane', *IEEE Transactions on Microwave Theory and Techniques*, vol. 66, no. 2, pp. 784–790, Feb. 2018, doi: 10.1109/TMTT.2017.2763142.
[26] A. L. C. Serrano *et al.*, 'Modeling and Characterization of Slow-Wave Microstrip Lines on Metallic-Nanowire- Filled-Membrane Substrate', *IEEE Transactions on Microwave Theory and Techniques*, vol. 62, no. 12, pp. 3249–3254, Dec. 2014, doi: 10.1109/TMTT.2014.2366108.
[27] A. L. C. Serrano *et al.*, 'Slow-wave microstrip line on nanowire-based alumina membrane', in *2014 IEEE MTT-S International Microwave Symposium (IMS2014)*, Jun. 2014, pp. 1–4, doi: 10.1109/MWSYM.2014.6848552.
[28] A. Cayron, C. Viallon, O. Bushueva, A. Ghannam, and T. Parra, 'High-Performance Compact 3-D Solenoids for RF Applications', *IEEE Microwave and Wireless Components Letters*, vol. 28, no. 6, pp. 479–481, Jun. 2018, doi: 10.1109/LMWC.2018.2831438.
[29] A. Cayron, C. Viallon, A. Ghannam, A. Magnani, and T. Parra, 'Wideband and Compact 3-D Quadrature Coupler for 5G Applications', in *2019 49th European Microwave Conference (EuMC)*, Oct. 2019, pp. 129–132, doi: 10.23919/EuMC.2019.8910742.
[30] A.-S. Grimault-Jacquin *et al.*, 'Characteristics of Coplanar Waveguide of Small Cross Section on BCB with Coplanar Ground to Conductor-Backed Plane Interconnection', *J*

Infrared Milli Terahz Waves, vol. 40, no. 10, pp. 1010–1020, Oct. 2019, doi: 10.1007/s10762-019-00624-x.
[31] H. J. Tang, G. Q. Yang, J. X. Chen, W. Hong, and K. Wu, 'Millimeter-wave and terahertz transmission loss of CMOS process-based substrate integrated waveguide', in *2012 IEEE/MTT-S International Microwave Symposium Digest*, Jun. 2012, pp. 1–3, doi: 10.1109/MWSYM.2012.6259786.
[32] M. S. Mahani and G. W. Roberts, 'A mmWave Folded Substrate Integrated Waveguide in a 130-nm CMOS Process', *IEEE Transactions on Microwave Theory and Techniques*, vol. 65, no. 8, pp. 2775–2788, Aug. 2017, doi: 10.1109/TMTT.2017.2661259.
[33] I.-J. Hyeon and C.-W. Baek, 'Millimeter-Wave Substrate Integrated Waveguide Using Micromachined Tungsten-Coated Through Glass Silicon Via Structures', *Micromachines*, vol. 9, no. 4, p. 172, Apr. 2018, doi: 10.3390/mi9040172.
[34] J. Tong, V. Sundaram, A. Shorey, and R. Tummala, 'Substrate-integrated waveguides in glass interposers with through-package-vias', in *2015 IEEE 65th Electronic Components and Technology Conference (ECTC)*, May 2015, pp. 2222–2227, doi: 10.1109/ECTC.2015.7159912.
[35] M. Bertrand *et al.*, 'Substrate Integrated Waveguides for mm-wave Functionalized Silicon Interposer', in *2018 IEEE/MTT-S International Microwave Symposium - IMS*, Jun. 2018, pp. 875–878, doi: 10.1109/MWSYM.2018.8439287.
[36] G. Gentile *et al.*, 'Silicon-Filled Rectangular Waveguides and Frequency Scanning Antennas for mm-Wave Integrated Systems', *IEEE Transactions on Antennas and Propagation*, vol. 61, no. 12, pp. 5893–5901, Dec. 2013, doi: 10.1109/TAP.2013.2281518.
[37] M. Bertrand *et al.*, 'Integrated Waveguides in Nanoporous Alumina Membrane for Millimeter-Wave Interposer', *IEEE Microwave and Wireless Components Letters*, vol. 29, no. 2, pp. 83–85, Feb. 2019, doi: 10.1109/LMWC.2018.2887193.
[38] D. Deslandes and K. Wu, 'Design Consideration and Performance Analysis of Substrate Integrated Waveguide Components', in *32nd European Microwave Conference, 2002*, Milan, Italy, Oct. 2002, pp. 1–4, doi: 10.1109/EUMA.2002.339426.
[39] P. Souzangar and M. Shahabadi, 'Numerical Multimode Thru-Line (TL) Calibration Technique for Substrate Integrated Waveguide Circuits', *Journal of Electromagnetic Waves and Applications*, vol. 23, no. 13, pp. 1785–1793, Jan. 2009, doi: 10.1163/156939309789566969.
[40] 'ANSYS HFSS 18 – Raising the Bar in Electronics | ANSYS Blog'. https://www.ansys.com/blog/ansys-hfss-18 (accessed May 27, 2020).
[41] H. J. Riblet, 'The Short-Slot Hybrid Junction', *Proceedings of the IRE*, vol. 40, no. 2, pp. 180–184, Feb. 1952, doi: 10.1109/JRPROC.1952.274021.

General conclusion and prospects

The work achieved in this PhD thesis was focused on the conception of amulti-beam antenna system, so called Butler matrix, for mm-wave applications. Two frequency bands were mainly addressed for that purpose in SIW topology. The first one is the band around 28 GHz, that is suited for 5G, where an extended beam concept was introduced for 4x4 Butler matrix, in PCB technology, to achieve a better spatial resolution, as compared to a 4x4 conventional system. The second one is the WR10 band (75 GHz-110 GHz) and beyond, WR5 (140-220 GHz) and WR3 (220-325 GHz) band, where the use of intermediate packaging platforms, so called interposers, allow the frequency rising as compared to the conventional PCB technologies. In both, the proposed structures were detailed, then theoretical analyses were developed, and simulation and measurement results were carried out, with retro-simulations when needed, which permitted to validate the proposed concepts by proofs of concept. The main goal of this manuscript is to enhance the spatial antenna coverage while keeping almost unchanged the surface (reduced costs and design complexity) and the performance of the beam forming system as compared to its conventional counterpart.

In the first chapter of this thesis, after a brief description of multi-beam antenna applications in the context of 5G, IoT and satellite communications, Butler matrix solutions for RF and mm-wave circuits were presented, with a state-of-the-art of the most classical BM structures, realized either with microstrip transmission lines or substrate integrated waveguides (SIW). This section also provides a distinction between single-layer or multi-layer technology. Finally, beam-steering enhanced ability BMs was detailed in this chapter. The techniques to improve the spatial coverage allowed demonstrating ever-increasing researcher's interests concerning this system in recent years.

In the second chapter attention focused on a detailed sensitivity study based on Monte Carlo approach. In the first part, a Monte Carlo analysis was applied to vary the input of four antennas to notice the influence on the radiation pattern, according to a uniform distribution. Secondly, the Monte Carlo analysis was carried out for stand-alone Butler matrix devices, so as to figure out their impact on the previous radiation pattern study. The crossover transmission path isolation level was proved to be an issue for Butler matrix designers, when it is as low as 20 dB. The latter one was also proved for a PCB technology. Analytical electromagnetic equations were provided to strengthen the thesis, as well. In the central part of the second chapter, the extended beam concept to enhance the beam capability was detailed, through the use of switched-line SIW tunable phase shifters. In the last part, reconfigurable radiation pattern antennas for extended beam Butler matrix agility were introduced along with a short state-of-the-art. A reconfigurable pattern antenna was designed and optimized, at 28 GHz, in PCB technology. The results showed the advantages of using such a kind of antenna as compared to conventional single beam antennas.

In the first part of third chapter, the pros and cons of continuous and digital phase shifting were discussed and a detailed state-of-the-art was reported for PCB technology. Based on this analysis, the choice of the approach for our tunable phase shifter was a digital switched-line one. A first prototype was presented at 5.8 GHz and its working principle was highlighted,

which consists in routing the EM wave towards one or the other of the two possible paths, paths 1 and 2, by enabling or disabling floating reconfigurable vias. A detailed study based on HFSS simulation was carried out to optimize the device. In the second part of this chapter, the target frequency increased to 28 GHz to be suited for 5G applications. Thus, a 28-GHz 1-bit phase shifter was designed and tested, using PIN diodes. The bias circuit technique was also introduced, which needs a three metal layer PCB technology. The measured FoM is 161°/dB and the size of the phase shifter is 13.72 mm × 10.9 mm without feeding lines and bias circuit.

In the fourth chapter, the design blocks for 28 GHz SIW Butler matrix were introduced and measured. In the first part, 3-dB coupler and crossover realized in short-slot topology are presented, along with the state-of-the-art of SIW couplers and crossovers for PCB technology. Afterwards, all the phase shifters included in the Butler matrix system were discussed and measured. For a proof-of-concept, for each 1-bit phase shifter two not reconfigurable phase shifters were fabricated, representing either a RF path or the other. They were arranged in the system with the couplers and crossovers, forming two whole Butler matrices. Design techniques and insights were given, either. In the second part of the chapter, the measurements of the Butler matrices give rise to a detailed analysis of the results, and their impact on the array pattern of the array antenna system was discussed, as well.

Frequencies from at least 60 GHz up to 1 THz are promising bands for the next generation of wireless communication systems, because of the wide unused and unexplored spectrum. In that context, new performing technologies so-called interposers, that can allow the frequency rising, were discussed in the fifth final chapter. In the first part, a general review of the advantages and disadvantages of the main interposers technologies (commercialized silicon, organic, glass, and under research CNT and MnM) was introduced . As a challenger to still under research technologies, the benzocyclobutene seemed to have very good properties for the design of performing high-frequency devices. Therefore, BCB SIW lines useful for Butler matrix blocks were designed and measured in WR10 and WR5 bands, which show the very interesting performance of such an interposer. In the second part of the chapter, by exploiting the SIW lines, 3-dB coupler and crossover were realized in short-slot topology. Design and measurements were discussed, that show good results in terms of loss, paving the way towards very interesting results at higher frequencies.

To conclude, the proposed SIW extended beam 4x4 Butler matrix system exhibit a high size reduction in comparison with conventional 8x8 Butler matrix counterpart. Moreover, it provides a much better spatial resolution as compared to its conventional 4x4 Butler matrix counterpart. Therefore, some prospects of this thesis work will be discussed here. Firstly, the phase shifter at 5.8 GHz could be made tunable by adding PIN diodes, so that a comparison can be done with its 28 GHz counterpart. Secondly, the whole Butler matrix could be made fully tunable and re-optimized to improve the performance. The use of MEMS could be an easier solution that could replace the use of PIN diodes in the system. Thirdly, the reconfigurable pattern antenna could be inserted in a 1x4 array to be simulated, fabricated and measured. The next step would be to plug it into the Butler matrix system to finalize the work. Furthermore, the extended beam Butler matrix concept could be implemented in BCB interposer for sub-THz

applications to test the feasibility. For that purpose, SIW devices in WR5, WR3 and WR2 (up to 500 GHz) bands were designed and fabricated. They are waiting for being tested.

Annexe 1

Details on the DC bias / RF-DC decoupling circuits (dimensions, results).

The DC bias feeding can be figured out by looking at Figure 1.

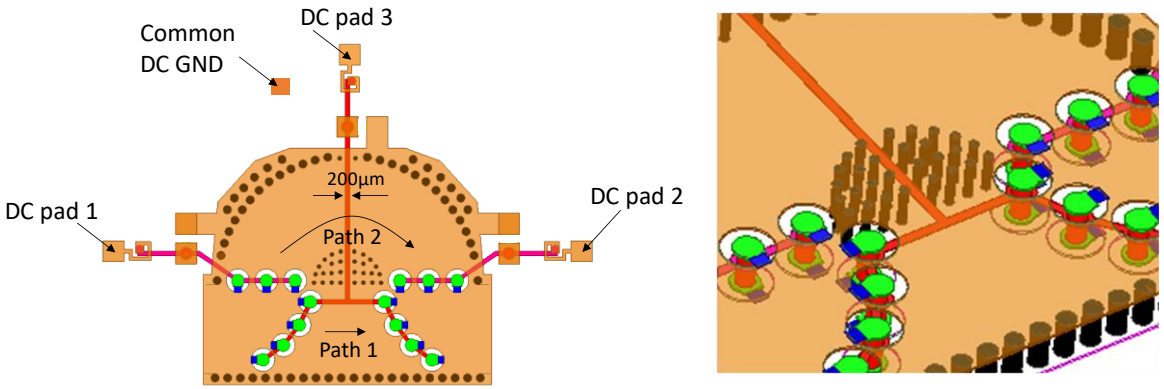

(a) (b)

Figure 1: DC bias 1-bit PS feeding

A DC current generator supplies the DC pads 1 and 2 with 180mA when path 1 is enabled, while a DC voltage generator provides a reverse bias of -5V to DC pad 3. On the contrary, a DC current generator feeds DC pad 3 with 240mA and a DC voltage generator feeds in reverse bias the DC pads 1 and 2 with -5V, when path 2 is enabled. All the generators are connected to the same common DC ground. The DC feeding is made by using the intermediate metal layer like in Figure 1(b). The DC decoupling is simply made by slotting the upper and bottom metal layer around the reconfigurable vias (G=250µm). All the reconfigurable vias corresponding to path 1 or path 2, respectively, were connected with each other through 0.2 mm width metal strips, whose length was set to avoid resonances in the RF path. On the other hand, the RF decoupling circuit is shown in Figure 2 with its dimensions.

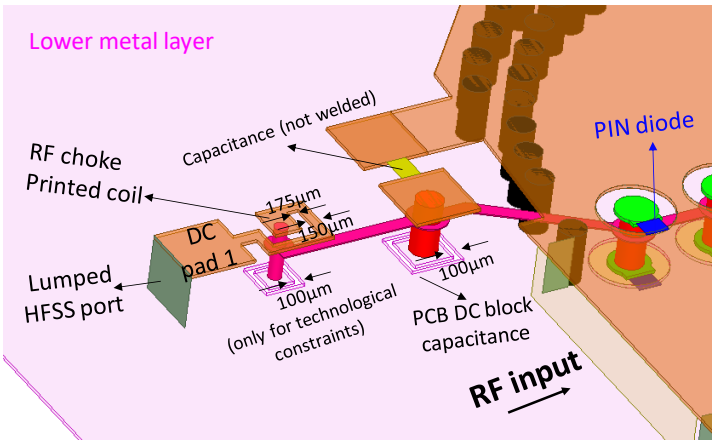

Figure 2: RF decoupling circuit

'Lumped ports' were inserted on HFSS to verify the RF level that heads to DC pad. The 'lumped ports' were renormalized as either 1 Ω or 1000 Ω, to simulate the internal impedance of a DC voltage or current generator, respectively.

The simulated results when path 1 and 2 are enabled, are shown in Figure 3 and Figure 4, respectively.

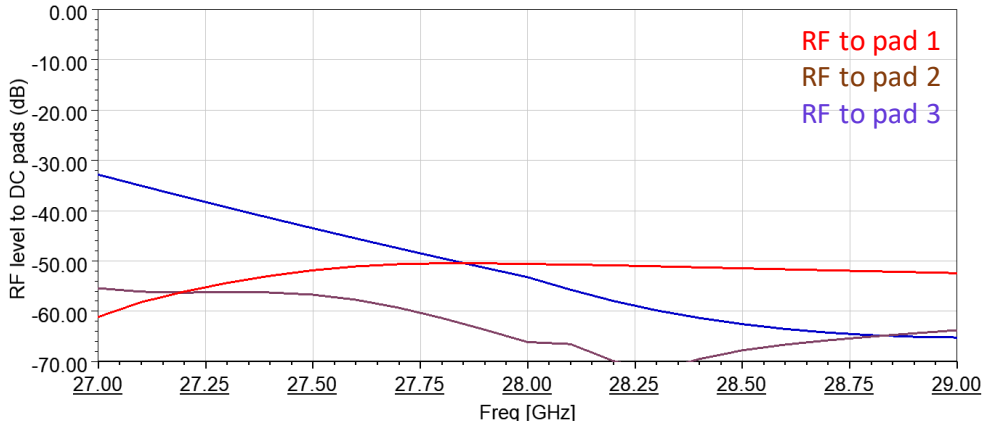

Figure 3: RF level to DC pads when path 1 is enabled

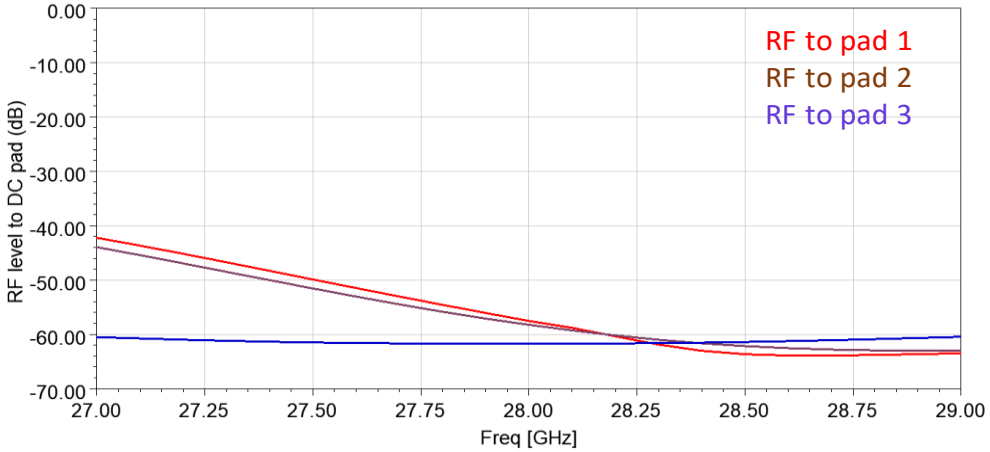

Figure 4: RF level to DC pads when path 2 is enabled

From the results, when path 1 is enabled, the RF transmission flowing from the waveguide input port towards DC pads 1 and 2 is lower than -50 dB, while it is lower than -30 dB for DC pad 3, from 27 GHz to 29 GHz.

When path 2 is enabled, the RF transmission is always lower than -40 dB, over the same frequency range.

Annexe 2

Details on the G-CPW - SIW feeding line transition (dimensions, results).

The dimensions of G-CPW to SIW feeding line transitions are shown in Figure 5.

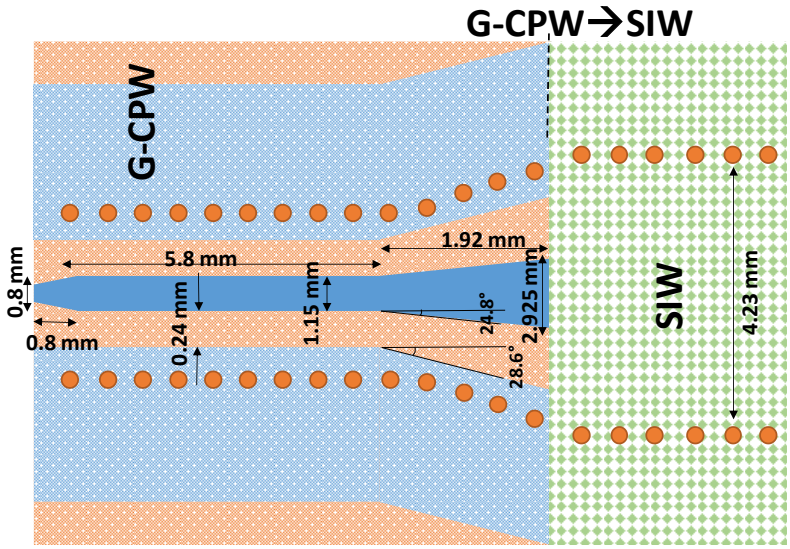

Figure 5: G-CPW to SIW transitions

The dimensions of G-CPW are related to $\lambda_g = 7.68\ mm$.

A first taper was used to avoid capacitance effect between the structure and the connectors, while the second one was used to turn the quasi-TEM G-CPW mode into a TE_{10} mode suited for SIW propagation. For this purpose, the second taper was modeled by adjusting two angles and its length is close to $\lambda_g/4$ to favor the matching.

Simulation results for different SIW lengths going from λ_g to $2\lambda_g$, are given in Figure 6.

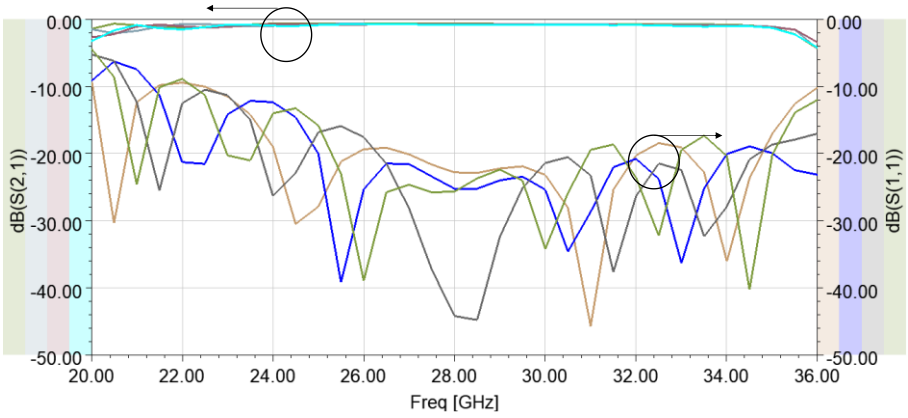

Figure 6: G-CPW to SIW transitions results

Annexe 3

Details on the design/dimensions of the calibration standards and on the calibration procedure.

Several calibration standards and procedures were adopted during this thesis, according to the device to be measured. For example, for 1-bit SIW PS a first SOLT (short-open-load-through) calibration was done to get the error matrices including the RF VNA cable effect. Afterwards a TRL method was made to remove the G-CPW to SIW feeding lines, as shown in Figure 7. The line is $\lambda_g/4$ longer than the through, that is 1.92 mm.

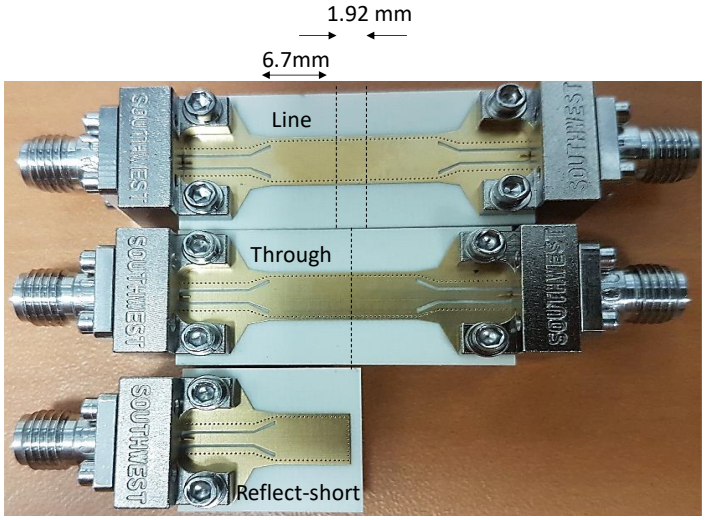

Figure 7: TRL samples with straight feeding lines

The reference planes are shown, as well. The reflect is short-circuited.

Measured results are shown in Figure 8.

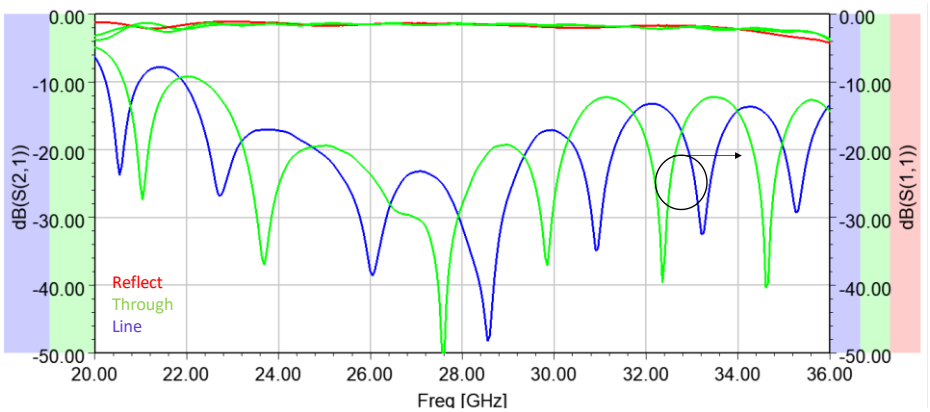

Figure 8: Measured TRL samples

The return loss is better than 10 dB between 22 and 36 GHz.

A similar procedure was also used to de-embed the fixed PSs, but a TRL was directly applied without a SOLT to de-embed both the RF VNA cables and the G-CPW to SIW feeding lines. Moreover, the feeding line sin matter are shorter in this case.

Moreover, a different feeding lines shape (bended-shaped) was used for the coupler, crossover and BM. Anyway, the procedure is the same. The bended-shaped TRL samples are displayed in Figure 9.

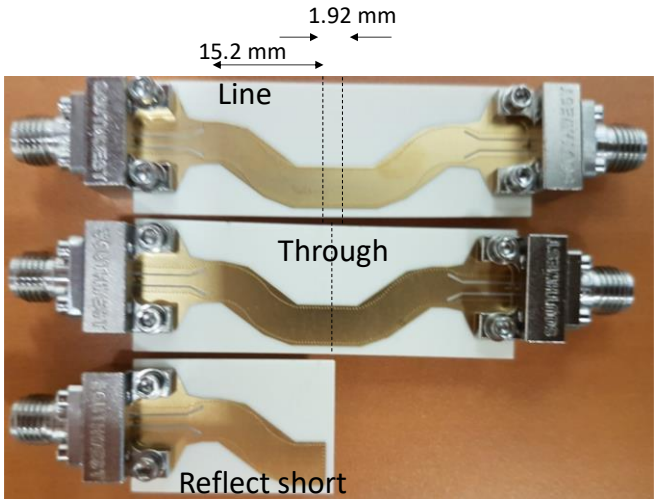

Figure 9: TRL samples with bended feeding lines

Assuming that no coupling occurs at feeding lines level, a 2-ports TRL can be used to de-embed 4-ports (coupler and crossover) and 8-ports (BM) devices.

The latter one is possible if the error matrix "ErrA" and "ErrB" are extracted after the TRL method. "ErrA" and "ErrB" matrices correspond to the left and right feeding lines error matrices, respectively. For example, if a coupler has to be de-embedded the following schematic has to be arranged on ADS, for a post TRL manipulation (see Figure 10).

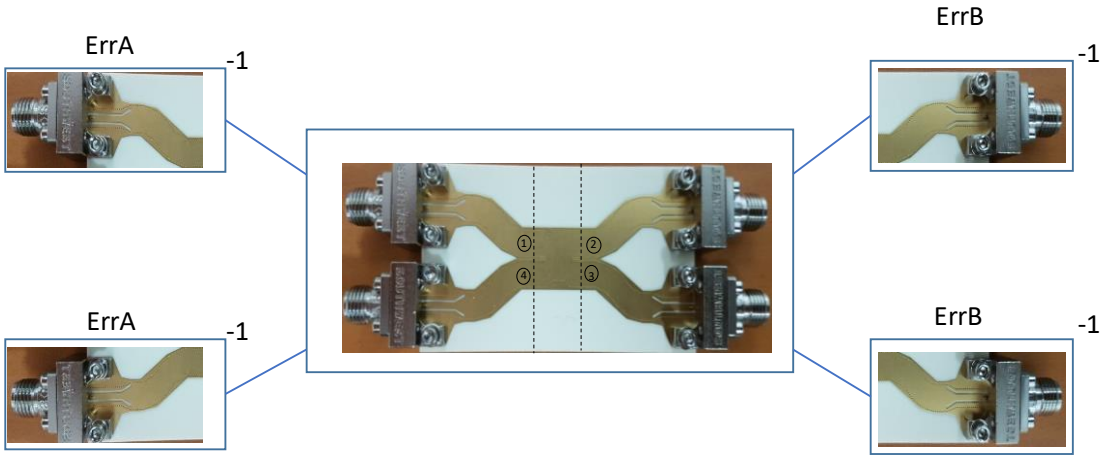

Figure 10: ADS procedure to de-embed more than 2-ports not coupled feeding lines

The same procedure was used for crossover and BM, as well.

Finally, to extract the attenuation and the propagation constant for TeraPacipode SIWs, as it is reported in chapter 5, a LRRM calibration at pad level was implemented first. Afterwards a two-line method was used in which the shortest SIW L0 is used as a 'through' and the other SIWs can be used as a 'line'. The dimensions and results of those SIWs are already reported in chapter 5.

Publications

Conference papers published during the thesis:

G.Acri, P. Ferrari, E.Pistono, L.Boccia, G.Amendola, D. Calzona, “Coupleur hybride miniature en technologie CMOS FDSOI 28 nm en bande millimétrique”, 20èmes journées nationales micro-ondes, May 2017, Saint Malo, France.

M. Bertrand, E. Pistono, **G. Acri**, D. Kaddour, F. Podevin, Vi. Puyal, S. Tolunay Wipf, Ch. Wipf, M. Wietstruck, M. Kaynak, P. Ferrari, "Substrate Integrated Waveguides for mm-wave Functionalized Silicon Interposer," 2018 IEEE/MTT-S International Microwave Symposium - IMS, Philadelphia, PA, 2018, pp. 875-878.

M. Wietstruck ; S. Marschmeyer ; S. Tolunay Wipf ; C. Wipf ; T. VoB ; M. Bertrand ; E. Pistono ; **G. Acri** ; F. Podevin ; P. Ferrari ; M. Kaynak, “Design Optimization of Through-Silicon Vias for Substrate-Integrated Waveguides embedded in High-Resistive Silicon Interposer”, 2018 IEEE 20th Electronics Packaging Technology Conference (EPTC), Singapore , 2018.

G. Acri, F Podevin., E.Pistono, P. Ferrari, L.Boccia, A. S. Grimault-Jacquin, N. Zerounian, F.Aniel, “Guides d'onde SIW sur interposeur polymère pour applications millimétriques’’, 21èmes journées nationales micro-ondes, May 2019, Caen, France.

G. Acri, E.Pistono, F Podevin., P. Ferrari, L.Boccia, “Déphaseur SIW accordable 2 voies à laide dune approche par via reconfigurable’’, 21èmes journées nationales micro-ondes, May 2019, Caen, France.

G.Acri, L.Boccia, N. Corrao, F.Podevin, E. Pistono, T. Lim, E. N. Isa, and P.Ferrari, ‘‘Compact and performing transmission lines for mm-wave circuits design in advanced CMOS technology’’, 2019 14th European Microwave Integrated Circuits Conference (EuMIC), Paris, France, 2019.

G.Acri, E.Pistono, F.Podevin , P.Ferrari, L.Boccia, A.-S. Grimault-Jacquin , N. Zerounian, F. Aniel, L.Vincent,‘‘BenzoCycloButene-based in-Package Substrate Integrated Waveguides for sub-THz Applications’’,2020 50th European Microwave Conference (EuMC), Utrecht, Netherlands, 2020.

Journal papers published during the thesis:

Duc-Long Luong, **G.Acri**, F.Podevin, D.Vincent, E.Pistono, A.Serrano, P.Ferrari, ‘‘Forward-wave Directional Coupler based on Slow-wave Coupled Microstrip Lines’’, IET Microwaves Antennas and Propagation, vol. 13, Issue 14, 27 November 2019, p. 2486 – 2489.

G. Acri, F. Podevin, E. Pistono, L. Boccia, N.Corrao, T. Lim, E.N. Isa, and P. Ferrari, ‘‘A Millimeter-Wave Miniature Hybrid Coupler in 22nm CMOS Technology’’, IEEE Solid-State Circuits Letters , vol. 2 , issue: 6 , June 2019, pp. 45 – 48.

Journal papers in preparation:

G. Acri, F. Podevin, E. Pistono, L. Boccia, P. Ferrari, "A 28-GHz reconfigurable 1-bit Substrate-Integrated-Waveguide based Phase Shifter", IEEE Microwave and Wireless Components Letters (MWCL).

“Life is like jumping off a waterfall: you never know where you’ll land.
Hence, live life to the fullest as long as you are on the top”.

—Giuseppe Acri